

INSTABILITY AND TRANSITION ON A SLICED CONE WITH A FINITE-SPAN  
COMPRESSION RAMP AT MACH 6

A Dissertation

Submitted to the Faculty

of

Purdue University

by

Gregory R. McKiernan

In Partial Fulfillment of the

Requirements for the Degree

of

Doctor of Philosophy

May 2020

Purdue University

West Lafayette, Indiana

**THE PURDUE UNIVERSITY GRADUATE SCHOOL  
STATEMENT OF DISSERTATION APPROVAL**

Dr. Steven P. Schneider, Chair

School of Aeronautics and Astronautics

Dr. Jonathan Poggie

School of Aeronautics and Astronautics

Dr. Sally P. Bane

School of Aeronautics and Astronautics

Dr. Bradley M. Wheaton

Johns Hopkins University Applied Physics Laboratory

**Approved by:**

Dr. Gregory Blaisdell

Head of the School Graduate Program

To Emily, my parents, grandparents, and Piper

## ACKNOWLEDGMENTS

This dissertation would not have been possible without the help of numerous individuals. I would first like to thank my committee members: Dr. Steven Schneider, Dr. Sally Bane, Dr. Jonathan Poggie and Dr. Bradley Wheaton. Their advice and guidance have been a great help to this dissertation and research. Funding for this work was provided by the Air Force Office of Scientific Research.

All the time spent at lab would have been unbearable without my current co-workers and lab alumni. There are too many to name individually but they all helped in accomplishing this dissertation. A special thanks to Brandon Chynoweth who, unlike the rest, never left and tolerated sharing an office for over six years. I would also like to acknowledge members of Dr. Sally Bane's lab group. I am grateful to: Lalit Rajendran, Bhavini Singh, Ravi Jagganath, Pransanth Bangalore, Aarthi Devarajan, Terry Zhou, Nick Schmidt, and Josh Strafaccia, who gave their time to help operate the nano-second pulser.

The continued success of research in the BAM6QT is entirely dependent on the ASL machine shop. Without their help in maintaining, designing, and fabricating BAM6QT parts and models, we would all be lost. The expert wizardry of Jim Younts, Robin Snodgrass, and Jerry Hahn have saved me from a lot of mistakes.

Without the support and encouragement of my parents, all this work would not have been possible. Further support from my grandparents cannot be overstated and was greatly appreciated. I would like to thank my wife, Emily. She moved and found a job in Indiana to be here with me and provided constant encouragement. Lastly, thank you to Piper for always making me smile when I get home.

## TABLE OF CONTENTS

	Page
LIST OF TABLES . . . . .	viii
LIST OF FIGURES . . . . .	x
SYMBOLS . . . . .	xix
ABBREVIATIONS . . . . .	xxi
ABSTRACT . . . . .	xxii
1 INTRODUCTION . . . . .	1
1.1 Hypersonic Laminar-Turbulent Boundary-Layer Transition . . . . .	1
1.2 Hypersonic Shock-Wave/Boundary-Layer Interactions . . . . .	4
1.2.1 Instability in High-Speed Shear-Layers . . . . .	6
1.2.2 Surface Heat Transfer and Streamwise Vortices in Transitional Hypersonic SBLI . . . . .	9
1.2.3 Instability in Laminar and Transitional Hypersonic Ramp-Induced Separations . . . . .	12
1.2.4 Effects of a Finite Span on Separation . . . . .	14
1.3 Objective of Research . . . . .	16
2 The BOEING/AFOSR MACH-6 QUIET WIND TUNNEL . . . . .	18
2.1 Determination of BAM6QT Run Conditions . . . . .	20
3 INSTRUMENTATION AND DATA PROCESSING . . . . .	24
3.1 Oscilloscopes . . . . .	24
3.2 Pressure Sensors . . . . .	24
3.2.1 PCB Pressure Transducers . . . . .	24
3.2.2 Kulite Pressure Transducers . . . . .	30
3.3 Heat Transfer Measurements . . . . .	32
3.3.1 Schmidt-Boelter Gauges . . . . .	33
3.3.2 Temperature Sensitive Paint . . . . .	33
3.3.3 Infrared Thermography . . . . .	36
3.4 Oil-Flow Imaging . . . . .	40
4 MODELS . . . . .	43
4.1 Short-Ramp Model . . . . .	45
4.2 Long-Ramp Model . . . . .	52
4.2.1 Determination of Reattachment Location . . . . .	52
4.2.2 Detailed Design of Long-Ramp Model . . . . .	61

	Page
4.3 Perturbation Models . . . . .	64
5 MEASUREMENTS USING THE LONG-RAMP MODEL WITHOUT PERTURBATION . . . . .	74
5.1 Surface Heat Transfer on the Ramp . . . . .	74
5.1.1 Comparison of IR and TSP Heat Transfer . . . . .	74
5.1.2 Effect of Small Angles of Attack on Ramp Heat Transfer . . . . .	78
5.1.3 Effect of Reynolds Number on Reattachment . . . . .	82
5.2 Natural Pressure Fluctuations Inside the Separation . . . . .	90
5.2.1 Natural Pressure Fluctuations on the Slice . . . . .	90
5.2.2 Natural Pressure Fluctuations on the Ramp . . . . .	97
5.3 Natural Post-Reattachment Pressure Fluctuations . . . . .	101
5.3.1 Post-reattachment Pressure Fluctuation Repeatability . . . . .	115
5.3.2 Effect of Reynolds Number on Post-reattachment Pressure Fluctuation Spectra . . . . .	122
5.3.3 Spanwise Variations in Post-Reattachment Pressure Fluctuations . . . . .	134
5.4 Summary of Results without Perturbation . . . . .	137
6 MEASUREMENTS OF GENERATED DISTURBANCES ON A 7° CONE . . . . .	142
6.1 Low-Pressure Breakdown of Air . . . . .	142
6.2 Plasma Perturbation on a 7° Half-Angle Cone . . . . .	146
6.2.1 Instability Growth without Artificial Disturbances . . . . .	154
6.2.2 Instability Growth with Artificial Disturbances . . . . .	154
7 MEASUREMENTS OF GENERATED DISTURBANCES ON THE LONG-RAMP MODEL . . . . .	170
7.1 Plasma Perturbation on the Long-ramp Model . . . . .	170
7.2 Measurements of Perturbations on the Cone-Slice-Ramp . . . . .	173
7.2.1 Effect of Perturbations within the Separated Region . . . . .	173
7.2.2 Measurements of Traveling Waves Post-Reattachment . . . . .	177
7.2.3 Effect of Reynolds Number on Post-Reattachment Waves . . . . .	192
7.2.4 Effect of Pulser Voltage on Instability Growth . . . . .	200
8 SUMMARY AND RECOMMENDATIONS . . . . .	205
8.1 Summary . . . . .	205
8.2 Recommendations for Future Work . . . . .	207
LIST OF REFERENCES . . . . .	209
APPENDICES	
A EFFECTS OF CORNER RADII ON RAMP SURFACE TEMPERATURE . . . . .	218
B SELECTED RUN CONDITIONS . . . . .	219
C SUPPLEMENTARY MEASUREMENTS OF PULSER BEHAVIOR . . . . .	225

	Page
D CUSTOM HARDWARE DRAWINGS . . . . .	227
D.1 Short-Ramp Model . . . . .	228
D.2 Long-Ramp Model . . . . .	234
D.3 7° Cone Perturbation model . . . . .	248
D.4 Long-Ramp Perturbation model . . . . .	256

## LIST OF TABLES

Table	Page
3.1 Sample pressure ratios for various methods and geometries . . . . .	27
3.2 PEEK Material and Thermal Properties. . . . .	38
4.1 Approximate reattachment locations on the long ramp model in quiet flow.	57
4.2 Sensor locations on the cone portion of the long-ramp model . . . . .	65
4.3 Sensor locations on the slice portion of the long-ramp model . . . . .	65
4.4 Sensor locations on the spanwise ramp . . . . .	66
4.5 Sensor locations on the cluster ramp . . . . .	67
4.6 Sensor locations on the Kulite-instrumented ramp . . . . .	68
4.7 Perturber and sensor locations on the 7° perturbation model. . . . .	71
4.8 Sensor locations for the perturber ramp. . . . .	73
5.1 Post-reattachment turbulent spot convection velocities at various Re. . .	106
5.2 Post-reattachment turbulent spot convection velocities at various Re and calculation methods. . . . .	128
5.3 Equations for exponential fits to pressure fluctuation magnitudes . . . .	132
6.1 Run conditions and electronics settings for artificially generated distur- bances on the 7° cone. . . . .	147
6.2 Behavior of RMS Voltage and current sent to the perturber electrodes. .	153
6.3 Behavior of RMS pressure fluctuations at the first PCB location. . . . .	159
7.1 Electronics settings for runs with artificially generated disturbances on the cone-slice-ramp. . . . .	171
7.2 Electronics Statistics for Run 2310. . . . .	171
7.3 Locations of sensors shown in Figure 7.8. . . . .	181
7.4 Post-reattachment wave packet convection velocities for 10 kV pulsing at various Re. . . . .	181
7.5 Pulse-to-pulse RMS pressure fluctuation statistics for the farthest down- stream PCB at $x = 0.407\text{m}$ and 10 kV pulsing. . . . .	188

Table	Page
7.6 Run-to-run RMS pressure fluctuation repeatability for three sample sensors.	188
B.1 Entry 2 (March 2016).	219
B.2 Entry 5 (August 2016).	219
B.3 Entry 7 (February 2017).	220
B.4 Entry 8 (April 2017).	220
B.5 Entry 9 (May 2017).	220
B.6 Entry 10 (May 2017).	220
B.7 Entry 18 (December 2018).	221
B.8 Entry 19 (June 2019).	221
B.9 Entry 20 (September 2019).	222
B.10 Entry 21 (October 2019).	222
B.11 Entry 22 (November 2019).	223
B.12 Entry 23 (December 2019).	223
B.13 Entry 23 continued.	224
C.1 Electronics settings for runs with artificially generated disturbances on the cone-slice-ramp.	225
C.2 Electronics statistics for relevant runs on the long-ramp perturbation model.	226

## LIST OF FIGURES

Figure	Page
1.1 Boundary-layer transition mechanisms. Redrawn from Figure 1 of Reference [4] . . . . .	2
1.2 Schematic of the turbulent spot model of transition. The gray triangles represent individual turbulent spots moving and growing with downstream distance. . . . .	4
1.3 Schematic of a generic two-dimensional ramp-induced SBLI. Flow is from left to right. . . . .	6
1.4 Schematic of shear-layer velocity profiles for a generic separated flow. Redrawn from Reference [24] . . . . .	7
2.1 Schematic of the BAM6QT. . . . .	19
2.2 Sample hot film and nozzle-wall Kulite traces for quiet and noisy flow. . .	21
2.3 Sample time trace of contraction Kulite. . . . .	22
3.1 Wavelet coefficients for a sample pressure fluctuation time trace. Lines indicate the wave packet and turbulent spot detection bandwidths. . . . .	30
3.2 Example pressure fluctuation trace with detected turbulent spots and wave packets. . . . .	31
3.3 Sample calibration of an individual Kulite. . . . .	32
3.4 Experimental setup of the 2 LED light sources and 14-bit CCD camera. . .	34
3.5 Steps for post-processing of TSP images into heat transfer. Conversion to Stanton number occurs after these steps are complete. . . . .	37
3.6 Sample IR post-processing of images into heat transfer. . . . .	41
3.7 Sample oil application within the BAM6QT. . . . .	42
4.1 Image of the precision AoA adapter. The top piece is the outer sleeve and the bottom piece is the inner support. . . . .	44
4.2 Schematic and images of the short-ramp family of models. . . . .	46
4.3 Oil flow on short-ramp model. Left column is noisy flow, right column is quiet flow. Flow is from right to left. . . . .	48

Figure	Page
4.4 TSP of the short-ramp model with 10°, 20°, and 30° ramp in quiet flow. Flow is from right to left. . . . .	50
4.5 TSP of the short-ramp model with 30° ramp. Flow is from right to left. . . . .	51
4.6 Schematic and images of the long-ramp family of models. . . . .	53
4.7 Oil flow images of long ramp model at $Re_\infty \approx 9.2 \times 10^6/m$ with various angle ramps under quiet flow. Flow is from right to left. . . . .	54
4.8 TSP of the long-ramp cone at similar unit Reynolds number in quiet flow. Flow is from right to left. . . . .	55
4.9 Laminar-scaled Stanton number of 20° long ramp from TSP. Flow is right to left. . . . .	56
4.10 Laminar-scaled Stanton number of 20° long ramp from IR. Flow is right to left. . . . .	57
4.11 Map of temperature at $Re_\infty = 9.2 \times 10^6/m$ . DNS completed by Thome with US3D [50]. . . . .	59
4.12 Comparison of surface Stanton number on the ramp from experiments and DNS completed by Thome with US3D [50]. Data were taken from 2 mm off the ramp centerline. . . . .	60
4.13 Schematics long-ramp model with relevant annotations of mechanical design.	62
4.14 Sample profile of the joint between the slice and ramp. Given profile is an average of 500 $\mu m$ worth of joint profiles. The right side is the upstream slice and the left side is the downstream ramp. . . . .	62
4.15 Images of a sample ramp corner on the long-ramp model. The markings on the scale in the left image are 0.254 mm (0.01 in) and the labeled marks are 2.54 mm (0.1 in). . . . .	63
4.16 Schematics of the various ramps used. . . . .	64
4.17 Schematic of the Macor inserts used on the perturber models. . . . .	69
4.18 Images of various cones with perturber inserts. . . . .	70
4.19 N-factors of most amplified frequencies on a 7° cone at 0° AoA. Perturber location is marked on the plot. Computations were completed at: $P_0 = 155$ psia, $T_0 = 433$ K, $\rho_0 = 8.605$ kg/m <sup>3</sup> , and $T_{wall} = 300$ K. . . . .	71
4.20 Images of a perturber ramp corner on the long-ramp model. The markings on the scale in the left image are 0.254 mm (0.01 in). . . . .	73

Figure	Page
5.1 Comparison of TSP and IR laminar-scaled Stanton number of the ramp at varying unit Reynolds number in quiet flow. TSP are on the left and IR is on the right. Flow is from right to left. . . . .	77
5.2 Comparison of IR and TSP Stanton number on the ramp at various unit Reynolds numbers. . . . .	78
5.3 Comparison of slight changes of AoA. Left column is TSP Stanton number for a single run and right column is the azimuthal PCB PSD. Top images are from a poorly aligned case, bottom images are from a properly aligned case. Flow is from right to left in TSP. . . . .	80
5.4 Qualitative comparison of computations and TSP heat transfer at small yaw angles. Top images are Thome's computation and bottom are TSP heat transfer [50]. Flow is from right to left. . . . .	81
5.5 IR laminar-scaled Stanton number of the 20° ramp at varying unit Reynolds number in quiet flow. Flow is from right to left. . . . .	83
5.6 IR laminar-scaled Stanton number of the ramp at $Re_\infty = 3.1 \times 10^6/m$ (Run2010). The lines represent locations where data was taken for streamwise and spanwise cuts in Figure 5.7. . . . .	85
5.7 Line cuts of IR Stanton number on the 2° ramp at varying unit Reynolds number in quiet flow. The ramp is 51 mm wide and 91 mm long. . . . .	86
5.8 IR laminar-scaled Stanton number of the 20° ramp at varying unit Reynolds number in noisy flow. Flow is from right to left. . . . .	88
5.9 Line cuts of IR Stanton number on the 20° ramp at varying unit Reynolds number in noisy flow. The ramp is 51 mm wide and 91 mm long. . . . .	89
5.10 TSP Stanton number of the full model at $Re_\infty = 2.9 \times 10^6/m$ (Run 1006). The red dots represent the five sensors located on the slice. The two red lines represent the start of the slice and the ramp. . . . .	91
5.11 PSD and coherence of PCB pressure fluctuations on the slice at $Re_\infty = 3.6 \times 10^6/m$ (Run 2107). . . . .	92
5.12 PSD and coherence of PCB pressure fluctuations on the slice at $Re_\infty = 6.03 \times 10^6/m$ (Run 2112). . . . .	93
5.13 Effects of Reynolds number on PCB pressure fluctuations on the slice. . . . .	94
5.14 Effects of small changes in Reynolds number on PCB pressure fluctuations on the slice. . . . .	96

Figure	Page
5.15 IR heat transfer of the ramp at $Re_\infty=2.5\times 10^6/m$ (Run 2013). The red dots represent the five sensors located in the separation on the ramp. The labels represent nomenclature for comparing pressure fluctuations. . . . .	97
5.16 PSD and coherence of PCB pressure fluctuations within separated region. Sensors are on the ramp centerline at $Re_\infty= 3.6\times 10^6/m$ (Run 2107). . . .	98
5.17 PSD and coherence of PCB pressure fluctuations within separated region. Sensors are arranged in a cluster at $Re_\infty= 3.6\times 10^6/m$ (Run 2107). . .	99
5.18 PSDs of clustered PCB pressure fluctuations within the ramp separated region at various unit Reynolds number. . . . .	100
5.19 Development of time traces post-reattachment with Reynolds number. All data is from the farthest downstream centerline PCB at $x=0.407$ m. . . .	102
5.20 Behavior of a single turbulent spot from various sensors on the ramp centerline at $Re = 2.5\times 10^6/m$ (Run 2312). . . . .	104
5.21 Turbulent spot tracking on a single spot at $Re = 2.5\times 10^6/m$ (Run 2312).	105
5.22 IR Stanton number of the ramp at $Re_\infty=2.5\times 10^6/m$ . The red circles represent the relevant PCBs located on the ramp. Flow is from right to left.	107
5.23 Behavior of a single turbulent spot from three sensors on the ramp centerline at $Re = 2.5\times 10^6/m$ (Run 2312). . . . .	109
5.24 Behavior of a single turbulent spot from three sensors on the ramp centerline at various unit Reynolds number. . . . .	110
5.25 Behavior of a single turbulent spot from three sensors on the ramp centerline at various unit Reynolds number. . . . .	112
5.26 Behavior of single turbulent spots from post-reattachment centerline sensors at various unit Reynolds number. . . . .	114
5.27 IR heat transfer of the ramp at $Re_\infty=2.5\times 10^6/m$ . The red dots represent the two sensors located downstream of separation on the ramp (Run 2013).	116
5.28 Repeatability of spectra for multiple runs at various unit Reynolds numbers.	117
5.29 PSDs of pressure sensors downstream of reattachment under quiet flow on various ramps. . . . .	119
5.30 Repeatability of magnitudes with unit Reynolds number for multiple runs.	121
5.31 PSDs of PCBs downstream of reattachment under quiet flow at various $Re_\infty$ .	124
5.32 PSD of PCBs downstream of reattachment on the perturber ramp without perturbations at $Re_\infty= 2.5\times 10^6/m$ (Run 2312). . . . .	125

Figure	Page
5.33 PSD of PCB at $x = 0.407$ m downstream at small changes of unit Reynolds number. The time traces that were processed for each PSD are included.	127
5.34 PSDs of Kulites downstream of reattachment under quiet flow at various $Re_\infty$ .	129
5.35 IR heat transfer of the ramp at $Re_\infty = 2.5 \times 10^6 / m$ (Run 2013). The red circles represent the PCB sensors and the black circles represent Kulite sensors.	130
5.36 PSDs of individual sensors downstream of reattachment under quiet flow at various $Re_\infty$ .	131
5.37 Magnitudes of pressure fluctuations on various ramps and sensor-based Reynolds number. Each color represents a different run.	133
5.38 PSDs of spanwise sensor arrays downstream of reattachment under quiet flow at various $Re_\infty$ . Color of the traces indicate spanwise location: Blue = -6.35mm off-centerline, Orange = Centerline, Green = 6.35mm off-centerline.	135
5.39 PSDs and coherences of PCB clusters downstream of reattachment under quiet flow at $Re_\infty = 2.5 \times 10^6 / m$ (Run 2312).	136
5.40 PSDs of Kulites at various spanwise locations under quiet flow at $Re_\infty = 2.5 \times 10^6 / m$ (Run 2212). Sensors from the entire length of the ramp are shown. Centerline reattachment occurs at approximately 0.36 m downstream from the nosetip.	138
5.41 Magnitudes of Kulite pressure fluctuations under quiet flow at various $Re$ . The black dotted line indicates the approximate reattachment at the ramp centerline.	139
6.1 DC breakdown of gas in terms of voltage and current. Adapted from Reference [111].	144
6.2 Schematic of the pulser triggering and measurement set up.	145
6.3 Pulser setup for the BAM6QT.	146
6.4 Electrical characteristics of pulser at $Re_\infty = 7.6 \times 10^6 / m$ (Run 1911).	149
6.5 Electrical characteristics of pulser during low-current pulsing at $Re_\infty = 7.6 \times 10^6 / m$ (Run 1911).	151
6.6 Electrical characteristics of pulser during high-current pulsing at $Re_\infty = 7.6 \times 10^6 / m$ (Run 1911).	152
6.7 FFT of a sample square wave with a 100 ns pulse duration and 40 ns rise and fall times.	153

Figure	Page
6.8 PCB PSD's down the length of the cone without perturbation at $Re_\infty = 7.7 \times 10^6/m$ (Run 1911). The legend reports axial distance from nosetip. . . . .	155
6.9 PCB PSD's down the length of the cone without perturbation at $Re_\infty = 10.7 \times 10^6/m$ (Run 1910). The legend reports axial distance from nosetip. . . . .	155
6.10 Sample time traces of pressure fluctuations on a $7^\circ$ cone. . . . .	157
6.11 Comparison of RMS amplitudes from plasma-generated perturbations. . . . .	158
6.12 Example pressure fluctuations from 0.243m downstream from the nosetip. Processed during the low-current portion at $Re_\infty = 7.6 \times 10^6/m$ (Run 1911) . . . . .	158
6.13 PDF's of the RMS pressure fluctuations 0.243m downstream from the nosetip at $Re_\infty = 7.6 \times 10^6/m$ (Run 1911) . . . . .	159
6.14 Example pressure fluctuations with and without filtering from 0.243m downstream from the nosetip. Processed during the low-current portion at $Re_\infty = 7.6 \times 10^6/m$ (Run 1911) . . . . .	161
6.15 Comparison of three different PSD calculations. . . . .	162
6.16 Comparison PSD's before, during, and after pulsing at $Re_\infty = 7.6 \times 10^6/m$ (Run 1911). . . . .	163
6.17 PSD down the length of the cone at $Re_\infty = 7.6 \times 10^6/m$ (Run 1911) during low-current pulsing. . . . .	166
6.18 PSD down the length of the cone at $Re_\infty = 7.6 \times 10^6/m$ (Run 1911) during high-current pulsing. . . . .	167
6.19 RMS pressure fluctuations on the cone for $Re_\infty = 7.6 \times 10^6/m$ during perturbations. . . . .	168
6.20 Maximum second mode amplitudes versus edge Mach for several models and facilities. Non-perturbation data were obtained from Chynoweth [12]. . . . .	168
6.21 Comparison of PSD spectra with various $V_{applied}$ at several Reynolds numbers 0.243 m from the nosetip. . . . .	169
7.1 Electrical characteristics of pulser at $Re_\infty = 1.9 \times 10^6/m$ (Run 2310). . . . .	172
7.2 Electrical characteristics of pulser sampled at 5 GHz at $Re_\infty = 2.1 \times 10^6/m$ (Run 2321). . . . .	174
7.3 Time trace of PCB directly downstream of the perturber insert ( $x = 0.273$ m) on the cone portion of the model at $Re_\infty = 2.0 \times 10^6/m$ (Run 2310). . . . .	175

Figure	Page
7.4 IR Stanton number of the ramp at $Re_\infty=2.5\times 10^6/m$ (Run 2013). The red circles represent the PCBs located within separation on the ramp. Flow is from right to left. . . . .	176
7.5 Time trace of last PCB on the slice ( $x = 0.312$ m) at $Re_\infty = 2.0\times 10^6/m$ (Run 2310). . . . .	177
7.6 Waterfall plots of ensemble averaged separation PCB time traces. Each time trace is offset from the others for clarity. TSP and IR indicated that reattachment occurs between 0.36-0.37 m downstream from nosetip. . . .	178
7.7 PSDs and coherences of separation PCBs with and without 10 kV perturbation at $Re_\infty = 2.0\times 10^6/m$ (Run 2310). . . . .	179
7.8 IR Stanton number of the ramp at $Re_\infty=2.5\times 10^6/m$ . The red circles represent the PCBs located on the ramp. Flow is from right to left. . . .	180
7.9 Waterfall plots of ensemble averaged post-reattachment PCB time traces with 10 kV pulsing. Each time trace is offset from the others for clarity. . . . .	182
7.10 PSDs and coherences of upstream post-reattachment PCBs with and without perturbation at $Re_\infty = 2.0\times 10^6/m$ (Run 2310). . . . .	184
7.11 PSDs and coherences of downstream post-reattachment PCBs with and without perturbation at $Re_\infty = 2.0\times 10^6/m$ (Run 2310). . . . .	185
7.12 Effect of streamwise distance on Perturbation RMS amplitudes. Each color represents an individual run and each point is data from a single sensor on the ramp. . . . .	186
7.13 Spectral repeatability for several sensors downstream of reattachment. . . . .	187
7.14 IR Stanton number of the ramp at $Re_\infty=2.5\times 10^6/m$ (Run 2013). The red circles represent the PCBs used in Figure 7.15. The black circles represent the PCBs used in Figure 7.16. Flow is from right to left. . . . .	190
7.15 Spanwise effects on perturbation PSDs and coherences for a post-reattachment spanwise sensor array at $x = 0.389$ m and $Re_\infty = 2.5\times 10^6/m$ (Run 2310). Coherences were taken from centerline sensor immediately in front of the spanwise array. . . . .	190
7.16 Spanwise effects on perturbation PSDs and coherences for a post-reattachment spanwise sensor array at $x = 0.401$ m and $Re_\infty = 2.5\times 10^6/m$ (Run 2310). Coherences were taken from centerline sensor immediately in front of the spanwise array. . . . .	191
7.17 Ensemble averages and individual pulses of a PCB 0.407 m from the nosetip at various unit Reynolds numbers. . . . .	194

Figure	Page
7.18 PCB PSDs and coherences during 10 kV perturbations at $Re_\infty = 2.5 \times 10^6/m$ (Run 2312). . . . .	195
7.19 PCB PSDs and coherences during 10 kV perturbations at $Re_\infty = 3.3 \times 10^6/m$ (Run 2314). . . . .	195
7.20 Effect of Reynolds number on perturbation instability growth at various centerline locations. . . . .	197
7.21 Comparison of PCB RMS pressure fluctuations magnitudes post-reattachment. The different colors represent runs of different unit Reynolds number. $Re_{sensor}$ is the Reynolds number based on sensor distance from nosetip. The black lines are the computed intermittency of the final sensor on the ramp for every run. . . . .	199
7.22 Effect of applied voltage on instability growth at $x = 0.395$ m. . . . .	201
7.23 Effect of applied pulser voltage on instability growth at various centerline locations at $Re_\infty = 2.0 \times 10^6/m$ . . . . .	202
7.24 Comparison of PCB RMS pressure fluctuations magnitudes post-reattachment. The different colors represent runs of different initial unit Reynolds number. $Re_{sensor}$ is the Reynolds number base on sensor distance from nosetip. The black lines are the computed intermittency of the final sensor on the ramp for every run. . . . .	204
A.1 Comparison of surface temperature with varying ramp corner radii. . . . .	218
D.1 Drawing of the sharp nosetip used for every model . . . . .	227
D.2 Drawing of the short-ramp cone assembly . . . . .	228
D.3 Drawing of the short-ramp cone body - Part 1 . . . . .	229
D.4 Drawing of the short-ramp cone body - Part 2. . . . .	230
D.5 Drawing of the short-ramp $10^\circ$ spanwise ramp. . . . .	231
D.6 Drawing of the short-ramp $20^\circ$ spanwise ramp. . . . .	232
D.7 Drawing of the short-ramp $30^\circ$ spanwise ramp. . . . .	233
D.8 Drawing of the Long-ramp cone assembly . . . . .	234
D.9 Drawing of the Long-ramp cone body - Part 1 . . . . .	235
D.10 Drawing of the Long-ramp cone body - Part 2. . . . .	236
D.11 Drawing of the Long-ramp cone body - Part 3. . . . .	237
D.12 Drawing of the Long-ramp cone body - Part 4. . . . .	238

Figure	Page
D.13 Drawing of the 20° spanwise ramp. . . . .	239
D.14 Drawing of the 20° cluster ramp - Part 1. . . . .	240
D.15 Drawing of the 20° cluster ramp - Part 2. . . . .	241
D.16 Drawing of the 20° cluster ramp - Part 3. . . . .	242
D.17 Drawing of the 20° cluster ramp - Part 4. . . . .	243
D.18 Drawing of the 20° Kulite ramp - Part 1. . . . .	244
D.19 Drawing of the 20° Kulite ramp - Part 2. . . . .	245
D.20 Drawing of the 20° Kulite ramp - Part 3. . . . .	246
D.21 Drawing of the 20° PEEK ramp - Part 1. . . . .	247
D.22 Drawing of the MACOR perturber insert. This was utilized in all perturbation models and was adapted from Casper [112]. . . . .	248
D.23 Drawing of the 7° cone assembly . . . . .	249
D.24 Drawing of the 7° cone exploded assembly . . . . .	250
D.25 Drawing of the 7° cone perturber body. . . . .	251
D.26 Drawing of the 7° cone sensor body - Part 1. . . . .	252
D.27 Drawing of the 7° cone sensor body - Part 2. . . . .	253
D.28 Drawing of the 7° cone sensor body - Part 3. . . . .	254
D.29 Drawing of the 7° cone baseplate . . . . .	255
D.30 Drawing of the long-ramp perturbation model assembly . . . . .	256
D.31 Drawing of the long-ramp perturbation model body - Part 1. . . . .	257
D.32 Drawing of the long-ramp perturbation model body - Part 2. . . . .	258
D.33 Drawing of the long-ramp perturbation model body - Part 3. . . . .	259
D.34 Drawing of the long-ramp perturbation model instrumented 20° ramp - Part 1. . . . .	260
D.35 Drawing of the long-ramp perturbation model instrumented 20° ramp - Part 2. . . . .	261
D.36 Drawing of the long-ramp perturbation model PEEK 20° ramp. . . . .	262
D.37 Drawing of the long-ramp perturbation model baseplate - Part 1. . . . .	263
D.38 Drawing of the long-ramp perturbation model baseplate - Part 2. . . . .	264

## SYMBOLS

$A$	Disturbance amplitude
$A_0$	Initial disturbance amplitude
$I$	Pixel intensity
$M$	Mach number
$P$	Pressure
$P'$	Pressure fluctuation
$q$	Heat transfer
$Re$	Reynolds number
$R$	Gas constant
$T$	Temperature
$t$	Time
$x$	Streamwise coordinate
$y$	Spanwise coordinate
<i>Greek Symbols</i>	
$\gamma$	Ratio of specific heats
$\Delta$	Change in a variable
$\kappa$	Thermal conductivity
$\beta$	Side slip angle
$\mu$	Viscosity
$\theta$	Ramp angle
<i>Subscripts</i>	
0	Stagnation condition
$i$	Initial condition
$ref$	Reference condition
$dark$	Image data without blue LED and pre-run

<i>off</i>	Image data with blue LED and pre-run
<i>on</i>	Image data with blue LED during the run
$\infty$	Freestream condition
<i>sensor</i>	Condition based on sensor distance from nosetip
<i>IR</i>	Infrared quantity
<i>AMB</i>	Ambient
<i>w</i>	Wall condition

## ABBREVIATIONS

SBLI	Shock/Boundary-Layer Interaction
CFD	Computational Fluid Dynamics
LST	Linear Stability Theory
AoA	Angle of Attack
BAM6QT	Boeing/AFOSR Mach 6-Quiet Tunnel
AFOSR	Air Force Office of Scientific Research
STABL	Stability and Transition Analysis for hypersonic Boundary Layers
PSD	Power Spectral Density
FFT	Fast Fourier Transform
RMS	Root Mean Square
SB	Schmidt-Boelter
TSP	Temperature Sensitive Paint
Ru(bpy)	99.95% Tris(2,2'-bipyridyl)ruthenium(II) chloride hexahydrate
CCD	Charged-Coupled Device
LED	Light-Emitting-Diode
IR	Infrared
PEEK	Poly-Ether Ether Ketone
PIRANHA	Purdue Infrared Registration and Heat Transfer App
GUI	Graphical User Interface
EMI	Electro-Magnetic Interference
DNS	Direct Numerical Simulation
PDF	Probability Density Function

## ABSTRACT

McKiernan, Gregory R. PhD, Purdue University, May 2020. Instability and Transition on a Sliced Cone with a Finite-Span Compression Ramp at Mach 6. Major Professor: Steven P. Schneider.

Initial experiments on separated shock/boundary-layer interactions were carried out within the Boeing/AFOSR Mach-6 Quiet Tunnel. Measurements were made of hypersonic laminar-turbulent transition within the separation above a compression corner. This wind tunnel features freestream fluctuations that are similar to those in flight. The present work focuses on the role of traveling instabilities within the shear layer above the separation bubble.

A  $7^\circ$  half-angle cone with a slice and a finite-span compression ramp was designed and tested. Due to a lack of space for post-reattachment sensors, early designs of this generic geometry did not allow for measurement of a post-reattachment boundary layer. Oil flow and heat transfer measurements showed that by lengthening the ramp, the post-reattachment boundary layer could be measured. A parametric study was completed to determine that a  $20^\circ$  ramp angle caused reattachment at 45% of the total ramp length and provided the best flow field for boundary-layer transition measurements.

Surface pressure fluctuation measurements showed post-reattachment wave packets and turbulent spots. The presence of wave packets suggests that a shear-layer instability might be present. Pressure fluctuation magnitudes showed a consistent transition Reynolds numbers of 900000, based on freestream conditions and distance from the nosetip. Pressure fluctuations grew exponentially from less than 1% to roughly 10% of tangent-wedge surface pressure during transition.

A high-voltage pulsed plasma perturber was used to introduce controlled disturbances into the boundary layer. The concept was demonstrated on a straight

7° half-angle circular cone. The perturbations successfully excited the second-mode instability at naturally unstable frequencies. The maximum second-mode amplitudes prior to transition were measured to be about 10% of the mean surface static pressure.

The plasma perturber was then used to disturb the boundary layer just upstream of the separation bubble on the cone with the slice and ramp. A traveling instability was measured post-reattachment but the transition location did not change for any tested condition. It appears that the excited shear-layer instability was not the dominant mechanism of transition.

# 1. INTRODUCTION

## 1.1 Hypersonic Laminar-Turbulent Boundary-Layer Transition

Hypersonic flight vehicles commonly reach altitudes where low Reynolds number environments produce entirely laminar boundary layers on the surface of the vehicle. As the altitude decreases, the Reynolds number increases to the point where the boundary-layer will transition from laminar to turbulent. The transition process affects heat transfer, surface pressure, skin friction, and other physical phenomena [1]. These variables play dominant roles in vehicle design and factor into thermal protection systems, control authority, and aero-optics [2]. A better understanding of the physical mechanisms that govern transition is needed to improve current prediction methods. Without better predictions of the transition process, designs will need to be over-conservative to avoid failure.

The location at which the laminar boundary layer becomes unstable and begins to transition is dependent on how disturbances enter and grow in the boundary layer. Figure 1.1 shows a flow chart of the mechanisms through which boundary-layer transition can occur. An initial disturbance feeds into the boundary layer from the freestream or the body itself through a process known as receptivity. Freestream disturbances can include atmospheric noise, wind tunnel noise, or particulates. Sample disturbance sources on the body include discrete roughness, backward or forward facing steps, and wall waviness [2]. These disturbances travel downstream and grow through one or several paths to turbulence.

Path A contains disturbances that enter the boundary layer and linearly amplify. These may be stationary or traveling within the boundary layer. Examples of traveling instabilities are the first Mack mode, second Mack mode, and traveling crossflow. Sample stationary disturbances include the Görtler instability or stationary crossflow

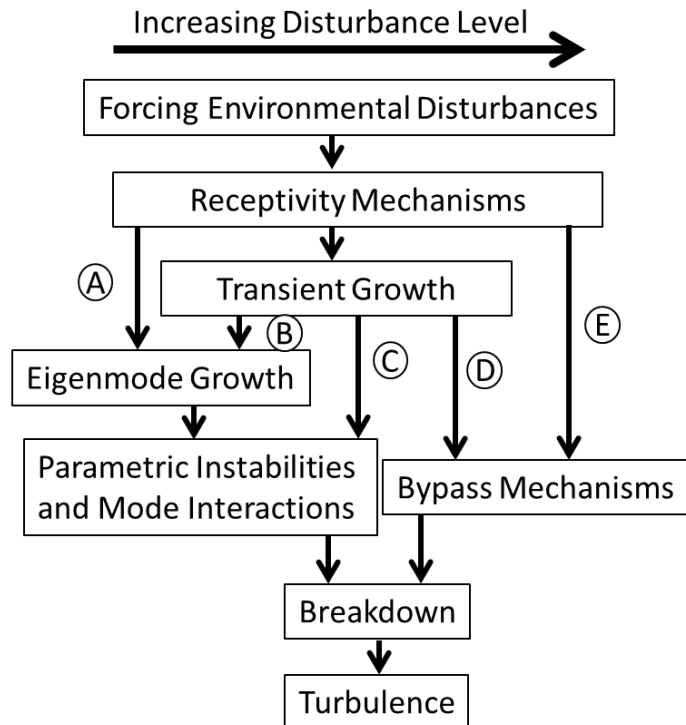


Figure 1.1. Boundary-layer transition mechanisms. Redrawn from Figure 1 of Reference [4]

instability [3]. Whether one or multiple of these are responsible for transition is dependent on all aspects of the geometry and environment. The problem is further complicated by these mechanisms developing non-linearities, and by interactions between multiple mechanisms. Detailed descriptions of the other paths can be found in Reshotko et al. [4].

When trying to predict when and where transition will occur on a vehicle, correlations are commonly used to simplify the problem. While simple one-variable correlations have a place in preliminary work, more advanced techniques are needed for precise modeling. A common method for relating the growth of boundary-layer instabilities to transition is the  $e^N$  method. It is a semi-empirical method of determining transition location by integrating the amplification of the disturbances within the boundary layer. The equation that governs it is

$$e^N = \frac{A}{A_0}. \quad (1.1)$$

The initial amplitude of the instability when it begins growing is defined as  $A_0$ . The amplitude at a known location is  $A$  and the natural logarithm of the amplitude ratio is  $N$  [5]. This method begins to take into account the physical mechanisms of the instabilities but more improvements are possible. Further improvements should include the contributions from phenomena such as nonlinear effects, roughness, and freestream disturbances.

Only considering linear growth is an issue because most ground testing relies on conventional hypersonic wind tunnels. These types of facilities have freestream fluctuations dominated by large amounts of acoustic radiation due to the turbulent boundary layer present along the tunnel walls. These fluctuations are typically 1 to 2 orders of magnitude larger than real flight levels [6]. These large freestream fluctuations can obscure transition mechanisms and cause the boundary layer to transition earlier than in flight. Facilities with laminar nozzle-wall boundary layers avoid this issue and are known as “quiet tunnels.” Quiet tunnel facilities can provide some of the research necessary to determine transition mechanisms and develop new prediction methods.

Determining the onset of transition from instabilities is not the only important aspect of modeling the effects on flight vehicles. Transition occurs over a finite length on the surface and accounting for this is important. During this transitional region, heat transfer rates increase rapidly from laminar levels to turbulent levels [7]. For example, the Reentry-F flight test reported transition lengths over a meter that encompassed a large portion of the cone [8]. A turbulent spot model of transition developed by Dhawan and Narasimha can help describe this process [9,10]. A schematic of this transition model can be seen in Figure 1.2. Turbulent spots are generated at a single streamwise location, which is considered the transition onset. If the spot generation rate and the downstream growth from the onset point are known, the transition length can be predicted. Experiments by Casper et al. studied this at Mach

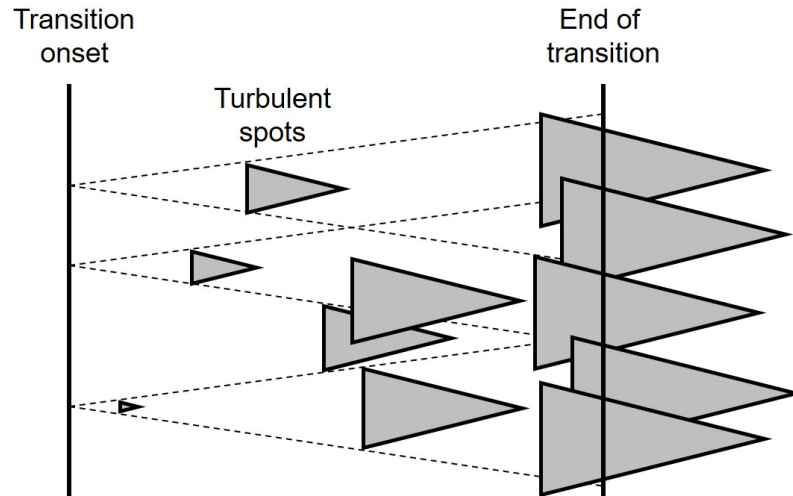


Figure 1.2. Schematic of the turbulent spot model of transition. The gray triangles represent individual turbulent spots moving and growing with downstream distance.

5 and 8 on a  $7^\circ$  half-angle cone and attempted to separate instability growth and turbulent spot generation [11]. Similar ideas were used to measure intermittency on a flared cone at Mach 6 by Chynoweth [12]. This model of the transitional region will also be considered for the present work.

## 1.2 Hypersonic Shock-Wave/Boundary-Layer Interactions

Prediction of vehicle performance is further complicated with the introduction of three-dimensional control surfaces. This technology is critical for the performance of maneuverable reentry vehicles. These vehicles do not fly ballistic trajectories and commonly require flaps for control. Flight tests of vehicles like AMaRV show the necessity of functional control surfaces [13]. Additionally, heat transfer and mean pressure on control surfaces is dependent on whether the incoming boundary layer is laminar, transitional, or turbulent [14]. For example, the X-33, X-38, and X-43, all reentry or scramjet demonstrators, had issues with predicting heating and transition on control flaps [15–17].

Boundary-layer flow approaching a ramp or control surface on a hypersonic vehicle is subjected to an adverse pressure gradient. The gradient is due to the turning angle that the oblique shock generates at the compression corner. The adverse pressure gradient will retard the incoming boundary layer and, if strong enough, inflect the boundary-layer velocity-profile. This inflection manifests physically as reversed flow and separates the boundary layer off the surface of the model. This phenomenon is categorized as a shock wave/boundary-layer interaction (SBLI) [18]. Figure 1.3 shows a generic schematic of a ramp-induced SBLI. In the image, separation is labelled as “S” and reattachment as “R”. Several flow features in an SBLI are present due to the change in flow direction. A separation shock forms at the separation point and extends downstream. Depending on the angle of the ramp, this shock could impinge on the surface further downstream and further complicate the interaction. Another shock forms at the reattachment point and is termed the reattachment shock. The boundary layer compresses at reattachment and thins. It then thickens as it progresses downstream.

SBLIs are not limited to compression corner geometries. This phenomenon will occur in any flowfield where an adverse pressure gradient is large enough to dominate the momentum within a boundary layer. Other common sources of SBLI include impinging oblique shocks, normal shocks, and oblique shocks from forward facing steps [18]. These interactions are termed “weakly interacting” if the adverse pressure gradient is not large enough to separate the incoming flow and “strongly interacting” if separation does occur.

Hypersonic flight vehicles can produce fully laminar SBLIs at high Mach and low Reynolds number. This complicates the transition process since the shock then acts as a perturbation that contributes to boundary-layer transition [18]. The boundary layer that separates from the surface is considered a shear layer and is known to transition at very low Reynolds numbers [14]. This interaction of a multitude of related phenomena is what creates the complexity of predicting the flowfield [19]. Furthermore, the wide

range of spatial and temporal scales creates difficulties in generating computational fluid dynamics (CFD) solutions [20].

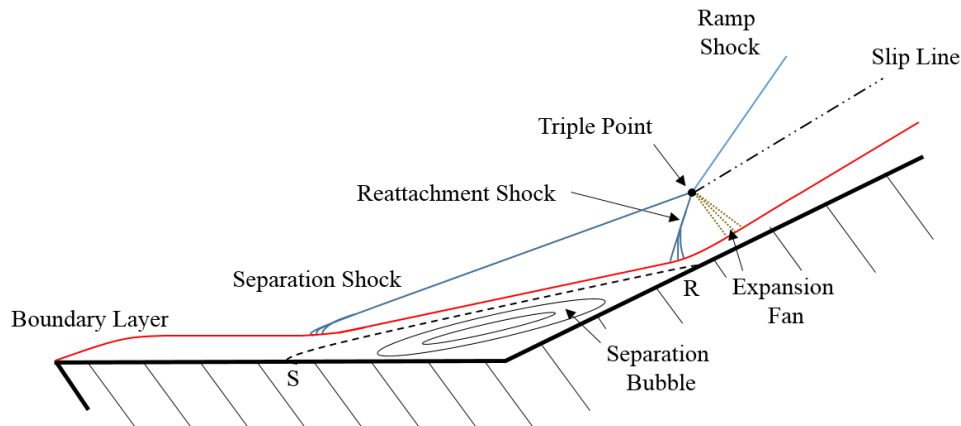


Figure 1.3. Schematic of a generic two-dimensional ramp-induced SBLI. Flow is from left to right.

Many early experiments on SBLI, such as those by Ackeret or Chapman, outlined the effects of the pre-separation boundary-layer state on the separation itself. It was found that different states of the boundary layer create drastically different interaction regions [21,22]. The increased momentum transfer of turbulent boundary layers greatly reduced the length of any separation. Due to this, transition created abrupt rises in pressure on the ramp and any parameter that affects transition will drastically change the pressure footprint. Therefore, the boundary conditions in computations need to accurately reflect any experiments. This problem is common enough that databases of well-defined experiments have been made to help computationalists test their codes [23].

### 1.2.1 Instability in High-Speed Shear-Layers

Separation of the boundary layer from a surface introduces a flow field known as a shear layer. This layer is defined as the region of rapidly varying velocity between the slow recirculating region within the bubble and the hypersonic freestream. However,

this is only one case of a shear layer. Any flow field of two parallel flows with non-zero and unequal velocities can be considered a shear-layer flow. Examples of other shear layers include symmetric and asymmetric wakes, jets, parallel streams of different velocities, and mixing layers. These flows develop in the streamwise direction and eventually reach an asymptotic velocity profile [24]. Figure 1.4 shows general velocity profiles for a separated boundary layer. The two edge conditions for this shear layer are the freestream flow and the zero velocity at the point where the flow reverses. The stability of the shear layer is dependent on the shape of the shear-layer velocity-profile. These effects are intrinsically included in experimental work and must be considered in theoretical and computational work. A primary physical difference between shear layers and boundary layers is that shear layers lack a no-slip condition and heat generation at solid boundaries. This section will review a subset of shear-layer instability and transition literature to provide justification for studying shear-layer instability in three-dimensional SBLI.

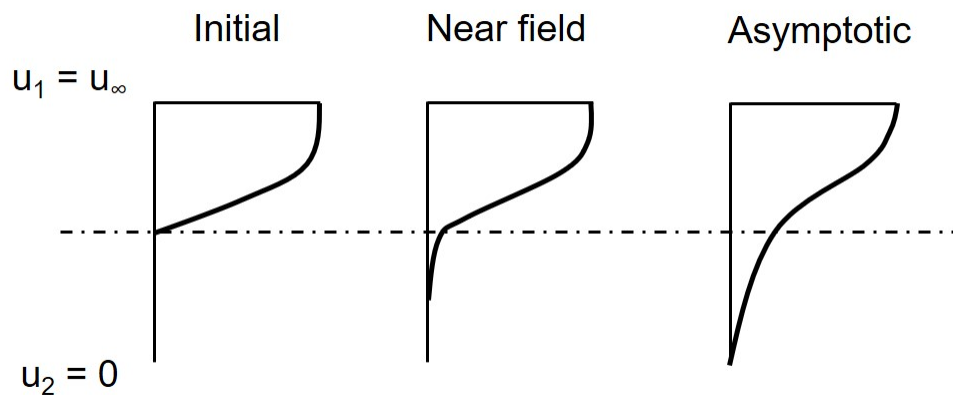


Figure 1.4. Schematic of shear-layer velocity profiles for a generic separated flow. Redrawn from Reference [24]

A review on the stability of the boundary layer above a separation bubble at low speeds was completed by Dovgal et al. [25]. Numerous parametric studies were presented and it was summarized that convective instabilities were a major factor in the transition from laminar to turbulent flow. However, the physics of high-speed shear

layers are drastically different than those at low-speed. A review of high-speed shear-layer transition was written by Demetriades [24]. Numerous transition correlations were presented and compared to previous data sets. Most of these only included transition location and not the physics of the transition process.

The role of instability in the high-speed shear-layer transition process has been investigated for numerous types of shear-layer flow. Not every flow field will be considered here, but a small subset of relevant data on mixing streams, cavities, and wakes will be presented. Two parallel flows of dissimilar velocities are commonly studied due to transition having a large effect on the mixing between them. Measurements by Demetriades et al. on such a flow field exhibited instability within the shear layer at supersonic Mach numbers. [26]. Liang et al. computed a mixing layer between Mach 3 and 8 streams and compared it to experiments by Demetriades [27]. Instability amplification was measured around 40 kHz in experiments and computations showed amplification of “slow mode” instabilities at these locations. Work by Papamoschou and Roshko correlated instability growth rates in free shear layers with a convective Mach number [28]. This is based on convection velocities of dominant waves within the shear layer.

Experiments by King et al. measured transition and instability in the shear layer at Mach 3.5 in quiet flow above a cavity [29]. Surprisingly, no effect of freestream noise was reported on the transition location. However, the effect of noise on transition in shear layers has not been determined for other geometries or different conditions. Instability content was measured with hot wires and no instability was measured under quiet flow. Possible instability was measured at  $\approx 16$  kHz for noisy flow and transition location correlated with convective Mach number.

Experiments and computations by Behrens measured linear and non-linear growth of instabilities within the wake shear layer behind slender bodies at Mach 6 [30]. Profiles used for computations were measured with hot wires to ensure accurate computations. Linear instabilities were measured near 50 kHz and matched Linear Stability Theory (LST). Non-linearities developed with increasing length Reynolds

number but limited interpretation was given. Computations by Papageorgiou showed the effect of Mach number on inviscid instabilities due to inflected velocity profiles [31]. Increasing Mach number delayed the growth of acoustic and vortical modes, especially when approaching Mach 20. Experiments of cone wakes by Maslov et al. at high Mach number ( $M_\infty = 21$ ) found natural oblique and plane waves. Density perturbations were damped within the shear layer behind a  $7^\circ$  cone [32]. Artificial disturbances led to instability at velocities that did not match predicted the first and second mode phase velocities.

Schmidt et al. carried out experiments at Mach 5 on a cone with gas injection on the surface [33]. While this is not an ideal comparison to separated flow, it features two streams of differing velocities and is considered a shear layer. Schlieren imaging and surface pressure measurements measured instability within the injection and were compared to computations. Their experiments measured a convective instability within the injection that behaved similar to those in other shear layers.

The behavior of the shear layer above a corner separation might be different than in some of the literature presented in this section, but previous work shows that convective instabilities have been measured in high-speed shear layers. Thus, the presence and contribution of these convective instabilities needs to be considered to help determine the transition mechanisms in flight.

### **1.2.2 Surface Heat Transfer and Streamwise Vortices in Transitional Hypersonic SBLI**

The effects of SBLI on surface heat transfer is directly related to the state of the boundary layer before and within the interaction. Much work has been done on SBLIs with fully laminar and fully turbulent interactions. However, fewer papers consider situations with a laminar incoming boundary layer and transition occurring in or near the separated region. An early paper by Gadd et al. published the effects of shock strength and Reynolds number on the surface pressure and flow structure of

SBLIs [34]. Parametric effects on the shape of surface pressure curves were plotted and transition location dominated the structure of separation. Similarly, Chapman et al. measured surface pressures in a 2D compression corner and found that transitional interactions were unsteady and dependent on Reynolds number [21].

Hung and Barnett attempted to compile and correlate surface heat transfer data sets for completely laminar, completely turbulent, and transitional SBLI [35]. Their analysis showed large Stanton number slope changes can identify transition within the interaction. They proposed transition correlations of peak heat transfer for each boundary-layer state.

Early heat transfer and hot-wire measurements were made on a hollow-cylinder flare with laminar and transitional boundary layers by Ginoux [36]. Streamwise streaks were measured downstream of reattachment and were believed to be due to leading-edge flaws that seed the flow with vorticity. These streaks caused large increases in local temperature and promoted transition. The streaks were not present post-reattachment on an ogive-cylinder-flare but returned when artificial roughness elements were placed near the tip. Thus, the streaks appear to be sensitive to the leading edge roughness distribution.

Numerous papers in the past 40 years have presented cases of transitional SBLI and their effects on surface heat transfer [37–52]. In several studies, peak surface heat transfer of transitional SBLI can match or sometimes exceed that of the turbulent or tripped-turbulent cases [36, 40, 43, 47]. The peak heat-transfer typically occurs just downstream of the reattachment point for SBLIs generated by both incident shock waves or compression corners. Additionally, the quantity and precise location of peak heating is dependent on where transition occurs with relation to the SBLI. Many of the correlations and computations used in the given literature underpredict the transitional heat transfer.

Post-reattachment heating is also affected by the presence of Görtler-like streaks. [36, 38–40, 42, 44, 45, 53, 54]. The development of Görtler vortices is due to acceleration of a fluid along a concave surface [55]. In strongly interacting SBLIs, the deflection

of the flow creates regions of high curvature at separation and reattachment. These vortices have been measured in laminar, turbulent, and transitional flow [56, 57]. The streamwise vortices produce spanwise variations in heat transfer and introduce three-dimensional behavior into cases that have nominally two-dimensional geometries. The streaks have been measured on flat plates with compression corners, hollow-cylinder-flares, and cone/flare geometries. They have been measured at numerous Mach numbers and model conditions. The extent, locations, and heating of these streaks in reattaching boundary-layers has been a focus of past transitional-SBLI research. Experiments across several facilities have reported that the wavelength of streamwise streaks is perhaps twice the local boundary layer thickness [53, 57].

The origin of the Görtler-like streaks has been researched in many papers. Computations have shown that the highly curved portions of the separating boundary layer can greatly amplify streamwise disturbances [58]. Many papers cite sub-critical roughness on or near the leading edge to be the source of disturbances [36, 39, 42]. Critically, the effect of tunnel noise on the presence of streamwise streaks has not been documented [7]. An attempt to utilize quiet flow on the Hyper-2000 scramjet forebody was made but the required Reynolds numbers did not allow for quiet flow at the time [59]. Whether Görtler-like vortices and streamwise streaks are the only cause of transition is debatable. Benay et al. states that possible convective instabilities must be included along with Görtler-like vortices to determine the physics of transition [45].

It is unclear if a smooth model with a flawless leading edge can produce vortex-free flow in a quiet flow facility. Brown et al. provided an alternative theory for the source of the vortices [46]. Their computations on a axisymmetric hollow-cylinder-flare found a secondary vortex flow within the recirculation region. This seemed to have been disturbing the flow within the separation. This disturbance of the separation bubble yielded an unsteady three-dimensionality that largely disturbed the shear layer. The authors conclude that the disturbed shear layer led to spanwise variations seen post-reattachment. Computations by Sidharth et al. used a biglobal analysis on a separation due to an impinging oblique shock wave. They showed large amplification

of a global non-convective instability in the shear layer above a separation [60]. This global instability then led to streamwise streaks post-reattachment. Computations by Dwivedi et al. utilized an input-output method for probing the flow above a separation bubble caused by a two-dimensional wedge. They found the streamwise streaks to be caused by selective amplification of streamwise velocity perturbations by baroclinic effects through the interaction. No consensus on the cause of streamwise streaks has been agreed upon. [61,62]

### 1.2.3 Instability in Laminar and Transitional Hypersonic Ramp-Induced Separations

While understanding the heating trends is important for the design of vehicles, a physics-based model of the transition process is needed. The presence of streamwise streaks has been measured in laminar and transitional SBLI, but the role of convective instabilities has not received as much attention. Measuring and computing boundary-layer or shear-layer instabilities can help illuminate the underlying physical mechanisms of the boundary-layer transition process. For this reason, literature on the stability behavior of this category of flows will be presented.

A sophisticated attempt at a theoretical solution to the stability of a separated flow was made by Cassel et al. [63,64]. They used an extension of triple-deck theory and found that an absolute instability is present near the corner of the ramp. The absolute instability manifests as a stationary wave packet near the ramp corner. Unfortunately, no comparisons to computation or experiment were given, so the assumptions have not been confirmed.

Balakumar used linear stability theory to investigate the effects of separation on the second-mode instability [58]. His results showed that the second-mode instability is essentially neutral through the mixing layer that is present above the separation bubble. Even though the second-mode instability is a dominant mode of transition

within a hypersonic boundary layer, the different profiles of shear layers alter the stability. [65].

Differences in boundary-layer stability appear if the SBLI source and computational methods are changed. Pagella et al. computed the stability of a Mach-4.8 boundary layer with an impinging oblique shock wave [66]. His computations found amplification of the second-mode instability and it was attributed to the growth of the supersonic layer within the boundary layer.

A large body of work on the growth and breakdown of instabilities through a compression corner has been completed by Egorov et. al. and Novikov et. al. [67–70]. Their approach was able to track the growth and progression of discrete wave packets through the separated region. These wave packets are artificially introduced into the flow field and are not the naturally occurring in-flow boundary condition. They confirmed the damping of second-mode instabilities through the corner and reported that instabilities within the first-mode frequency range are amplified by the new resonances within the separation bubble. Additionally, the growth and structure of the instability waves is dependent on the location of any computational forcing.

Experiments by Whalen et al. at Mach 6 in conventional flow show images of second-mode-like rope waves entering a separation on a flat plate with a wedge [71]. The waves formed “shocklets” and the shear layer reattached turbulent. No sensor or heat transfer data was available. Other recent flat-plate-wedge experiments were completed by Hedlund et al. at Mach 4.5 in both cold and higher enthalpy flow [72]. Optical measurement techniques were used to measure fluctuations within the shear layer above a 30° ramp in conventional flow. Perturbations believed to be acoustic waves were measured but limited conclusions regarding transition mechanisms could be made.

Leinemann et al. did experimental and computational work on a hollow-cylinder flare in quiet and noisy flow [52]. A combination of surface pressure measurements and LST show second-mode instability peaks upstream of separation. In noisy flow the boundary layer reattached turbulent so no distinct instability frequencies could be

measured. Quiet flow results were limited and measuring the boundary layer upstream and downstream of the separation bubble was difficult.

Experiments on a cone-cylinder-flare were done by Benitez under quiet flow at Mach 6 [73]. Heat transfer measurements from temperature sensitive paint and infrared thermography under quiet flow did not measure conclusive streamwise streaks downstream of reattachment. However, it is possible that the lower disturbance flow is reducing the growth of post-reattachment streamwise vortices. It is possible to measure Görtler streaks under quiet flow. Experiments by Portoni have measured Görtler streaks under quiet flow with infrared thermography. Portoni's measurements with temperature sensitive paint under similar conditions did not reliably measure Görtler streaks [74].

Surface pressure fluctuations from Benitez on the cone and cylinder show growth and damping of the second-mode instability, respectively [73]. The second mode continues to amplify on the flare. A second traveling instability is seen between 50 and 150 kHz on the flare and seems to be related to the separation bubble. This traveling instability is not seen on cone-cylinder-flare geometries that do not separate. Complementary computations by Esquieu were compared to the quiet-flow experiments [75]. Computations accurately predict second mode growth on the cone and cylinder but deviate on the flare. The unknown traveling instability is not predicted in the 2D axisymmetric computation.

#### **1.2.4 Effects of a Finite Span on Separation**

All the previous experiments and measurements outlined in this chapter utilize nominally two-dimensional flat-plates or axisymmetric geometries. Although the two-dimensional case is sometimes considered simpler, the presence of end effects make it very difficult to create a truly two-dimensional interaction [40]. A review of turbulent SBLI by Green states that two-dimensional interactions are practically impossible to achieve. [76]. A discussion of the difficulties in achieving two dimensional flows

was given by Lewis [77]. He stated that two-dimensional models did not have purely two-dimensional flow and a fenced axisymmetric model gave better, but not perfect, results. If computations are to match experimental work, the effects of the edges need to be considered. This requires that all computations must be three-dimensional and modeling the edge effects is difficult. While new discoveries can still be made on a nominally two-dimensional geometry, real flight vehicles will more likely use finite-span and three-dimensional control surfaces. Therefore, defining a well-posed three-dimensional geometry is desired for the present work. For these reasons, an attempt to measure shear-layer instability on a finite-span compression-corner at Mach 6 under quiet flow is necessary. Few transition experiments have been made on three-dimensional geometries but some limited studies are discussed here.

Experiments completed at Mach 8 by Oberkampf et al. studied the effects of a finite-span compression corner on the aerodynamic properties of a cone with a slice in Mach-8 flow [78]. All the data were collected under conditions that maintained a laminar boundary layer over the surface of the model. The flow visualization shows a nearly symmetric separation with an elliptic shape that has the largest streamwise extent on the centerline. Additionally, for  $0^\circ$  angle of attack (AoA) the flow only reattached for the  $10^\circ$  ramp case. The  $20^\circ$  and  $30^\circ$  ramp cases did not reattach. This paper provided the basis for the current model design in these experiments.

Computations by Thome were done on the Oberkampf geometry and on the current geometry described in this thesis. His work showed that the separation point extends almost the entire way to the edge of the slice region of the cone for both geometries [50]. No streamwise streaks were seen in the heat transfer and various angles of attack were computed. Thome's work highlighted the sensitivity of a three-dimensional separation bubble to small yaw angles.

Computations by Tan et al. showed the effects of transition on the separation bubble of a cone-slice-ramp at Mach 10 [79]. Transition location was varied by changing the streamwise position where the turbulent computation began. The separation

length decreased once transition was included in the computation. Transitional surface pressures and Stanton numbers exceeded those of both laminar and turbulent flow.

A cone-slice-ramp was tested by Vogel and Chynoweth et al. at Mach-6 under quiet flow [80]. Ramps with angles of  $5^\circ$ ,  $10^\circ$ ,  $20^\circ$ , and  $30^\circ$  were measured. Temperature sensitive paint shows a very large separation that encompasses the entire slice and the ramp. Reattachment was not clearly seen in the heat transfer and therefore conclusions were limited. Surface pressure fluctuations indicated disturbances between 40 and 120 kHz. The cause of these is not known. Complementary computations were made and showed moderate agreement with experiments. These experiments were carried out in parallel with the current work.

### 1.3 Objective of Research

The current research attempts to measure evidence of a convective hypersonic shear-layer instability in a low-noise environment. The contribution of convective instabilities to hypersonic boundary-layer transition is of particular importance. If successful measurements are made, a clearer understanding of the physical transition mechanism in a shear layer above a compression corner is achievable. The following steps are needed to reach this goal:

1. Iterate the design of a public-release three-dimensional compression-corner geometry. Use heat transfer, oil flow, and pressure fluctuation measurements to ensure the separation reattaches entirely on the ramp. This decouples the wake flow from the SBLI and provides room for surface measurements downstream of reattachment.
2. Study the effects of Reynolds number on post-reattachment boundary-layer state. In order to measure the effects of the shear layer on transition, current quiet flow capabilities need to permit laminar, transitional, and turbulent post-reattachment flow. If the flow field is well defined, then future computational comparisons can better model the experimental results.

3. Study pressure fluctuations upstream and downstream of the separation bubble to see if any instability develops within the shear-layer. The effects of ramp angle and Reynolds number will be investigated.
4. If no measurable convective instability is naturally present, develop a method to introduce artificial disturbances into the shear layer. Previous work has utilized high-voltage electronics to develop a localized plasma disturbance within the boundary layer and observe wave packets traveling downstream. This technique can be used on the cone-slice-ramp to measure convective instabilities and their growth through the shear layer. The ability for a perturbation to excite naturally unstable instability mechanisms should be tested on a known geometry. Computational comparisons can then be used evaluate the effectiveness of the artificial disturbance.

## 2. The BOEING/AFOSR MACH-6 QUIET WIND TUNNEL

The Boeing/AFOSR Mach-6 Quiet Tunnel (BAM6QT) at Purdue University is the larger of only two operational quiet hypersonic wind tunnel facilities in the United States. Figure 2.1 shows an annotated schematic of the BAM6QT. The tunnel is designed as a Ludwieg tube facility and provides low-cost experiments at a relatively high unit Reynolds number.

Operation of the tunnel consists of filling the driver tube with 160°C air to the desired pressure for testing. A set of double burst diaphragms is downstream of the nozzle and separates the high-pressure upstream side from the downstream vacuum side. Depending on stagnation pressure, the diaphragms are either thin sheets of aluminum or sheets of acetate plastic. The entire model and instrumentation is held at full stagnation pressure prior to a run. During the filling process, the pressure in between the two diaphragms is maintained at approximately half the difference between the driver tube and vacuum tank. A ten minute settling period occurs after the desired upstream pressure is achieved. This allows time for any transience in the air and model temperature to damp. When ready, the air gap between diaphragms is evacuated, causing the diaphragms to burst and initiate the run.

After the diaphragms are burst, a shock wave is sent downstream into the vacuum tank. At the same time, an expansion wave travels upstream through the converging-diverging nozzle and into the driver tube. After the expansion wave travels through the throat of the nozzle, Mach-6 flow is initiated. The expansion wave continues upstream until it reflects off the far end of the driver tube. The expansion wave comes back and reflects off the nozzle throat and this cycle repeats. This process takes approximately 200 ms and the stagnation pressure remains quasi-static while the

expansion wave travels. Only when the expansion wave reflects off the nozzle throat does a small drop in stagnation pressure occur. A standard tunnel run duration is approximately four seconds.

Models are placed within the downstream end of the nozzle. Two windows are available for optical access on either side of the nozzle. Depending on the type of experiment, a 17.8x35.6 cm (7x14 inches) rectangular window or 12.7 cm (5 inch) diameter porthole window can be installed. A stainless steel blank can be used if neither window is needed.

A quiet tunnel provides lower freestream noise levels than a conventional hypersonic facility and is a better representation of flight pressure fluctuations. Quiet flow is achieved by maintaining a laminar boundary layer on the nozzle wall. Steen measured the ratio of freestream pitot-pressure fluctuations to the mean pitot pressure ( $P'/P_0$ ) to be on the order of 0.01% [81]. These measurements were recently confirmed by Gray [82]. The BAM6QT is also capable of being run with conventional freestream noise levels and a turbulent boundary layer on the nozzle wall. Freestream pitot-pressure fluctuations are approximately 2% for BAM6QT conventional flow. Due to the thicker boundary layers in turbulent flow the freestream Mach number is reduced to 5.8.

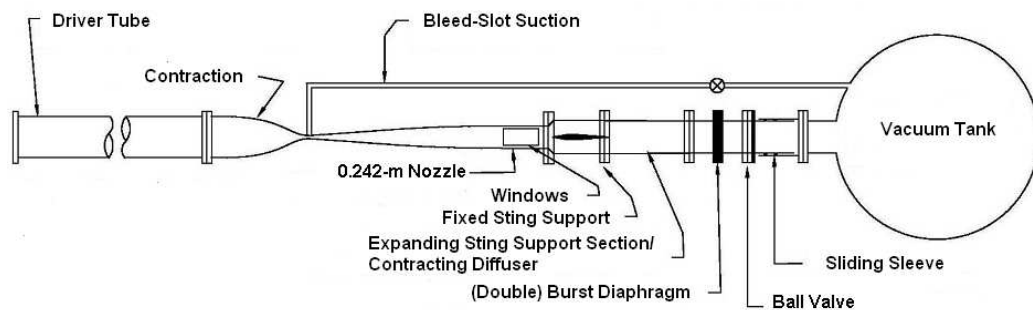


Figure 2.1. Schematic of the BAM6QT.

The BAM6QT includes several unique features that create a low pressure-fluctuation environment. First, the diverging portion of the nozzle has been polished to a mirror

finish. This avoids any roughness-induced boundary-layer transition as the air expands downstream. This finish is particularly important since individual imperfections can reduce the maximum quiet flow Reynolds number. Secondly, fine air filters are present at the upstream end of the driver tube. Before the air is pumped into the tube, the filter removes any particles larger than  $1\ \mu\text{m}$  from the air in order to preserve the finish of the diverging portion of the nozzle. The nozzle is lengthened in order to limit the growth of the Görtler instability along the curved surfaces. Lastly, a bleed slot is present at the nozzle throat. When a run is initiated, a fast-acting butterfly valve opens and exposes the bleed slot to the vacuum tank. The boundary-layer from the converging portion of the nozzle is removed and a fresh laminar boundary layer is allowed to grow downstream on the polished diverging portion.

There is a limit for how high the Reynolds number can be increased before loss of quiet flow. Until 2016, the present work had a maximum quiet Reynolds number of approximately  $\text{Re}_\infty \approx 12 \times 10^6/\text{m}$ , or a stagnation pressure of 170 psia. A leak was repaired upstream of the nozzle. Despite precautions, the repair reduced the quiet-flow Reynolds number. It is believed that some small particulate got into the nozzle and scratched the surface. At this time the tunnel was limited to  $\text{Re}_\infty \approx 9.5 \times 10^6/\text{m}$ , corresponding to  $P_0 \approx 135$  psia. The nozzle was repolished in 2018 and the maximum Reynolds number increased to  $\text{Re}_\infty \approx 11.5 \times 10^6/\text{m}$ , corresponding to  $P_0 \approx 155$  psia.

## 2.1 Determination of BAM6QT Run Conditions

Several sensors are in place for measuring the conditions within the BAM6QT before and during a run. Qualitative confirmation of quiet flow was completed by measuring heat transfer and pressure fluctuations on the nozzle wall. Heat transfer fluctuations were initially measured with a Senflex multi-element hot-film array. This was replaced in 2018 with a Model 55R45 Dantec single-element hot-film array. A constant temperature was maintained across the hot films by a Bruhn-6 Constant Temperature Anemometer. After the hot film swap, nozzle-wall pressure fluctuations

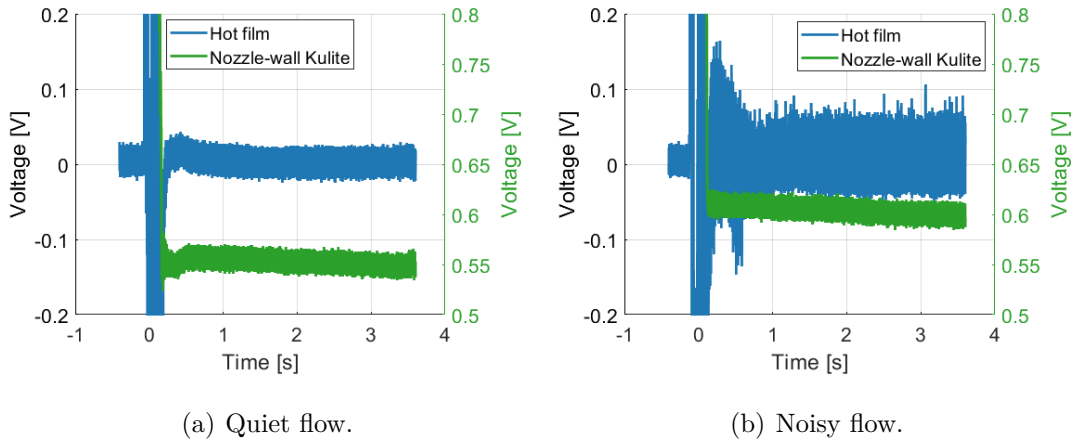


Figure 2.2. Sample hot film and nozzle-wall Kulite traces for quiet and noisy flow.

were measured with a Kulite model ETL-79-HA-DC-190 pressure sensor. Sample hot film voltages can be seen in Figure 2.2. Noisy flow exhibits hot film voltage fluctuations nearly twice that of quiet flow. Every run was examined to determine if any turbulent spots were present on the nozzle wall. Kulite traces exhibit similar pressure fluctuations in quiet and noisy flow but the mean pressure increases for turbulent flow. The Kulite and hot film can also be used to qualitatively determine if the nozzle wall boundary layer has separated due to a tunnel unstart.

A Kulite XTEL-190-500A sensor was used to measure the stagnation pressure during every test. This sensor is flush mounted upstream of the throat in the entrance to the nozzle contraction and is denoted the contraction Kulite. The flow is relatively stationary at this point and the measured pressure is approximately the stagnation pressure. The sensor is rated to 500 psia [83]. During testing, the sensor is calibrated weekly. The pre-run pressure recorded on the contraction Kulite is compared to reference pressures measured on a Paroscientific Inc. Model 740 Digi-quartz Portable Standard. A linear fit is applied and is used to determine stagnation pressure from the contraction Kulite. A sample time trace of the contraction Kulite is seen in Figure 2.3. The typical stair step pattern from the reflection of the expansion can be seen approximately every 0.2 seconds.

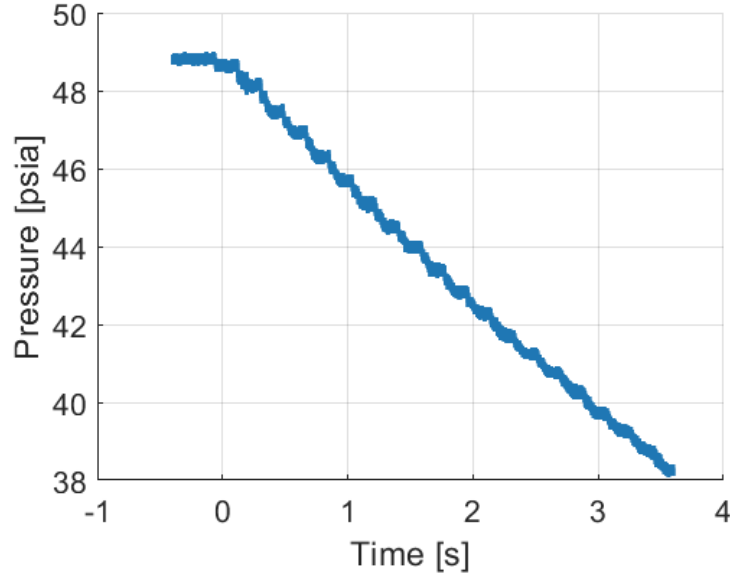


Figure 2.3. Sample time trace of contraction Kulite.

Calculation of the stagnation pressure and temperature during a run was based on isentropic relations. Initial stagnation temperature was measured from a thermocouple present on the upstream wall of the driver tube. The isentropic stagnation temperature during the run is computed using

$$T_0(t) = T_{0,i} \left( \frac{P_0}{P_{0,i}} \right)^{\frac{\gamma-1}{\gamma}}. \quad (2.1)$$

The instantaneous stagnation pressure during the run was recorded on the contraction Kulite ( $P_0(t)$ ). After calculating stagnation values, the static pressure and temperature are

$$T(t) = T_0(t) \left( 1 + \frac{\gamma-1}{2} M^2 \right)^{-1} \quad (2.2)$$

and

$$P(t) = P_0(t) \left( 1 + \frac{\gamma-1}{2} M^2 \right)^{\frac{-\gamma}{\gamma-1}}. \quad (2.3)$$

With these conditions calculated, the freestream unit Reynolds number was defined as

$$Re_{\infty}(t) = \frac{P(t)M}{\mu} \sqrt{\frac{\gamma}{RT(t)}}. \quad (2.4)$$

Mach number was dependent on whether the BAM6QT was run with quiet or noisy flow. The dynamic viscosity was calculated assuming an ideal gas with Sutherland's law and without the low-temperature correction. Changes in Reynolds number are primarily controlled by differences in density caused by the variation in tunnel stagnation pressure.

### 3. INSTRUMENTATION AND DATA PROCESSING

#### 3.1 Oscilloscopes

The signals output by the sensors were recorded on the following models of digital oscilloscopes: Tektronix DPO5034B, DPO7054, DPO7104, and MDO3014. Four channels of data were recorded on each scope. Sampling rates were chosen to avoid aliasing of any signal below 1 MHz. All the oscilloscopes were run in Hi-Res mode, which captures the data at the maximum sampling rate and averages the data in real time to the desired sampling rate and a vertical resolution of about 12 bits. Hi-Res mode allows the scope to record data with lower noise levels and a built-in low-pass filter [84]. The DPO7054, DPO5034, and DPO7104 all collected data at 2-5 MHz for 5 seconds during the run. The MDO3014's were sampled at 2.5 MHz for four seconds. The channels were AC coupled for PCB sensors and DC coupled for all others. All channels were set to a 1 M $\Omega$  impedance.

Voltage and current measurements for plasma generation on the 7° and cone-slice-ramp model were measured on a Keysight Technologies DSO9104A Oscilloscope. A 1 GHz bandwidth at 12-bit vertical resolution was used and sampling rates of either 50 MHz or 5 GHz were used for measuring an entire series of pulses or individual pulse, respectively. All channels were DC coupled and either 1 M $\Omega$  or 50  $\Omega$  impedance was used.

#### 3.2 Pressure Sensors

##### 3.2.1 PCB Pressure Transducers

PCB Model 132A31 and 132B38 sensors were used to measure the pressure fluctuations on the surface of wind tunnel models. Both sensors consist of an epoxy

surface that covers a piezoelectric crystal. When exposed to a change in pressure, the crystal deflects and produces a voltage change. The voltage can then be related to the pressure change across the surface of the sensor by using a calibration. These sensors were originally designed to measure shock arrival times and come with a single-point factory calibration and a pressure resolution of 0.001 psia [85]. Work has been done by Berridge [86] and Wason [87] to improve the calibration by using a multi-point dynamic method. Due to time and availability, the sensors used for the current experiments did not have these calibrations. Previous work has shown these sensors used successfully to measure high frequency phenomena in hypersonic testing facilities [88, 89].

The sensor cannot register frequencies below 11 kHz due to a built-in high-pass filter and has a resonance above 1 MHz [85]. The frequency response remains flat up to roughly 300kHz [90]. The sensor is connected to a PCB-482A22 conditioner box and the AC signal is recorded on a Tektronix oscilloscope operating in Hi-Res mode. All sensors were AC coupled and sampled above 2 MHz to avoid aliasing the 1 MHz upper limit. The sensor is 3.18 mm in diameter and 7.62 mm long. All sensors were wrapped in 0.025 mm (0.001 in.) Kapton tape to reduce electrical noise in the data and ensure a tight fit in models.

The differences between the A and B models are in the sensing element of the piezoelectric crystal. The PCB132A31 sensors have a sensing element that is a 0.76 mm square. This element is not necessarily centered in the sensor [86]. The PCB132B31 utilizes a centered circular element in order to reduce the uncertainty in the measurement. This element is 0.889 mm in diameter.

Data recorded from PCBs were normalized depending on the type of model being used and the location of the sensor. Sensors on conical models were normalized by surface static pressure from the Stability and Transition Analysis for hypersonic Boundary Layers (STABL) software [91]. Documentation for 7° sharp cone gridding and solutions was created by Heath Johnson at the University of Minnesota and can be found in the STABL manual. This procedure was used for the present work. Mean

flow computations used a grid containing 360 streamwise and wall-normal points with exponential clustering of points near the nose and wall.

Sensor data from the cone-slice-ramp models were normalized with a tangent-wedge approximation of the surface pressure. This was preferred over a computational mean pressure due to differences between the extent of separation in experiments and computations. These differences are discussed in Section 4.2.1. Tangent-wedge is a local surface inclination method that only considers the angle that a single point on the surface makes with the incoming flow. A solution was found by taking the angle of the ramp as the turning angle for an oblique shock wave. The flow was considered isentropic and a perfect gas with  $\gamma = 1.4$ . The governing equation for the shock-wave angle is

$$\tan\theta = 2\cot\beta \frac{M_1^2 \sin^2\beta - 1}{M_1^2(\gamma + \cos 2\beta) + 2} \quad (3.1)$$

where  $\theta$  is the ramp angle and  $\beta$  is the shock-wave angle. The weak-shock solution was chosen and values were obtained from Reference [92]. The shock-wave angle was then used to calculate the pressure ratio across the shock with the oblique-shock relation:

$$\frac{p_2}{p_1} = 1 + \frac{2\gamma}{\gamma + 1}(M_1^2 \sin^2\beta - 1) \quad (3.2)$$

This pressure ratio was used with isentropic flow relations to scale the tangent-wedge pressure with BAM6QT stagnation pressure. Table 3.1 shows the ratios used to normalize the pressure data. If a sensor was not on a conical surface, the tangent-wedge pressure for a  $20^\circ$  ramp was used to normalize the pressure data. This includes sensors that were upstream of the compression corner on the slice.

The Power Spectral Density (PSD) was then calculated for the normalized pressure fluctuations. The PSD is a measure of the power present at individual frequencies within the digital signal and can illustrate the behavior of instabilities in the boundary-layer. First, voltages were converted to pressure with the PCB factory calibration and then normalized. The mean of the normalized signal is then subtracted out before

Table 3.1. Sample pressure ratios for various methods and geometries

Method	Pressure Ratio	Locations of sensors normalized by each method
Tangent-wedge for 20° ramp ( $P_{TW}/P_0$ )	0.00684	Ramp and slice
Mean surface static pressure for a 7° cone from STABL ( $P_{mean}/P_0$ )	0.00125	7° cones
Isentropic freestream static pressure ( $P_{static}/P_0$ )	0.00063	None

the PSD calculation. PSDs are generated by averaging Fast-Fourier Transformations (FFT) of individual sections of signal. A Blackman window with 50% overlap was used to partition the time series and FFT's of the segments were averaged. The frequency resolution of the PSD is dependent on the sampling rate and the number of points in the windows. A constant frequency resolution of 2 kHz was maintained for all PSD's by varying the number of points in a window. Reynolds numbers were calculated at the same instant in time as PSD's.

Methods of calculating the Root Mean Square (RMS) pressure fluctuation magnitudes varied depending on the physics and the application for the data. RMS pressure magnitudes from experiments without plasma perturbation were calculated by integrating the PSD and taking the square root of the result. Integration was calculated using a trapezoidal approximation in a specific band of frequencies. This was commonly 15-200 kHz to allow comparison to pressure data from Kulite sensors. If the plasma perturbation was present on the model, less than 10% of the time had wave packets present on the model. This caused concern with how the averaging in the PSD would affect the calculated RMS fluctuations. Details on how these cases were treated is found in Section 6.2.2.

Determining the relation between two signals helps to understand the behavior of instabilities across multiple sensors. The magnitude squared coherence is a way to measure the degree of linearity between the input and output of a system. This was used to calculate the relation between two pressure sensors. The first sensor's signal would be considered the input and the second sensor's signal would be considered the output. The coherence was calculated as

$$C_{xy}(f) = \frac{|P_{xy}(f)|^2}{P_{xx}(f)P_{yy}(f)} \quad (3.3)$$

where  $P_{xx}(f)$ ,  $P_{yy}(f)$ , and  $P_{xy}(f)$  are the PSD's of the two individual signals and the cross-spectral density of both. The coherence varies between 0 and 1 for a given frequency. High coherence at an individual frequency represents a strong relation between the two signals for that specific frequency. Coherence itself is not

a true indication that instability is present within the boundary layer but when combined with PSD's and RMS amplitudes, instability behavior can be studied. If strong coherence is present, the convection velocities of instabilities can be calculated with the cross-correlation. If a low coherence is found there could be no instability, nonlinear effects, or no dependence of the two signals on each other. For example, absolute instabilities which don't travel within the boundary-layer might appear across several sensors but would not strongly cohere.

The intermittency of the pressure signals were calculated through the use of a wavelet transformation. This method was developed by Casper et al. for use on a  $7^\circ$  cone at  $0^\circ$  AoA [11]. The technique is capable of separating second-mode wave packets from turbulent spots to determine the amount of time the flow experiences turbulent fluctuations. It was adapted for use in the current experiments. An intermittency of 0 pertains to fully laminar flow and 1 correlates to a fully turbulent flow. Values between 0 and 1 indicate a proportion of time which turbulent fluctuations are observed.

A continuous wavelet transformation with Morlet wavelets was used to process the pressure time traces. The wavelet transformation provides fluctuation frequency content with high resolution in time. A sample map of the wavelet coefficients for pressure fluctuation data is shown in Figure 3.1. Two bandwidths are defined to separate wave packets from turbulent spots. A 40-120 kHz bandwidth was chosen for wave packets and turbulent spots were identified by high frequency content between 150-300 kHz.

For every moment in time, the wavelet coefficients are averaged and compared to user-defined threshold levels to determine wave packets and spots. If the mean wavelet coefficient within a frequency band is greater than the threshold, a wave packet or turbulent spot was present at that moment in time. Choosing a threshold level is based on the physics of the flow and the expertise of the user. For the current experiments, a 0.3 and 0.1 threshold were chosen for wave packets and turbulent spots, respectively. An example of detected wave packets and turbulent spots within

a time trace can be seen in Figure 3.2. The selected thresholds can accurately pick out high-frequency turbulence and low-frequency wave packets within the pressure fluctuation time trace.

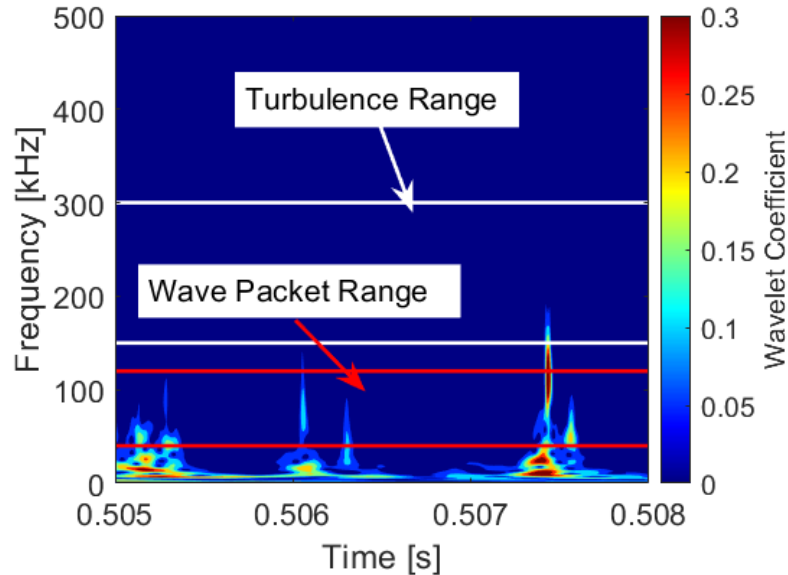


Figure 3.1. Wavelet coefficients for a sample pressure fluctuation time trace. Lines indicate the wave packet and turbulent spot detection bandwidths.

### 3.2.2 Kulite Pressure Transducers

Kulite XCQ-062-15A pressure transducers were used to measure run conditions in the BAM6QT and also surface pressure fluctuations on the long-slice model. A Kulite consists of a metal sheath that houses a silicon diaphragm with a Wheatstone bridge embedded upon the surface. In order to protect the diaphragm, a screen is present at the tip of the sensor and several types exist. A-screen Kulites feature a single hole on the sensor head and were used in the present experiments. When exposed to pressure, the diaphragm deflects and the Wheatstone bridge records the deformation as a voltage change [90]. These Kulites are 1.7 mm in diameter, 9.5 mm tall and have an infinitesimal resolution [93]. The Kulites available for use within the

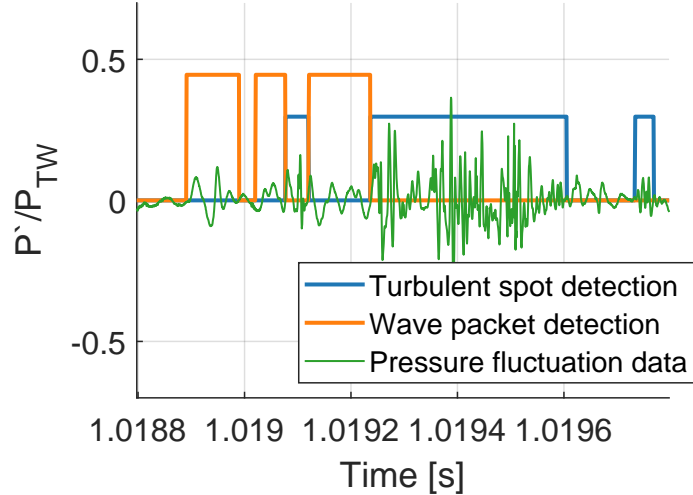


Figure 3.2. Example pressure fluctuation trace with detected turbulent spots and wave packets.

BAM6QT have been customized to be mechanically stopped at 15 psia. This prevents damage to the sensor while the model sits at stagnation pressure prior to the run. The signal is processed through electronics fabricated at Purdue that allow for DC and AC measurements. For AC measurements, the signal has a gain of 10000 and DC measurements have a gain of 100. DC measurements were used for the current experiments.

An in-situ calibration was completed every week for the Kulite sensors. Typically, five pressures between atmosphere and vacuum were used to create a linear fit for converting voltage to pressure. Reference pressures were measured on the Paroscientific Inc. Model 740 Digi-quartz Portable Standard. An example of a Kulite calibration can be seen in Figure 3.3. The fit is nearly linear except for the point near zero. This is similar to the procedure used for calibrating the contraction Kulite. Processing of the Kulite pressure fluctuation data was identical to the PCB sensors. An attempt to

measure mean pressure was made with the Kulites but the static pressure within the BAM6QT is so low ( $\approx 0.1$  psia) that the measurements are not accurate.

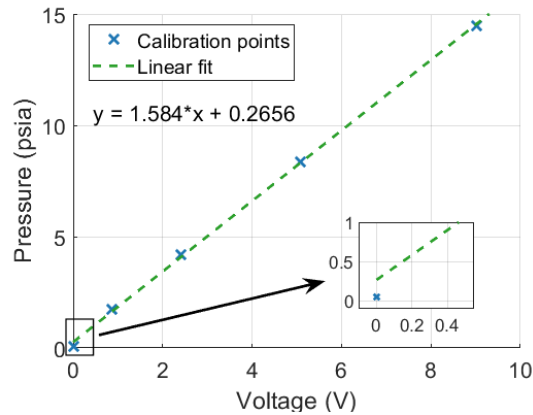


Figure 3.3. Sample calibration of an individual Kulite.

### 3.3 Heat Transfer Measurements

Both global imaging and discrete sensors were used to calculate the heat transfer on the surface of wind tunnel models. Images of heat transfer were reported as Stanton number and were scaled to correlate laminar heating [94]. Stanton number is defined as

$$C_H = \frac{q_w}{\mu_\infty Re_\infty c_p (T_0 - T_w)}, \quad (3.4)$$

where  $q_w$  is the heat transfer at the wall,  $c_p$  is the specific heat, and  $T_w$  is the temperature at the wall. The Stanton number was then scaled as

$$C_{H,laminar} = C_H \sqrt{Re_\infty}. \quad (3.5)$$

This has been found to correlate laminar flat-plate heating and was used as an approximate way to correlate laminar heating in the present experiments [95].

### 3.3.1 Schmidt-Boelter Gauges

Medtherm Schmidt-Boelter (SB) B-2-0.25-48-208535KBS gauges with built-in thermocouples were used to measure the heat flux and temperatures at discrete locations on the surface of the model. The sensor consists of a thermopile that can measure a temperature differential using an array of thermocouples to infer the heat flux. The SB models used for the cone-slice-ramp model also featured K-type thermocouples that were used to measure wall temperature prior to the run. The SB gauges are used to calibrate the temperature sensitive paint to obtain heat transfer on the model surface.

### 3.3.2 Temperature Sensitive Paint

Global temperature changes and heat transfer were measured on the surface of the models through the use of a temperature sensitive paint (TSP). The TSP is a paint mixture where a luminophore is dissolved into ethanol and combined with a clear coat and hardener. Experiments in the BAM6QT utilize 99.95% Tris(2,2'-bipyridyl) ruthenium(II) chloride hexahydrate [Ru(bpy)] as the luminophore. The Ru(bpy) is excited by light at 452 nm and subsequently emits light at 588 nm [96]. The intensity of emitted light is inversely proportional to temperature and this process is known as thermal quenching. TSP can help discern flow features that manifest as an increase in surface heat transfer. Since the mechanism is dependent on temperature, changes in surface temperatures can be determined from recording the intensity of the light on a charged-coupled device (CCD).

In order to maximize the excitation of the TSP, two arrays of light-emitting-diodes (LEDs) were used to illuminate the model. An Innovative Scientific Solutions Inc. (ISSI) LMA LM4 array and an ISSI LM2xLZ-465 array were used. Both LED's emit light at 465 nm, which is ideal for exciting the luminophores while still allowing for transmission through a conformal UVA Plexiglas window. Images were recorded on an IMPERX Bobcat IGV-B1620 14-bit CCD camera. The camera was equipped with

a 24 mm focal length lens and an orange filter. The orange filter was a 556 nm long pass filter and allows the emitted light to reach the CCD while blocking the 452 nm light. The camera was set to collect images at 1608x1208 resolution at a frequency of 15 Hz. Data were collected at 14 bits and exposure time and aperture settings were adjusted to maximize signal without saturating the CCD. An image of the 17.8x35.6 cm (7x14 inches) Plexiglas<sup>TM</sup> window and a typical camera setup is shown in Figure 3.4.

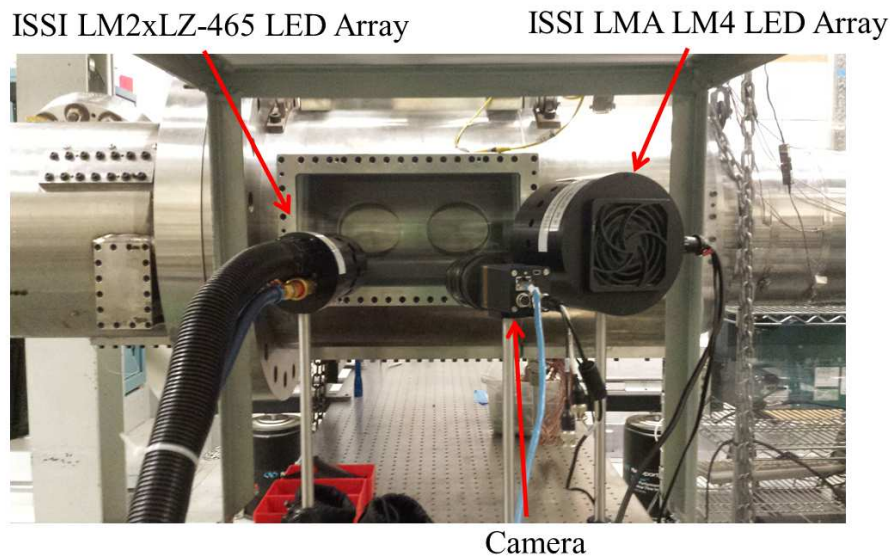


Figure 3.4. Experimental setup of the 2 LED light sources and 14-bit CCD camera.

Application of the TSP on a model was completed in-house before every tunnel entry. Prior to painting, the aluminum model surface was lightly sanded to aid paint adhesion and then cleaned with acetone. Sensor holes were left open and a layer of paint was allowed to build up inside the holes. This provided extra insulation between sensors and the aluminum model. Several base layers of Fastline FA3XEP gray self-etching primer were applied to the surface for better adhesion to flat surfaces. Top Flite Lustrekote Jet White paint was then applied as an insulating layer and a neutral background to the TSP. Coats of Jet White were added until the grey primer was completely covered. The primer and insulating layer were given 24 hours to

dry and then sanded with 500-2000 grit sandpaper. Special attention was given to the upstream end of the paint to ensure no forward-facing steps were present. TSP mixing and application was identical to that of Chynoweth, and details can be found in Reference [12]. The TSP coats were sanded with 500-2500 grit sandpaper.

Several steps are taken to convert the intensity values from the CCD to a temperature map. Three sets of images are recorded for every run: “dark” images, “off” images, and four seconds of “on” images. The “dark” images were taken with the LED lights off and no flow in the tunnel. They are used as a reference in order to reduce the noise in the images. The “off” images were taken with the LED lights on and no flow within the tunnel. They are used as another reference within the heat transfer computation. Twenty “dark” and “off” images were averaged to calculate the heat transfer. The “on” images are taken during the run after a trigger is received from the oscilloscopes. The calculation of temperature change based on the intensity values is

$$\Delta T = f \left( \frac{I_{on} - I_{dark}}{I_{off} - I_{dark}} \right). \quad (3.6)$$

The temperature change is defined as  $\Delta T$ .  $I_{on}$ ,  $I_{dark}$ , and  $I_{off}$  are the intensity values of the “on”, “dark”, and “off” images, respectively. The function  $f$  is an empirical function based on the type of TSP used and the calibration method. The TSP calibration can be found in Figure 3.13 of Reference [97]. The result of using the empirical calibration with a known pre-run reference temperature is

$$\Delta T = (362 - T_{ref}) \left( 1 - \frac{I_{on} - I_{dark}}{I_{off} - I_{dark}} \right). \quad (3.7)$$

Extracting heat transfer from the temperature profiles required additional calculation and assumptions. Fourier’s law of heat conduction is simplified by assuming one-dimensional heat transfer in the radial direction. Ward determined that the model temperature can be considered constant during the course of the run [96]. Equations 3.8 and 3.9 show the simplified version of Fourier’s law with the assumptions applied.

$$q = \frac{\kappa}{l} (\Delta T + T_{ref} - T_b) \quad (3.8)$$

$$\Delta T = T - T_{ref} \quad (3.9)$$

The heat transfer on the model surface is  $q$ , the temperature of the model surface just before the start of the run is  $T_{ref}$ ,  $\kappa$  is the thermal conductivity of both the insulating layers and the TSP,  $l$  is the depth of the insulating layer, and  $T_b$  is the temperature at the base of the insulator.

SB gauges were used as a reference for the TSP heat transfer calibration. For every run, a square comparison patch is chosen nearby the SB being used. A sample of SB and comparison patch locations can be seen in Figure 3.5(a). Figure 3.5(b) shows a least-squares fit between the SB heat transfer and the TSP to infer heat transfer across the surface. The best possible fit is achieved by iterating  $\frac{\kappa}{l}$  and  $T_b$  until a good agreement is found. Figure 3.5(c) shows a representative fit between the TSP heat transfer and SB gauge. Figure 3.5(d) shows the final inferred heat transfer from this process.

TSP was used as one method for measuring the global surface heat transfer. TSP was the only method that could image an entire model during the present work. The large conformal Plexiglas window provides the largest optical access for the BAM6QT. TSP is limited by the quality of the paint job for individual runs. This can vary week to week and alter the repeatability of results. Additionally, the spatial resolution is limited by the output of light from the Ru(bpy) and the resolution of the camera.

### 3.3.3 Infrared Thermography

Development of an improved method to measure global heat transfer with an infrared (IR) camera was completed in parallel with the present work by Edelman, Cerasuolo, and Zaccara. Later experiments utilized this method to measure the surface heat transfer. This section will only be a summary of the IR imaging and heat transfer

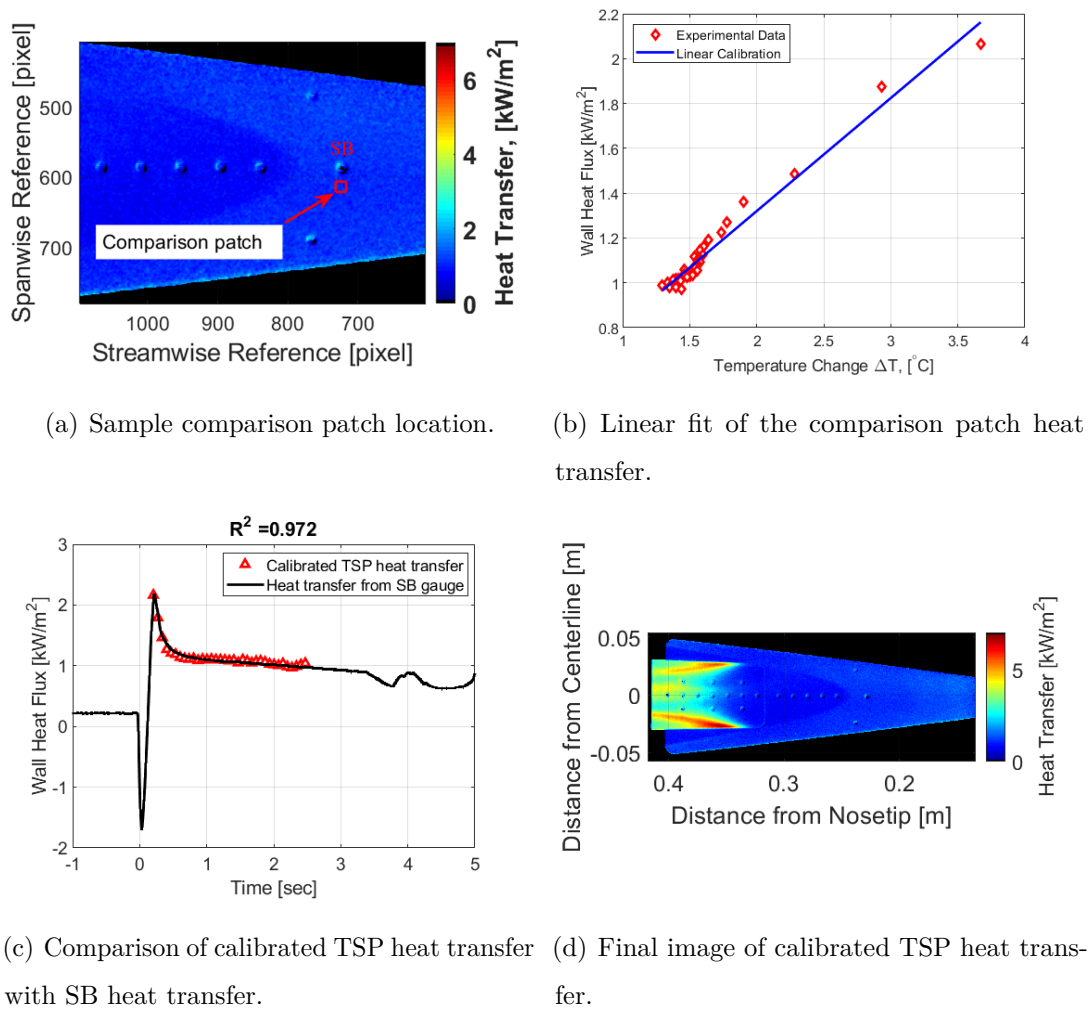


Figure 3.5. Steps for post-processing of TSP images into heat transfer. Conversion to Stanton number occurs after these steps are complete.

reduction process. A full treatment of this topic can be found in References [98], [99], and [100].

Images of surface temperature were taken with an Infratec ImageIR 8300 hp camera. The camera has a mid-wave IR sensor and measures light with wavelengths between 2.0 and 5.7  $\mu\text{m}$ . The camera has a pixel resolution of 640x512, a temperature resolution of 0.02 K, and an accuracy of  $\pm 1$  K. Images can be recorded up to 355 Hz but were captured at 350 Hz for the current experiments [101]. The camera was

outfitted with a 12mm f/3.0 wide-angle lens. The camera software includes individual calibrations for the specific lens being used. A temperature calibration range needs to be chosen prior to a tunnel run. Lower Reynolds number runs utilized the -10-60°C calibration and higher Reynolds number runs used a 0-100°C calibration. Optical access was through a 81 mm calcium fluoride window designed by Borg [102].

IR ramps were made out of Poly-Ether Ether Ketone (PEEK). This material is a high-emissivity plastic that is optimal for IR measurements. PEEK thermal properties are outlined in the Purdue IR system handbook [100] and References [98] and [99]. Additionally, Cerasuolo and Zaccara made detailed measurements of the directional emissivity for PEEK [98, 99]. An overview of applicable properties can be found in Table 3.2. The emissivity is defined as a function of  $\theta$ , the angle between the local surface normal of the PEEK and the camera plane.

Table 3.2. PEEK Material and Thermal Properties.

Specific Heat	$1026 \frac{J}{kgK}$
Thermal Conductivity	$0.29 \frac{W}{mK}$
Density	$1300 \frac{kg}{m^3}$
Thermal Diffusivity	$2.17 \times 10^5 \frac{m^2}{s}$
Emissivity, $f(\theta)$	$0.91 \cos(\theta) \frac{0.03}{\cos(\theta)^{1.35}}$

Prior to imaging with the IR camera, a spatial calibration is needed for converting the camera pixels to physical points. A series of images are taken with calibration plates at known normal distances from the IR window. The normal distances encompass the depth range of the model section being imaged during testing. These points are then used with a nonlinear pinhole camera model to transform images into physical coordinates. A detailed treatment of the calibration process can be found in Section 4.1 of Reference [99]. If any part of the IR system is moved or re-positioned, a new calibration must be made.

The model is installed after calibration and the IR camera is ready for measurements. The lack of extra hardware and run procedures, compared to TSP, greatly simplifies heat transfer measurements in the BAM6QT. Post-processing of the IR images is completed with the Purdue Infrared Registration ANd Heat transfer App (PIRANHA). This was created by Edelman and is a self-contained Graphical User Interface (GUI) for calibrating, meshing, registering, and processing IR images.

Use of PIRANHA is divided into separate steps that must be completed to process IR images. First, the numerical model for the camera spatial calibration must be made. This utilizes the images of the calibration plates and a least-squares fit to determine the final mapping. For a good calibration, the standard residual of the spatial fit was desired to be under one pixel and the effective focal length should be near the lens focal length [103]. Next, a mesh must be applied to the surface of the PEEK model. This is dependent on the geometry being tested and a sample of a meshed 20° compression ramp can be seen in Figure 3.6(a). The ramp can be parameterized by the axial distance ( $x$ ) and spanwise distance ( $y$ ). The spatial calibration is then used to relate pixel coordinates on the model to their physical ( $x,y,z$ ) locations. Offsets are applied to the mesh to align it with the model.

Image registration is used to remove any movement of the model or tunnel during a run. The compression ramp was registered based on the back edge of the ramp. A two-dimensional cross-correlation method is used to calculate the registration of the images. Figure 3.6(b) shows a sample output from the PIRANHA image registration tool. The  $x$ -displacement and  $y$ -displacement plots show differences between subsequent images in time. The quality metric is a built-in MATLAB metric for registration quality. During the quiet flow portion of runs, IR images were not displaced by more than 0.1 mm as can be seen in the sample registration.

After image registration, the temperature of each individual frame is interpolated onto the mesh. This step takes into account the emissivity of the PEEK and the transmission of IR light through the window. The window transmission loss was calculated by

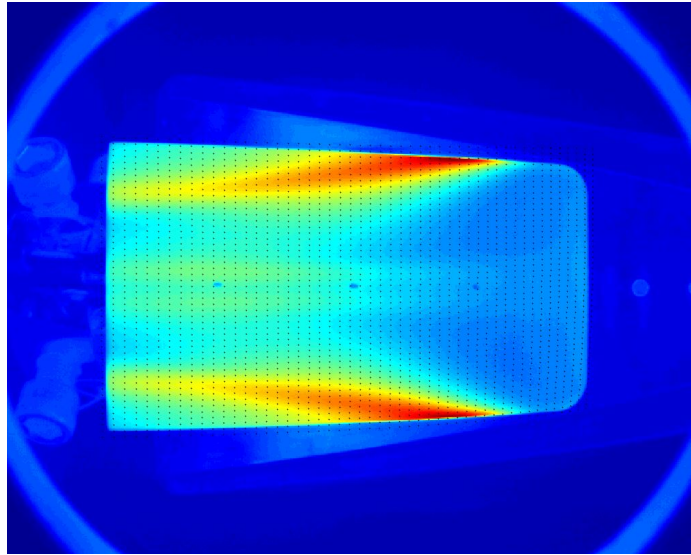
$$T_{actual} = \left( \frac{T_{IR}^4 - (1 - \tau\epsilon_\theta)T_{amb}^4}{\tau\epsilon_\theta} \right)^{1/4} \quad (3.10)$$

where  $T_{amb}$  is assumed to be 300K, the transmissivity  $\tau$  is 95%, and the directional emissivity of PEEK is  $\epsilon_\theta$ . The reasons for these values are defined and discussed by Edelman [100]. PIRANHA calculates heat transfer from the temperature history of the model with the QCALC MATLAB script and a 1D FFT method. This was chosen due to the speed of the calculation and the simplicity of a planar surface on a flat compression ramp. The QCALC algorithm has previously been shown to provide reasonable calculations of heat transfer on sub-scale HIFiRE-5 experiments [102]. QCALC utilizes a second order Euler-explicit finite difference method to solve for the temperature distribution pixel-by-pixel [104]. An adiabatic rear-wall boundary condition was used for the calculation.

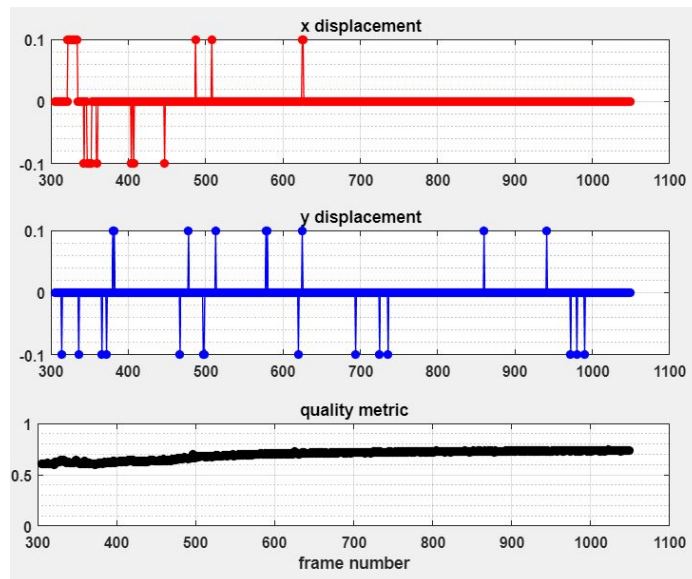
### 3.4 Oil-Flow Imaging

Oil-based flow visualization was used in combination with IR and TSP to gain a qualitative knowledge of separation and reattachment of an SBLI. Oil flow is particularly helpful when features of the flow cannot be resolved with TSP or IR. Measurement of separation points with TSP has not been accomplished during previous BAM6QT measurements [105]. Oil flow has also been used to image vortices and nozzle wall wakes [106]. Other flow visualization techniques were not available within the BAM6QT at the time. Windows capable of Schlieren imaging are currently being manufactured and tested for future work.

When oil is applied to the surface of the model, it will respond to the wall shear stress and move accordingly. This only occurs if the layer of oil is sufficiently thin and other effects, such as gravity and pressure gradients, are minimized. During tunnel runs, the oil will thin and move away from regions with high wall shear stress and increase in locations with low wall shear stress. For separated flows, this is particularly useful since oil will accumulate at separation and reattachment locations.



(a) Sample mesh of a 20° compression ramp.



(b) Sample of the GUI image registration outputs.

Figure 3.6. Sample IR post-processing of images into heat transfer.

Models were prepared by painting the surface with Rustoleum Specialty High Heat Ultra black paint. This provided a consistent base to contrast the oil. The oil was created by mixing 100 mL of DayGlo Color Aurora Pink powder and 30 mL of 100

centiStoke Dow Corning 200 silicone oil. Optical access was limited to the tunnel side-wall so gravity was a constant issue in keeping oil on the model. Before a run, the oil was applied by brushing a uniform thin layer on the model surface. There was then a waiting period where any excess oil was allowed to drip from the model and be removed from the tunnel. The tunnel was then filled and immediately run to limit oil dripping. An image of the model with regions of oil applied to the surface can be seen in Figure 3.7.

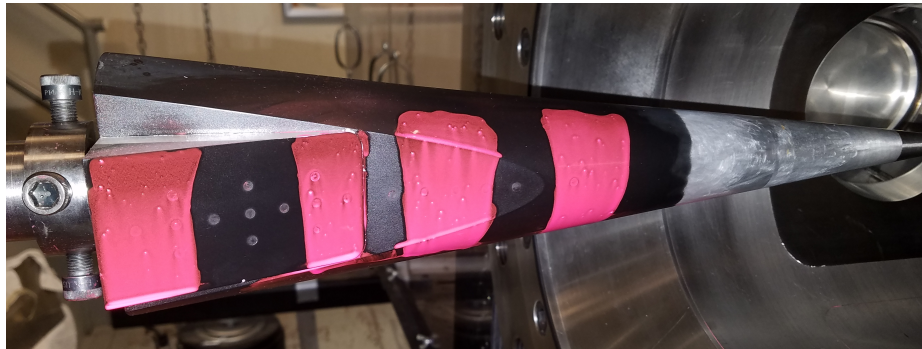


Figure 3.7. Sample oil application within the BAM6QT.

Images of the oil were captured with the same setup as the TSP. The two blue 452 nm LED lights were used to illuminate the pigmented oil. The images were then captured on the IMPERX Bobcat camera. The camera was equipped with a 24 mm focal-length lens and an orange filter. The aperture was fully opened to increase the amount of light captured on the CCD. Images were captured at 1608x1208 resolution and 15 Hz. Images were not processed since the raw images were sufficient in resolving flow features.

## 4. MODELS

Several models based on a design tested by Oberkampf et al. were designed and fabricated for use within the BAM6QT [78]. The geometry consists of a  $7^\circ$  cone forebody followed by a slice. The slice was created by machining a flat portion onto one side of the cone. This flat was then used as the upstream half of a compression corner created by a ramp held in place by 1/4-20 screws. The cone was limited to a 0.1016 m (4 inch) base diameter to ensure acceptable blockage. All models were machined in the Aerospace Science Laboratories machine shop. This was chosen as a generic public-release geometry that could exhibit the physics of finite-span compression corners and shear layers. This would avoid the simplifications of axisymmetric and two-dimensional geometries and provide transition measurements on a more realistic shape.

All models shared several features for use within the BAM6QT. The first is a common nosetip that was machined from 17-4 stainless steel and has a nominally  $110\text{-}\mu\text{m}$  radius tip. The nosetip was measured using a Zygo ZeGage white light interferometer and an optical microscope. Every model also featured four fast pressure sensors around the azimuth for use with the precision AoA adapter designed by Chynoweth [12]. The adapter, seen in Figure 4.1, featured an inner sting support and an outer support sleeve. Four screws were threaded into the outer sleeve and constrained the inner support. By adjusting these screws the model AoA could be adjusted. The four azimuthal sensors were aligned with the adapter screws and measured second-mode waves. The wave frequencies were used to determine appropriate adjustments. The frequencies of second-mode waves around the azimuth will align for a model at  $0.0^\circ$  AoA.

Initial measurements focused on determining a geometry that would create a flowfield that reattaches upstream of the cone base and allows room for post-



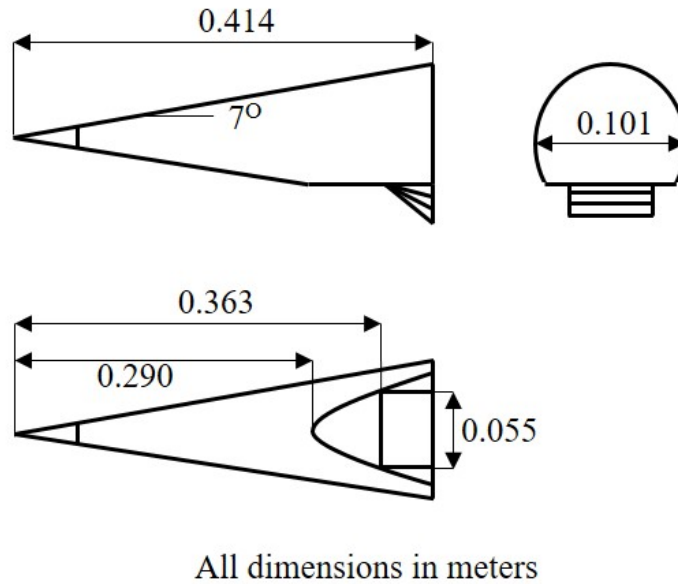
Figure 4.1. Image of the precision AoA adapter. The top piece is the outer sleeve and the bottom piece is the inner support.

reattachment measurements. This geometry would ideally have laminar, transitional, and turbulent post-reattachment flow within the Reynolds number range of the BAM6QT. If these conditions are met, experimental data can be collected on the effect of hypersonic shear layers on transition. If the separation is too close to the cone's aft-end, the separated flow will couple with the wake flow behind the cone. This creates a flowfield that is too complicated and cannot be computed easily [107]. For this reason, such cases will be avoided in the current experiments. Oil flow, TSP, and IR thermography were used to image the flow field and determine the separation and reattachment points. Knowing these locations will aid in interpretation of instability and transition measurements. The specific run conditions for all presented data can be found in Appendix B. A four-digit naming convention was used to organize the conditions. The first two numbers indicate which tunnel entry it is from and the last two indicate the run number. For example, Run 0810 would be the tenth run in entry eight.

#### 4.1 Short-Ramp Model

The initial model was designed with the same relative slice and ramp positions as the Oberkampf cone but had a  $7^\circ$  half angle instead of a  $10^\circ$  half angle. This model has been termed the “short ramp” model and was the focus for initial experiments. The slice begins 0.290 m from the nosetip and a 0.55 m wide ramp was fastened 0.363 m, from the nosetip. A schematic of the short-ramp model can be seen in Figure 4.2(a). Figure 4.2(b) shows an image of a nominal short ramp model.  $10^\circ$ ,  $20^\circ$ , and  $30^\circ$  ramps were made for this model and drawings of all components can be found in Appendix D. In order to measure pressure fluctuations through separation and after reattachment, the centerline of the short ramp model has an array of holes sized for PCB sensors.

Flow visualization of the three-dimensional finite-span compression corner was completed for the short-ramp model. Determining the separation and reattachment



(a) Schematic of the cone with slice and “short” ramp. Adapted from Reference [78]



(b) Image of the short ramp model.

Figure 4.2. Schematic and images of the short-ramp family of models.

locations in quiet and noisy flow was crucial for determining whether measurements of instability and transition could be made in the BAM6QT.

Figure 4.3 shows the raw intensities of the illuminated oil flow imaged on a CCD camera at various ramp angles in quiet and noisy flow for nominally equal unit Reynolds numbers. Separation and reattachment manifest as lines of accumulated oil

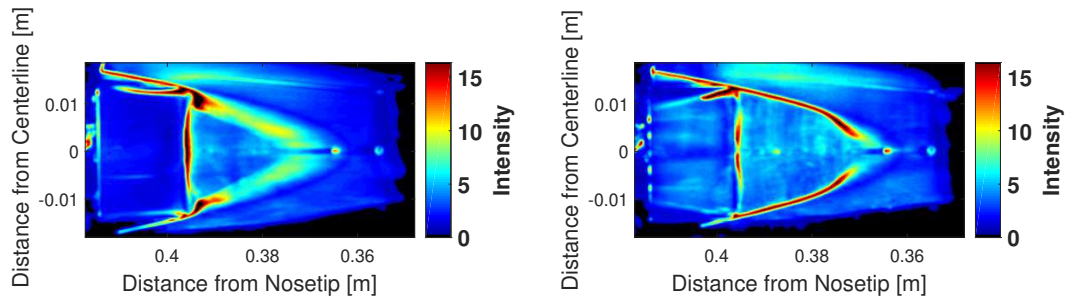
on the surface of the model. Accumulated oil then registers as higher intensities on the CCD camera.

Figures 4.3(a) and 4.3(b) show the raw oil-flow images for the model with the  $10^\circ$  ramp. For the noisy flow image, the shear stress on the ramp is too large for the oil to remain on the surface. This was tested with several oil viscosities and none of the available oil could withstand the surface shear stress from noisy flow on the ramp surface. Oil did remain on the slice surface and as a result the images are included in this section. Figure 4.3(b) shows the quiet flow image. Oil accumulation can be seen in the  $10^\circ$  ramp images on the upstream edges of the slice. This could be indicative of the entire slice being separated. No evidence of reattachment is present for either quiet or noisy flow. It is possible that the separation is not large enough to be seen or extends to the back of the slice.

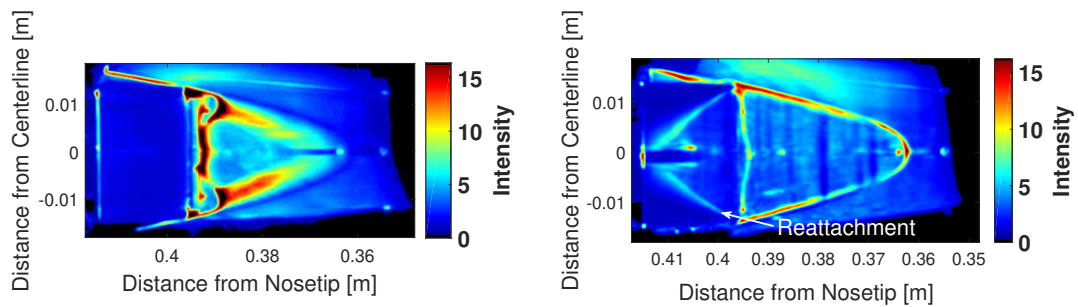
Figures 4.3(c) and 4.3(d) show images of the oil in similar conditions for the  $20^\circ$  ramp. For quiet flow, the oil shows a thin line of accumulated oil near the ramp corner on the slice. It is not clear what the cause of this accumulation is. A line of accumulated oil stretches the streamwise and spanwise extent of the ramp and is presumed to be reattachment. Noisy flow shows spiral accumulations of oil near the ramp on the slice. The cause of these are unknown although they could be due to the three-dimensionality causing a complicated recirculation region.

Figures 4.3(e) and 4.3(f) show similar images for the  $30^\circ$  ramp. For the quiet flow case the oil line indicative of reattachment point has moved upstream compared to the  $20^\circ$  ramp. A second oil line is present just upstream of the ramp. This could be separation or a flow structure within the recirculating flow. In noisy flow the large spiral oil accumulations have grown and extend farther upstream. Even though reattachment in quiet flow has moved upstream, enough space for sensors is not present.

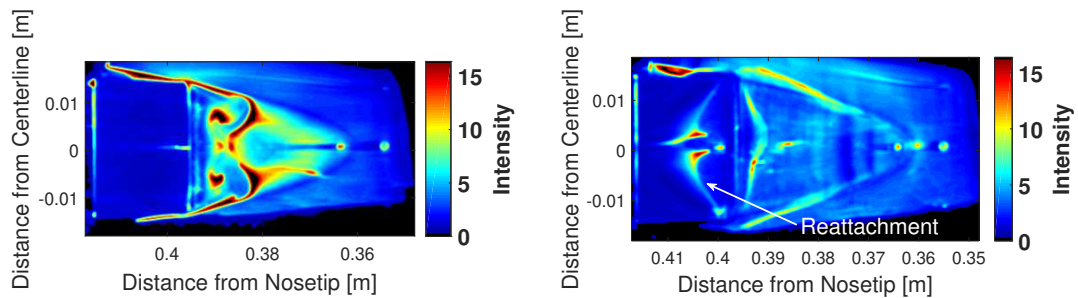
Comparing the oil flow images with a map of the surface heat transfer should provide a better idea of reattachment in quiet and noisy flow. Reattachment typically



(a)  $10^\circ$  ramp at  $Re = 11.8 \times 10^6/m$  (Run 0526). (b)  $10^\circ$  ramp at  $Re = 11.6 \times 10^6/m$  (Run 0525).



(c)  $20^\circ$  ramp at  $Re = 11.6 \times 10^6/m$  (Run 0522). (d)  $20^\circ$  ramp at  $Re = 11.1 \times 10^6/m$  (Run 0521).



(e)  $30^\circ$  ramp at  $Re = 11.6 \times 10^6/m$  (Run 0518). (f)  $30^\circ$  ramp at  $Re = 11.4 \times 10^6/m$  (Run 0517).

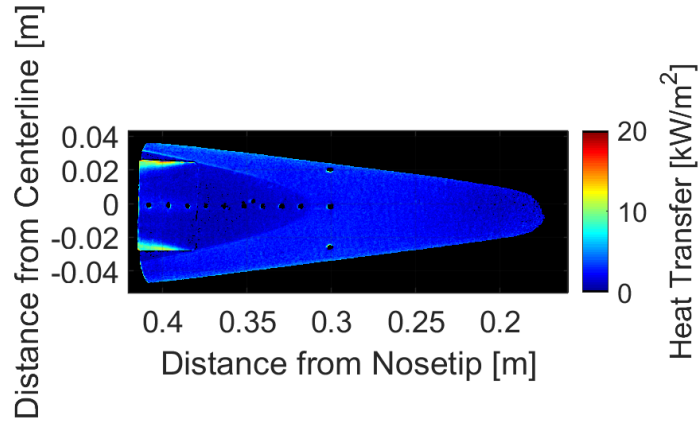
Figure 4.3. Oil flow on short-ramp model. Left column is noisy flow, right column is quiet flow. Flow is from right to left.

manifests as a large increase in heating due to the high momentum flow impinging on the surface.

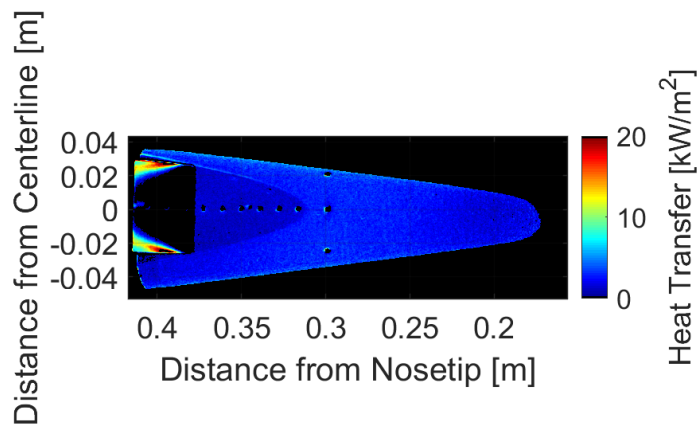
Figure 4.4 shows TSP heat transfer on the short-ramp model with  $10^\circ$ ,  $20^\circ$ , and  $30^\circ$  ramps. Increased heating across the span of the ramp is not seen for the  $10^\circ$  and  $20^\circ$  cases. It does not appear that the flow has fully reattached in these cases. The  $30^\circ$  case exhibits increased heating near the end of the ramp and was the only ramp that had evidence of reattachment.

Figure 4.5 compares the surface heat transfer for a  $30^\circ$  ramp in both quiet and noisy flow at  $Re = 12.4 \times 10^6/m$ . The color bars for these two cases are different to better show the heating. The  $30^\circ$  ramp is shown since it had the farthest upstream reattachment of any ramp angle. In the quiet flow image, the slice portion of the model does not show any significant change in heating that could be associated with separation. Neither the oil or the TSP clearly define a separation point. Farther downstream on the ramp, a large increase in heat transfer is the presumed reattachment line near the aft end of the ramp. Reattachment in quiet flow is three-dimensional, slightly asymmetric and produces over twice the heating present for the noisy case. Figure 4.5(b) shows noisy flow at the same Reynolds number. The predominant difference in noisy flow is the reduced streamwise extent of separation and the lower values of heat transfer on the ramp. This is due to the state of the pre-separation boundary layer being transitional or turbulent in noisy flow. This is not seen in quiet flow since the pre-separation boundary layer remains laminar. Comparisons for the smaller ramp angles at equivalent flow conditions in quiet and noisy flow were not completed before altering the geometry.

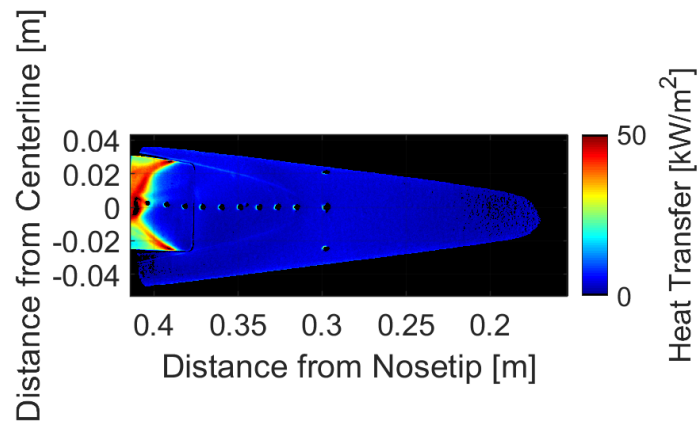
For smaller ramp angles, evidence of reattachment does not span the width of the ramp. These are interpreted as having either no reattachment on the model or reattachment too close to the end to measure. These cases are not of use since base pressure effects have an unknown effect on the flow structure. Without evidence of reattachment, measurement of the boundary layer after the SBLI is not possible. It is therefore not useful to continue running experiments on the short-ramp model.



(a)  $10^\circ$  ramp at  $Re_\infty = 12.6 \times 10^6/m$  (Run 0203).

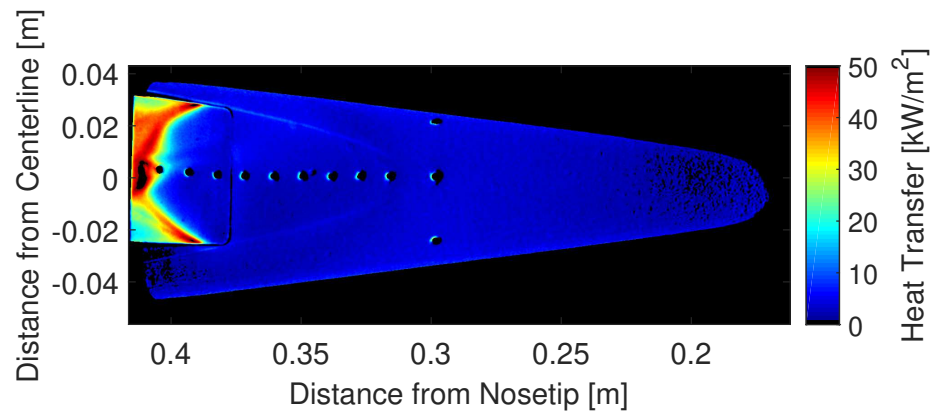


(b)  $20^\circ$  ramp at  $Re_\infty = 12.5 \times 10^6/m$  (Run 0204).

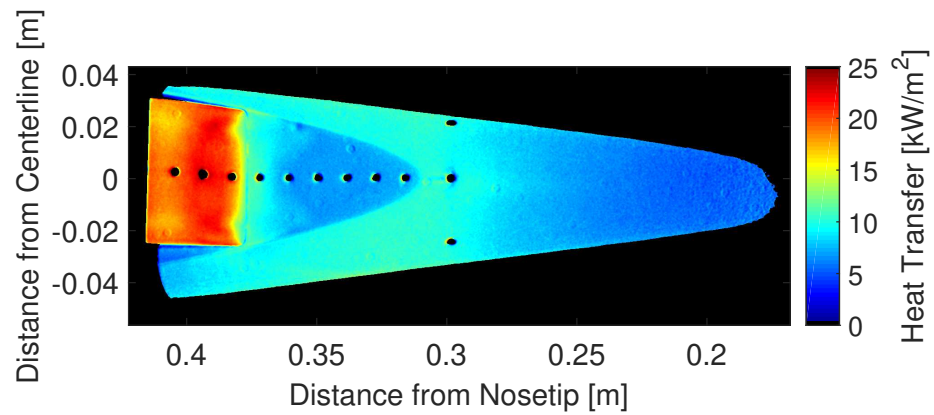


(c)  $30^\circ$  ramp at  $Re_\infty = 12.4 \times 10^6/m$  (Run 0206).

Figure 4.4. TSP of the short-ramp model with  $10^\circ$ ,  $20^\circ$ , and  $30^\circ$  ramp in quiet flow. Flow is from right to left.



(a)  $Re = 12.4 \times 10^6 / \text{min}$  quiet flow (Run 0206).



(b)  $Re = 12.4 \times 10^6 / \text{m}$  in noisy flow (Run 0212).

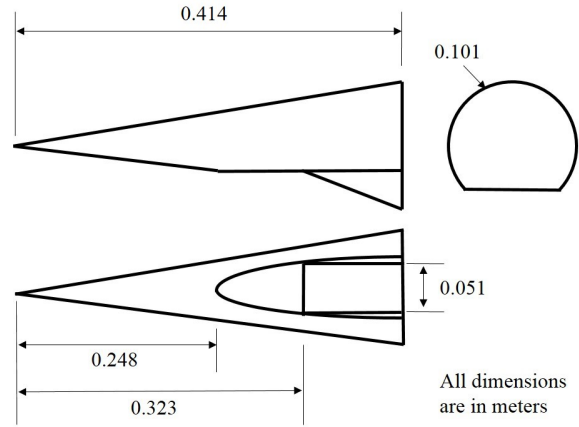
Figure 4.5. TSP of the short-ramp model with  $30^\circ$  ramp. Flow is from right to left.

## 4.2 Long-Ramp Model

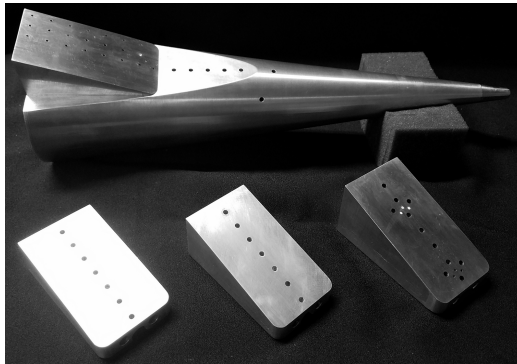
The short slice model did not have a ramp long enough to allow for reliable measurements of the post-reattachment boundary layer. Since post-reattachment measurements are needed for determining the effect of the free shear layer on transition, a new model was designed. The new model has been termed the “long ramp” model and can be seen in Figure 4.6. A schematic of the cone can be seen in 4.6(a) The model consists of the common nosetip followed by a  $7^\circ$  cone section. At 0.248 m downstream of the nosetip, a slice is machined on the cone. This slice is parallel with the model’s axis and provides the upstream surface for the compression corner. Four interchangeable 0.091 m long ramps were made and have deflection angles of  $5^\circ$ ,  $10^\circ$ ,  $15^\circ$ , and  $20^\circ$ . These ramps are 0.051 m wide and span the width of the slice at their upstream edge.

### 4.2.1 Determination of Reattachment Location

Oil flow and heat transfer measurements were made to determine if the long-ramp model can facilitate post-reattachment boundary-layer measurements. Figure 4.7 shows oil flow measurements on three different long-ramp angles. Figure 4.7(a) shows the  $10^\circ$  ramp. For this case not enough oil was applied to the surface upstream of the ramp and no indication of separation was seen. The oil on the ramp has been swept off on the far outboard edges. No arc of oil accumulation that could represent reattachment is present across the span of the ramp. Figure 4.7(b) shows similar oil flow on a  $15^\circ$  ramp. For this ramp angle, oil was applied on the entire surface of the model. An accumulation of oil can be seen on the entire front edge of the slice. It seems that the separated flow extends all the way to the expansion onto the slice. Oil on the ramp has been removed from the outboard edges, similar to the  $10^\circ$  case. However, more oil has been swept off the  $15^\circ$  ramp and the oil lines are closer to the ramp centerline. No oil accumulation spans the entirety of the ramp. Evidence of a fully reattached flow is not present. Figure 4.7(c) shows a similar run for the  $20^\circ$  ramp.



(a) Schematic of the cone with slice and “long” ramp.



(b) Image of the long-ramp model with various ramps.

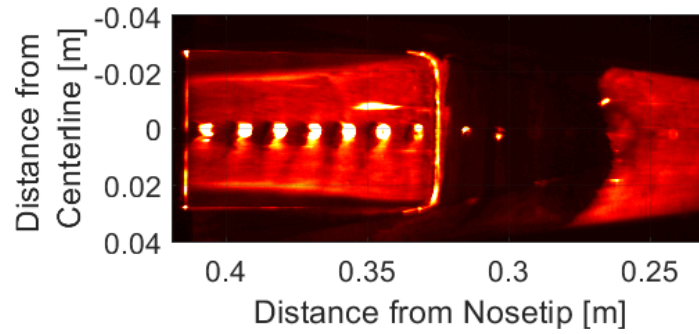


(c) Image of the long-ramp model with per-turber insert.

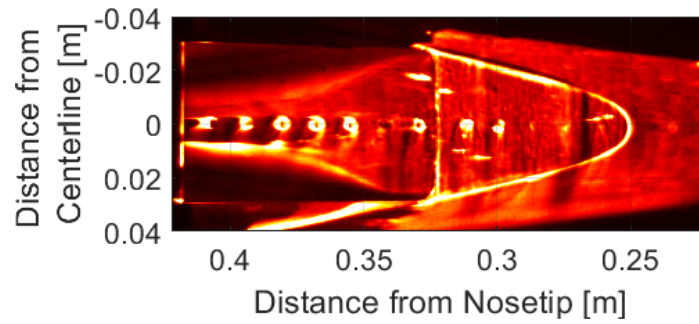
Figure 4.6. Schematic and images of the long-ramp family of models.

Oil has accumulated at the front of the slice, indicating that the boundary-layer is separated for the entire slice. An arc of oil spanning the entire ramp can be seen at  $x = 0.363$  m on the centerline. This was the only ramp angle that had an indication of reattachment.

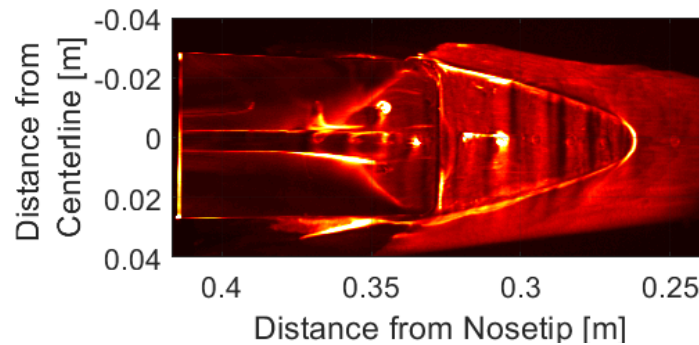
Based on the oil flow measurements, the  $20^\circ$  ramp appears to be the only fully reattached case. TSP images were collected under quiet and noisy flow for the  $10^\circ$ ,  $15^\circ$ , and  $20^\circ$  ramps to confirm the behavior observed with oil flow. The TSP images are representative of every quiet flow Reynolds number tested in the BAM6QT. There



(a) 10° long ramp (Run 1817).



(b) 15° long ramp (Run 1815).



(c) 20° long ramp (Run 1812).

Figure 4.7. Oil flow images of long ramp model at  $Re_\infty \approx 9.2 \times 10^6/m$  with various angle ramps under quiet flow. Flow is from right to left.

were no large changes in reattachment behavior with Reynolds number. Figure 4.8 shows the long-ramp model under quiet flow at various deflection angles. Figure 4.8(a) shows no spanwise arc of high heating at any point on the 10° ramp. This could be indicative of no separation, small separation, or separation that extends to the end of

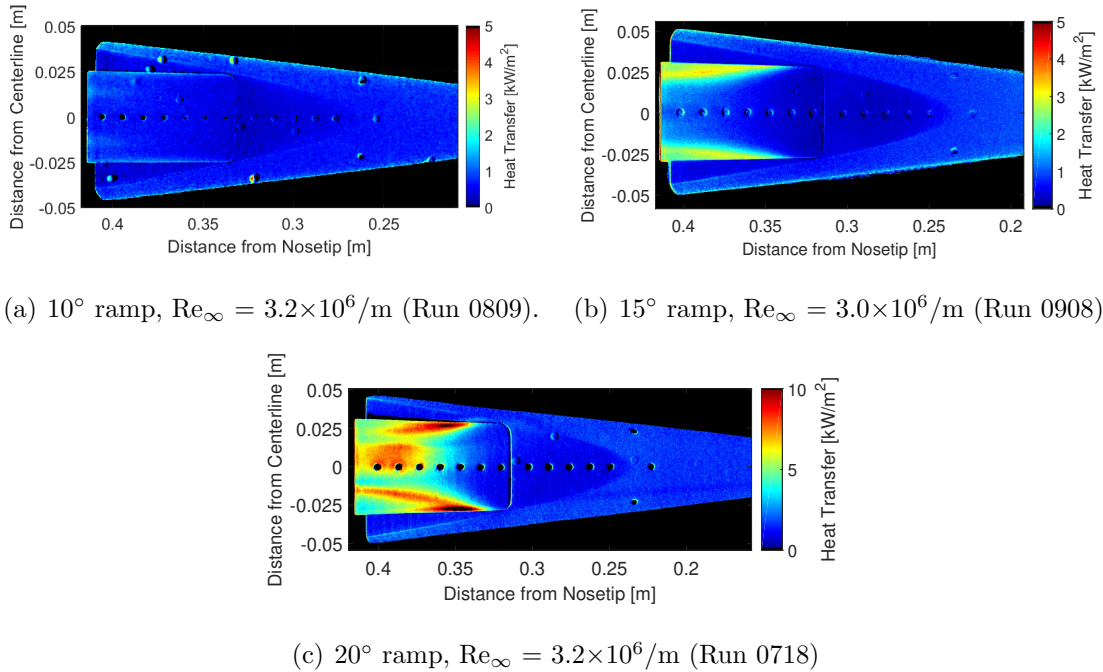
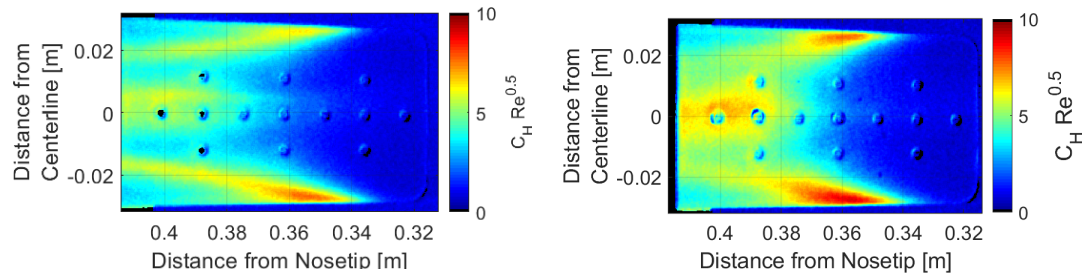


Figure 4.8. TSP of the long-ramp cone at similar unit Reynolds number in quiet flow. Flow is from right to left.

the ramp. This is similar to the observed oil flow in in Figure 4.7(a). Figure 4.8(b) shows the heat transfer on the 15° ramp. This ramp exhibits streaks of heating on the edges near  $\pm 0.025$  m off-centerline, but no changes in heat transfer can be seen on the centerline. The heat streaks present on the ramp edges are presumed to be edge effects due to the finite span. Figure 4.8(c) shows the 20° ramp. This case has a clear arc of increased heating spanning the ramp width. This is interpreted as reattachment. This matches the results from oil flow in Figure 4.7(c). The image shows approximately 0.04 m of ramp left post-reattachment.

Several different ramps were fabricated for each geometry, to allow for different sensors layouts. Heat-transfer-based reattachment locations were measured on these ramps to see if they are dependent on the finish and fit of a specific ramp. An aluminum ramp with TSP and a PEEK ramp for IR were used to determine reattachment repeatability in both quiet and noisy flow. Figure 4.9 shows the TSP Stanton number

for two cases at similar Reynolds number in quiet and noisy flow on the  $20^\circ$  ramp. For both quiet and noisy flow, sensor data on the cone showed the incoming boundary layer remained laminar prior to separation. The upstream portion of the ramp is within separated flow and has low heat transfer. A large increase in heating is seen at 0.36m downstream of the nosetip in both images. This is interpreted as reattachment heating the reattachment location. The location matches the oil accumulation lines seen in Figure 4.7(c).

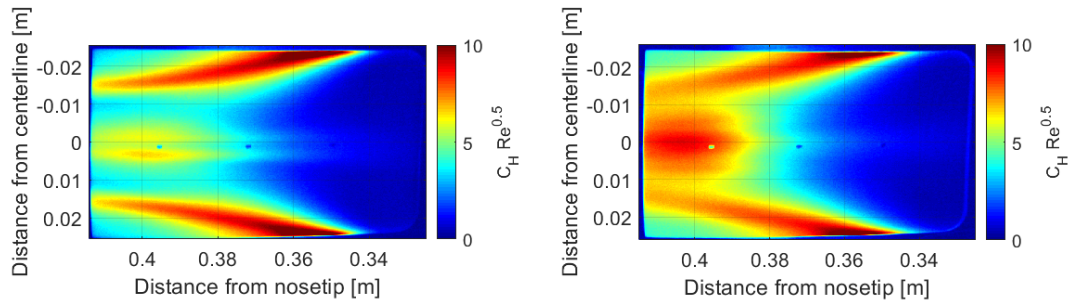


(a)  $Re_\infty = 2.9 \times 10^6/m$  in quiet flow (Run 1007). (b)  $Re_\infty = 2.6 \times 10^6/m$  in noisy flow (Run 1018).

Figure 4.9. Laminar-scaled Stanton number of  $20^\circ$  long ramp from TSP. Flow is right to left.

This measurement was repeated with IR thermography approximately a year after the TSP measurements were made. Figure 4.10 shows the Stanton number in both quiet and noisy flow. The general flow structure in both quiet and noisy flow is nearly identical to that seen in the TSP images. Low heating is present on the upstream half of the ramp and an increase in centerline heating is seen at roughly 0.36 m downstream. The repeatability of the reattachment location was verified by comparing the results from the three different imaging techniques. Quantification of reattachment location was done with all three methods. Location of oil accumulations and heat transfer increasing above the upstream values were used to quantify reattachment location. The measured locations of centerline reattachment are summarized in Table 4.1. The

oil flow measurement was found by taken an approximate centerline location by extending the oil accumulations.



(a)  $Re_\infty = 3.1 \times 10^6/m$  in quiet flow (Run 2015). (b)  $Re_\infty = 2.9 \times 10^6/m$  in noisy flow (Run 2020).

Figure 4.10. Laminar-scaled Stanton number of  $20^\circ$  long ramp from IR. Flow is right to left.

Table 4.1. Approximate reattachment locations on the long ramp model in quiet flow.

Method of Measurement	Reattachment location (m)	Percent of ramp length
Oil flow	0.363	44%
TSP	0.360	41%
IR	0.364	45%

Laminar mean-flow computations by Thome at the University of Minnesota were completed with US3D to compare to early results on the long-ramp model [50]. US3D is a compressible Navier-Stokes solver developed at the University of Minnesota. The grid used for computation consisted of 50 million cells, with 250 wall normal cells. Thome's computation utilizes the exact model geometry featured in the experiments. Figure

4.11 shows the computed flow temperature at various spanwise slices downstream of the nosetip. The computed separation encompasses the entire slice and, according to the wall shear stress and near-wall velocity, reattaches 0.375 m from the nosetip. This is slightly farther downstream of the reattachment than was measured in the BAM6QT. However, it is reassuring that the computation indicates reattached flow under these conditions. A quantitative comparison of surface Stanton number on the ramp is shown in Figure 4.12. The  $Re_\infty = 2.1 \times 10^6/m$  experiments exhibited laminar flow and the higher unit Reynolds number experiments had a transitional or turbulent reattaching boundary layer. For both Reynolds numbers, the computation under-predicts the heating near the centerline. This could be due to transition occurring in the experiment for the higher Reynolds number case. However, the lower Reynolds number experiments did not show transitional flow and is still under-predicted by the computation. The reason for this behavior is not known but it emphasizes the difficulty of comparing computations to experimental SBLI.

Based on the agreement of reattachment locations between several experimental techniques and confirmation of reattachment in the computations, the  $20^\circ$  long-ramp model provides a valid test case for measuring the boundary layer after reattachment on a finite-span compression corner. It was used as the primary geometry for transition and shear-layer instability measurements.

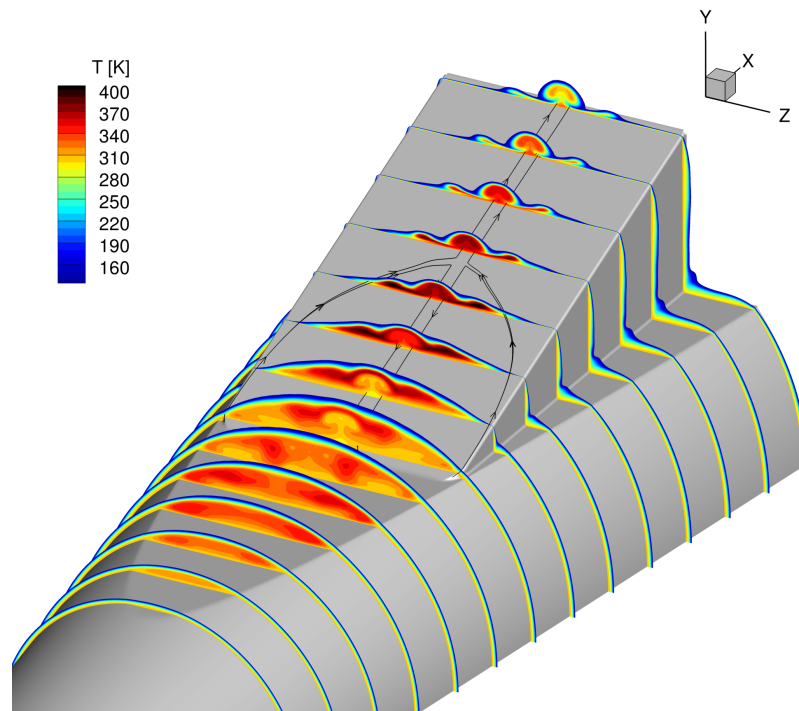


Figure 4.11. Map of temperature at  $Re_\infty = 9.2 \times 10^6/m$ . DNS completed by Thome with US3D [50].

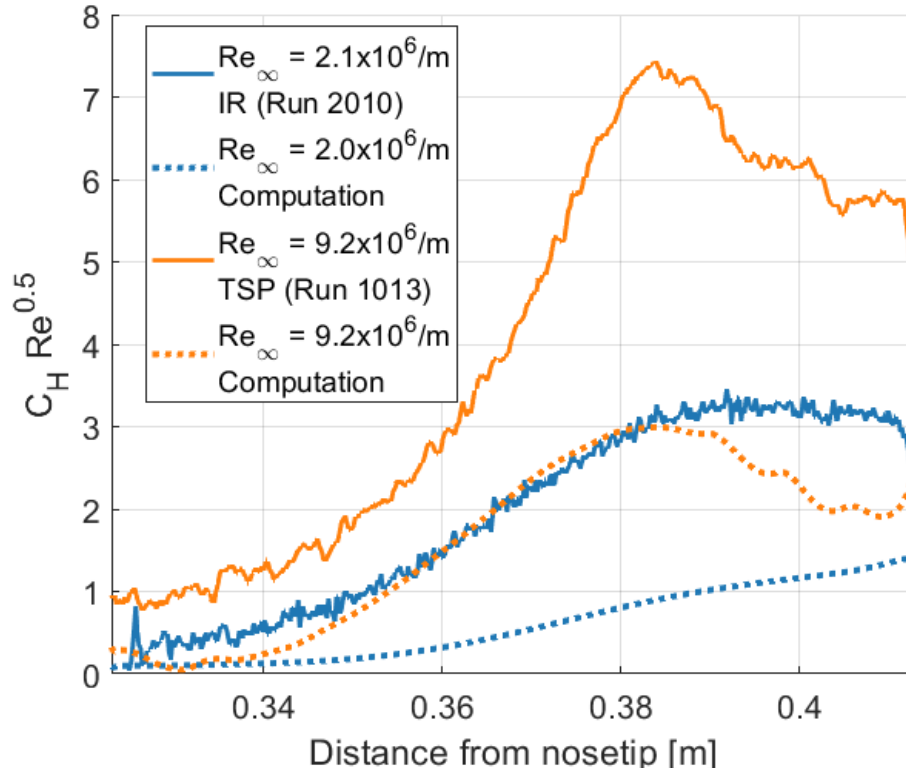
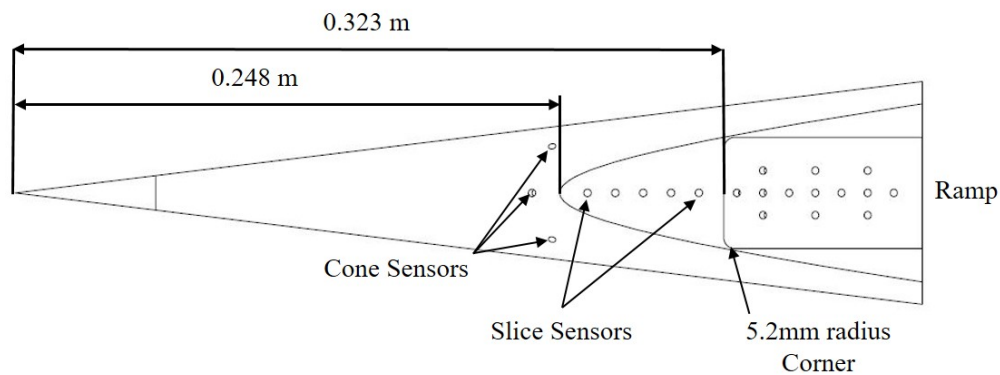


Figure 4.12. Comparison of surface Stanton number on the ramp from experiments and DNS completed by Thome with US3D [50]. Data were taken from 2 mm off the ramp centerline.

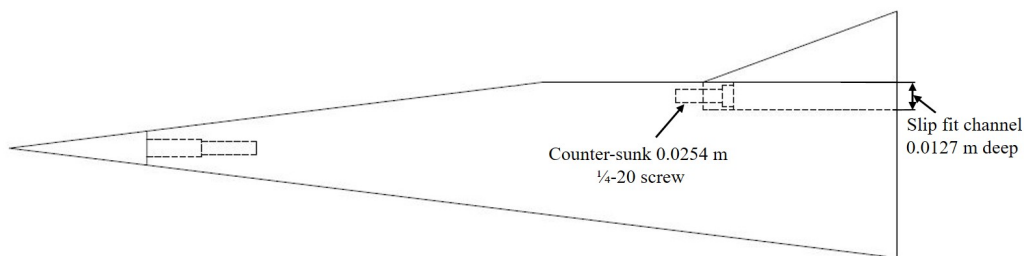
### 4.2.2 Detailed Design of Long-Ramp Model

The long-ramp model was machined from 6061-T6 aluminum and designed with dedicated ports for surface pressure transducers. A schematic of the model with important dimensions labeled was given in Figure 4.6(a) and detailed drawings can be found in Appendix D. Figure 4.13 shows another drawing of the long-ramp model with relevant design features labeled. A slot was machined on the slice that allows a ramp to be slip fit into the model. Ramps are secured to the model with two 1/4-20 screws threaded from the base of the model. Once fastened, the front of the ramp is flush with the slice and cannot move within the slot. Figure 4.14 shows a sample profile of a negative mold of the joint at the front of the ramp. The mold was taken with a Struer's Repliset T3 material and measured on Zygo Zegage optical profiler. Since the mold is a negative of the surface, peaks in the mold measurements are cavities on the model surface. The joint features a rearward facing step onto the slice from 280  $\mu\text{m}$  to 240  $\mu\text{m}$ . This is the transition onto the ramp and ramp surface is seen from 240  $\mu\text{m}$  to 0  $\mu\text{m}$ . The average step height for nine samples taken from three different ramps was 144.7  $\mu\text{m}$ . No sealing was applied to the interface of the ramp and slice. Due to the way it was machined, a radius was required on the front corners of the ramps. A standard size was chosen and the original long-ramp model had a 4.8 mm radius in the corners. Images of them are shown in Figure 4.15. The radius introduced a small step at the edge of the corner. For the 4.8 mm corner, this step was 1.7 mm on the edge of the ramp and gradually reduced to zero at 4.8 mm from the ramp edge. This step can be seen in Figure 4.15(b). No gaps were observed between the slice and the ramp for these ramps.

Numerous sensor locations were available for measuring surface pressure fluctuations on the long-ramp model. They are organized by whether the sensors are located on the cone, slice, or an individual ramp. Five sensors were present on the cone portion of the model. Four of these were PCBs placed around the azimuth of the model and were used for fine adjustment of angle of attack. A fifth sensor port was aligned with the



(a) Top down view of long-ramp model.



(b) Side view of long-ramp model with interior structure visible.

Figure 4.13. Schematics long-ramp model with relevant annotations of mechanical design.

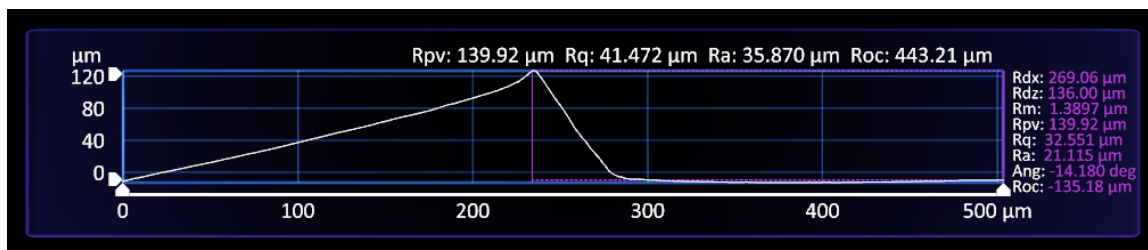
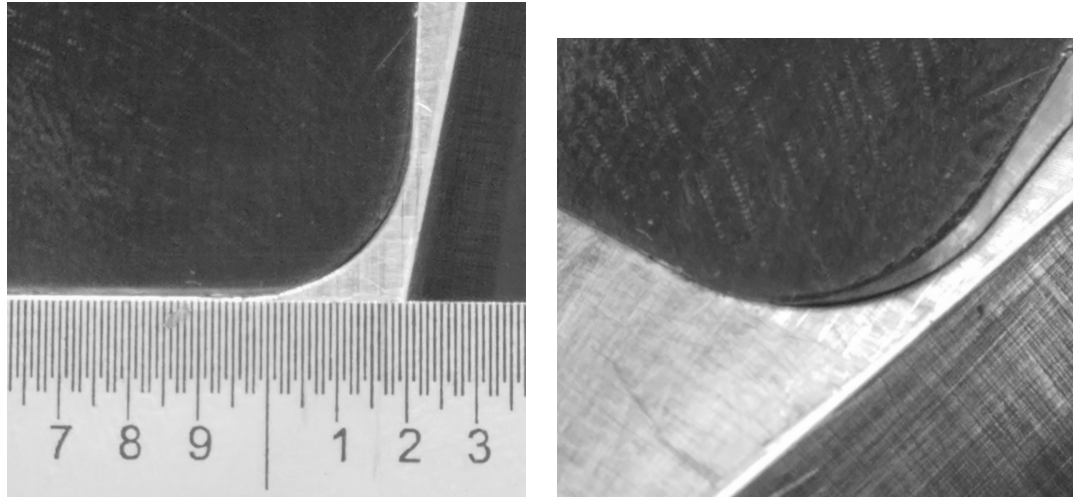


Figure 4.14. Sample profile of the joint between the slice and ramp. Given profile is an average of 500  $\mu\text{m}$  worth of joint profiles. The right side is the upstream slice and the left side is the downstream ramp.



(a) Front view of a sample ramp corner. (b) Isometric view of a sample ramp corner.

Figure 4.15. Images of a sample ramp corner on the long-ramp model. The markings on the scale in the left image are 0.254 mm (0.01 in) and the labeled marks are 2.54 mm (0.1 in).

ramp centerline and could be used for either PCB or SB measurements. The locations of these ports can be found in Table 4.2 and seen in Figure 4.13(a). Downstream of the cone, an expansion occurs and the slice begins. Five sensors were present on the centerline of the slice and to measure pressure fluctuations. Sensor locations for the slice can be found in Table 4.3 and seen in Figure 4.13(a).

Several ramps were fabricated to measure the post-reattachment boundary layer. Schematics of the four 20° ramps used can be found in Figure 4.16. Initial experiments were carried out on a ramp fitted with both centerline and spanwise sensors. This was termed the spanwise ramp. The sensor locations can be found in Table 4.4. Two other ramps were created to measure different features of the flow. The cluster ramp featured groups of sensors designed to measure possible phase speeds and the angles of traveling instabilities. Clusters of sensors have previously been used to measure phase velocity and angle of traveling instabilities by Poggie [108] and Borg [109]. The sensor locations for this ramp can be found in Table 4.5. The Kulite ramp featured

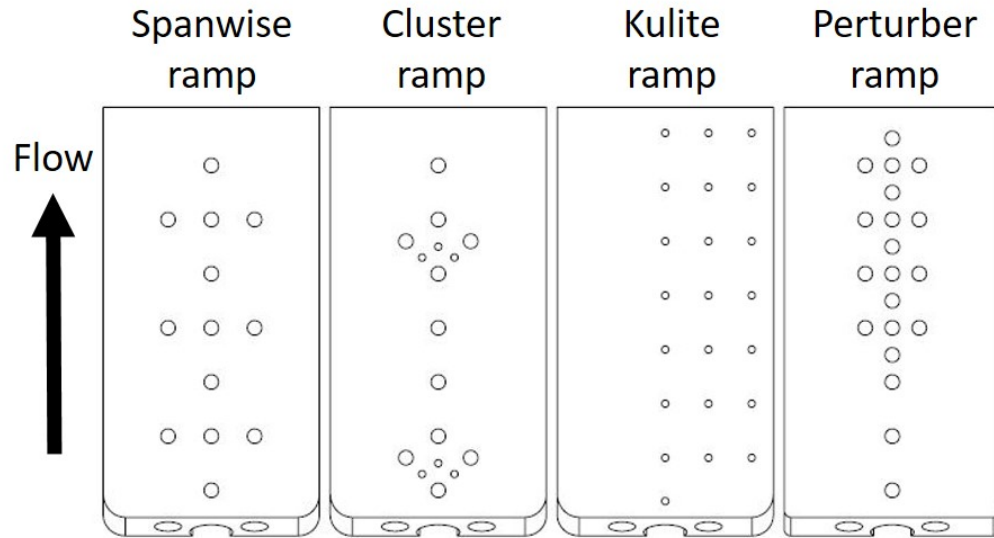


Figure 4.16. Schematics of the various ramps used.

a dense grid of ports designed to fit Kulite sensors. Their locations can be found in Table 4.6. This ramp measured the farthest outboard on a ramp. It was fabricated in an attempt to obtain mean pressure measurements. Previous experiments had shown the flow to be symmetric about the centerline. In order to facilitate a higher spatial density of measurements, the symmetry was exploited and only half the ramp was instrumented. Lastly, a new model was built for the measurements of artificially generated perturbations within the boundary layer. This model had slightly different dimensions and required a new ramp to be built. This ramp was termed the perturber ramp and will be discussed in detail in Section 4.3. Drawings for these ramps can be found in Appendix D.

### 4.3 Perturbation Models

Three additional models were made to facilitate plasma perturbations on the surface of the model. These models feature a custom designed insert on the upstream half of the cone that allows for the generation of a glow or spark perturbation for

Table 4.2. Sensor locations on the cone portion of the long-ramp model

Sensor type	Distance from nosetip (mm)	Azimuthal angle
SB	235.4	0°
PCB	245.5	45°
PCB	245.5	135°
PCB	245.5	225°
PCB	245.5	315°

Table 4.3. Sensor locations on the slice portion of the long-ramp model

Sensor type	Distance from nosetip (mm)	Distance from centerline (mm)
PCB	260.8	0
PCB	273.4	0
PCB	286.7	0
PCB	299.2	0
PCB	312.0	0

controlled boundary-layer disturbances. The perturbation hardware was placed on a 7° half-angle circular straight cone, the short-ramp model, and the long-ramp model. Dimensioned drawings of these models can be found in Appendix D.

The perturber consists of a MACOR cylinder with two stainless-steel welding rods that act as electrodes. The rods are epoxied into the MACOR with high-temperature two-part epoxy. These rods are soldered to 25 kV high-voltage wires which connect to electronics outside the BAM6QT. The electrodes are aligned parallel to the flow to ensure the disturbance is generated in-line with centerline sensor arrays. The ideal distance between the electrodes is dependent on the mean pressure within the

Table 4.4. Sensor locations on the spanwise ramp

Sensor Type	Distance from nosetip (mm)	Distance from Centerline (mm)
PCB	329	0
PCB	341	0
PCB	353	0
PCB	365	0
PCB	377	0
PCB	389	0
PCB	401	0
PCB	341	-10.2
PCB	341	10.2
PCB	365	-10.2
PCB	365	10.2
PCB	389	-10.2
PCB	389	10.2

tunnel and the applied voltage. The spacing of the electrode was determined by using Paschen's law for the breakdown of air. Paschen found that the breakdown of a gas was determined by the equation

$$V_B = \frac{Bpd}{\ln(Apd) - \ln[1 - \frac{1}{\gamma_{se}}]} \quad (4.1)$$

where  $V_B$  is the breakdown voltage in volts,  $p$  is the pressure in pascals,  $d$  is the distance between the electrodes in meters, and  $\gamma_{se}$  is the secondary-electron-emission coefficient.  $A$  and  $B$  are empirically derived variables. This equation generates a curve called Paschen's curve [110]. By differentiating the equation and setting it equal to zero, the minimum breakdown voltage can be determined. For the current

Table 4.5. Sensor locations on the cluster ramp

Sensor Type	Distance from nosetip (mm)	Distance from Centerline (mm)
PCB	329.2	0
PCB	336	-7.6
PCB	336	7.6
PCB	342	0
PCB	354	0
PCB	365	0
PCB	378	0
PCB	384	-7.6
PCB	384	7.6
PCB	390	0
PCB	401	0
Kulite	332.7	-3.8
Kulite	332.7	3.8
Kulite	336	0

model design,  $V_B = 327$  V and  $pd = 0.754$  Pa·m [111]. Based on this, the distance between electrodes was found to be 0.635 mm. This is the same distance that was used by Casper for previous  $7^\circ$  cone measurements with a plasma perturber within the BAM6QT. [112]. A schematic of the perturber insert can be seen in Figure 4.17.

The Macor inserts were epoxied in the model with Hysol Epoxi-patch 1C White 2-part epoxy resin. The wires were soldered to the electrodes by John Phillips, the AAE electronics technician. The perturber wires were run through the model with a dedicated channel that ideally did not house any sensor wires. Some models featured sensors that shared a channel with perturber wires due to space constraints. Separating the perturber wires from sensor wires reduces the electro-magnetic interference (EMI)

Table 4.6. Sensor locations on the Kulite-instrumented ramp

	Distance	Distance		Distance	Distance
Sensor	from	from	Sensor	from	from
Type	nosetip	Centerline	Type	nosetip	Centerline
	(mm)	(mm)		(mm)	(mm)
Kulite	328	0	Kulite	384	-10.2
Kulite	337	0	Kulite	397	-10.2
Kulite	349	0	Kulite	409	-20.4
Kulite	361	0	Kulite	337	-20.4
Kulite	373	0	Kulite	349	-20.4
Kulite	384	0	Kulite	361	-20.4
Kulite	397	0	Kulite	373	-20.4
Kulite	409	0	Kulite	384	-20.4
Kulite	349	-10.2	Kulite	397	-20.4
Kulite	361	-10.2	Kulite	409	-20.4
Kulite	373	-10.2			

generated by the high-voltage pulsing. The perturber wires were then fed into a hollow sting adapter and run behind the model. The wires were then passed through the tunnel wall and clipped to the high-voltage electronics. Additional EMI shielding was wrapped around the wires within the model and sting adapter. Both perturber wires were run through a rigid stainless-steel tube that was wrapped in a nickel-iron-cobalt foil. Any crease or fold in the foil reduces the effectiveness of the shielding and extreme care was taken in the assembly and implementation of the shielding and wires.

These inserts were placed in a  $7^\circ$  straight cone, the short slice geometry, and the long slice geometry. Pictures of these models can be seen in Figure 4.18. Experiments with the short-ramp perturbation model were limited due to the insufficient space

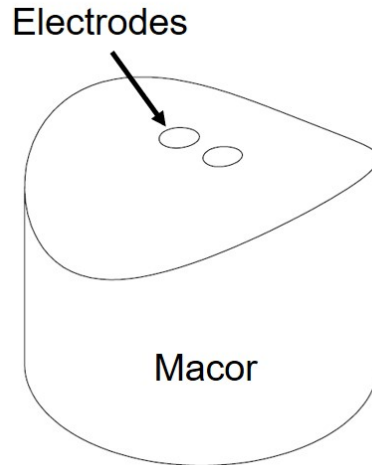
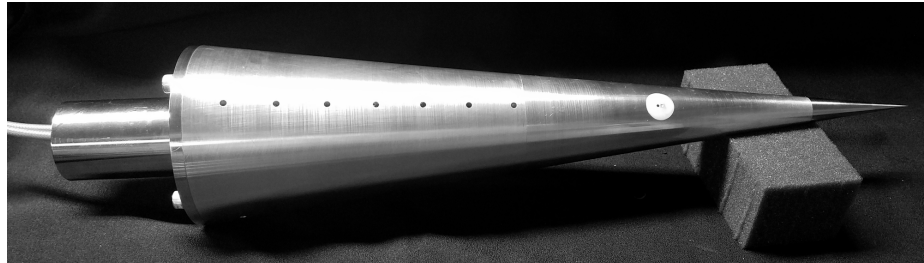


Figure 4.17. Schematic of the Macor inserts used on the perturber models.

post-reattachment for measurement. An image of this model can be seen in Figure 4.18(b).

The  $7^\circ$  straight cone with perturbation was used as a proof of concept for the generation of disturbances in a hypersonic boundary layer. An image of this model can be seen in Figure 4.18(a). Calculations completed with STABL-2D at maximum quiet flow conditions determined the unstable second-mode frequencies on a  $7^\circ$  cone at  $0^\circ$  AoA. The Macor insert was placed downstream of the point at which these frequencies begin growing on the model. Figure 4.19 shows the growth of unstable frequencies in relation to the perturber insert location. The location of the perturber insert was downstream of the neutral point on the cone to prevent damaging the solder connections by bending the wires too sharply. A single line of sensors was placed downstream of the perturber to measure the growth of waves after perturbation. Table 4.7 lists the locations of relevant sensors on the  $7^\circ$  cone.

The long-ramp perturbation model was the final model to be built for the current experiments. An image of the model can be seen in Figure 4.18(c). The model featured two holes that could accommodate a Macor perturbation insert, one on the cone portion and one on the slice. A perturber was placed 221 mm from the nosetip.



(a) 7° perturbation model



(b) Short-ramp perturbation model



(c) Long-ramp perturbation model

Figure 4.18. Images of various cones with perturber inserts.

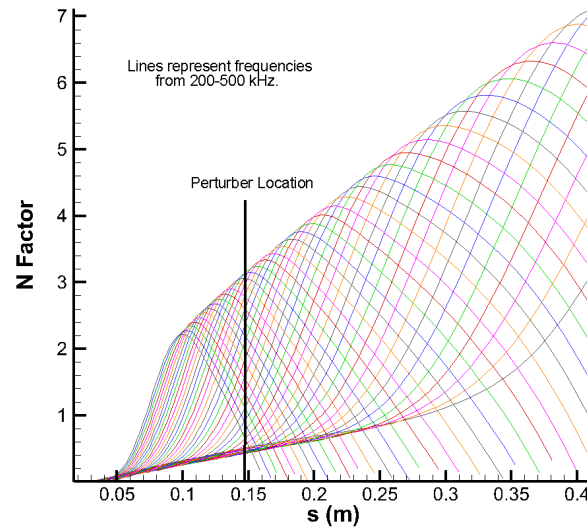


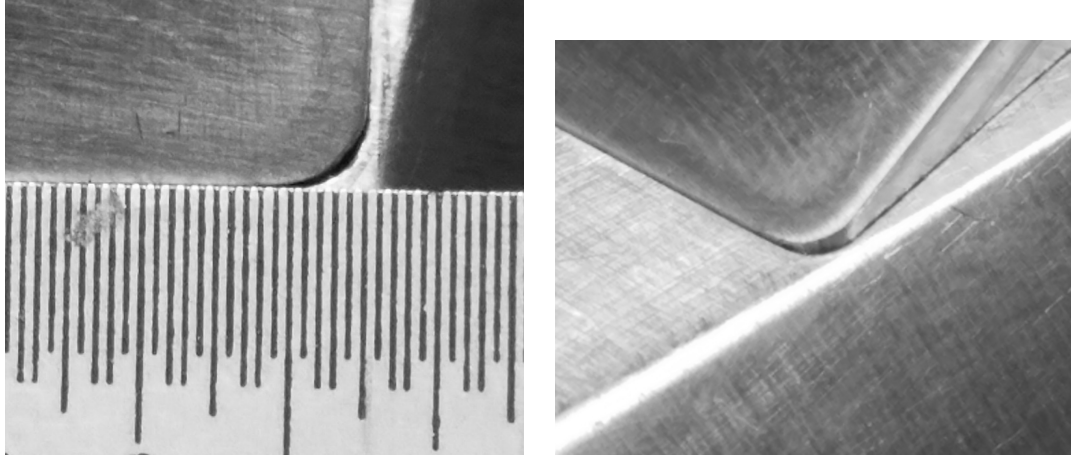
Figure 4.19. N-factors of most amplified frequencies on a  $7^\circ$  cone at  $0^\circ$  AoA. Perturber location is marked on the plot. Computations were completed at:  $P_0 = 155$  psia,  $T_0 = 433$  K,  $\rho_0 = 8.605$  kg/m<sup>3</sup>, and  $T_{wall} = 300$  K.

Table 4.7. Perturber and sensor locations on the  $7^\circ$  perturbation model.

Sensor Type	Distance from Nosetip (mm)
Perturber	156.8
PCB	243
PCB	268
PCB	293
PCB	319
PCB	344
PCB	369
PCB	395

This location was just upstream of the slice on the cone portion of the model. Since separation is believed to occur at the expansion onto the slice, the slice location was not used. No perturber was placed on the slice and the large hole on the slice was filled with dental plaster and sanded smooth to the model surface. The perturber location on the cone was placed close to the beginning of the slice. This was to limit the growth of second-mode waves on the  $7^\circ$  cone section and isolate the growth of instability in the shear layer.

A new ramp was made to focus instrumentation on the post-reattachment boundary-layer of the perturber model. This ramp was termed the “perturber” ramp and had a higher density of sensors downstream of reattachment. The perturbation long-ramp model was the second iteration of the long-ramp geometry and adjustments were made to certain dimensions. In order to reduce the effect of any corner radii or corner steps, a smaller radius corner was chosen for the front of the ramp. The perturber ramp had front corners with radii of 1.6 mm, which are smaller radii than for the previous ramps. A schematic of this ramp can be seen in Figure 4.16 and images of the ramp corners can be seen in Figure 4.20. The corner had a 0.6 mm step at the ramp edge. A small 0.3mm gap was present within the curve of the corner. This was present on both sides. A comparison of surface temperatures for the two ramp corner radii can be found in Appendix A. The perturber ramp had sparse sensors within the separated region and dense centerline and spanwise arrays downstream of reattachment. Sensor locations can be found in Table 4.8. Full drawings for the long-ramp perturber model can be found in Appendix D.



(a) Front view of a Perturber ramp corner. (b) Isometric view of a Perturber ramp corner.

Figure 4.20. Images of a perturber ramp corner on the long-ramp model. The markings on the scale in the left image are 0.254 mm (0.01 in).

Table 4.8. Sensor locations for the perturber ramp.

Sensor Type	Distance	Distance	Sensor Type	Distance	Distance
	from	from		from	from
	nosetip	centerline		nosetip	centerline
	(mm)	(mm)		(mm)	(mm)
PCB	329	0	PCB	401	0
PCB	341	0	PCB	407	0
PCB	353	0	PCB	365	-10
PCB	359	0	PCB	365	10
PCB	365	0	PCB	377	-10
PCB	371	0	PCB	377	10
PCB	377	0	PCB	389	-10
PCB	383	0	PCB	389	10
PCB	389	0	PCB	401	10
PCB	395	0	PCB	401	10

## 5. MEASUREMENTS USING THE LONG-RAMP MODEL WITHOUT PERTURBATION

This chapter will include measurements of the separation and post-reattachment boundary layer on the long-ramp model with a  $20^\circ$  ramp. Section 4.2.1 provided the justification of geometry choice by observing the behavior of the boundary layer and approximate separation and reattachment points. This chapter will first focus on the effects of Reynolds number and AoA on post-reattachment heat transfer. After, pressure-fluctuation measurements within the separation and post-reattachment regions will be discussed. The specific run conditions for all presented data can be found in Appendix B. The four-digit naming convention was the same that was used in the previous section. The first two numbers indicate which tunnel entry it is from and the last two indicate the run number. For example, Run 0810 would be the tenth run in entry eight.

### 5.1 Surface Heat Transfer on the Ramp

#### 5.1.1 Comparison of IR and TSP Heat Transfer

IR and TSP were both used to measure the surface heat transfer on the  $20^\circ$  ramp. Both measurement techniques suffer from uncertainties in the post-processing required to obtain heat transfer and Stanton number. Post-processing techniques for the IR and TSP differ significantly. The TSP uses an empirical correlation developed in-house to infer one-dimensional heat transfer from a temperature change of the model surface and a heat transfer reference. Historically, TSP has been the main method of measuring surface heat transfer in the BAM6QT. IR directly measures temperature from the PEEK and the current work used a similar one-dimensional assumption.

Recent experiments by Cerasuolo, Zaccara, and Edelman have shown that this method can accurately measure heat transfer on a  $7^\circ$  cone at  $0^\circ$  and  $6^\circ$  AoA [98–100]. A comparison of the two techniques will be made to determine the benefits of both on the cone-slice-ramp.

Figure 5.1 shows a comparison of the IR and TSP at three Reynolds numbers on the  $20^\circ$  ramp. An immediate difference between the images is the increase in spatial resolution for the IR imaging. This is most apparent in Figures 5.1(c) and 5.1(d). The TSP image features a single wide streamwise streak near the centerline of the model, while the IR image shows two streamwise streaks at the same location. This is believed to be due to the decreased spatial resolution of the TSP. Improved spatial resolution is important for accurate heat transfer measurements.

A qualitative look at Figure 5.1 shows that the Stanton numbers calculated from the TSP and IR measurements are similar near the centerline of the model. However, the streaks coming off the sides of the ramp are much hotter in the IR images. The reason for this is not known but each technique’s response to two-dimensional effects from the sides of the ramp could cause differences. The general flow structures are similar and the IR measurements show increased spatial resolution. Figure 5.2 shows line cuts 2 mm off-centerline to quantitatively compare Stanton number on the ramp. This location is directly below the centerline sensors and registration marks in Figure 5.1. At  $Re_\infty = 2.1 \times 10^6/m$ , the IR and TSP Stanton numbers are similar after 380 mm downstream from the nosetip. Upstream of 380 mm, the TSP shows higher Stanton number. The Stanton number for each technique at  $Re_\infty = 3.1 \times 10^6/m$  is similar, with approximately equal amplitudes downstream of reattachment and higher TSP amplitudes on the upstream half. The agreement indicates that either technique can be used to obtain reliable measurements of Stanton number. The high Reynolds number case varies by a significant amount due to a difference in Reynolds numbers caused by unreliable burst pressures of that specific diaphragm. Recent introduction of a diaphragm that can reliably burst between 55 and 85 psia fixes this issue, but these were not available for the present experiments. Even so, Stanton numbers match

until 370 mm and the locations of peak heating are equal for both cases. Upstream of 360 mm from the nosetip, the TSP consistently reports higher heat transfer for every Reynolds number. This could be due to the TSP having a worse signal-to-noise ratio than the IR. The IR has a better signal-to-noise ratio due to the PEEK material and the camera capabilities and should be a better representation of low-amplitude heating. Therefore, flow features will be easier to distinguish in the IR.

Due to the increased spatial resolution and better signal-to-noise ratio, IR measurements will be the primary method of mapping surface heat transfer on the cone-slice-ramp.

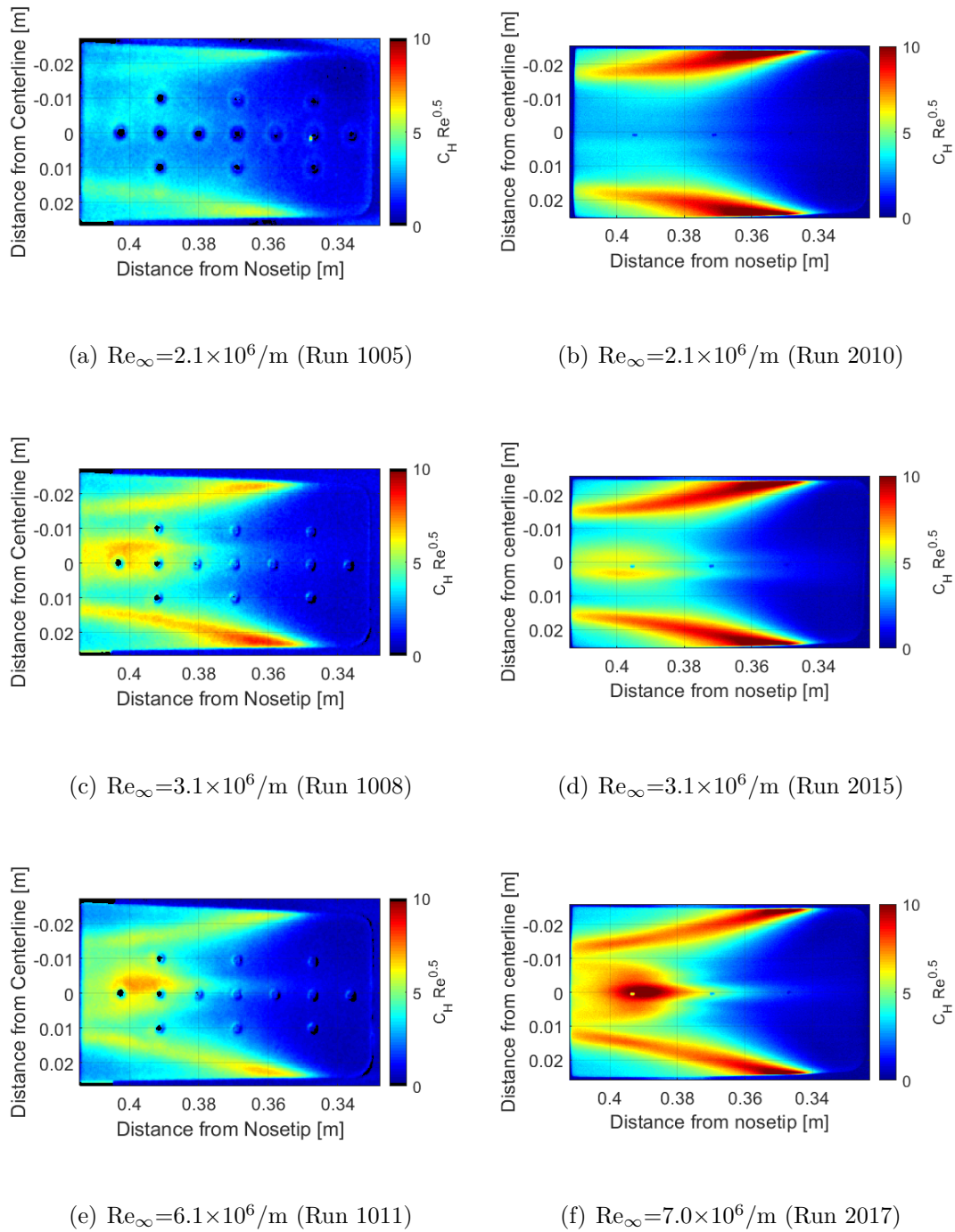


Figure 5.1. Comparison of TSP and IR laminar-scaled Stanton number of the ramp at varying unit Reynolds number in quiet flow. TSP are on the left and IR is on the right. Flow is from right to left.

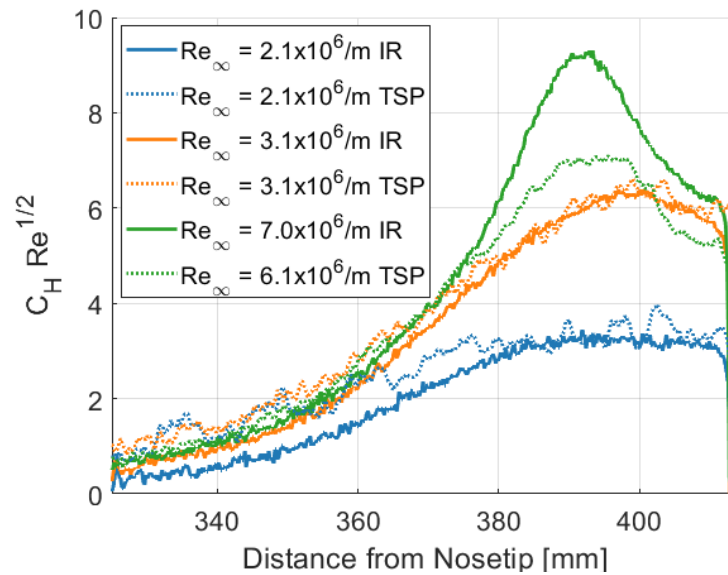


Figure 5.2. Comparison of IR and TSP Stanton number on the ramp at various unit Reynolds numbers.

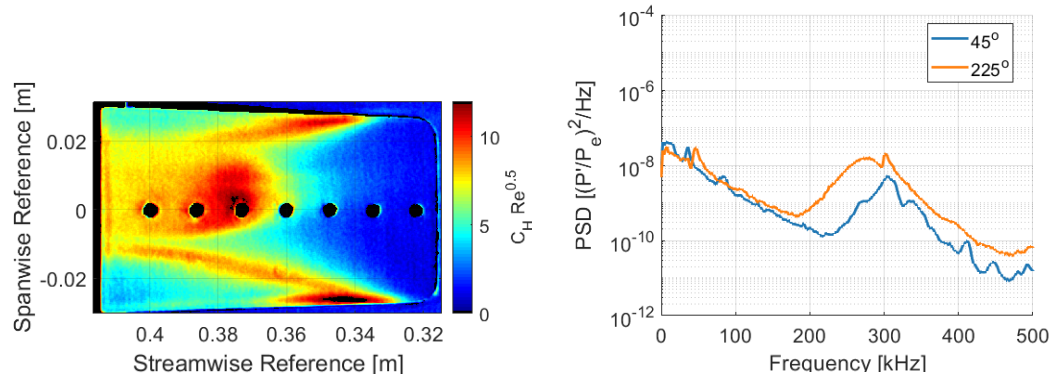
### 5.1.2 Effect of Small Angles of Attack on Ramp Heat Transfer

Maintaining a repeatable general flow structure for every experiment is required for reliable measurements of instability and transition in the shear layer above the separation bubble. Previous experiments have shown that fine-tuning the AoA of models in the BAM6QT is necessary to ensure a  $0.0^\circ$  alignment. A precision AoA adapter designed by Chynoweth [12] was used to make micro-adjustments to the AoA of the long-ramp model. This alignment of the AoA is necessary to obtain a near-symmetric flow on the ramp and ensure measurement of possible instabilities.

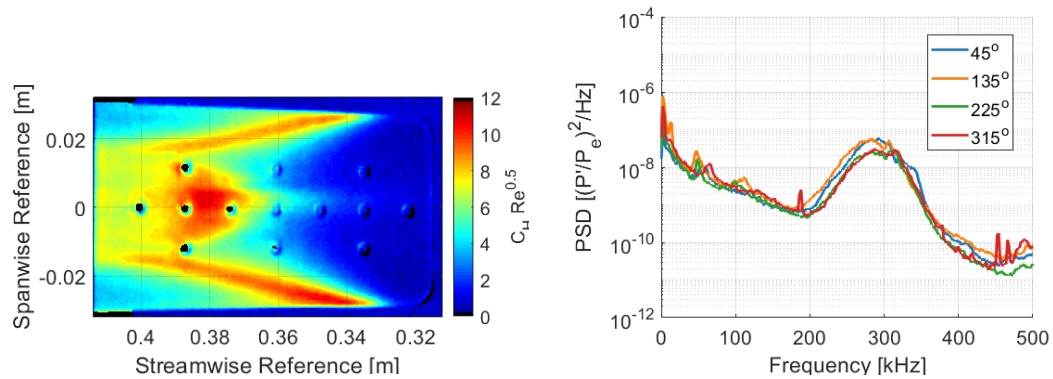
Figure 5.3 shows the effects of small changes in AoA on the behavior of the ramp heat transfer. The top image represent a poorly aligned case where broken azimuthal sensors made zeroing the alignment difficult. The model was zeroed under noisy flow for measurable amplitudes of second-mode instability on the  $7^\circ$  portion of the long-ramp model. The ramp heat transfer is under quiet flow. Over 20 kHz difference in peak frequency can be seen in the poorly-aligned PSD's, and the TSP in Figure

5.3(a) is noticeably asymmetric. The bottom images represent a well-aligned case. Figure 5.3(d) shows the PSDs for all four azimuthal sensors. All four sensors show a peak due to second mode at approximately 285 kHz. The peaks are all within 5 kHz of each other. Figure 5.3(c) shows the TSP for this case. The heat transfer is approximately symmetric and a single streak is present near the centerline of the ramp. The model was aligned to this level of accuracy for all entries after Entry 10.

Comparisons to Thome's computations were completed for cases with small angles of yaw [50]. Figure 5.4 shows a comparison of a fully-laminar simulation with TSP heat transfer at  $\beta = 0^\circ$  and  $0.414^\circ$ . Thome ran computations at several angles until good agreement was found. Figure 5.4(a) has the computation with  $0.414^\circ$  of yaw. The slight change in angle has altered the flow enough to reproduce the asymmetry seen in the poorly aligned TSP case. Both images show a single streak of heat transfer approximately 0.01 m off-centerline on the ramp. The asymmetry appears to be a result of the yaw angle. Figure 5.4(b) shows a similar comparison for an aligned case. The computation was completed for entirely laminar flow while the experiment at this Reynolds number had transitional or turbulent reattaching flow. The computation shows symmetric low heating on the centerline of the ramp. The TSP image also exhibits symmetric heating and has a single streak extending upstream on the centerline of the ramp. The differences between the computation and experiment could be attributed to the boundary-layer state, or to numerical uncertainties.

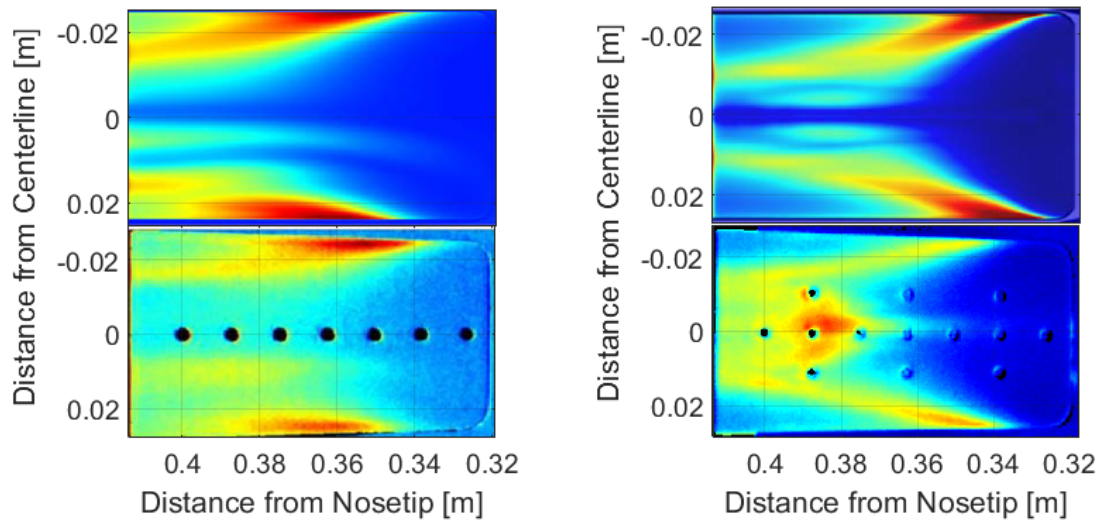


(a)  $20^\circ$  ramp under quiet flow,  $Re_\infty = 5.5 \times 10^6/\text{m}$  (Run 0720). (b) Azimuthal sensors under noisy flow,  $Re_\infty = 9.0 \times 10^6/\text{m}$  (Run 0704).



(c)  $20^\circ$  ramp under quiet flow,  $Re_\infty = 5.4 \times 10^6/\text{m}$  (Run 1010). (d) Azimuthal Sensors under noisy flow,  $Re_\infty = 8.8 \times 10^6/\text{m}$  (Run 1003).

Figure 5.3. Comparison of slight changes of AoA. Left column is TSP Stanton number for a single run and right column is the azimuthal PCB PSD. Top images are from a poorly aligned case, bottom images are from a properly aligned case. Flow is from right to left in TSP.



(a) Mis-aligned case at  $Re_\infty = 2.0 \times 10^6/m$  and  $\beta = 0.414^\circ$ . (b) Properly aligned case at  $Re_\infty = 9.2 \times 10^6/m$  and  $\beta = 0.0^\circ$ .

Figure 5.4. Qualitative comparison of computations and TSP heat transfer at small yaw angles. Top images are Thome's computation and bottom are TSP heat transfer [50]. Flow is from right to left.

### 5.1.3 Effect of Reynolds Number on Reattachment

Ramp heat transfer under quiet flow was measured to determine heating patterns and to see if streamwise streaks developed post-reattachment, like in the papers discussed in Section 1.2.2. Figure 5.5 shows IR ramp heat transfer over a sweep of unit Reynolds numbers. For every case tested, two “streaks” of high Stanton number begin at approximately 0.34 m downstream at  $\pm 0.02$  m off-centerline of the ramp. The streaks are believed to be related to edge effects of the ramp. As the Reynolds number increases, the streaks increase in amplitude and move towards the centerline. Figure 5.5(a) shows the lowest unit Reynolds number tested. Two streamwise streaks, symmetric about the centerline, can be seen at  $\pm 0.005$  m off the centerline. A heating increase indicative of reattachment is hard to interpret but appears to begin with the two streaks at 0.36 m downstream. As the Reynolds number increases in Figures 5.5(b) and 5.5(c), a single streak can be seen at approximately 0.005 m off-centerline. The top half of the ramp shows lower heating than the bottom. The reason for this asymmetry is not known since the model was not adjusted between these runs, but residual AoA or yaw could be a cause. An increase in heating is clearer at the higher Reynolds number and begins near 0.36 m downstream in Figures 5.5(b) and 5.5(c). Figures 5.5(d) and 5.5(e) show higher Reynolds numbers and, based on sensor data and an increase in laminar-scaled Stanton number, represent transitional reattaching boundary layers. Two streaks can be seen just off the centerline for both of these cases. They begin immediately at reattachment, 0.36 m downstream. Figure 5.5(f) shows heat transfer under a completely transitional or turbulent case. A single streak can be seen on the ramp centerline and high heat transfer is present on the downstream portion of the ramp. The two streamwise streaks appear to have merged for this case.

A better comparison of Stanton number can be made by looking at individual spanwise and streamwise locations on the ramp. Figure 5.6 shows the ramp Stanton number. The streamwise and spanwise locations used for data comparisons are labeled with black lines. The farthest upstream edge of the image is the start of the 20° ramp.

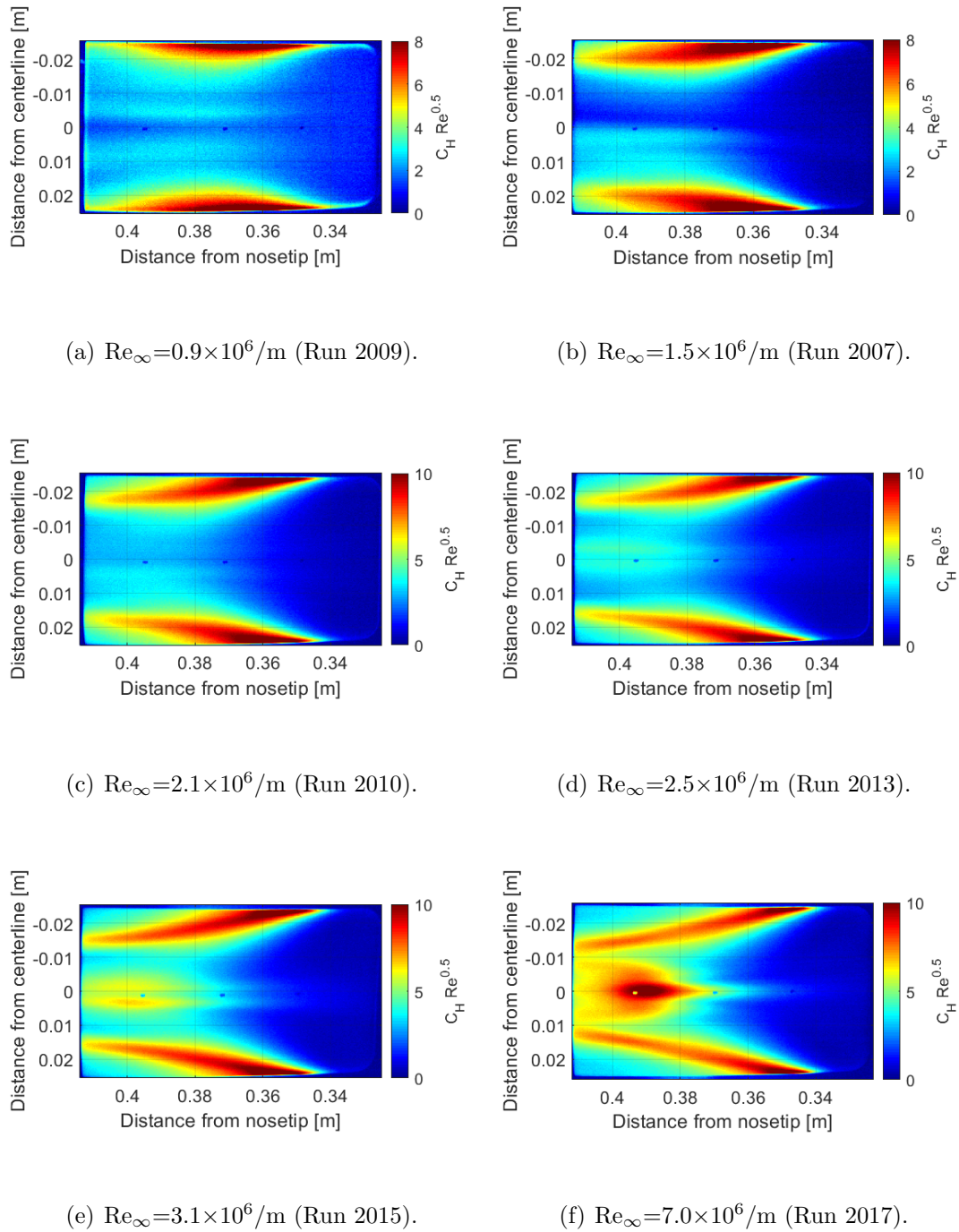


Figure 5.5. IR laminar-scaled Stanton number of the  $20^\circ$  ramp at varying unit Reynolds number in quiet flow. Flow is from right to left.

Figure 5.7(a) shows the spanwise Stanton number at 0.4 m downstream. This location is downstream of the perceived reattachment for every Reynolds number. The edge effects of the ramp can be seen on both sides of the span. As the Reynolds number increases, the peak heating locations from these edge effects move from 24 mm off-centerline at the lowest Reynolds number to 14 mm off-centerline for the highest Reynolds number. The streaks that were present near the centerline can be seen and the Stanton number gradually increases with unit Reynolds number. The two lowest Reynolds number cases have similar amplitudes of centerline heating which would indicate the  $\sqrt{Re}$  scaling is successfully collapsing these laminar cases. At these Reynolds numbers, pressure fluctuation measurements also indicate a laminar boundary layer.

Figure 5.7(b) shows a similar plot but for a line just off-centerline in the streamwise direction. The cuts were offset due to registration dots present on the centerline of the ramp causing unphysical spikes in heat transfer if the centerline is chosen. Upstream of 360 mm from the nosetip, all Stanton number measurements are below a value of 2. Heat transfer increases with downstream distance for every case and the boundary layer is believed to be reattaching. For nearly all tested cases, this increase in Stanton number is gradual and levels out near 400 mm downstream of the nosetip. The exact location of reattachment, and the effect of Reynolds number on reattachment, is unclear without a way to correlate surface Stanton number. As the Reynolds number increases, the heat transfer downstream of 370 mm increases. The highest Reynolds number case exhibits a peak in heat transfer at 390 mm that then drops farther downstream. This is similar to other experimental work that show a peak in heat transfer just downstream of reattachment from the local thinning of the boundary layer [18].

A similar analysis of the effect of unit Reynolds number on ramp heat transfer was completed under noisy flow. Comparison between the results can help to show the effect of freestream noise on transitional surface heating. Figure 5.8 shows the laminar-scaled Stanton number computed from IR thermography for noisy flow. At every

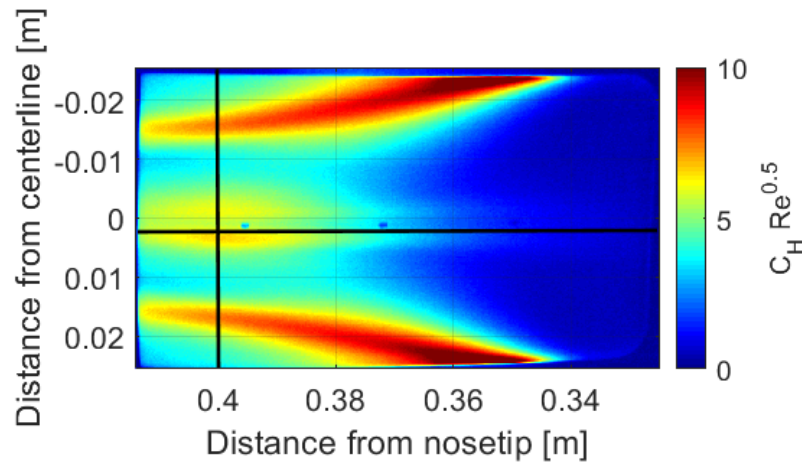


Figure 5.6. IR laminar-scaled Stanton number of the ramp at  $Re_\infty = 3.1 \times 10^6/m$  (Run2010). The lines represent locations where data was taken for streamwise and spanwise cuts in Figure 5.7.

tested Reynolds number, heating streaks can be seen at the sides of the ramp. These seem to be the same edge effects seen previously in quiet flow. Figures 5.8(a) and 5.8(b) show the lowest tested Reynolds number. The heat transfer is slightly asymmetric. Reattachment is hard to detect and is unclear in these cases. Figures 5.8(c) and 5.8(d) show results from a slightly higher Reynolds number. The Stanton number has increased 0.37 m downstream of the nosetip and is becoming more symmetric about the centerline. A single streak is beginning to develop on the centerline of the ramp. This trend continues for Figure 5.8(e). A larger jump in Reynolds number is seen to Figure 5.8(f). The reattachment location has moved drastically upstream. For this Reynolds number, pressure fluctuation data on the  $7^\circ$  portion of the model show large second-mode growth and an increase in broadband power. This indicates that the upstream boundary-layer is beginning to transition at this Reynolds number. Due to

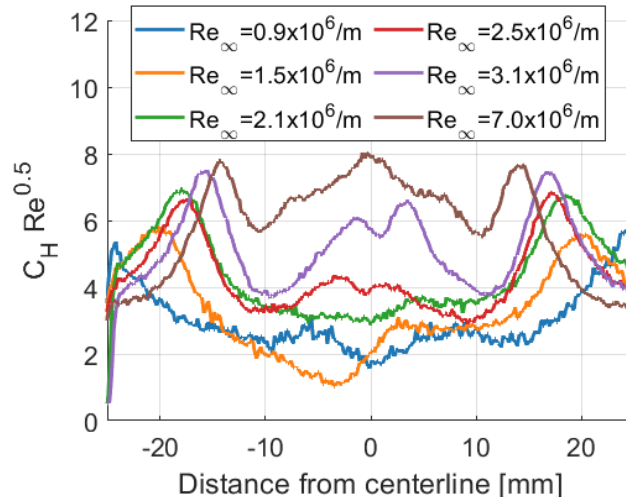
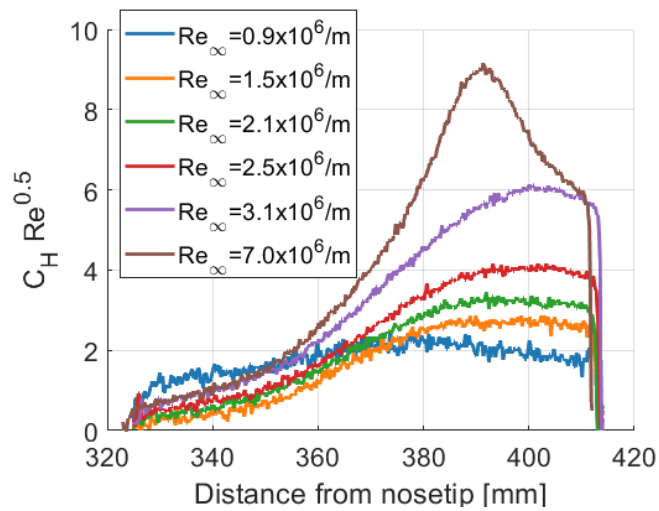
(a)  $x = 0.400$  m downstream.(b)  $y = 0.002$  m off-centerline.

Figure 5.7. Line cuts of IR Stanton number on the  $2^\circ$  ramp at varying unit Reynolds number in quiet flow. The ramp is 51 mm wide and 91 mm long.

this, the boundary layer is more resistant to separation, reattaches farther upstream, and has a different separated region than any other case.

Stanton number was compared at a single streamwise and spanwise location on the ramp to better demonstrate the effects of Reynolds number. Figure 5.9(a) shows the spanwise Stanton number at  $x = 400$  mm downstream. As the Reynolds number increases the edge effects that are approximately 20 mm off-centerline move closer to the centerline. At the three lowest Reynolds numbers, asymmetry near the centerline is seen. At higher Reynolds numbers, the heating becomes more symmetric and a wide peak in heating is present on the ramp centerline. The highest tested Reynolds number has a transitional or turbulent incoming boundary-layer and near-even heating is seen across the span. Figure 5.9(b) shows a line of streamwise Stanton number at various Reynolds numbers. The upstream part of the ramp shows similar heat transfer patterns for every case except the highest tested Reynolds number. As the Reynolds number increases the heating on the downstream half of the ramp increases. At the three highest Reynolds numbers a maximum develops on the ramp. The heat transfer then drops and levels out. This can be seen best for the highest Reynolds number case which reattaches much earlier than any other due to the turbulent incoming boundary layer.

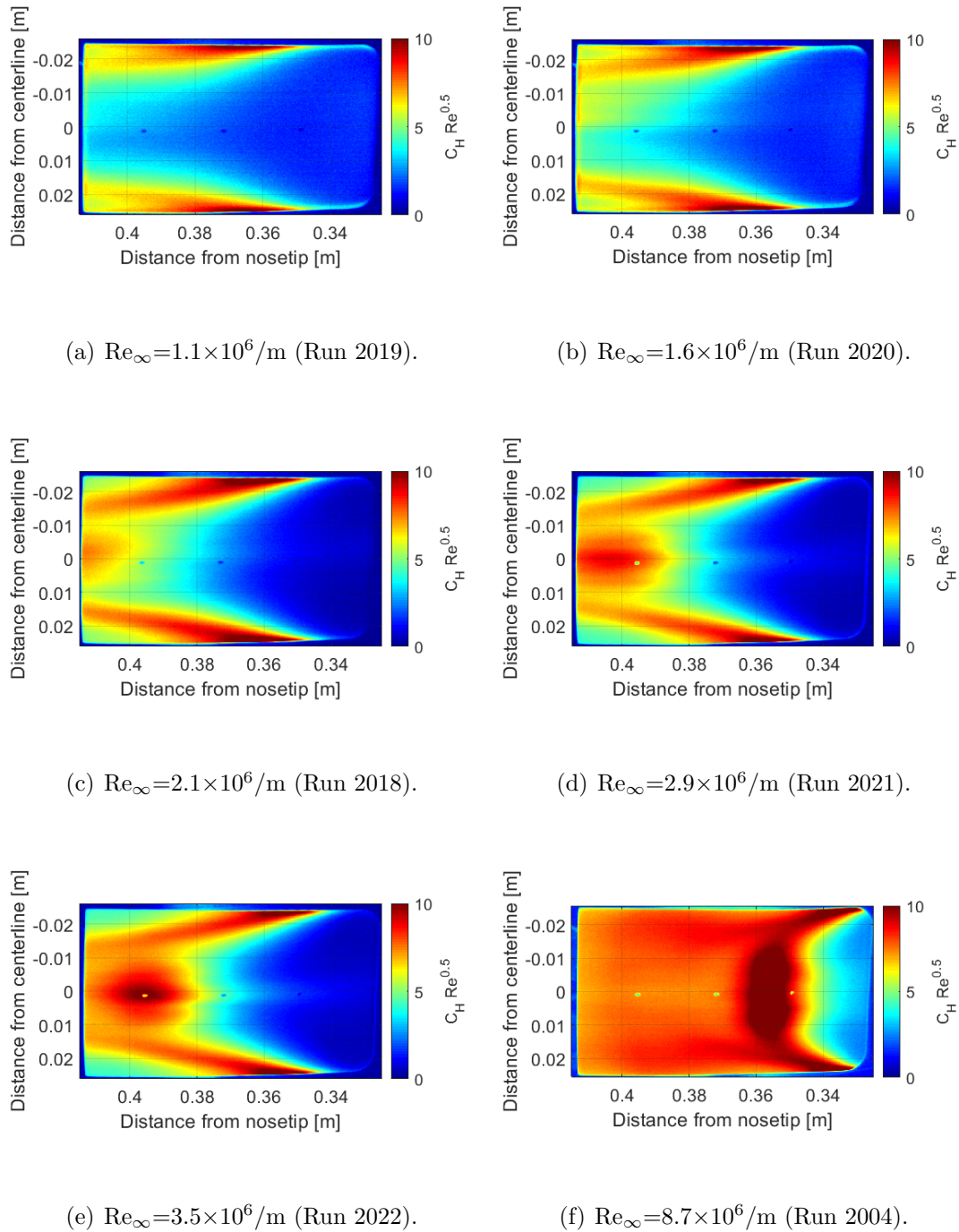


Figure 5.8. IR laminar-scaled Stanton number of the  $20^\circ$  ramp at varying unit Reynolds number in noisy flow. Flow is from right to left.

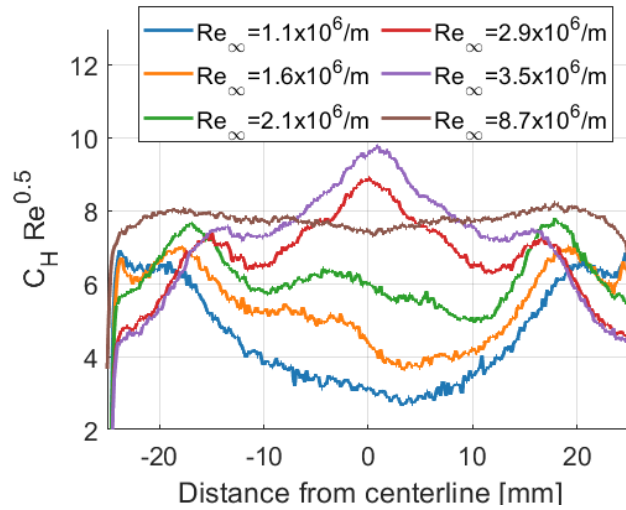
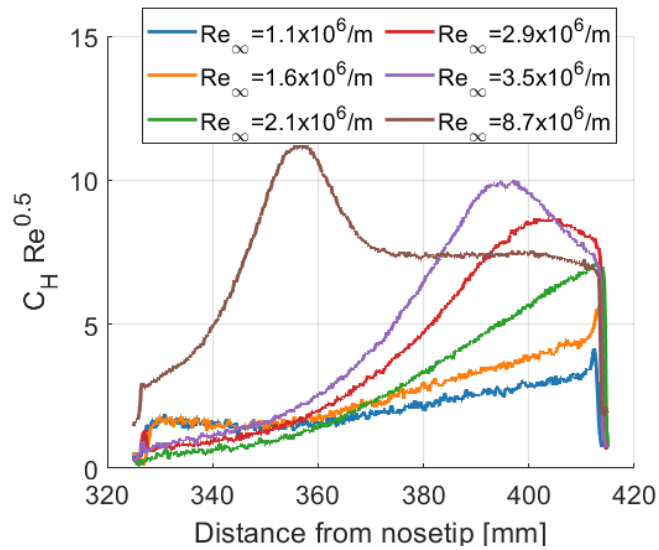
(a)  $x = 0.400$  m downstream.(b)  $y = 0.002$  m off-centerline.

Figure 5.9. Line cuts of IR Stanton number on the  $20^\circ$  ramp at varying unit Reynolds number in noisy flow. The ramp is 51 mm wide and 91 mm long.

## 5.2 Natural Pressure Fluctuations Inside the Separation

This section will outline measurements taken at the model surface within the separated flow region. Determination of the separated region of the flow was shown in Section 4.2.1 with oil flow, surface heat transfer, and comparisons to computation. This section will include sensors on the slice and the first half of the ramp. No perturbations were introduced for any case within this section.

### 5.2.1 Natural Pressure Fluctuations on the Slice

Five PCB sensors were present on the slice to measure the surface pressure fluctuations within the separation. Figure 5.10 shows TSP Stanton number with the locations of the five slice PCBs and the front edge of the ramp. Only centerline sensors were present on the slice.

Figure 5.11 show PSDs and coherences from the slice for a single run. The full frequency range can be seen in Figures 5.11(a) and 5.11(b). Peaks in the power spectra can be seen at various frequencies. The peaks are sharp and are concentrated between 70-100 kHz and 280-350 kHz. The reason for this behavior is not known. The coherence of these signals were calculated to see if any traveling instabilities were present within the separation. Very little coherence is seen between most of the slice sensors. This suggests that the fluctuations are not traveling or growing linearly with distance on the centerline. A small peak in coherence is seen on the last two sensors at 50 kHz. To better show the low-frequency behavior, the same PSDs are plotted over a smaller frequency range in Figures 5.11(c) and 5.11(d). The peaks between 70-100 kHz are better shown and do not follow a consistent trend with streamwise distance. Additionally, it can be seen that the peak in coherence is below the peaks seen in the PSDs. The reason for this is not known but it does not appear that the source of peaks in the PSD are convecting in the streamwise direction.

Figure 5.12 shows similar plots at a higher Reynolds number. Figures 5.12(a) and 5.11(b) show more peaks present at most streamwise locations. Similar peaks are seen

between 70-120 kHz and 280-350 kHz. Additional spectral content is visible at 30 kHz and at frequencies greater than 350 kHz. This case has even less coherence between each individual sensor. The last two sensors show a peak at 60 kHz. Figures 5.12(c) and 5.12(d) show the same plots over a smaller frequency range. The peak at 30 kHz is largest at  $x = 0.288\text{m}$  but damps with farther downstream distance. A small peak in coherence is seen at this location but does not persist at other sensors. Peaks in coherence do not occur within the 75-100 kHz frequency band. It does not appear that peaks in that frequency band of the PSD highly coherent. No waves at frequencies seen in the PSDs within the separation appear to be coherent with streamwise distance. Low coherence is possible if waves are not traveling with streamwise distance but are instead traveling in three-dimensions. However, the cause of these fluctuations is not known with data from the current instrumentation.

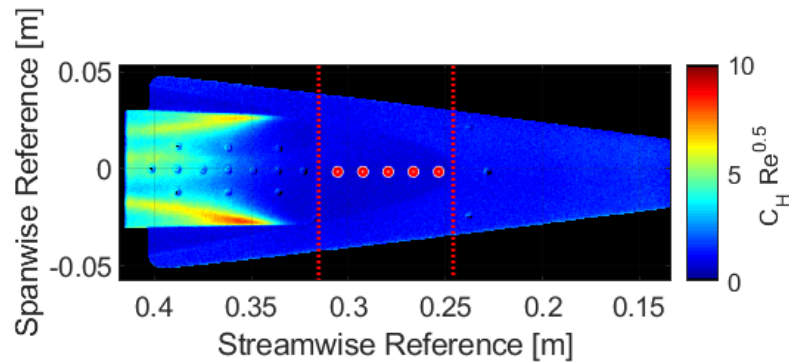


Figure 5.10. TSP Stanton number of the full model at  $Re_\infty=2.9\times 10^6/\text{m}$  (Run 1006). The red dots represent the five sensors located on the slice. The two red lines represent the start of the slice and the ramp.

The effects of Reynolds number on two of the slice PCBs can be seen in Figure 5.13. Both sensors show similar frequency behavior with numerous sharp peaks. As the Reynolds number increases, the amplitude and number of peaks increase at both sensor locations. This suggests that the peaks are real features within the separation bubble. The peaks do not change frequency with Reynolds number and remain at

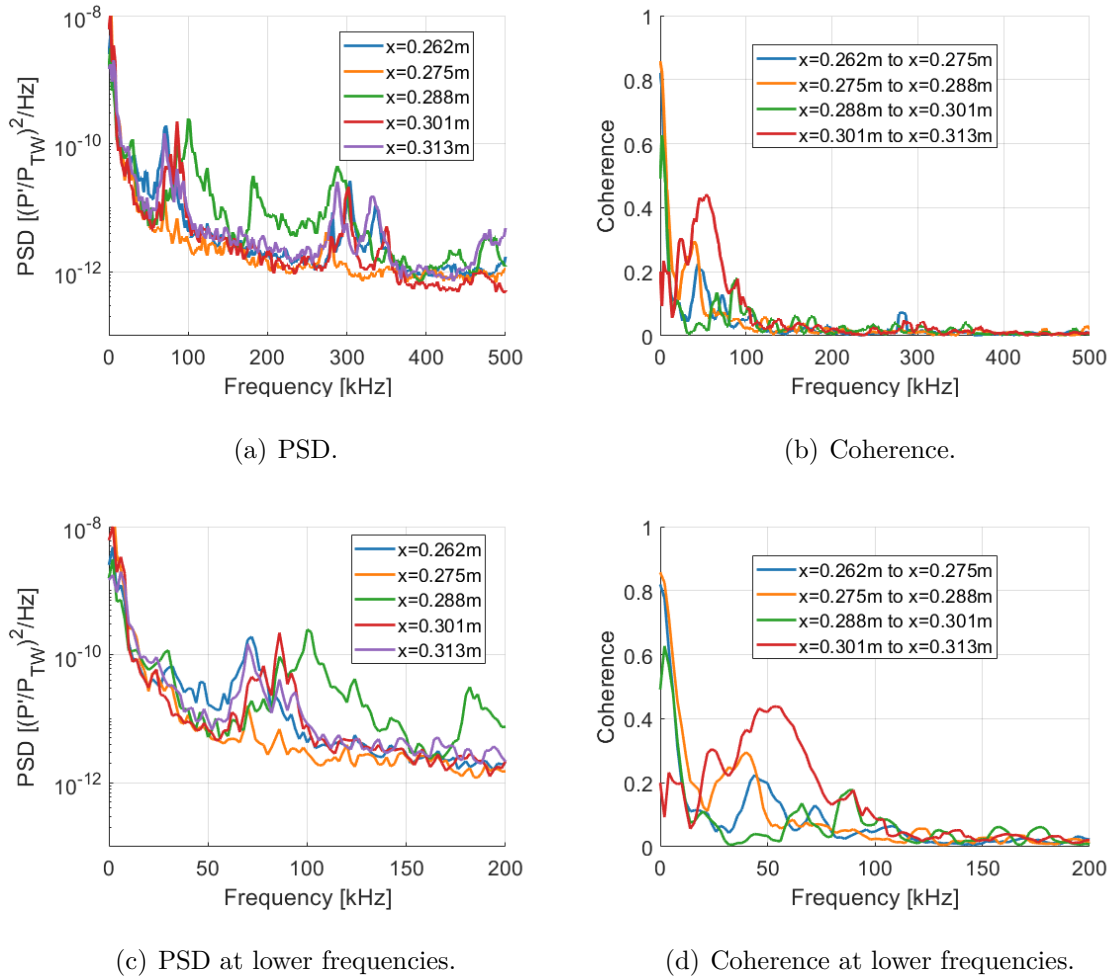


Figure 5.11. PSD and coherence of PCB pressure fluctuations on the slice at  $Re_\infty = 3.6 \times 10^6/m$  (Run 2107).

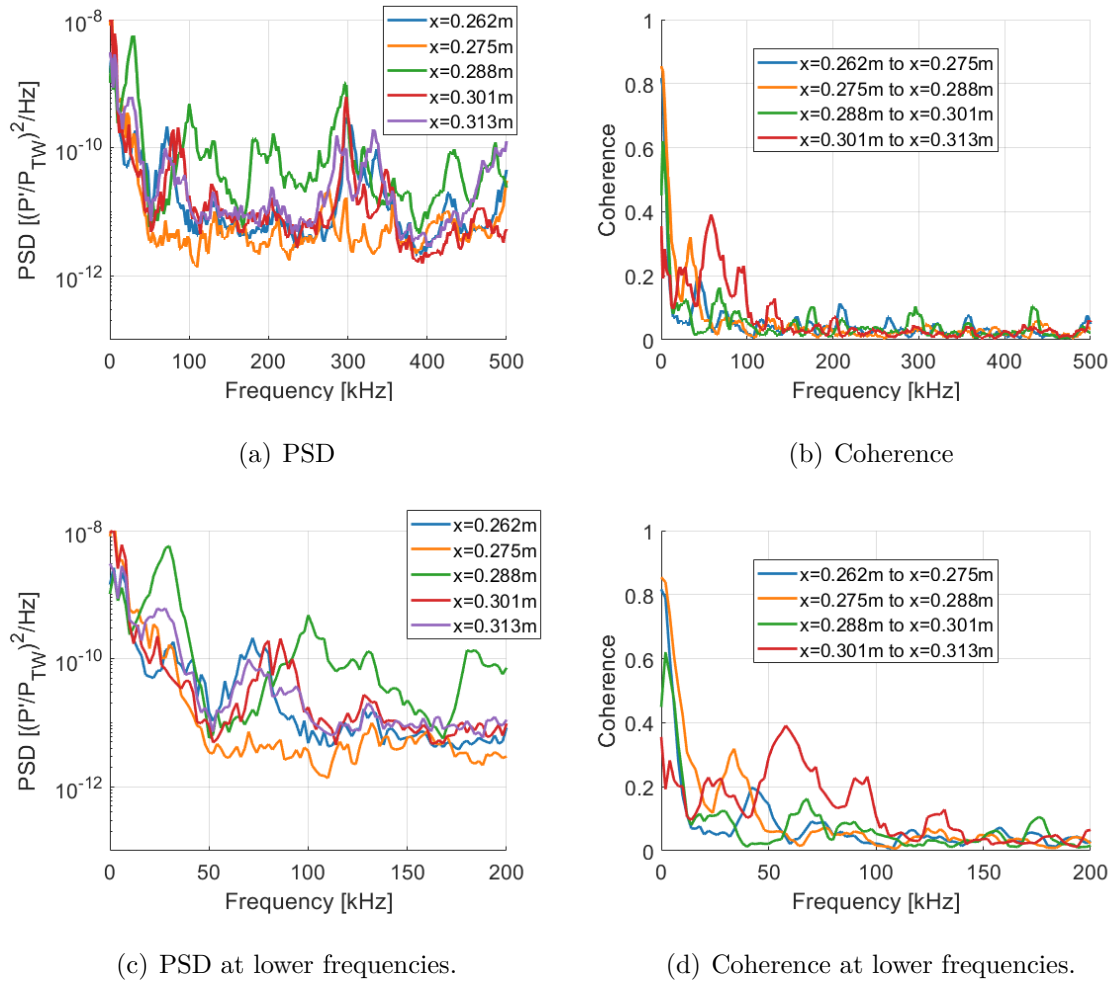


Figure 5.12. PSD and coherence of PCB pressure fluctuations on the slice at  $Re_\infty = 6.03 \times 10^6/\text{m}$  (Run 2112).

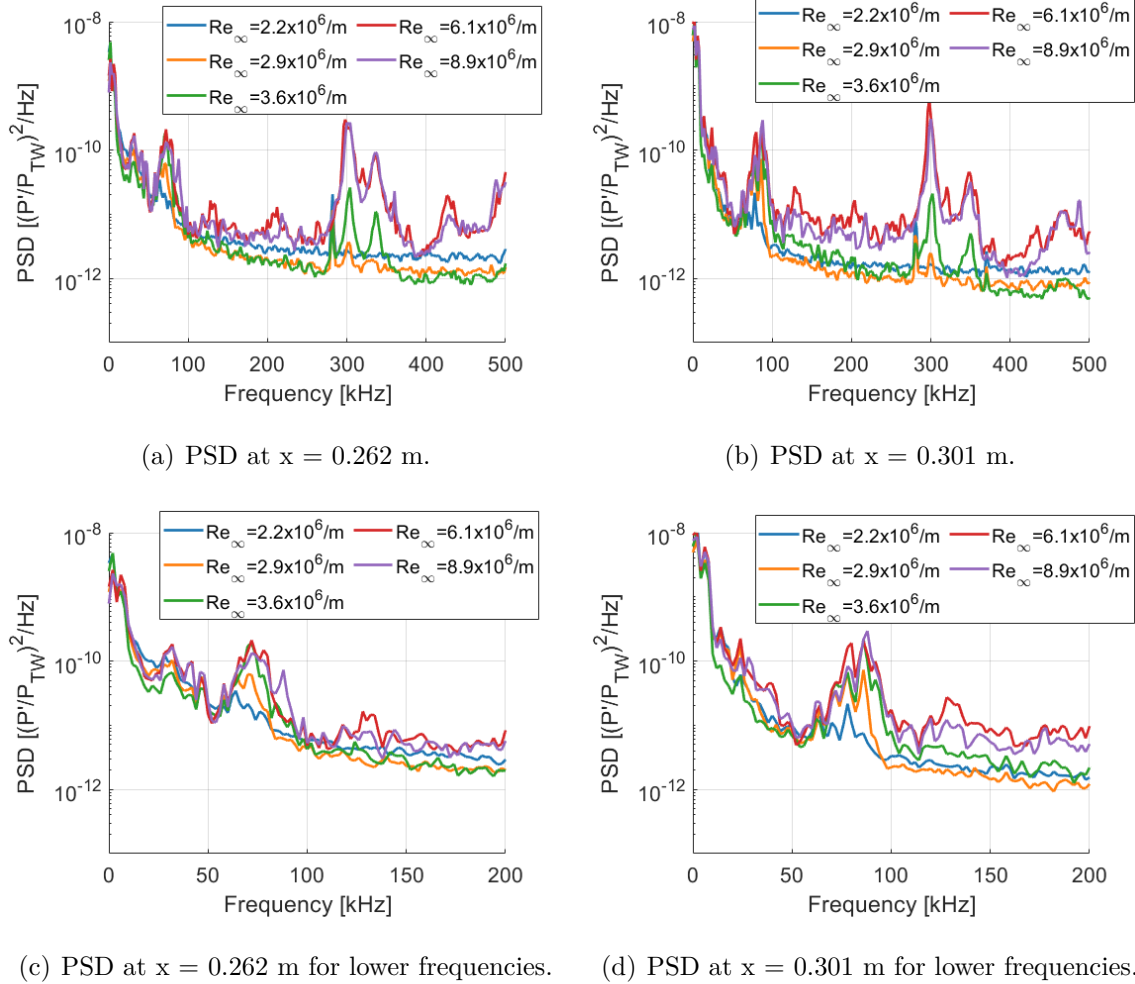
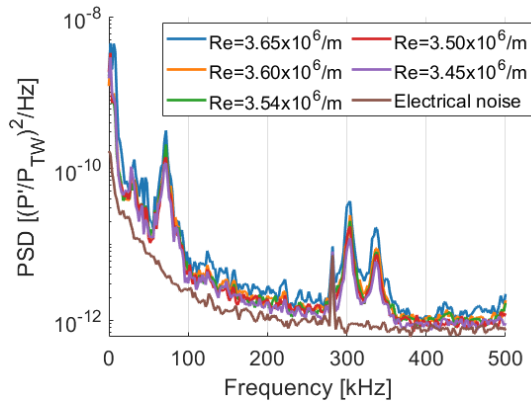


Figure 5.13. Effects of Reynolds number on PCB pressure fluctuations on the slice.

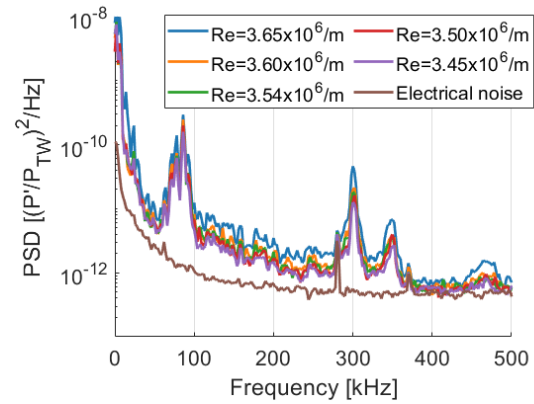
a constant frequency when present. This could be due to the size of the separation bubble not changing much with Reynolds number. The two highest Reynolds numbers show far more peaks than the three lower Reynolds number. It possible that the large jump in Reynolds number has amplified these frequencies above the sensor noise for these cases. The same power spectra were plotted over a smaller frequency range in Figures 5.13(c) and 5.13(d). The peaks in the PSD between 50-100 kHz consistently occur at the same frequencies and grow in amplitude with increasing Reynolds numbers.

The effects of small changes in unit Reynolds number during a single run is shown in Figure 5.14. Data were processed between 0.4-2.1 s into the run at two locations during two runs. The lower Reynolds number case in Figures 5.14(a) and 5.14(b) shows that as the Reynolds number drops over the course of the run, the peaks drop in amplitude slightly but do not change in frequency. This is similar to what was seen over larger Reynolds numbers differences. The cause of the pressure fluctuations remains constant during the run. A higher Reynolds number case is seen in Figures 5.14(c) and 5.14(d). The broadband power of the PSD has increased for both locations and the number of peaks has increased. The behavior of the peaks is similar to the lower frequencies. The higher Reynolds number does show that the amplitudes of peaks at higher frequencies change more with Reynolds number.

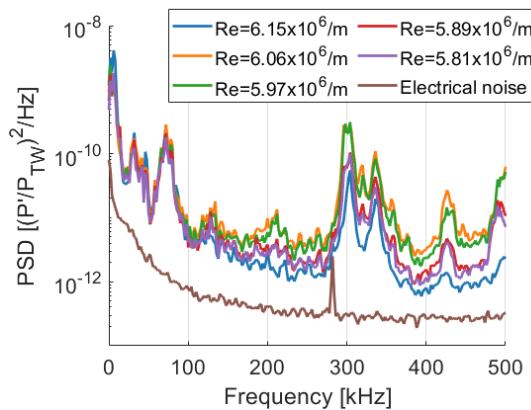
Without more measurements within the separation, it is difficult to determine the cause of peaks seen in the pressure fluctuation PSDs. The frequency at which the fluctuations oscillate is dependent on the location within the separation. A clear trend in the location of peaks with streamwise distance was not seen. The low coherence between sensors suggest that the fluctuations are not traveling in the streamwise direction. The peaks in the PSDs seen at a single sensor location are independent of the Reynolds number and only slightly grow in amplitude with increasing Reynolds number. Without off-surface measurements, it is difficult to determine if this behavior is a result of interactions with the shear layer or are solely due to the recirculating region.



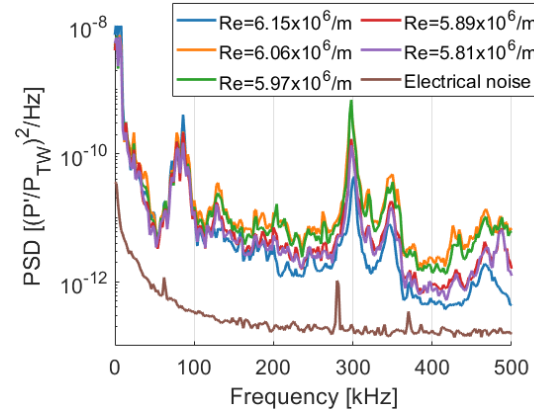
(a) PSD at  $x = 0.262$  m for numerous times during Run 2107.



(b) PSD at  $x = 0.301$  m for numerous times during Run 2107.



(c) PSD at  $x = 0.262$  m for numerous times during Run 2112.



(d) PSD at  $x = 0.301$  m for numerous times during Run 2112.

Figure 5.14. Effects of small changes in Reynolds number on PCB pressure fluctuations on the slice.

### 5.2.2 Natural Pressure Fluctuations on the Ramp

PCB and Kulite pressure transducers were used to measure pressure fluctuations within the separation on the ramp. Figure 5.15 shows a typical plot of Stanton number on the ramp. Five PCB locations are marked with red circles on the figure. These five sensors were within the apparent separation bubble for all tested quiet-flow conditions. A cluster of sensors was present to enable measurement of any oblique traveling waves within the separated region. These have individual labels for clarity of comparisons. A fifth sensor is present on the centerline downstream of the cluster and is not labeled.

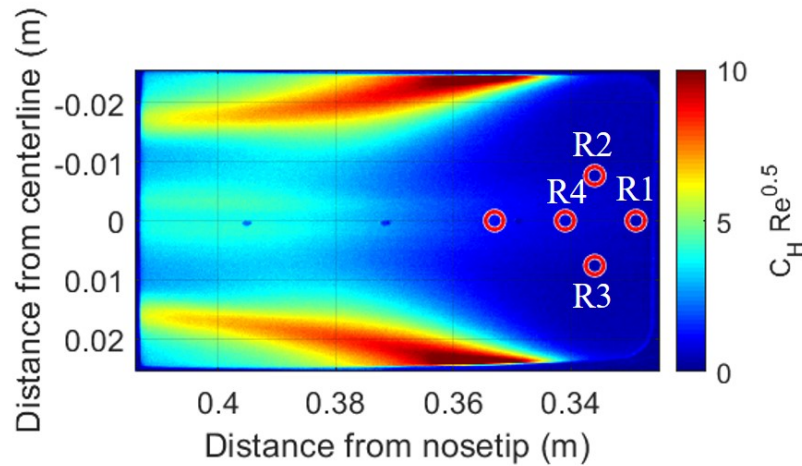


Figure 5.15. IR heat transfer of the ramp at  $Re_\infty = 2.5 \times 10^6/m$  (Run 2013). The red dots represent the five sensors located in the separation on the ramp. The labels represent nomenclature for comparing pressure fluctuations.

Figure 5.16 shows the PSDs and coherences from the centerline sensors within the separation. The PSDs seen in Figure 5.16(a) show behavior that is similar to the slice pressure fluctuations. Several disparate peaks are seen and there is no trend with downstream location. The coherences seen in Figure 5.16(b) do not show significant levels between any of the ramp centerline sensors. A similar comparison was made

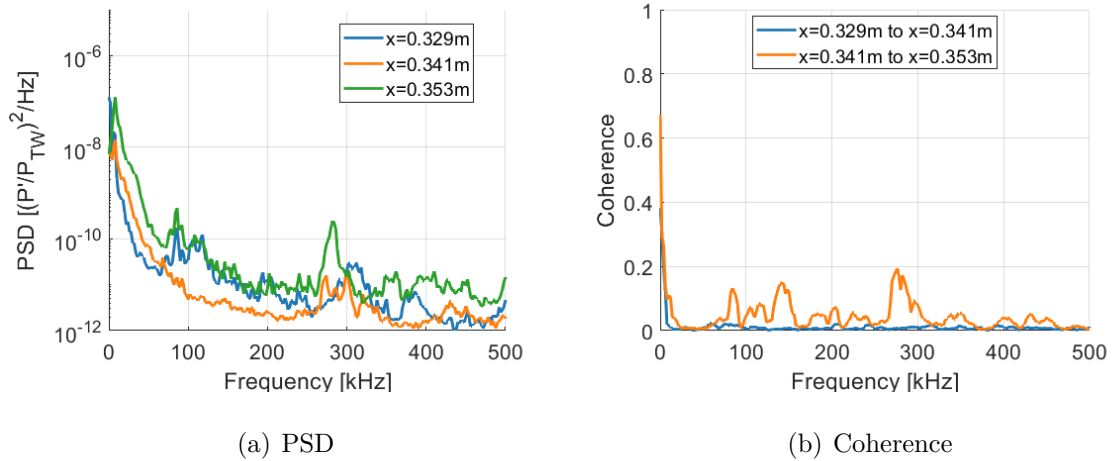


Figure 5.16. PSD and coherence of PCB pressure fluctuations within separated region. Sensors are on the ramp centerline at  $Re_\infty = 3.6 \times 10^6/m$  (Run 2107).

for the four sensors within the cluster and can be seen in Figure 5.17. Several peaks are seen on R1, R2, and R3. Peaks in power can be seen at 110 kHz and 275-325 kHz. The coherences for these sensors are shown in Figure 5.17(b). No significant coherence exists between any two sensor locations in this cluster. The peaks seen in the PSD do not appear to be traveling within the separated region.

The effect of Reynolds number on the ramp pressure fluctuations within the separation is plotted in Figure 5.18. The four locations on and off the centerline all show similar behavior. Spectral peaks exist at various frequencies. The frequencies do not change with Reynolds number when the peaks are present. As the unit Reynolds number increases the amplitude of the peaks increase but their locations are constant. The two highest Reynolds numbers show additional peaks at higher frequencies. Similar behavior was seen on the slice and the similarities confirm the belief that the entire slice is separated. While the pressure fluctuations within the separation are interesting, they do not seem to tell us much about the state of the boundary layer or shear layer. Due to this, they will not be discussed further.

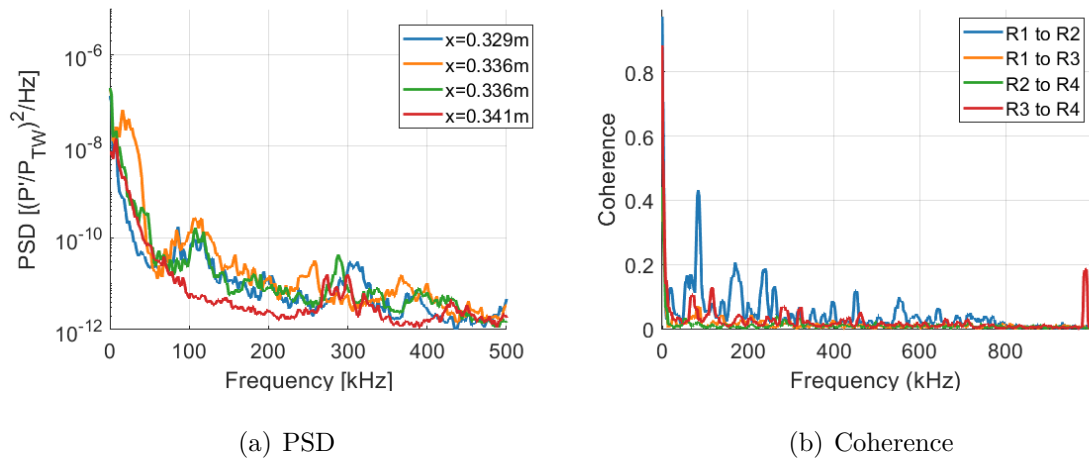


Figure 5.17. PSD and coherence of PCB pressure fluctuations within separated region. Sensors are arranged in a cluster at  $Re_\infty = 3.6 \times 10^6/\text{m}$  (Run 2107).

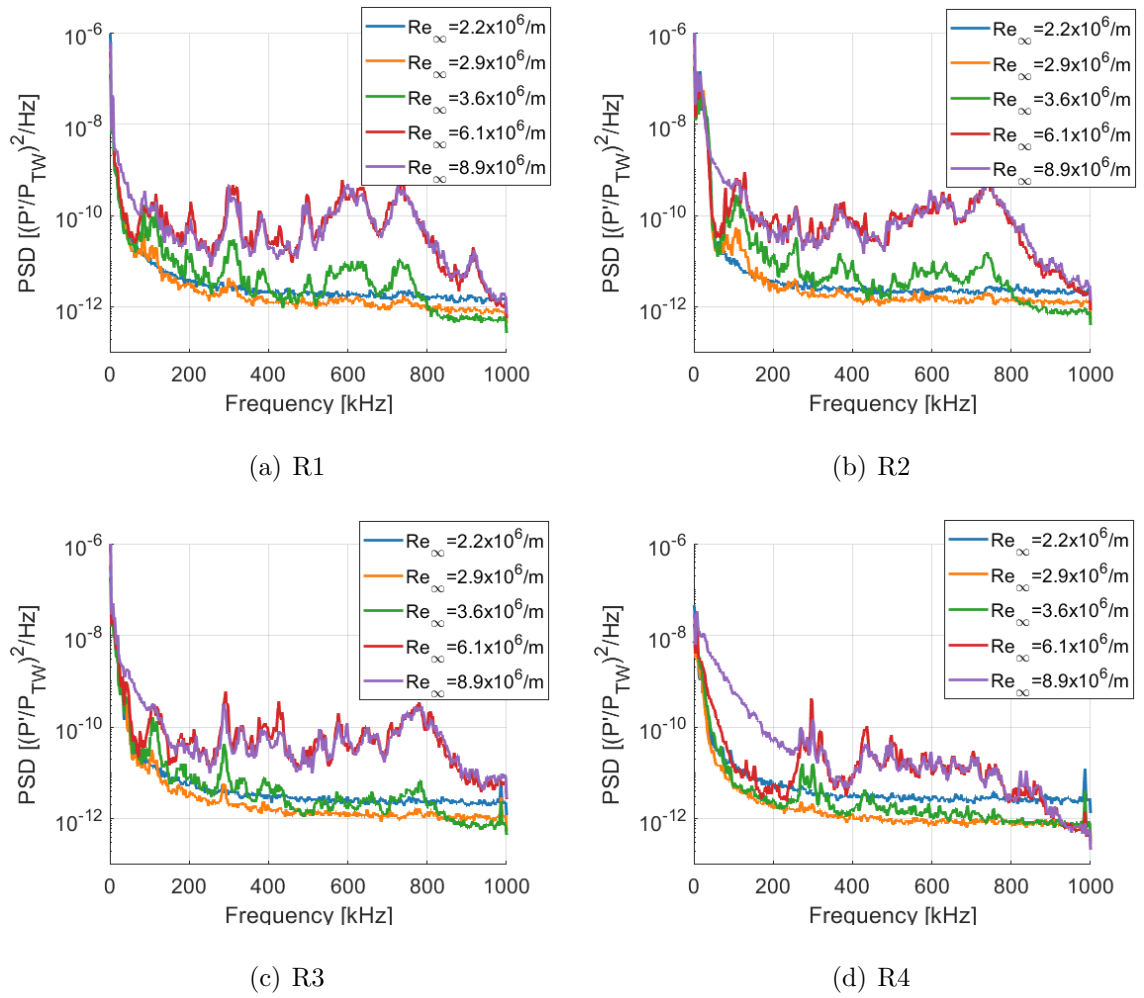


Figure 5.18. PSDs of clustered PCB pressure fluctuations within the ramp separated region at various unit Reynolds number.

### 5.3 Natural Post-Reattachment Pressure Fluctuations

The primary goal of the present work was to make measurements of traveling instabilities amplified within the shear layer between a separation bubble and the freestream flow. As discussed in Section 4.2, the ability for this flow to have laminar, transitional, and turbulent flow post-reattachment should allow for possible instabilities to be measured by modulating the Reynolds number under quiet flow. As the post-reattachment flow goes from laminar to transitional, any unstable frequencies from the shear layer should convect onto the model surface. At this point they should be measurable on the surface pressure sensors.

Figure 5.19 shows sections of the time trace for a PCB near the end of the ramp at various Reynolds numbers. The time traces allow for a qualitative look at the state of the boundary layer post-reattachment. Figure 5.19(a) shows a low Reynolds number case. The fluctuations are small and few spikes are present during this time. This Reynolds number is primarily laminar after reattachment. Figure 5.19(b) shows a slightly higher Reynolds number. Spikes of high-amplitude fluctuations are randomly interspersed over the low-amplitude mean. These indicate the presence of turbulent spots within the boundary layer. Figure 5.19(c) shows another small increase in Reynolds number. The frequency and amplitude of the turbulent spots have increased and the amount of time that the ramp surface sees laminar fluctuations is small. At  $Re_\infty = 3.4 \times 10^6/m$  the time series is completely dominated by large turbulent spots and very little laminar flow is seen. The inset in Figure 5.19(d) shows a smaller segment of time to illustrate that the boundary layer is not fully turbulent and some limited windows of time see laminar fluctuations. The unit Reynolds number at which the boundary layer transitions is remarkably low under quiet flow. Axisymmetric models tested by Leinemann and Benitez under quiet flow did not see transition at  $Re_\infty = 9.5 \times 10^6/m$  and  $Re_\infty = 12.0 \times 10^6/m$ , respectively [52, 73]. The finite-span compression corner on the cone-slice-ramp lowers the unit Reynolds number required for transition by a factor of four when compared to axisymmetric geometries under quiet flow. This

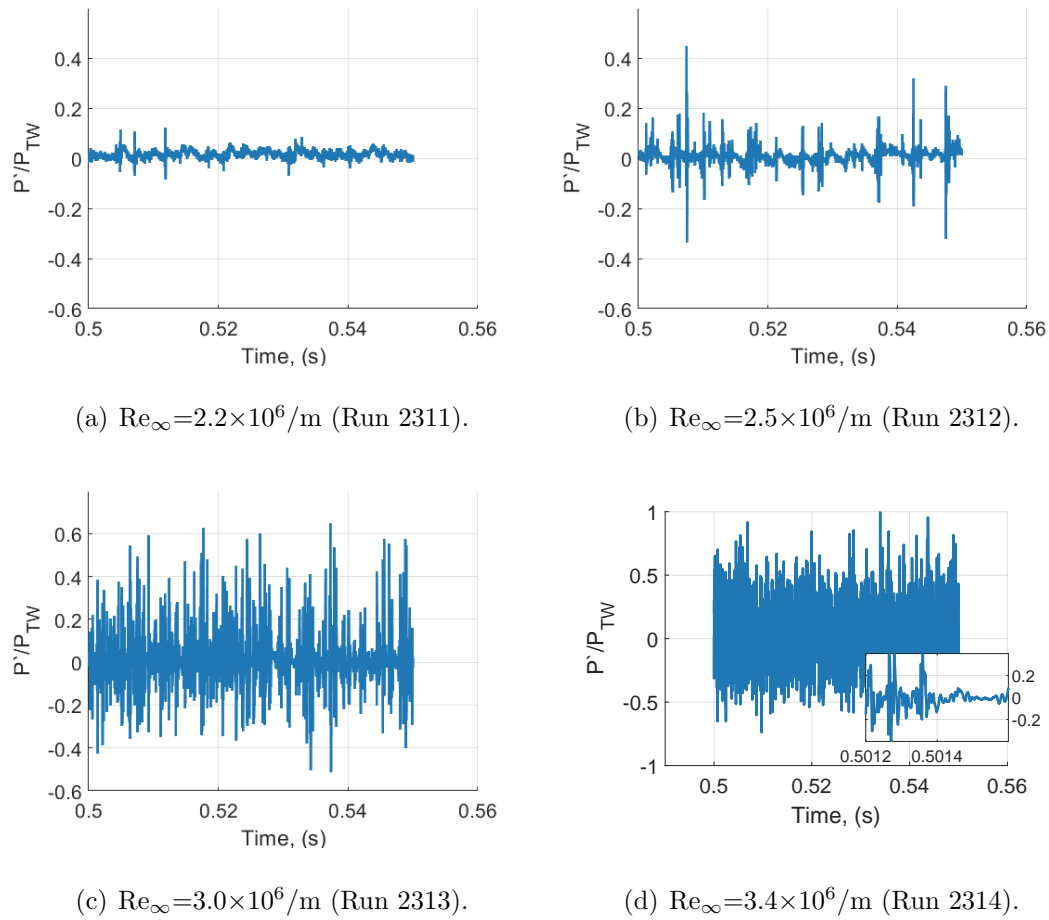


Figure 5.19. Development of time traces post-reattachment with Reynolds number. All data is from the farthest downstream centerline PCB at  $x=0.407$  m.

corresponds to a freestream Reynolds number based on distance from the nosetip of  $0.9 \times 10^6$  on the long-ramp model.

Figure 5.20 shows a close-up view of a turbulent spot from the  $Re_\infty = 2.5 \times 10^6 / m$  case. A single turbulent spot was analyzed to show the downstream progression. Figure 5.20(b) features a waterfall plot created by applying a constant offset to the time traces of each subsequent PCB. The top pressure trace is the farthest upstream post-reattachment sensor. The first three sensors show perturbations in the post-reattachment flow. By  $x = 0.389$  m, the perturbation has grown and begins to

look more like a wave packet. The three farthest downstream sensors show erratic and random fluctuations. This is a common sign of breakdown to turbulence. The fluctuations have broken down and become a turbulent spot. By the final sensor on the ramp, the disturbance has grown to a peak-to-peak amplitude of 77% of  $P_{TW}$ .

The method of Ching and Lagraff was used to track the spots [113]. This method has been used by Casper to track turbulent spots in the BAM6QT nozzle-wall boundary-layer [112]. The procedure emphasizes the high-frequency portions of the signal by applying a detector function ( $D[t]$ ). The detector function is the result of multiplying the square of the first derivative with the scaled signal magnitude and is shown in Equations 5.1 and 5.2. The detector function is then smoothed using an exponential weighted central moving average. Twelve sampling periods were used for determining the moving average. The criterion function ( $S[t]$ ) was then calculated and used to determine the state of the boundary layer. Equations 5.3 and 5.4 show how the criterion function was calculated. Previous work used an arbitrary threshold applied to the output of the criterion function to differentiate laminar and turbulent flow. The threshold value was based on the specific flowfield and expertise of the author. For this work, the maximum of the criterion function was selected as the spot location. Figure 5.21 shows an example of how this process tracks the spot.

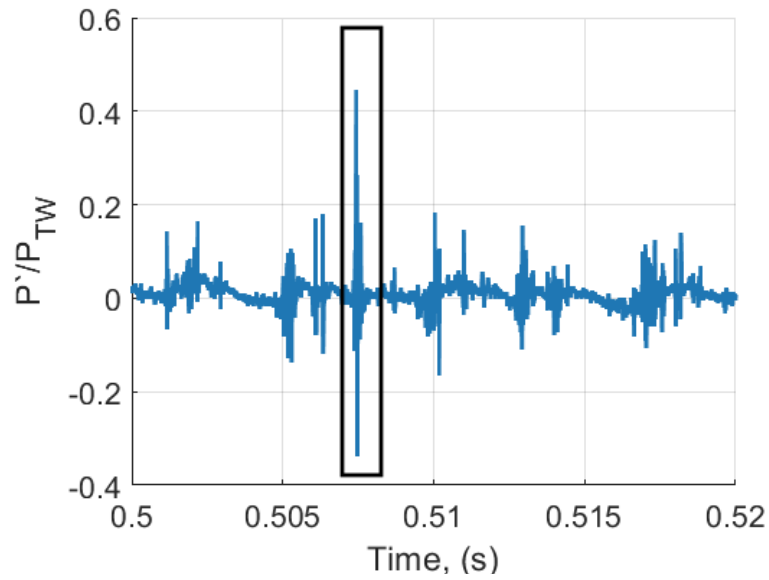
$$D(t) = m(t) \left( \frac{\partial p(t)}{\partial t} \right)^2 \quad (5.1)$$

$$m(t) = \left| \frac{p(t) - p_{min}}{p_{max} - p_{min}} \right| \quad (5.2)$$

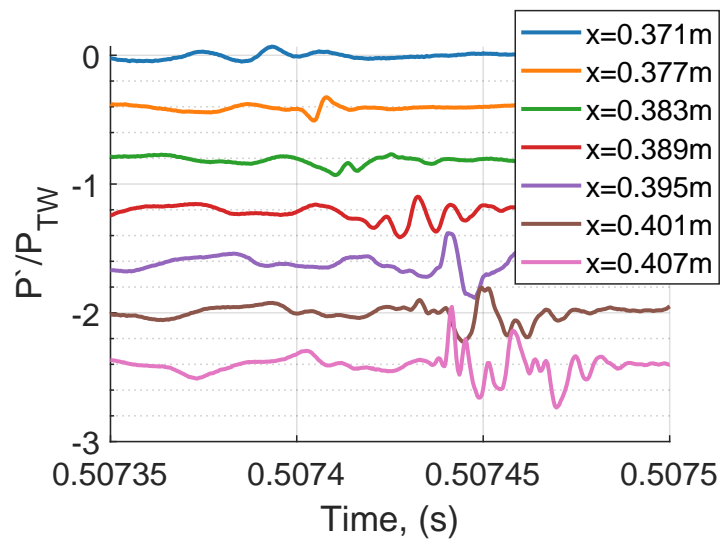
$$S(t) = \frac{(\Delta t)^2}{1 + \tau_s/\Delta t} \sum_{j=i+(\tau_s/2\Delta t)}^{j=i-(\tau_s/2\Delta t)} \omega_j D(j\Delta t) \quad (5.3)$$

$$\omega = \exp \left[ - \left( \frac{.625}{\tau_s/\Delta t} \right) |j - i| \right] \quad (5.4)$$

Results of the spot tracking were scrutinized for non-physical results. In this case, the final two sensors in Figure 5.21(b) show upstream movement of the spot. This

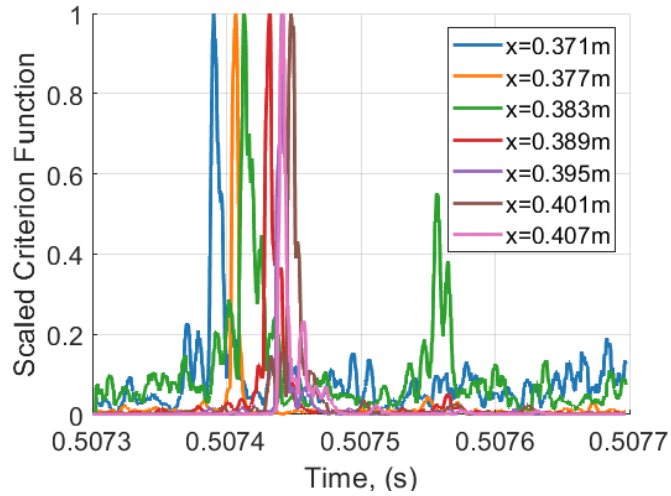


(a) Time trace of PCB at  $x = 0.407$  m. The box highlights the turbulent spot of interest.

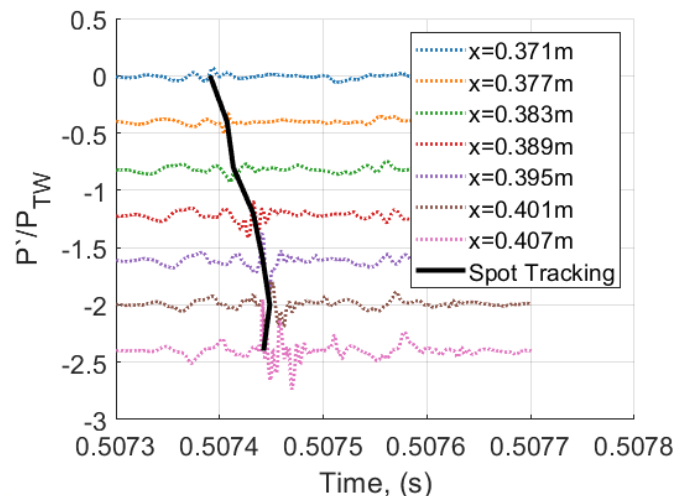


(b) Waterfall plot of the times inside the boxed region.

Figure 5.20. Behavior of a single turbulent spot from various sensors on the ramp centerline at  $Re = 2.5 \times 10^6/m$  (Run 2312).



(a) Scaled correlation function for each sensor.



(b) Waterfall plot of pressure traces with the spot tracking overlaid.

Figure 5.21. Turbulent spot tracking on a single spot at  $Re = 2.5 \times 10^6/m$  (Run 2312).

could be due to spots naturally spreading and adjacent spots, perturbations merging or problems with the algorithm. When this occurred, the velocity from those sensors was not used in determining the average spot velocity. Average convection velocities were calculated by taking the velocities of individual spots between every sensor for five individual spots at a single  $Re_\infty$  and averaging them. Convection velocities and standard deviations normalized by isentropic freestream velocity for two Reynolds numbers are shown in Table 5.1. Lower Reynolds numbers were not used due to the lack of spots and higher Reynolds were not used due to an overabundance of spots merging and moving together.

Table 5.1. Post-reattachment turbulent spot convection velocities at various  $Re$ .

$Re_\infty$	Average Convection Velocity ( $\frac{u_{spot}}{u_\infty}$ )	Standard Deviation ( $\frac{u_{spot}}{u_\infty}$ )
$2.5 \times 10^6 / m$	73.7	0.08
$3.0 \times 10^6 / m$	74.9	0.07

Single turbulent spots were processed directly to determine if any coherent waves were present within the spot before becoming turbulent. Figure 5.22 shows the locations of the sensors with respect to the IR heat transfer. Figure 5.23 shows a closeup of a wave packet or turbulent spot on three sensors from Figure 5.20. Time traces are seen in Figure 5.23(a). The first sensor shows fluctuations that look like a low-amplitude wave packet. At  $x=0.389$  m, the fluctuations have grown and still appear to be a coherent wave packet. At the farthest downstream sensor, the wave packet has more peaks at various time intervals. This is a sign that high frequency content has developed within the spot.

Scaled FFT's of these time traces are shown in Figure 5.23(b). The FFT was calculated and then scaled by

$$PSD = \frac{2|FFT|^2}{N \cdot S}, \quad (5.5)$$

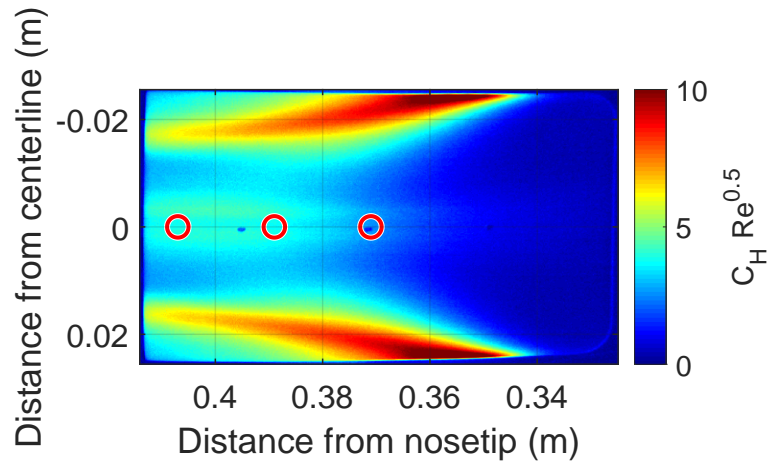


Figure 5.22. IR Stanton number of the ramp at  $Re_\infty=2.5\times 10^6/m$ . The red circles represent the relevant PCBs located on the ramp. Flow is from right to left.

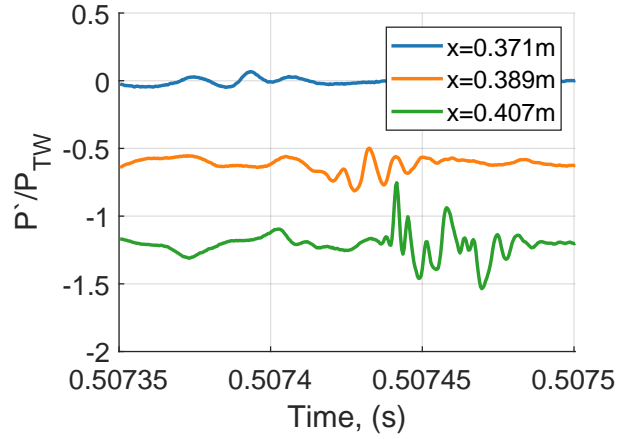
Where FFT is the discrete fast-fourier transform,  $N$  is the number of points in the sample, and  $S$  is the scaling factor for a Hamming window. This scaling produced an estimate of the PSD for this sensor [114]. At  $x = 0.371$  m, a small peak in frequency is seen at approximately 50 kHz. At  $x=0.389$  m, a large peak is present at 110 kHz. This corresponds to the wave packet that is seen in the time trace. The final location shows several peaks and frequency content extends out to much higher frequencies. The high-frequency content is due to small length scales within turbulence producing broadband spectral power. This is a sign that the spot is breaking down to turbulence.

Two other spots were analyzed to see if the waves were repeatable and to determine the effects of Reynolds number on the wave structures. Figure 5.24 shows the time traces and scaled FFTs for these two cases. Figures 5.24(a) and 5.24(b) show a spot at  $Re_\infty=2.2\times 10^6/m$ . This is slightly lower than the previous Reynolds number. The time traces show small wave packets that grow in amplitude and duration with increasing streamwise distance. No obvious breakdown of the waves is seen. This

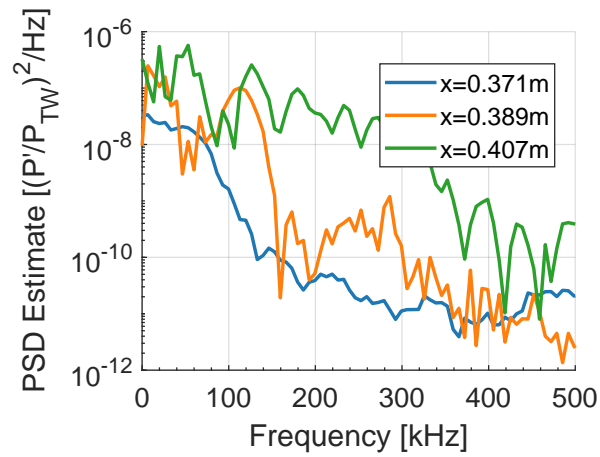
can be confirmed by analyzing the FFTs shown in Figure 5.24(b). A 3-point moving average filter was applied to the FFTs to reduce spikiness and improve readability. No frequency content above 200 kHz was seen for any sensor. This agrees with the observation that the packet has not begun to break down to turbulence. At  $x=0.407$  m, a possible broad peak can be seen from 50-105 kHz. This is a lower frequency than in Figure 5.23. The small change in Reynolds number appears to have altered which frequencies are amplified.

Figures 5.24(c) and 5.24(d) show the same two plots for a different spot at a unit Reynolds number of  $2.5 \times 10^6/\text{m}$ . This spot occurred 0.001 s before the one seen in Figure 5.23 and is approximately at the same  $Re_\infty$ . At  $x = 0.371$  m, the spot is larger in amplitude than in Figure 5.23. Consequently, the development of high-frequency content appears much sooner in this spot. This is confirmed in the FFTs in Figure 5.24(d). The two downstream sensors show a broadband increase in frequency content. At  $x = 0.371$  m, a broad peak is present between 50 and 170 kHz. This range encompasses the peak seen in 5.23, but more frequencies are present. The differences in wave packets that are close together in the same run is likely due to the flow field being hyper-sensitive to various factors, such as surface temperature, separation bubble dynamics, or the initial disturbances that developed into the packet. The wave packets and spots appear to be generated within the shear layer and reattach to the surface at various amounts of amplification and stages of breakdown. Measuring fluctuations at repeatable frequencies is difficult.

Figure 5.25 shows the behavior of sample wave packets and turbulent spots as the unit Reynolds number increases. Figures 5.25(a) and 5.25(b) show the behavior of an individual spot at  $Re_\infty = 3.0 \times 10^6/\text{m}$ . The behavior is similar to the previously shown cases. The first sensor shows a wave packet with frequency content below 200 kHz. At  $x = 0.389$  m downstream, higher frequency content has begun to develop and a small peak can be seen at 112 kHz. This is similar to a previous case but much more high frequency content exists at this higher Reynolds number. This wave packet then rapidly breaks down to turbulence with downstream distance and high frequency

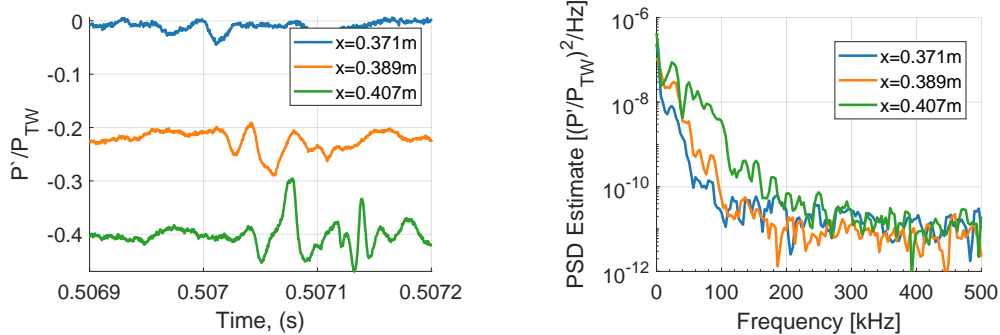


(a) Waterfall plot of three individual sensors.

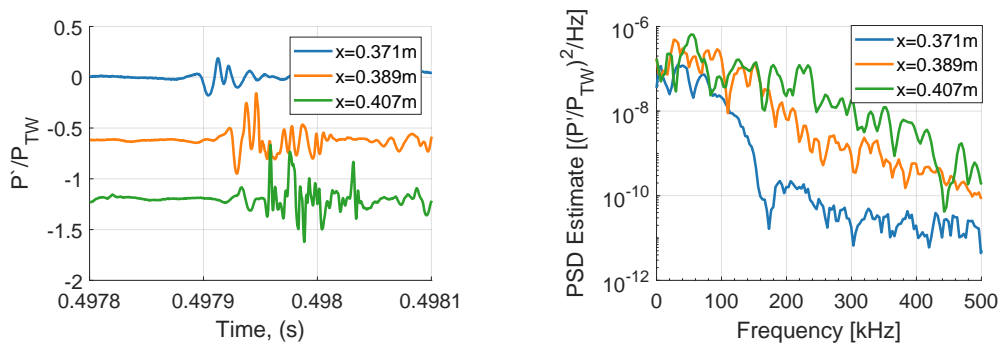


(b) Scaled FFT of the time traces for an individual spot at various sensor locations.

Figure 5.23. Behavior of a single turbulent spot from three sensors on the ramp centerline at  $Re = 2.5 \times 10^6/m$  (Run 2312).



(a) Waterfall plot of three individual sensors at  $\text{Re} = 2.2 \times 10^6/\text{m}$  (Run 2311). (b) Scaled FFT of the time traces for an individual spot at  $\text{Re} = 2.2 \times 10^6/\text{m}$  (Run 2311).

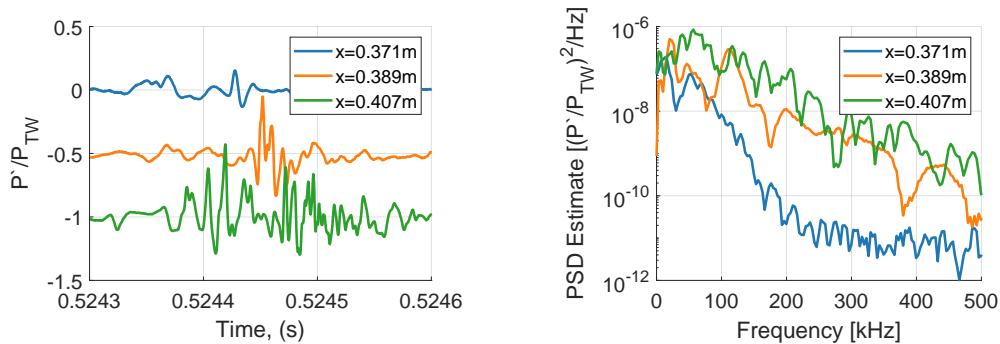


(c) Waterfall plot of three individual sensors at  $\text{Re} = 2.5 \times 10^6/\text{m}$  (Run 2312). (d) Scaled FFT of the time traces for an individual spot at  $\text{Re} = 2.5 \times 10^6/\text{m}$  (Run 2312).

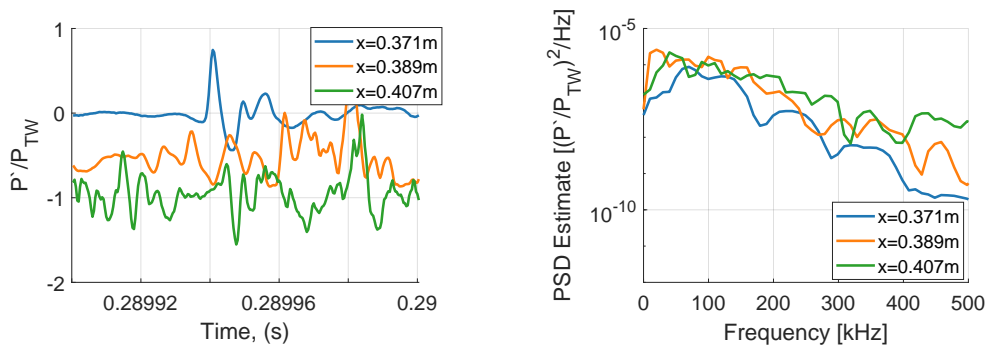
Figure 5.24. Behavior of a single turbulent spot from three sensors on the ramp centerline at various unit Reynolds number.

content is seen in the final FFT. Figures 5.25(c) and 5.25(d) show a slightly higher unit Reynolds number of  $3.4 \times 10^6/\text{m}$ . The farthest upstream time trace shows a large amplitude wave packet. However, the FFT of it shows broadband frequency content that is typically seen in turbulence. This suggests that it might have reattached in a state of break down. At farther downstream locations, the whole time trace has broken down to turbulence and similar broadband frequency content is seen in the FFTs. It appears that the wave packet that was measured at  $x = 0.371$  m downstream has already begun breaking down by this location and is not purely a wave packet. At these higher Reynolds numbers, the boundary layer after reattachment very quickly breaks down to turbulence. This break down occurs even without a clear wave packet upstream of the turbulent fluctuations.

Similar plots of turbulent spots were measured during an earlier entry on the cluster ramp. A comparison of spot behavior on a different ramp was made. Figure 5.26 shows the time traces and FFTs for four sensors downstream of reattachment at various unit Reynolds numbers. Figures 5.26(a) and 5.26(b) show a turbulent spot at  $\text{Re}_\infty = 2.6 \times 10^6/\text{m}$ . At  $x = 0.365$  m downstream, small fluctuations indicative of a low-amplitude wave packet are seen at  $t = 0.5324$  s. This wave packet grows and is clearly visible by the next sensor location. The FFTs of these first two sensors show frequency content at frequencies below 150-175 kHz. At farther downstream locations, the spot has begun to break down and high frequency content is seen in the FFTs. A spot at  $\text{Re}_\infty = 3.4 \times 10^6/\text{m}$  is seen in Figures 5.26(c) and 5.26(d). A wave packet is seen at the farthest upstream sensor. The FFTs again show frequency content below 200 kHz. This is similar to the previously measured wave packets. The wave packet grows and becomes more chaotic by  $x = 0.377$  m downstream. The FFT shows some higher frequency content developing at this location. By the final two locations the wave packet, and the time before and after it, have broken down to turbulence. Figures 5.26(e) and 5.26(f) show data from a much higher Reynolds number. In this case the boundary has fully transitioned off-surface. The pressure fluctuations at every sensor location are turbulent and the FFTs show broadband frequency content.



(a) Waterfall plot of three individual sensors at  $\text{Re} = 3.0 \times 10^6/\text{m}$  (Run 2313). (b) Scaled FFT of the time traces for an individual spot at  $\text{Re} = 3.0 \times 10^6/\text{m}$  (Run 2313).



(c) Waterfall plot of three individual sensors at  $\text{Re} = 3.4 \times 10^6/\text{m}$  (Run 2314). (d) Scaled FFT of the time traces for an individual spot at  $\text{Re} = 3.4 \times 10^6/\text{m}$  (Run 2314).

Figure 5.25. Behavior of a single turbulent spot from three sensors on the ramp centerline at various unit Reynolds number.

From the sample cases shown, it can be concluded that wave packets exist with frequency content below 200 kHz during the transition of the post-reattachment boundary layer. It is believed that these wave packets are generated off-surface within the shear layer and then reattach to the ramp and breakdown. As the Reynolds number increased, the wave packets reattached with higher frequency content and could be possible turbulent spots. This suggests that transition could occur entirely within the shear layer above separation. At higher Reynolds numbers, the post-reattachment boundary layer rapidly transitioned to turbulence irrespective of a wave packet existing upstream. If the Reynolds number was high enough, a fully turbulent boundary reattached onto the ramp.

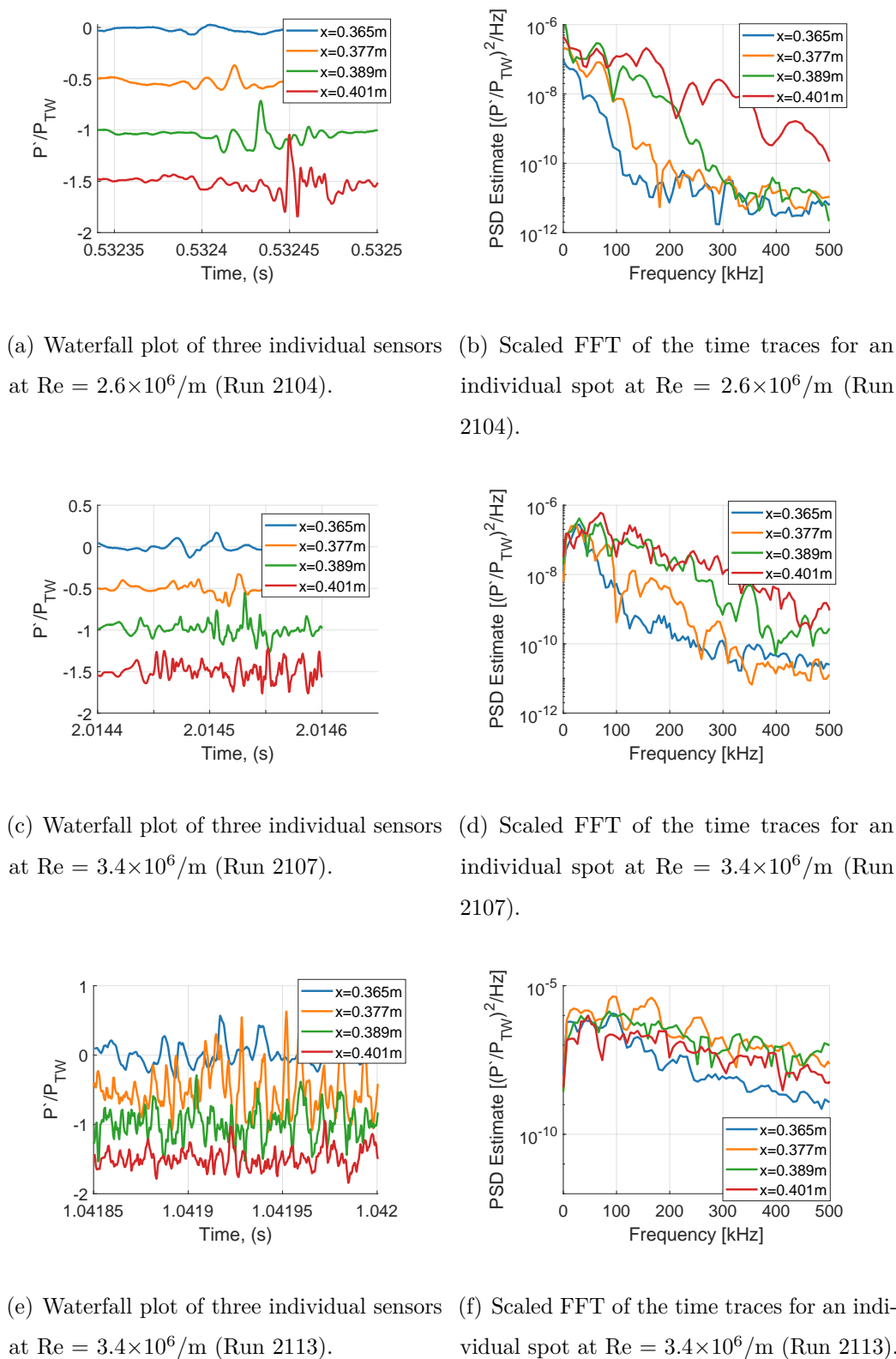


Figure 5.26. Behavior of single turbulent spots from post-reattachment centerline sensors at various unit Reynolds number.

### 5.3.1 Post-reattachment Pressure Fluctuation Repeatability

The repeatability of the post-reattachment boundary-layer pressure fluctuations was investigated during the course of this research. Data were taken over four entries with properly zeroed AoA and yaw. Data from the numerous ramps outlined in Section 4.2 were collected and comparisons of discrete pressure fluctuations were made. The ramps had some pressure sensors at common locations and numerous runs were performed at similar Reynolds numbers. This allowed the calculation of run-to-run and entry-to-entry repeatability for several ramps. This section calculated the frequency content using PSDs. This technique averages numerous FFTs to determine which frequencies contain the power in a signal. If consistent instability growth is present within the shear layer at a given time, the averages should reflect this.

Two post-reattachment sensor locations were analyzed at various unit Reynolds numbers to determine if transition was repeatable on the ramp. Figure 5.27 shows the location of the two sensors on a representative plot of Stanton number. Several ramps had sensors in these locations and comparisons of results from varying sensors could be made. Several different PCB sensors and Kulites were compared.

Spectra were analyzed during a sweep of Reynolds numbers that included laminar, transitional, and turbulent flow. Figure 5.28 shows the spectra gathered from numerous runs at a single location over three tunnel entries. At  $Re_\infty \approx 2.0 \times 10^6/m$  the boundary layer is laminar and very few features are seen in the PSD. The PCB data does not exceed the electrical noise. The Kulite spectra is the brown line and features a different noise floor but shows a featureless spectra without instability growth. At this  $Re$ , the spectra repeatably have no fluctuations that exceed the sensor noise floor.

Figure 5.28(b) shows data at  $Re_\infty \approx 2.5 \times 10^6/m$  and represents a transitional boundary-layer. This data were taken over several runs during three entries. The transitional spectra at  $x = 0.395$  m vary between every measured case. Even data taken over three runs on the same entry and sensor, Runs 2312, 2319, and 2336, show differences. Kulite spectra show slightly different broadband power and have a sensor

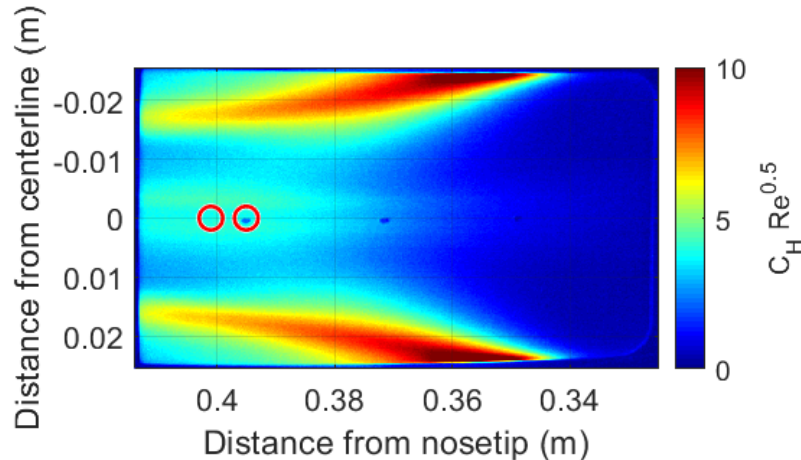


Figure 5.27. IR heat transfer of the ramp at  $Re_\infty=2.5 \times 10^6/m$ . The red dots represent the two sensors located downstream of separation on the ramp (Run 2013).

resonance at 300 kHz. Data from Run 1006 showed much higher power levels than any other run. This was seen on every sensor for that entry and the reason is not known. The transitional boundary layer PSD are not very repeatable. Care was taken to ensure that the PSDs were calculated at similar Reynolds numbers. Based on the time series, the post-reattachment transition process was dominated by wave packets and turbulent spots that are generated within the shear layer and reattachment region. The factors that control generation and growth of these spots are not well-understood and cause issues with averaged spectral repeatability.

Figure 5.28(c) shows numerous PSDs for a slightly higher Reynolds number. The spectra indicate a transitional or turbulent boundary layer. Variations in broadband power levels exist between entries and runs but every case shows a widespread increase in spectral power from the laminar case in Figure 5.28(a). Other than the labeled Kulite resonance, no discrete peaks are seen in the PSD.

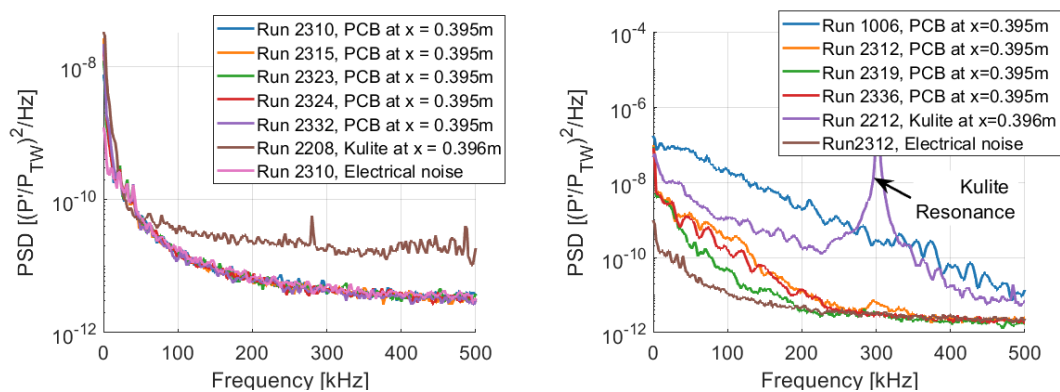
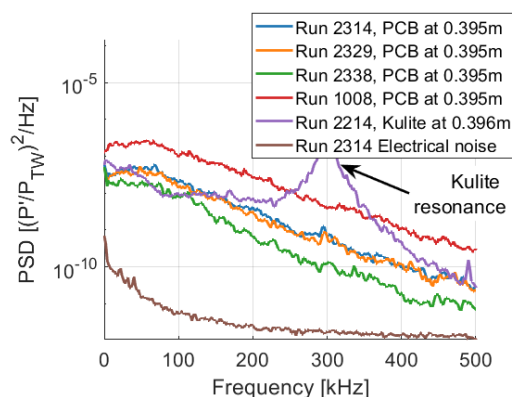
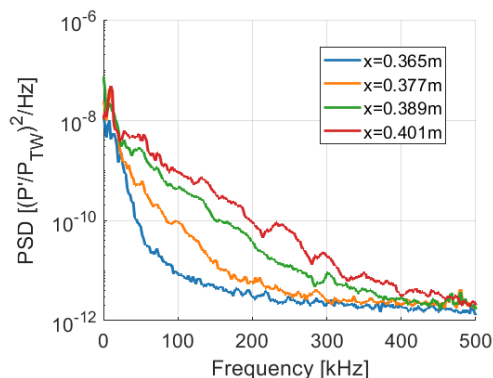
(a)  $Re_\infty \approx 2.0 \times 10^6/m$ .(b)  $Re_\infty \approx 2.5 \times 10^6/m$ .(c)  $Re_\infty \approx 3.3 \times 10^6/m$ .

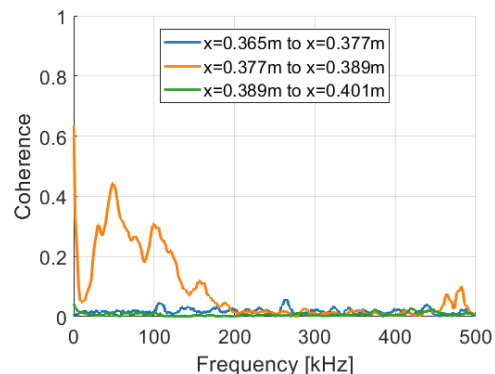
Figure 5.28. Repeatability of spectra for multiple runs at various unit Reynolds numbers.

The repeatability was investigated further by plotting the development of transitional pressure spectra with post-reattachment streamwise distance. Figure 5.29 shows the progression of transitional PSDs for three different ramps and sensor configurations. Every case was taken at  $Re_\infty = 2.5 \times 10^6 / m$ . Figures 5.29(a) and 5.29(b) show PSDs and coherences for centerline PCBs on the cluster ramp. Broadband power is increasing with streamwise distance but no peaks that could be instabilities are present. Some coherence is present but without corresponding spectral peaks, few conclusions can be drawn. A similar plot for Kulites at different post-reattachment locations can be seen in Figures 5.29(c) and 5.29(d). No distinct peaks are present in the PSDs but larger coherences were measured at various frequencies. The exact reason for this is not known but it could be indicative of low-amplitude waves at common frequencies. If they are weak, compared to the random turbulent spot fluctuations, they might produce coherence without clear spectral evidence. Lastly, data from the perturber ramp is plotted in Figures 5.29(e) and 5.29(f). Sensor spacing on this ramp was half of that on the Kulite and cluster ramps. Small peaks are present at several frequencies in the PSDs and strong coherences are present at several frequencies. A discussion of this behavior is given in Section 5.3.2. However, it serves to show how different the transitional PSDs are for all tested ramps. The transitional pressure spectra must be sensitive to factors that vary slightly between entries and runs. It is possible that surface temperature or small fluctuations above the separation bubble exist and affect transition. The wave packets present within the time series of the pressure fluctuations do not appear to have power present at a narrow band of frequencies or are not strong enough to appear within the averaged signal.

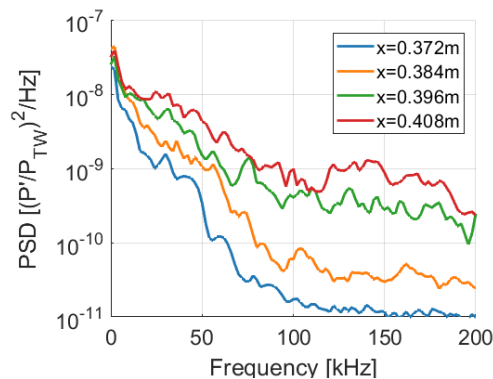
An investigation of the repeatability of the pressure fluctuation magnitudes was completed to determine if the transition Reynolds number was repeatable for the long-ramp geometry. Figure 5.30 shows the pressure fluctuation magnitudes for two downstream locations for several tunnel entries. Every entry had a different ramp and different sensors for the measurements. Magnitudes for the sensors 0.395 m downstream of the nosetip can be seen in Figure 5.30(a) and magnitudes for a sensor



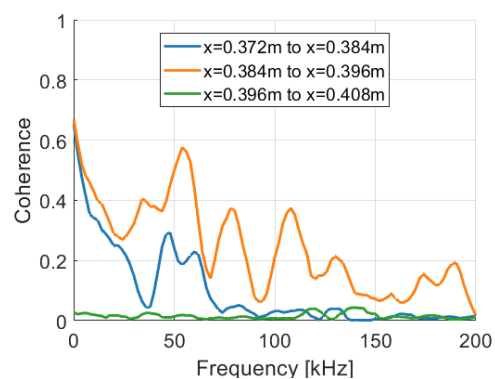
(a) PSDs on the cluster ramp at  $Re_\infty = 2.5 \times 10^6/m$  (Run 2104).



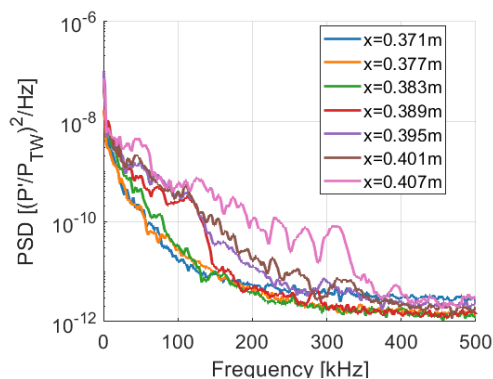
(b) Coherences on the cluster ramp at  $Re_\infty = 2.5 \times 10^6/m$  (Run 2104).



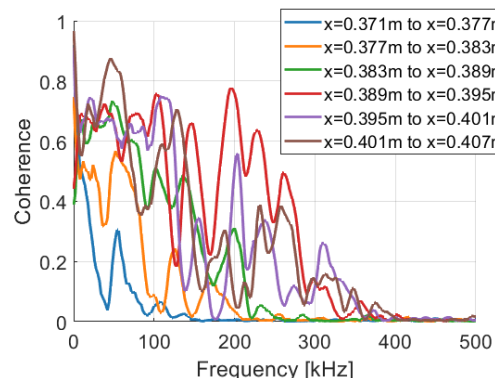
(c) PSDs on the Kulite ramp at  $Re_\infty = 2.5 \times 10^6/m$  (Run 2212).



(d) Coherences on the Kulite ramp at  $Re_\infty = 2.5 \times 10^6/m$  (Run 2212).



(e) PSDs on the perturber ramp at  $Re_\infty = 2.5 \times 10^6/m$  (Run 2312).



(f) Coherences on the perturber ramp at  $Re_\infty = 2.5 \times 10^6/m$  (Run 2312).

Figure 5.29. PSDs of pressure sensors downstream of reattachment under quiet flow on various ramps.

6 mm farther downstream can be found in Figure 5.30(b). The data is also shown on a log-linear plot in Figures 5.30(c) and 5.30(d). This plot will highlight the lower Reynolds number data and determine if the fluctuations are growing exponentially. Unit Reynolds numbers of less than  $2.4 \times 10^6/\text{m}$  produced SBLI that were entirely laminar and, according to pressure fluctuation data, the boundary layer remained laminar until the end of the model. As the Reynolds number increased, turbulent spots began to emerge and the pressure fluctuation magnitudes began to increase. This is interpreted as transition onset for the post-reattachment boundary layer. For all tested ramps and models, this occurred at approximately  $\text{Re}_\infty = 2.4 \times 10^6/\text{m}$  at  $x = 0.395$  m and  $\text{Re}_\infty = 2.2 \times 10^6/\text{m}$  at  $x = 0.401$  m. Both of these values indicate a transition Reynolds number based on freestream conditions and axial distance from the nosetip of  $0.9 \times 10^6$ . This data includes measurements made on both PCB and Kulite pressure transducers. The increase in magnitudes is clearer on the log-linear plots. The laminar fluctuations are approximately constant at small unit Reynolds numbers. After transition begins, the magnitudes increase exponentially during the transition process. At  $x = 0.401$  m, data from Entry 10 and the spanwise ramp exhibited larger pressure fluctuations at every location. However, this was the case for every sensor and run during this entry. These differences could be a result of small differences in AoA and yaw, or small errors in the ramp edge. Even with the higher amplitude fluctuations, transition location did not change.

Data show that the transition of the post-reattachment boundary layer occurs at a consistent Reynolds number on the model. It appears that while entry-to-entry and run-to-run repeatability of transitional PSDs are not consistent; the transition location based on an increase in pressure fluctuation magnitudes is repeatable. Both of these findings could be due to the appearance of turbulent spots without significant instability growth post-reattachment. The cause of turbulent spots was not apparent but caused PSD variations at similar Reynolds number.

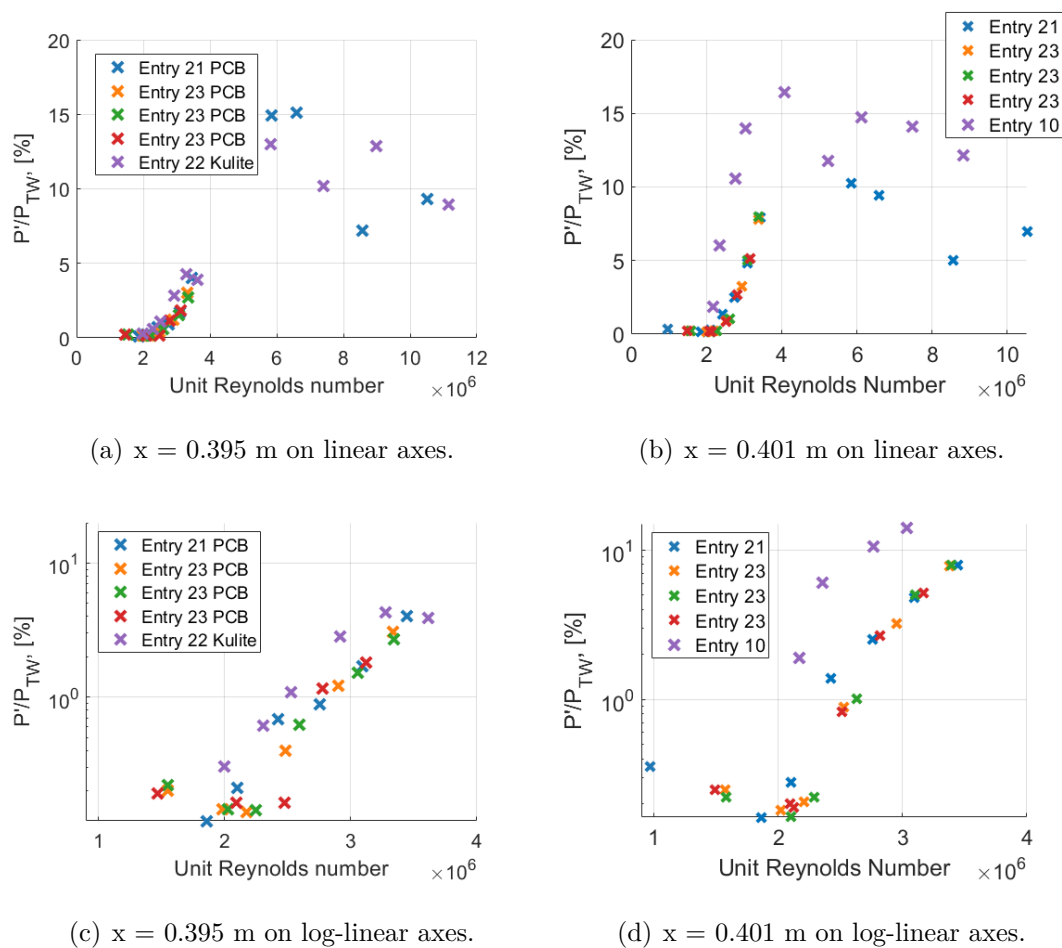


Figure 5.30. Repeatability of magnitudes with unit Reynolds number for multiple runs.

### 5.3.2 Effect of Reynolds Number on Post-reattachment Pressure Fluctuation Spectra

An investigation into the effects of Reynolds number on the boundary layer was completed with several ramps in quiet flow. If any traveling instabilities grow within the shear layer, adjusting the Reynolds number should affect their amplitudes and frequencies post-reattachment. This can then be seen in the measured surface pressure fluctuations.

Figure 5.31 shows the streamwise spectral progression of pressure fluctuations on the perturber ramp. This ramp had twice as many post-reattachment sensors as the other  $20^\circ$  long ramps. At  $Re_\infty = 2.0 \times 10^6/m$ , there is no frequency content or coherence between any of the ramp sensors. Increasing the Reynolds number to  $Re_\infty = 2.5 \times 10^6/m$  yields small peaks at numerous frequencies in the power spectra. This was seen in the previous sub-section. Coherences show significant values between several sensors at various frequencies. This behavior is likely due to the presence of wave packets within the boundary layer after reattachment. At  $Re_\infty = 3.4 \times 10^6/m$ , no peaks are present and a broadband increase in spectral power is seen. Coherence exists at frequencies below 100 kHz and the flow is considered transitional or turbulent.

A close look at the  $Re_\infty = 2.5 \times 10^6/m$  case was made due to the possible traveling waves that could be present. The data presented in Figure 5.31(c) and 5.31(b) was separated into multiple plots in Figure 5.32 to help clarify the behavior of the spectra. The first two sensors in Figure 5.32(a) show no amplification in power and little coherence between them. An increase in power is seen at frequencies below 100 kHz by  $x = 0.383$  m from the nosetip. An increase in coherence is seen at these low frequencies. A closer look at this behavior can be seen in Figure 5.32(e). The amplitudes within that low-frequency band remain flat for the first two sensors and then grow with distance downstream. A peak can be seen on the last sensor at 110 kHz but little coherence is seen at that frequency. Instead, large coherence is seen at frequencies below 110 kHz. This plot used the same time trace as Figure 5.23 and the 110 kHz

peak is similar to the one seen in the FFT of an individual wave packet. The four farthest downstream sensors can be seen in Figures 5.32(c) and 5.32(d). Several small peaks can be seen at various frequencies and no trend or consistent location of peaks can be seen. Coherences are similarly scattered with significant values occurring at many frequencies and could be due to the spots and waves that are being created within the shear layer. The peak at 110 kHz is still present at these locations and coherences are high at that frequency. The wave packets at those frequencies appear to be traveling at these locations on the ramp. It appears that many possible instabilities or waves are growing and cohering post-reattachment but no clear trend was seen in their behavior. While wave packets precede turbulent spots at several times during the run, there is no clear and consistent pattern of a traveling instability within a narrow frequency-band that is amplifying and breaking down.

To better understand the behavior of the transitional post-reattachment boundary layer, power spectra at small intervals of Reynolds numbers were taken during a single run and plotted in Figure 5.33(a). The corresponding time traces that were used to generate the PSDs were also plotted. The lowest Reynolds number in Figure 5.33(a) has spectral power below 200 kHz with small peaks present at several frequencies. The corresponding time trace is seen in Figure 5.33(b) and has two spots that could be wave packets or turbulent spots. The insets on the plots of the time traces show close ups of these features. The left inset shows a turbulent spot present and the right inset shows a wave packet. The time trace shows similar behavior to the previously shown cases where turbulent spots and wave packets appear to be sensitive to factors not controlled in these experiments. The  $Re_\infty = 2.43 \times 10^6/m$  PSD has little frequency content and the corresponding time trace show some small amplitude fluctuations. The inset show small wave packets present at a couple locations. This case has less spectral power and fewer spots than the previous case at a lower Re. This is the only case where this was seen and is not typical on average. However, it shows that the transitional spectra is dependent on the presence of wave packets and turbulent spots. Increasing the Reynolds number to  $Re_\infty = 2.47 \times 10^6/m$  and  $Re_\infty = 2.50 \times 10^6/m$  increases the power

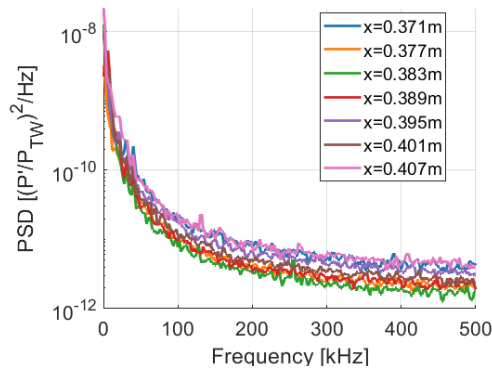
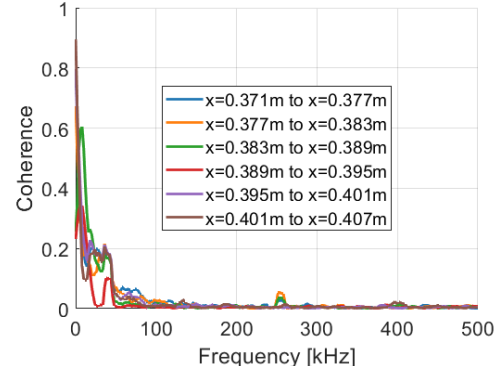
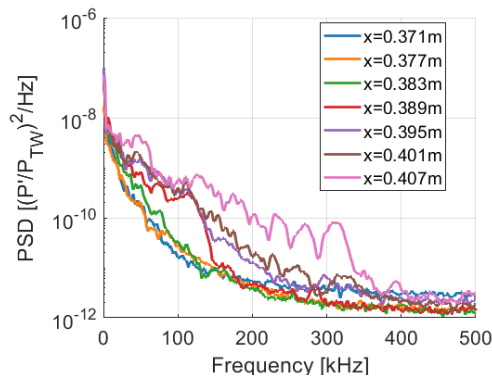
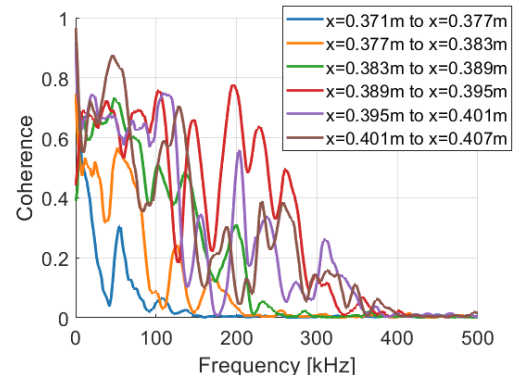
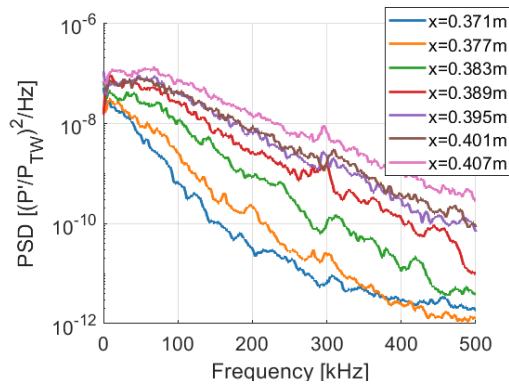
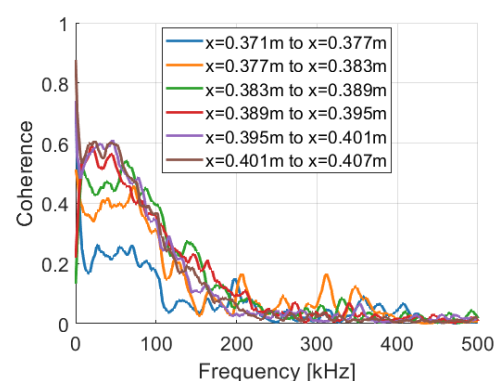
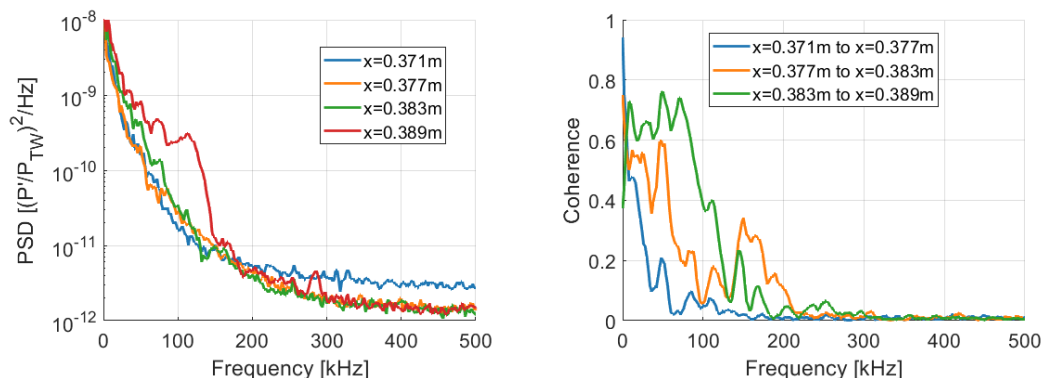
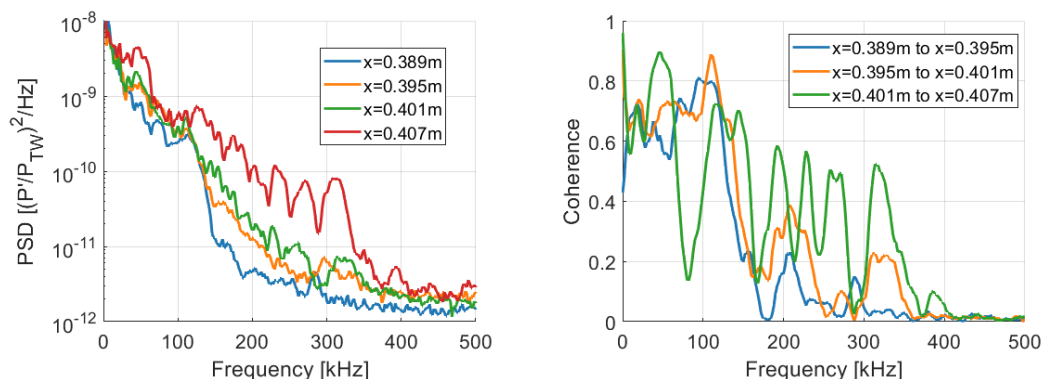
(a)  $Re_\infty = 2.0 \times 10^6/m$  PSD (Run 2310).(b)  $Re_\infty = 2.0 \times 10^6/m$  coherence (Run 2310).(c)  $Re_\infty = 2.5 \times 10^6/m$  PSD (Run 2312).(d)  $Re_\infty = 2.5 \times 10^6/m$  coherence (Run 2312).(e)  $Re_\infty = 3.4 \times 10^6/m$  PSD (Run 2314).(f)  $Re_\infty = 3.4 \times 10^6/m$  coherence (Run 2314).

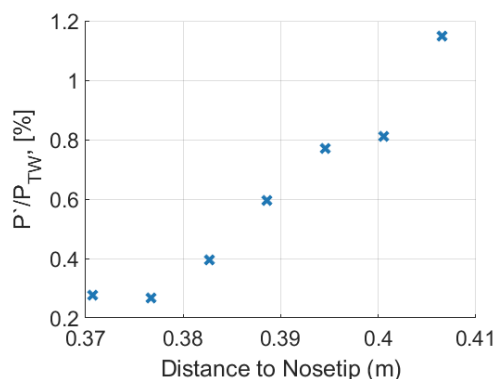
Figure 5.31. PSDs of PCBs downstream of reattachment under quiet flow at various  $Re_\infty$ .



(a) PSDs of four sensors immediately after reattachment. (b) Coherences four sensors immediately after reattachment for a single run.



(c) PSDs of last four sensors. (d) Coherences of last four sensors.

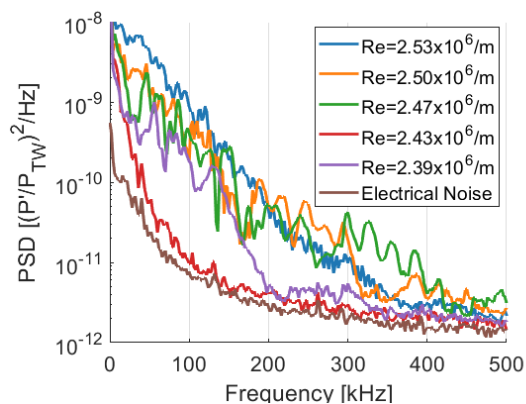


(e) Amplitudes of pressure fluctuations within a 30-80 kHz frequency band.

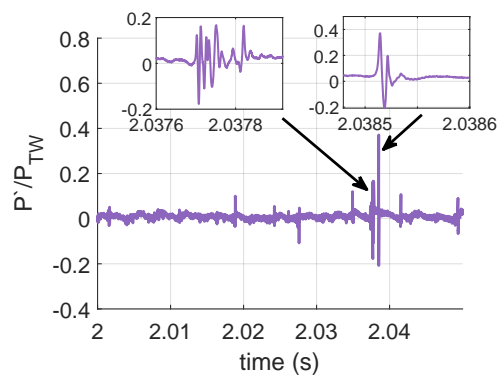
Figure 5.32. PSD of PCBs downstream of reattachment on the perturber ramp without perturbations at  $Re_\infty = 2.5 \times 10^6/\text{m}$  (Run 2312).

present in the PSD and small peaks develop at many frequencies. The time traces for these Reynolds numbers show more turbulent spots and wave packets at higher amplitudes. The insets for both of these Reynolds numbers show large wave packets or turbulent spots. The peaks for each Reynolds number do not occur at the same frequencies. It is believed that the averaged spectra in the PSD is dependent on the frequency and size of wave packets or turbulent spots. Furthermore, control of the wave packets and spots was not achieved and narrow bandwidth instabilities do not develop. It appears that contributions from coherent wave packets are not significant enough to reliably appear as peaks in the power spectra. Additionally, the appearance of large wave packets at random intervals during the time trace could promote a broadband spectra. The  $Re_\infty = 2.53 \times 10^6/m$  PSD has broadband power without distinctive peaks and a time trace of frequent large turbulent spots. Samples of these can be seen in the insets. Pressure fluctuations at these five Reynolds numbers have transitional spectra and no clear evidence of a traveling instability. Additionally, the coherences and small peaks appear to be related to individual waves and turbulent spots that contain various periodic fluctuations. The mechanism that is generating these spots and waves is not known but contributions from an individual traveling instability were not clearly seen.

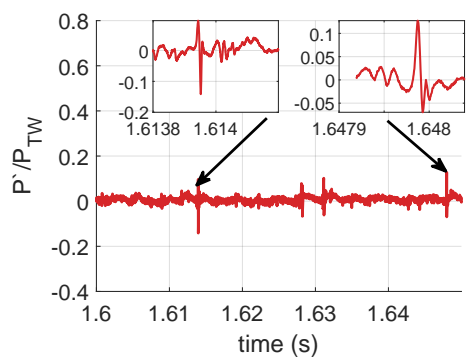
To confirm the PCB results, the downstream spectral progression of the pressure fluctuations was calculated on the same geometry with a different ramp instrumented with Kulite sensors. Figure 5.34 shows PSDs and coherences for post-reattachment Kulites at various unit Reynolds numbers that encompass transition. Spectral behavior is similar to the PCBs with laminar and turbulent spectra at the  $Re_\infty = 2.0 \times 10^6/m$  and  $Re_\infty = 3.3 \times 10^6/m$ , respectively. The  $Re_\infty = 2.5 \times 10^6/m$  case again shows a rise in low frequency power with distinct coherence peaks at various frequencies. This behavior is similar to the PCBs and supports the belief that the transitional behavior is related to the presence of wave packets that precede turbulent spots. These wave packets are indicative of an instability being present within the shear layer or reattached boundary layer. However, clear evidence of the instability does not show up within the power



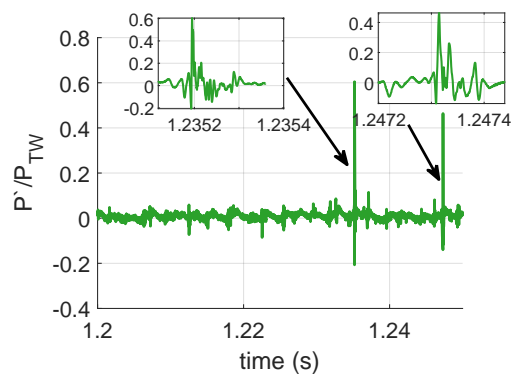
(a) PSDs at various times of a single run (Run 2312).



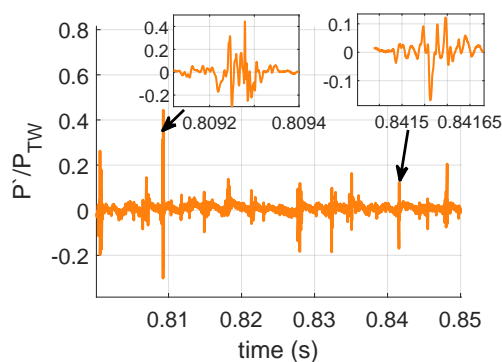
(b)  $Re_\infty = 2.39 \times 10^6 / m$ .



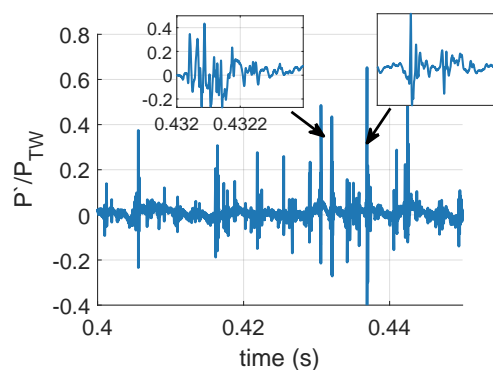
(c)  $Re_\infty = 2.43 \times 10^6 / m$ .



(d)  $Re_\infty = 2.47 \times 10^6 / m$ .



(e)  $Re_\infty = 2.50 \times 10^6 / m$ .



(f)  $Re_\infty = 2.53 \times 10^6 / m$ .

Figure 5.33. PSD of PCB at  $x = 0.407$  m downstream at small changes of unit Reynolds number. The time traces that were processed for each PSD are included.

spectra. It appears that the wave packets and spots are generated within the shear layer and are reattaching to the surface.

Since coherences were present for some of the cases, an attempt at calculating convection velocities based on the cross-correlation was made. Table 5.2 shows the results for both the detector function velocities and the cross-correlation velocities. The cross-correlation based convection velocities were slightly higher and had smaller standard deviations than the detector function velocities. The cross-correlation measurement is less susceptible to user-defined thresholds, like the detector function, and is believed to be a more accurate result.

Table 5.2. Post-reattachment turbulent spot convection velocities at various  $Re$  and calculation methods.

$Re_\infty$	Method	Average Convection Velocity ( $\frac{u_{spot}}{u_\infty}$ )	Standard Deviation ( $\frac{u_{spot}}{u_\infty}$ )
$2.5 \times 10^6/m$	Detector function	73.7	0.08
$3.0 \times 10^6/m$	Detector function	74.9	0.07
$2.5 \times 10^6/m$	Cross-correlation	81.3	0.03
$3.0 \times 10^6/m$	Cross-correlation	83.1	0.02

A closer look at the development of power spectra at individual locations with unit Reynolds number was made. Several common locations on the cluster ramp and Kulite ramp were investigated. Figure 5.35 shows a representative heat transfer plot with relevant sensor locations annotated. Three PSDs at three downstream locations for the PCBs and Kulites can be found in Figure 5.36. PSDs at  $x=0.383$  m show spectra that are near the sensor noise floor until  $Re_\infty \approx 2.4 \times 10^6/m$ . Above this, an increase in broadband power begins at lower frequencies and extends to higher frequencies as  $Re_\infty$  increases. Possible small peaks occur at 250-300 kHz on the PCB and 105 kHz on the Kulites. These peaks are small and hard to distinguish from the surrounding PSD power. Figures 5.36(c) and 5.36(d) show PSDs slightly

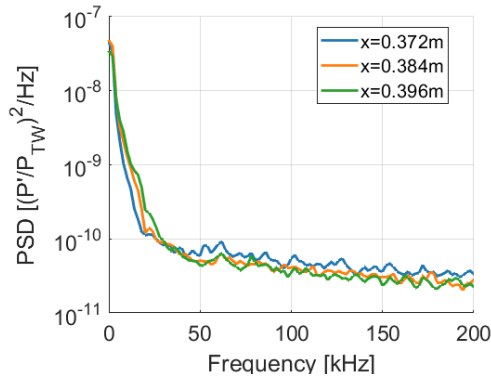
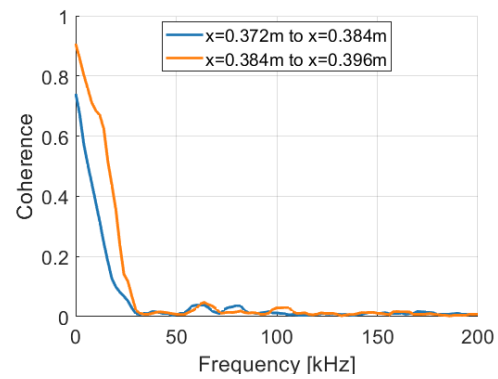
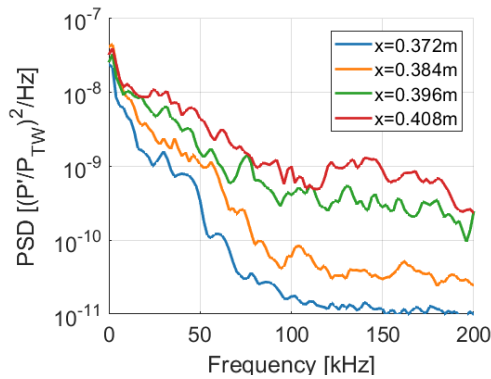
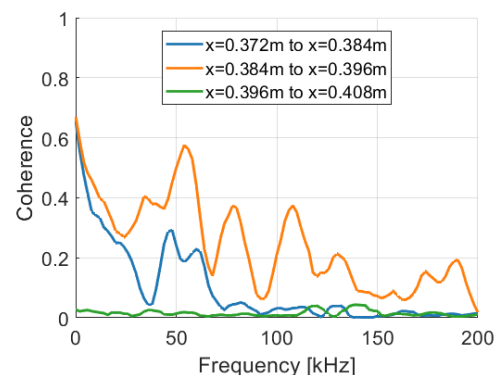
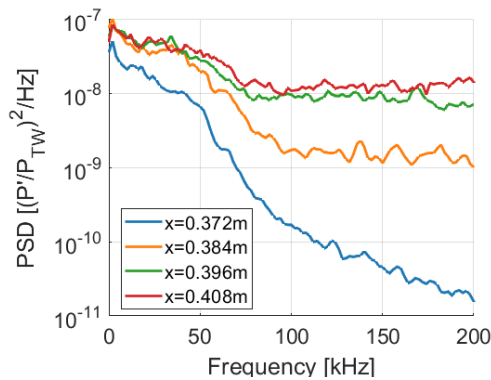
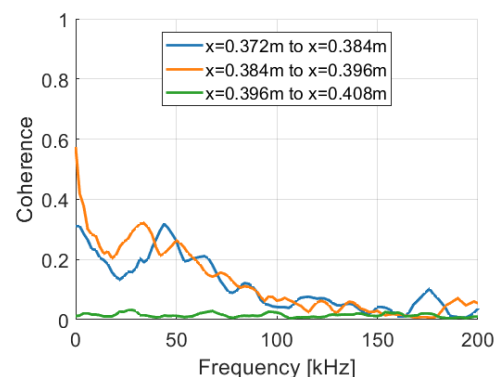
(a)  $Re_\infty = 2.0 \times 10^6/m$  PSD (Run 2208).(b)  $Re_\infty = 2.0 \times 10^6/m$  coherence (Run 2208).(c)  $Re_\infty = 2.5 \times 10^6/m$  PSD (Run 2212).(d)  $Re_\infty = 2.5 \times 10^6/m$  coherence (Run 2212).(e)  $Re_\infty = 3.3 \times 10^6/m$  PSD (Run 2214).(f)  $Re_\infty = 3.3 \times 10^6/m$  coherence (Run 2214).

Figure 5.34. PSDs of Kulites downstream of reattachment under quiet flow at various  $Re_\infty$ .

farther downstream at  $x = 0.395$  m. PSDs at this location do not show any peaks or spectral behavior that could be indicative of boundary layer instability. It does not appear that any frequency content from the upstream sensors have grown or amplified while traveling downstream. PSDs of the farthest downstream sensors can be seen in Figures 5.36(e) and 5.36(f). PCB results show possible peaks in power at numerous frequencies at  $Re_\infty = 2.6 \times 10^6/m$ . None of the peaks are exceedingly distinct from the surrounding spectral power and they are not seen at the higher or lower Reynolds numbers. Additionally, they are not seen on the comparable Kulite sensor. Much like the previous discussions, the wave packets and turbulent spots within the post-reattachment boundary layer indicate the presence of instability but do not produce consistent narrow-bandwidth frequency content in the PSD.

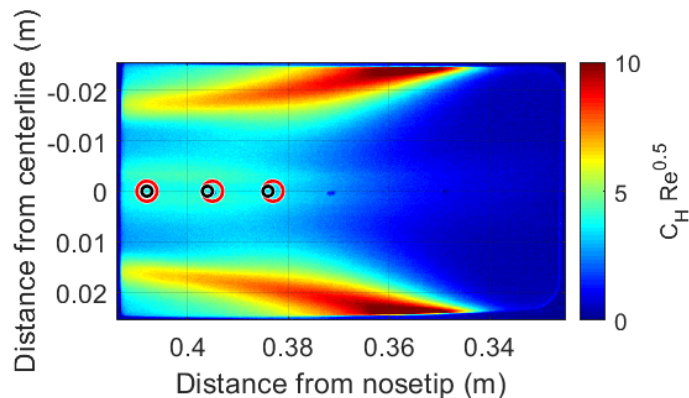


Figure 5.35. IR heat transfer of the ramp at  $Re_\infty = 2.5 \times 10^6/m$  (Run 2013). The red circles represent the PCB sensors and the black circles represent Kulite sensors.

The effects of varying Reynolds number on the fluctuation magnitudes was investigated for several ramps and sensor types. Figure 5.37(a) shows the natural fluctuation behavior for the perturber ramp. It is plotted as Reynolds number varies and the Reynolds number is based on the sensors axial distance from the nosetip and freestream conditions. The colors represent individual runs and each point is a

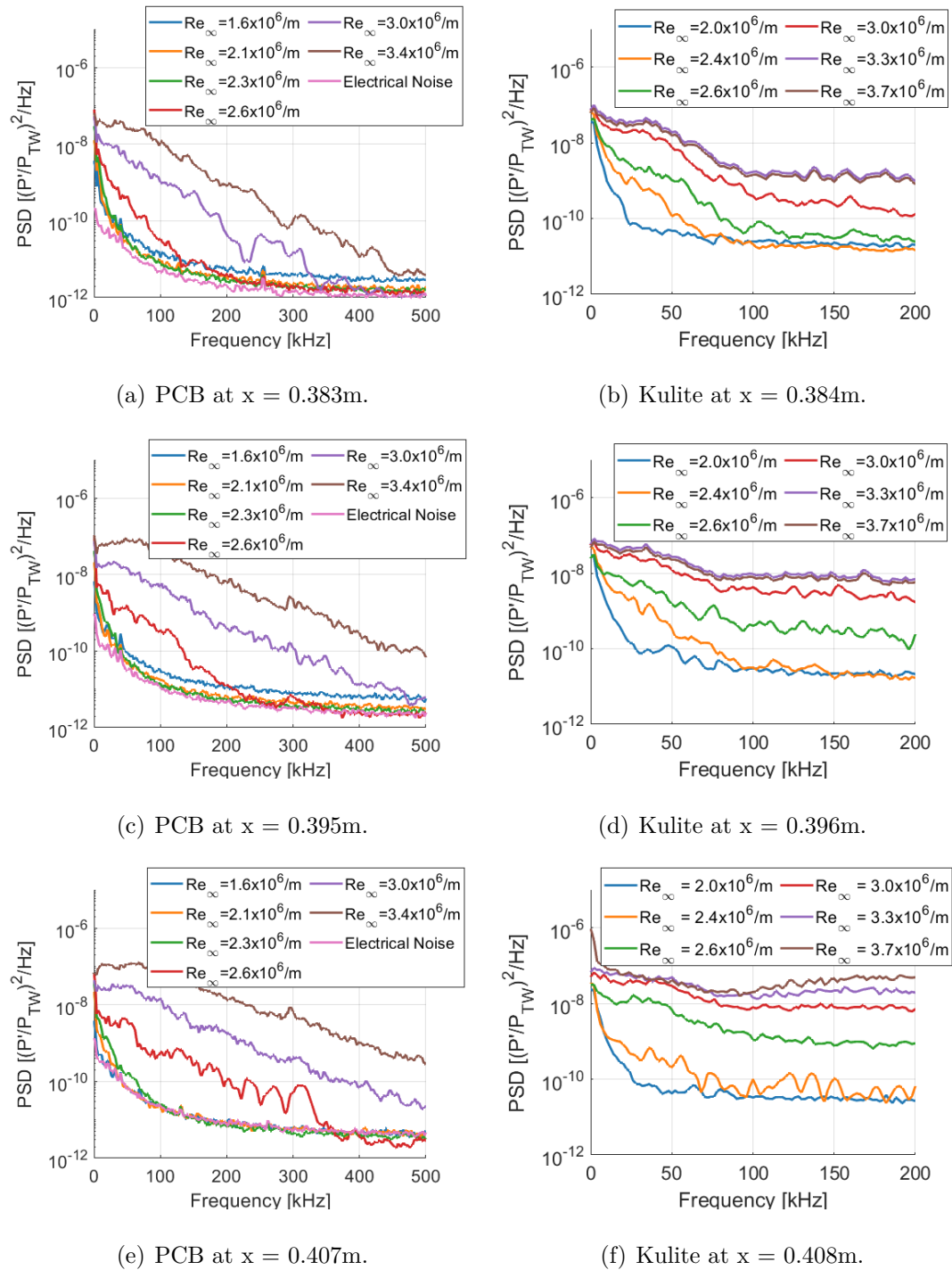
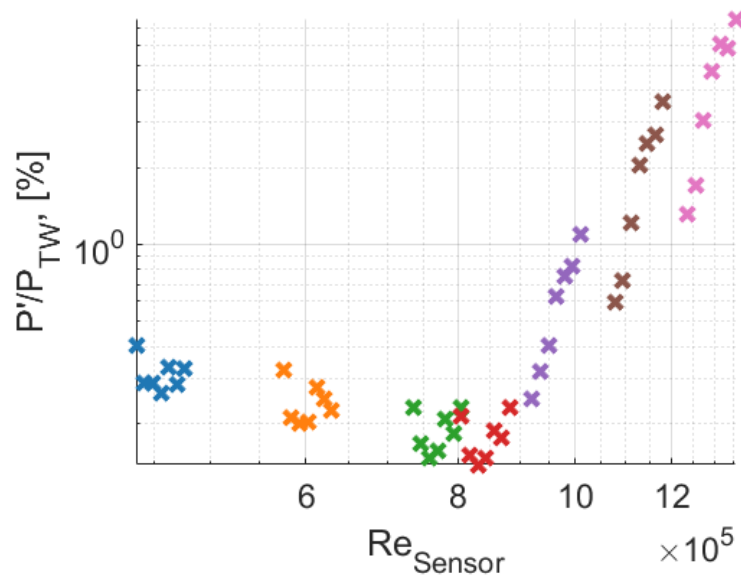


Figure 5.36. PSDs of individual sensors downstream of reattachment under quiet flow at various  $Re_\infty$ .

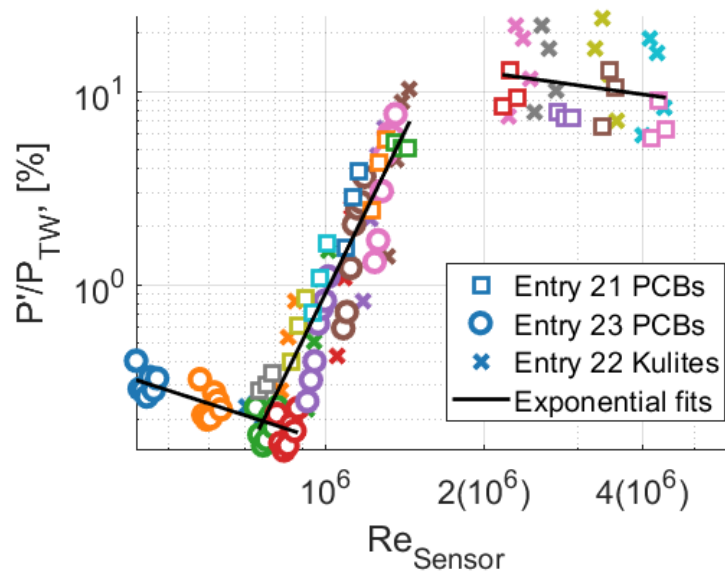
measurement from a single sensor. At low  $Re_{sensor}$ , the magnitudes are approximately linear on the log-log plot, so the relation is exponential. As the Reynolds number increases from  $5 \times 10^5$  to  $8 \times 10^5$ , the fluctuation magnitudes decrease slightly. The reduction in amplitude is due to  $P_{TW}$  increasing with stagnation pressure. At  $Re_{sensor} = 9 \times 10^5$ , the slope of the curve rapidly changes and the fluctuation magnitudes increase drastically. The change in slope is indicative of transition onset and the growth of the fluctuations is exponential. To check how repeatable this behavior is with Reynolds number, additional data was plotted. Figure 5.37(b) shows Reynolds number effects for several entries with both PCBs and Kulites. Pressure fluctuations magnitudes after transition onset collapse onto a line until magnitudes of 10% of  $P_{TW}$  are reached. At this point, the fluctuation levels flatten out and are representative of turbulent boundary layers. Exponential fits were applied to the data and are shown. The equations used to generate the lines of best fit are shown in Table 5.3. From this data, transition onset occurs at sensor-length Reynolds numbers of  $0.9 \times 10^6$  and ends at approximately  $Re_{sensor} = 2.0 \times 10^6$ . The gap between the transitional and turbulent data is due to a lack of diaphragms that burst at that pressure. This issue was fixed in January 2020 but time was not available to redo these experiments. The extent of transition based on length Reynolds numbers is approximately  $1.1 \times 10^6$ . The progression of RMS pressure fluctuation magnitudes is independent of which  $20^\circ$  ramp or sensor is used in the measurement.

Table 5.3. Equations for exponential fits to pressure fluctuation magnitudes

Boundary-layer state	Pressure fluctuation fit
Laminar	$\frac{P'}{P_{TW}} = e^{10.36} Re_{sensor}^{-0.89}$
Transitional	$\frac{P'}{P_{TW}} = e^{-76.95} Re_{sensor}^{5.56}$
Turbulent	$\frac{P'}{P_{TW}} = e^{8.08} Re_{sensor}^{-0.38}$



(a) Pressure fluctuation magnitudes from Perturber ramp.



(b) Comparison of pressure fluctuations on perturber ramp, cluster ramp, and Kulite ramp.

Figure 5.37. Magnitudes of pressure fluctuations on various ramps and sensor-based Reynolds number. Each color represents a different run.

### 5.3.3 Spanwise Variations in Post-Reattachment Pressure Fluctuations

Spanwise sensors were present post-reattachment to see if off-centerline pressure fluctuations contained evidence of possible instability. Figure 5.38(d) shows three arrays of PCBs downstream of reattachment at various unit Reynolds numbers. For all nine spanwise and streamwise locations, the lowest Reynolds number shows laminar spectral behavior. At the farthest upstream location, Figure 5.38(a), the PSDs also show laminar flow at the middle Reynolds number. At  $Re_\infty = 3.3 \times 10^6/m$ , broadband power levels begin to rise due to transition. The middle array of spanwise sensor is shown in Figure 5.38(b). At  $Re_\infty = 2.5 \times 10^6/m$ , low frequency power begins to rise in various peaks. This is similar to the results shown in the previous section. The spanwise sensors show similar broadband amplification. Figure 5.38(c) shows the farthest downstream sensors. Numerous peaks are present at transitional Reynolds numbers but no clear trends can be seen between spanwise sensors. This is similar to the previous results of this section and without clear evidence of the source of these fluctuations, drawing conclusions is difficult.

Spectra and coherences were again inspected for repeatable frequency content for clusters of post-reattachment sensors. The cluster of sensors is useful for seeing if any waves or pressure fluctuations are moving at an angle with respect to the model axis. Figure 5.39(e) shows sensor locations for two clusters of PCB sensors. Figures 5.39(a) and 5.39(b) show PSDs and coherences for the upstream clusters. Little frequency content is present at most of the sensors, although C4 shows some frequency content between 75-200 kHz. Coherences show a single peak between C2 and C4 at 110 kHz. No peak power is seen at this frequency for either sensor, but it is within the broadband power increase for C4. The downstream sensor cluster is seen in Figures 5.39(c) and 5.39(d). Several peaks are present in the frequency content but no large peaks or trends are seen. The coherence plot shows several peaks in coherence between some of the sensors but the results are hard to interpret without clear spectral peaks.

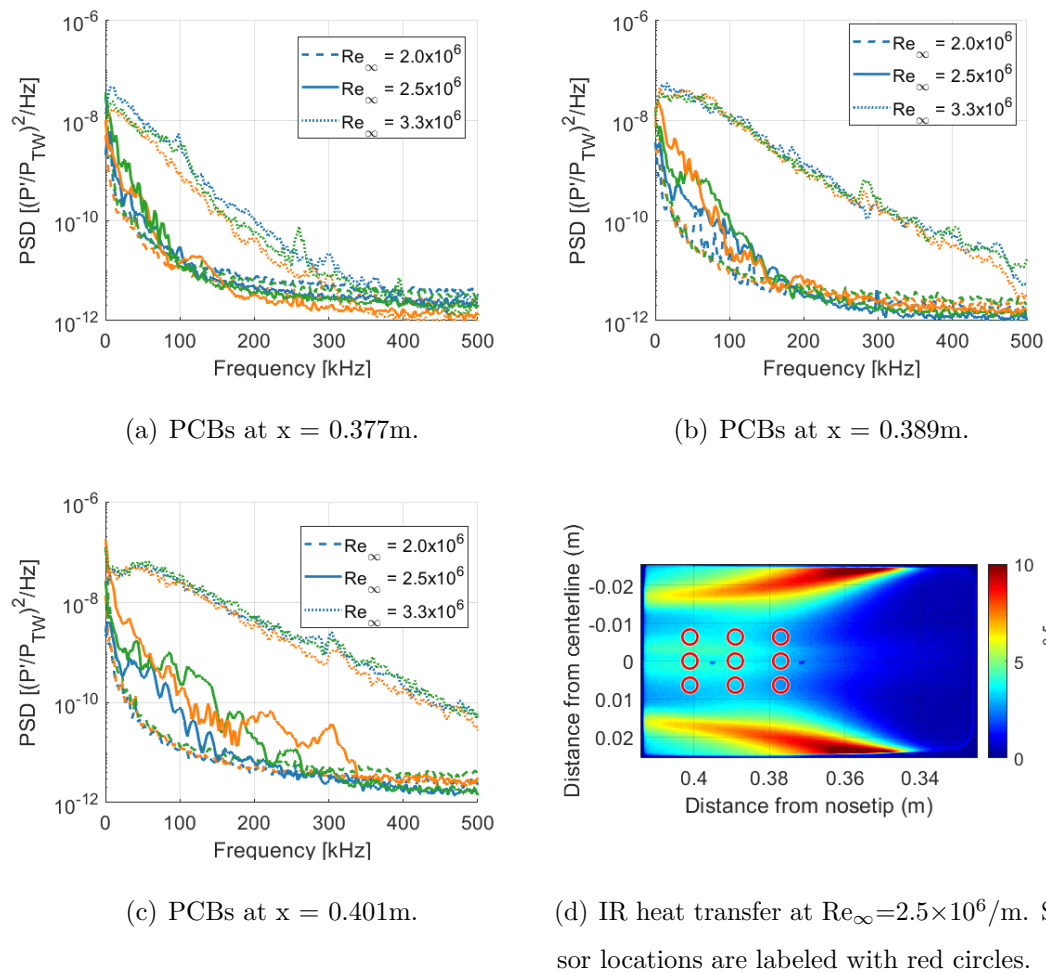
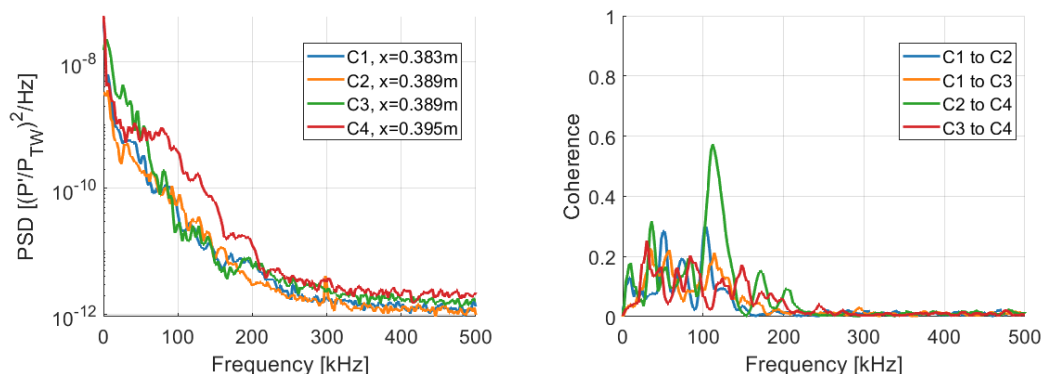
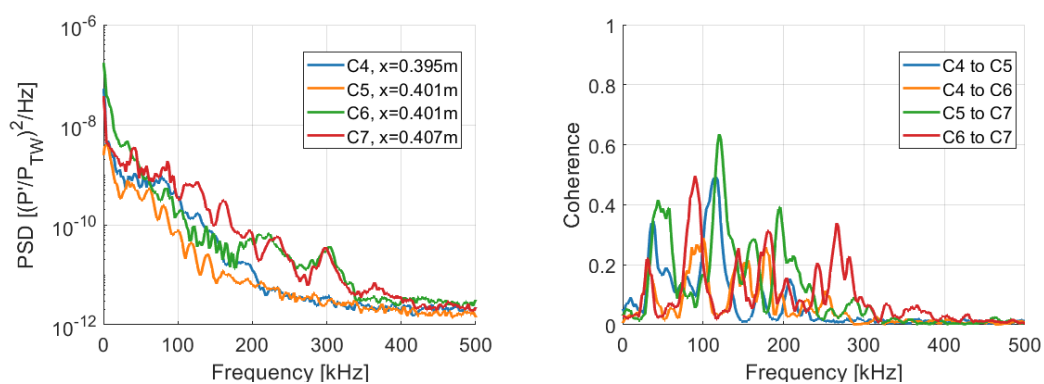


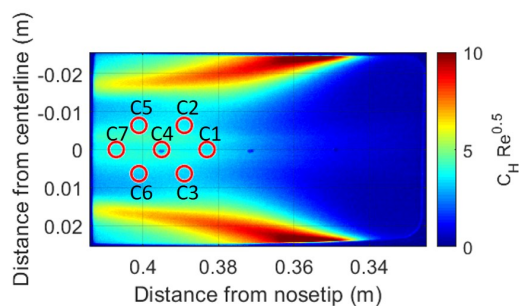
Figure 5.38. PSDs of spanwise sensor arrays downstream of reattachment under quiet flow at various  $Re_\infty$ . Color of the traces indicate spanwise location: Blue = -6.35mm off-centerline, Orange = Centerline, Green = 6.35mm off-centerline.



(a) PSDs of the upstream sensor group. (b) Coherences of the upstream sensor group.



(c) PSDs of the downstream sensor group. (d) Coherences of the downstream sensor group.



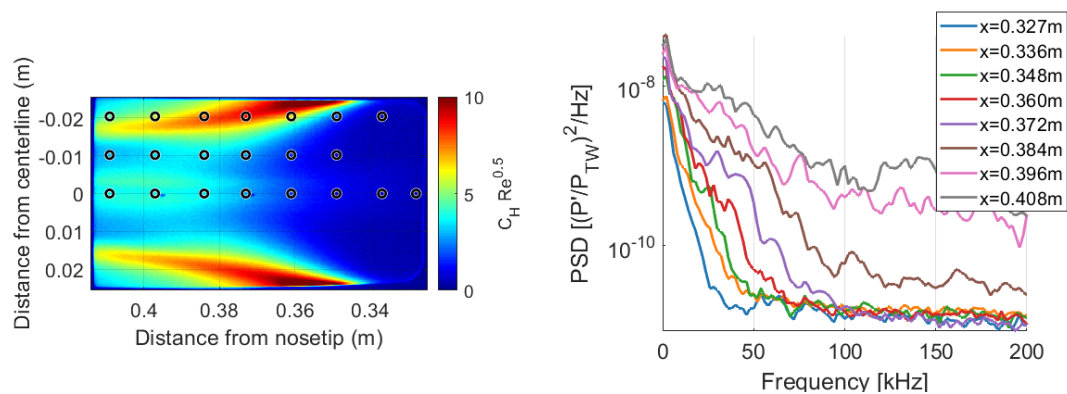
(e) IR Stanton number at  $Re_\infty = 2.5 \times 10^6 / m$ . Sensor locations are labeled with red circles and the naming convention is labeled.

Figure 5.39. PSDs and coherences of PCB clusters downstream of reattachment under quiet flow at  $Re_\infty = 2.5 \times 10^6 / m$  (Run 2312).

The Kulite ramp featured a full grid of Kulites on half of the ramp to gain a better understanding of the pressure behavior at locations even farther off-centerline. The grid featured three streamwise arrays of Kulites and details on the ramp can be found in Section 4.2. PSDs of these sensors at a transitional Reynolds number of  $Re_\infty = 2.5 \times 10^6/m$  can be seen in Figure 5.40. The location of the Kulite sensors are labeled in Figure 5.40(a). Centerline spectral behavior is similar to the many PSDs that have been shown in this section. PSDs of off-centerline sensors in Figure 5.40(c) show an increase in broadband spectral content with downstream distance but the amplitudes are lower than on the centerline. PSDs of Kulites -0.020 m off-centerline show no spectral content. The pressure fluctuations are largest on the centerline of the ramp and decrease with off-centerline distance. A visualization of this effect can be seen in Figure 5.41. Kulite pressure fluctuation magnitudes for two Reynolds numbers are presented for each streamwise array of sensors. The black line indicates the approximate centerline reattachment location. At the lower Reynolds number, the sensors immediately downstream of reattachment show similar amplitudes on the centerline and -10.2 mm off-centerline. As streamwise distance increases the amplitudes on the centerline sensors exceed the off-centerline. For the higher Reynolds number, the post-reattachment magnitudes are the largest on the centerline and fall-off with off-centerline distance. Additionally, the fluctuations within the separation are smaller than the post-reattachment magnitudes for both Reynolds numbers. Based on this, it is expected that the earliest boundary layer transition will occur on the centerline of the ramp.

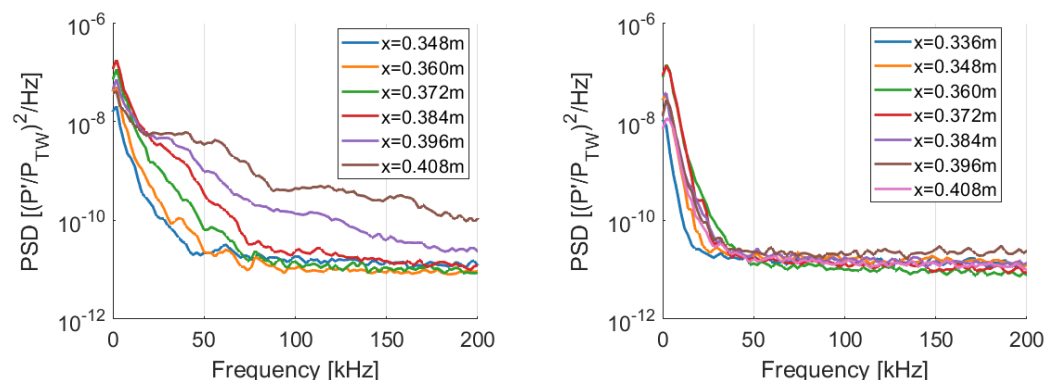
#### 5.4 Summary of Results without Perturbation

Heat transfer and pressure fluctuation measurements were made on the cone-slice-ramp model with a  $20^\circ$  ramp. Heat transfer results were made with both TSP and IR instrumentation. Results from both techniques produced ramp Stanton numbers of similar magnitudes. Early TSP results showed that the reattachment locations



(a) IR heat transfer of the ramp at  $Re_\infty=2.5\times 10^6/\text{m}$ . The black dots represent the locations of Kulite sensors on the ramp (Run 2013).

(b) PSDs of centerline Kulites.



(c) PSDs of Kulites -0.010 m off-centerline.

(d) PSDs of Kulites -0.020 m off-centerline.

Figure 5.40. PSDs of Kulites at various spanwise locations under quiet flow at  $Re_\infty = 2.5\times 10^6/\text{m}$  (Run 2212). Sensors from the entire length of the ramp are shown. Centerline reattachment occurs at approximately 0.36 m downstream from the nosetip.

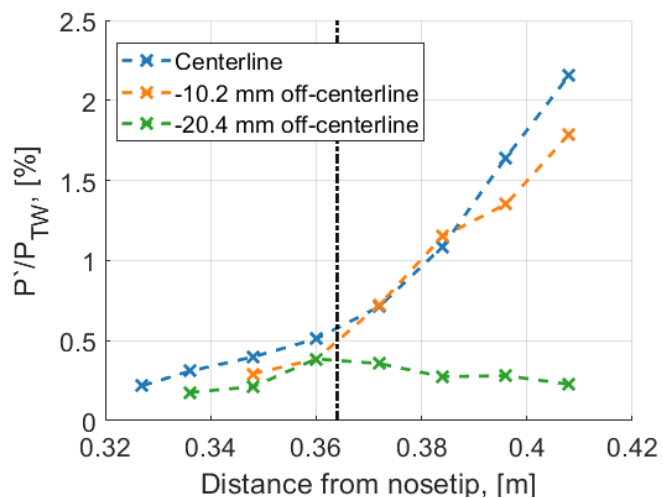
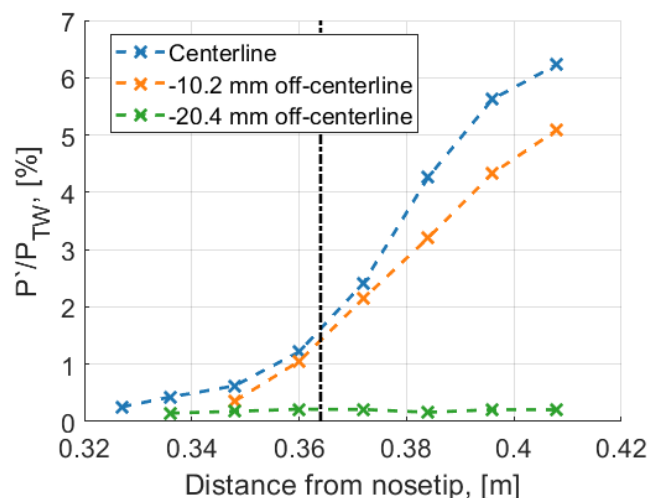
(a)  $Re_\infty=2.5 \times 10^6/m$  (Run 2212).(b)  $Re_\infty=3.3 \times 10^6/m$  (Run 2214).

Figure 5.41. Magnitudes of Kulite pressure fluctuations under quiet flow at various  $Re$ . The black dotted line indicates the approximate reattachment at the ramp centerline.

and the post-reattachment heating patterns are heavily dependent on small angles of attack and yaw. Computations by Thome confirmed this behavior and future experiments had finely controlled AoA and yaw. Quiet flow heat transfer featured two streamwise streaks roughly symmetric about the centerline for Reynolds numbers below  $Re_\infty = 7.0 \times 10^6/m$ . Above this, a single streamwise streak was present on the centerline. The single streak results featured a local maximum of heat transfer after reattachment. Noisy flow results featured a single streamwise streak on the centerline and produced higher levels of heating. The location where the heat transfer departs from the upstream ramp values was used as a reference for the reattachment location.

Numerous measurements of pressure fluctuations were presented. Fluctuations within separation on the slice and ramp displayed similar behavior to each other. Pressure sensors showed generation of wave packets and turbulent spots at Reynolds numbers as low as  $Re_\infty = 2.2 \times 10^6/m$ . This is significantly lower than for other axisymmetric geometries with separation bubbles in the BAM6QT. It appears that the spots are generated within the shear layer and are measurable once they reattach to the surface. The convection velocities of the spots were measured to be 650-710 m/s depending on the method used to calculate them. Wave packets preceded the turbulent spots in several cases. FFT's of the wave packets showed that they developed high-frequency content during their breakdown to turbulence. As the Reynolds number increased, possible turbulent spots were measured reattaching to the ramp surface. At Reynolds numbers exceeding  $6.0 \times 10^6/m$ , fully turbulent boundary layers reattached to the surface. This suggests that transition can entirely occur off-surface within the shear layer. Peaks in the frequency content within individual wave packets at similar unit Reynolds numbers varied but were consistently below 150 kHz. A large number of transitional PSDs were shown to emphasize that they were highly dependent on the quantity and magnitude of wave packets and turbulent spots. Contributions from wave packets at coherent frequencies were not strong enough to be noticeable within the PSDs.

Pressure fluctuation magnitudes were repeatable and the transition location was approximately constant for every ramp and sensor type used. Transitional RMS pressure fluctuations grew exponentially after the onset of transition and exponential fits of the data were given for each boundary-layer state. Transition occurred over length Reynolds numbers, based on freestream conditions and axial distance from the nosetip, of  $Re_{sensor} = 0.9 \times 10^6$  to  $2 \times 10^6$ . A shear-layer instability could be generating the wave packets seen in the time traces. However, a lack of coherent power at repeatable frequencies indicates it might not be a dominant cause of transition.

## 6. MEASUREMENTS OF GENERATED DISTURBANCES ON A $7^\circ$ CONE

Measurements of natural pressure fluctuations on the cone-slice-ramp showed wave packets but not repeatable spectral content due to a traveling shear-layer instability. Therefore, an attempt was made to artificially introduce traveling instabilities. By artificially generating the disturbances, measurements of how they convect and grow can be made. Comparisons to the no-perturbation data can then shed light on how convective instabilities affect boundary-layer transition. The present chapter utilizes a localized plasma to introduce a temperature disturbance to the boundary layer. The disturbance operates as an impulsive point source and will hopefully introduce wave packets into the boundary layer. Testing the generation of disturbances on a simpler geometry was done to determine the effectiveness of the technique. A  $7^\circ$  half angle cone at  $0^\circ$  AoA was chosen since it is a well-studied geometry within the hypersonic boundary-layer community and is known to have smooth-wall transition dominated by the 2nd-mode instability. This chapter will outline the preliminary experiments of plasma generation on a  $7^\circ$  cone, for justification of the technique.

### 6.1 Low-Pressure Breakdown of Air

Controlled artificial disturbances were generated within the boundary-layer of a  $7^\circ$  cone using a plasma caused by the high-voltage breakdown of air. A detailed treatment of this topic is covered in Reference [115]; only relevant basic points are provided in this section. Downstream of the disturbance, instability waves that lead to transition and breakdown to turbulence can be measured on the cone surface. Generation of the plasma is dependent on the electrical breakdown of gas at low pressures. The present apparatus utilizes two stainless-steel electrodes on the surface

of the model separated by a known distance. In order to ionize the gas, a voltage is applied between these two electrodes. One stainless steel rod will take the role of the anode while the other will be the cathode. When the voltages are low and no breakdown is present, a small current still exists between the electrodes. As the applied voltage increases, a threshold is reached where the energy of the air within the gap begins to ionize nearby particles. Once ionization begins, electrons begin to collide with adjacent electrons and rapidly form a plasma within the gap. This electron avalanche allows a large increase in current without much change in voltage. Where the applied voltage saturates is known as the threshold of breakdown voltage ( $V_t$ ). The general behavior of the breakdown of air for given currents can be seen in Figure 6.1. Once the breakdown voltage is exceeded, the ionized gas becomes what is known as a glow discharge. Above this current, the plasma becomes more filamentary and begins to behave like an arc discharge. This is not ideal since higher current discharges generate more EMI and will affect sensitive measurements.

Generation of the high-voltage pulses was completed with a Eagle Harbor Technologies NSP-330-20-F nanosecond pulser [116]. The pulser is powered by a TDK-Lambda power supply that can output 0-600 V DC. This is linearly related to the pulser output which has a range of 0-25 kV. The electronics are limited by a bank of resistors that decrease the maximum voltage to 20 kV. The pulser was triggered by a Stanford Research Systems DG535 delay generator. The delay generator received a trigger from a Tektronix oscilloscope and waited 1-1.5 seconds to trigger the pulser. This ensured that pulsing occurred during quiet flow. The pulser output is symmetric about ground with one wire being the anode and the other being the cathode. The downstream electrode was chosen as the cathode for the current experiments. Two Tektronix P6015A high voltage probes were used to measure the applied voltage. The grounds of each probe were connected together so that the difference between the two probes is the total output voltage. Current was measured with a Magnelab CT-D1.0 current transformer. All voltage and current measurements were recorded on a Keysight Technologies DSO9104A Oscilloscope. Information on the oscilloscope

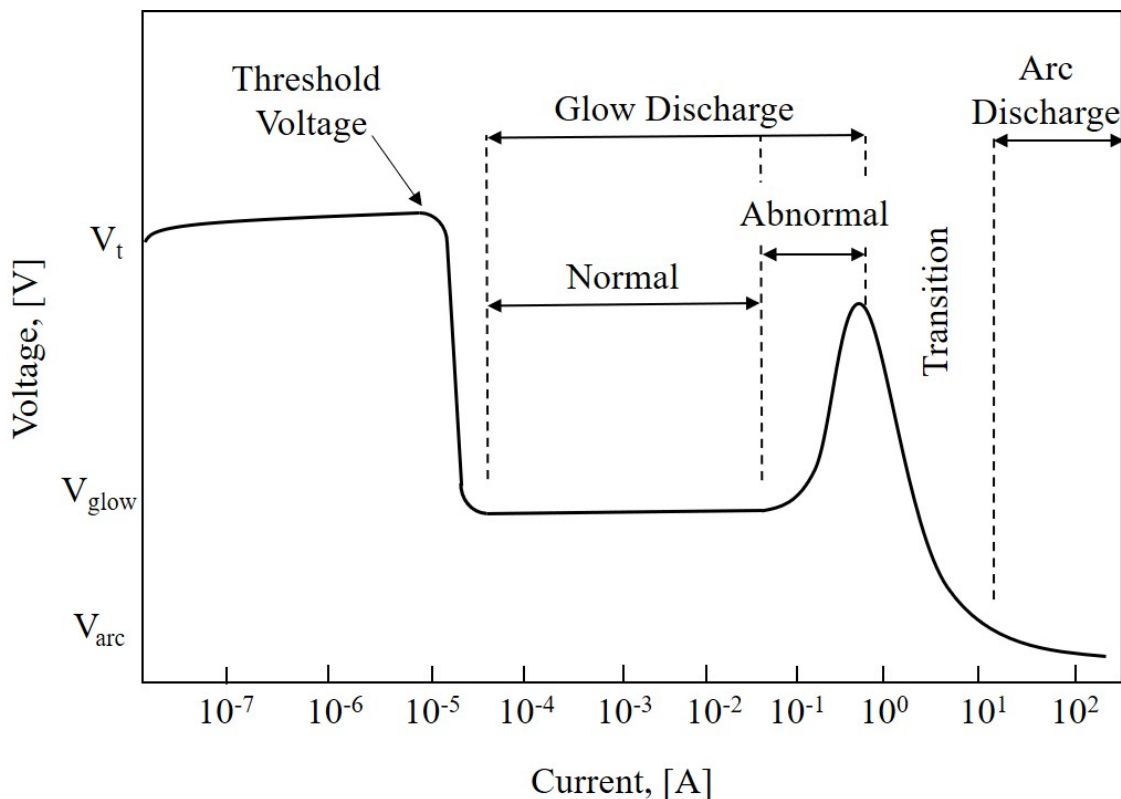


Figure 6.1. DC breakdown of gas in terms of voltage and current. Adapted from Reference [111].

can be found in Section 3.1. The oscilloscope was triggered off the delay generator so a short time window could be acquired at a high sample rate. A schematic of the pulser apparatus and data acquisition system can be found in Figure 6.2.

An image of the final BAM6QT pulse apparatus can be seen in Figure 6.3. The green panel is the custom pulser sitting atop the white TDK-Lambda power supply. The pulser was connected to a 3-phase 240 volt outlet installed for use of these electronics. The pulser controls and the power supply can be seen in Figure 6.3(a). If a single burst of pulses is desired, durations can be adjusted between 20-110 ns for frequencies up to 400 kHz. Figures 6.3(b) and 6.3(c) show the apparatus for measuring voltage and current. The whole apparatus was supported by wood and foam to prevent the high-voltage components from shorting to any metal. Bends in

wires were kept to a minimum to avoid shorting within the wire insulation. On the tunnel exterior, the wires were separated from the tunnel wall by another piece of foam. Once inside the tunnel, the insulated wires were allowed to contact metallic surfaces as was necessary due to space constraints.

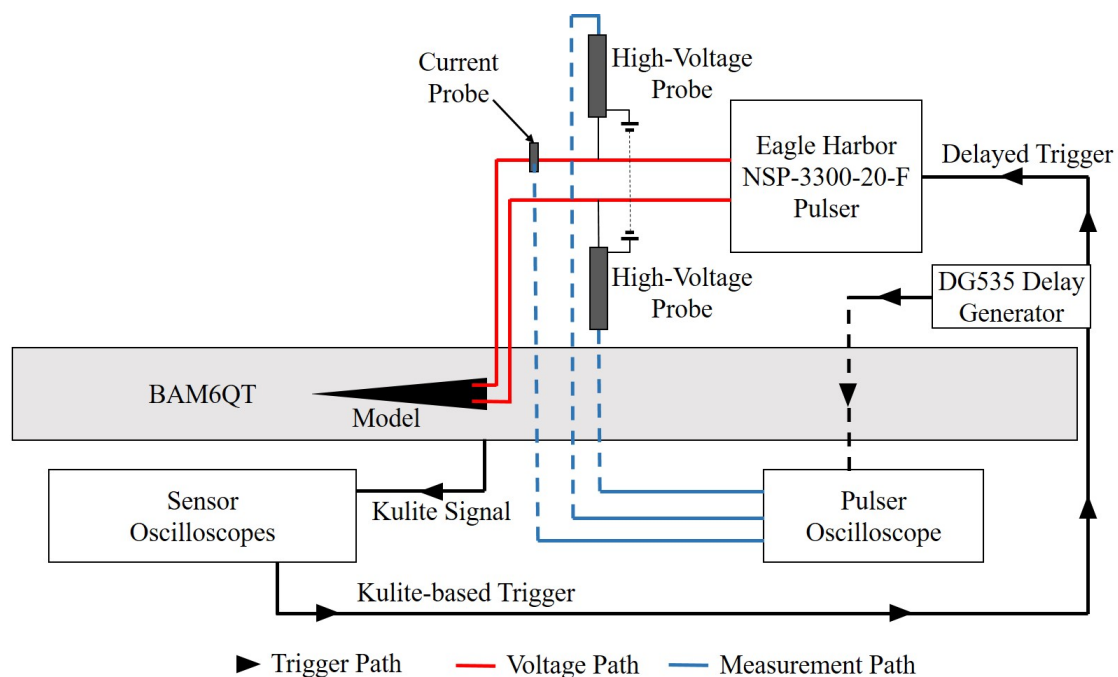
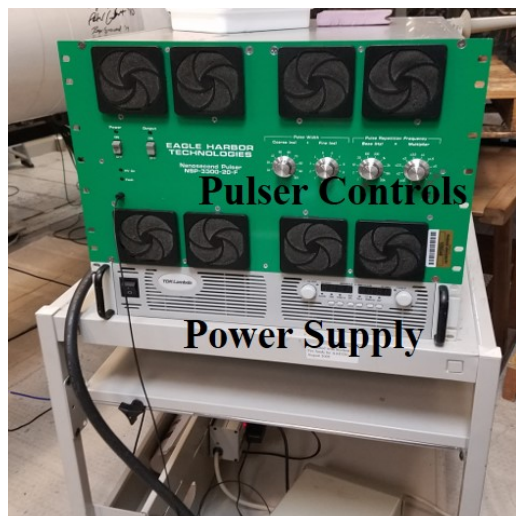
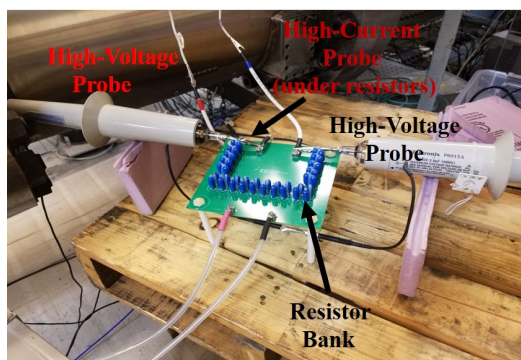


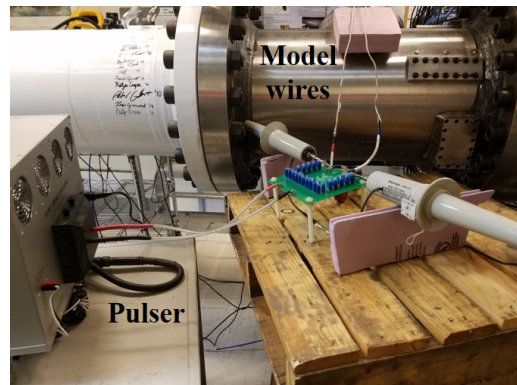
Figure 6.2. Schematic of the pulser triggering and measurement set up.



(a) Front of the Eagle Harbor Pulser.



(b) Resistor bank set up on pulser output.



(c) Second view of Resistor bank set up.

Figure 6.3. Pulser setup for the BAM6QT.

## 6.2 Plasma Perturbation on a $7^\circ$ Half-Angle Cone

Creation of an artificial disturbance on the surface of the model is one way to promote the growth of traveling instabilities within the boundary layer. Previous experiments by Ladoon [115] used this technique to generate wave packets on a  $5^\circ$  cone at Mach 4. Casper has completed a significant amount of work using this technique to study fluid-structure interactions on a  $7^\circ$  cone within the BAM6QT [112, 117–120].

Casper generated glow and spark perturbations on the surface of a cone and measured instability wave packets and turbulent spots convecting downstream.

Table 6.1 shows the Reynolds numbers and the pulser electronics settings for the present experiments on the  $7^\circ$  cone. Two Reynolds numbers were tested with several voltages between the perturber electrodes. For every run, the artificial disturbances were generated 1.5 seconds into the run. This allowed for data to be taken before, during, and after the plasma generation. Depending on when data were processed during the run, comparisons of natural second-mode waves to the artificially generated disturbances can be made. The voltage was pulsed at a frequency of 2 kHz, corresponding to  $500 \mu\text{s}$  between each pulse. The time it will take for the disturbances to convect off the end of the cone was estimated using perfect gas relations and boundary-layer edge temperatures for a Taylor-Maccoll solution on a  $7^\circ$  cone. The convection time for the perturbation reaching the cone base is about  $115 \mu\text{s}$ . Complete measurements of the resulting perturbation can be made before EMI from the next pulse interrupts the sensor data. The effect of the applied voltage was measured by altering the voltage setting in the electronics.

Table 6.1. Run conditions and electronics settings for artificially generated disturbances on the  $7^\circ$  cone.

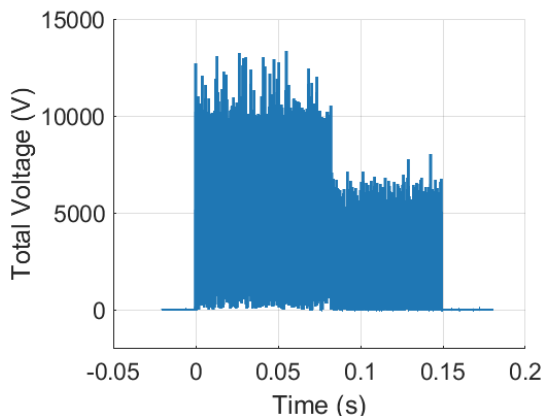
Run	$\text{Re}_\infty(1/\text{m})$	Pulse Duration (ns)	Frequency (kHz)	Number of Pulses	Voltage (kV)
1907	$10.5 \times 10^6/\text{m}$	100	2	300	7.5
1908	$10.5 \times 10^6/\text{m}$	100	2	300	10
1910	$10.5 \times 10^6/\text{m}$	100	2	300	12.5
1911	$7.6 \times 10^6/\text{m}$	100	2	300	12.5

Voltage and current measurements were taken during each run. These help to determine the consistency and the type of perturbation generated. Figure 6.4 shows these for the  $\text{Re}_\infty = 7.6 \times 10^6/\text{m}$  case (Run 1911). The full time traces are presented

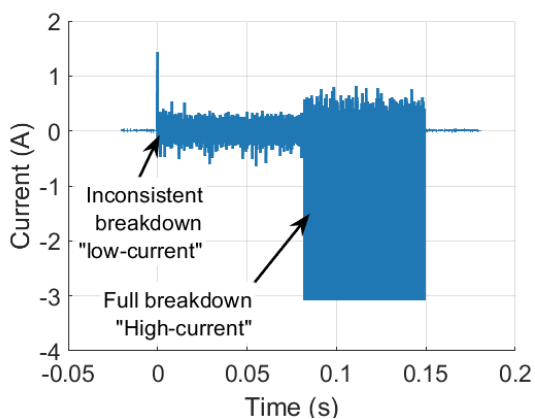
here to show the variations in the pulsing. Figure 6.4(a) shows the total voltage applied to the individual electrodes. The first half of pulsing exhibits high-voltage near the 12.5 kV applied voltage from the pulser. After 0.8 s this drops for the remaining pulses. Figure 6.4(b) shows the current, where the inverse is seen. The beginning pulses show low current and the latter pulses show high current. Based on the current measurements and Figure 6.1, the initial low-current pulsing is indicative of glow discharges and the high-current pulsing indicates abnormal glows or spark discharges. The sudden change could be due to the build up of spare electrons in between the electrodes. This makes every subsequent pulse easier to initiate, and causes a change in pulsing behavior. Once the spark discharges began during the high-current pulsing, every pulse after that fully broke down. Due to this behavior, the run will be treated as two individual cases. All other pulser conditions and runs saw consistent breakdown behaviors for every pulse. The precise reason for this is not known but the change in density from changing the Reynolds number will affect the breakdown of the air.

A close up of the individual voltage and current pulses during the low-current pulsing can be seen in Figure 6.5. Ensemble averages were taken for current and voltage measurements. These were plotted with three individual pulses taken from representative times in the beginning, middle, and end of the burst. Three methods were used to approximate the probability density functions (PDF). The first is a histogram that has been normalized to represent a PDF. The second was a Gaussian-mixture method and the third was a kernel-smoothing estimate. These two estimate continuous PDFs for discrete sets of data. These methods typically produced identical PDFs. The non-histogram estimates provided the best result for calculating means and standard deviations.

The current time traces for the low-current pulsing can be seen in Figure 6.5(a). Small currents were present intermittently during the run. A PDF of the RMS current can be seen in Figure 6.5(b). The mean and standard deviation of these pulses can be seen in Table 6.2. The current was low enough that it did not reliably produce perturbations on the model surface. The ensemble average did not accurately represent



(a) Time trace of pulser positive voltage.



(b) Time trace of pulser current.

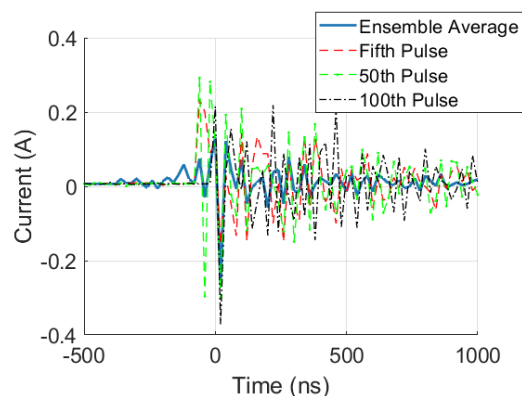
Figure 6.4. Electrical characteristics of pulser at  $Re_\infty = 7.6 \times 10^6/m$  (Run 1911).

every pulse as a result. The reason for this behavior is not known. Similar plots were made for the voltages in Figures 6.5(c) and 6.5(d). The voltage traces showed large clear peaks in voltage for every pulse. The voltage was more repeatable than the current for this case. This is expected since the electronics always applied the voltage potential whether or not the air between the electrodes broke down.

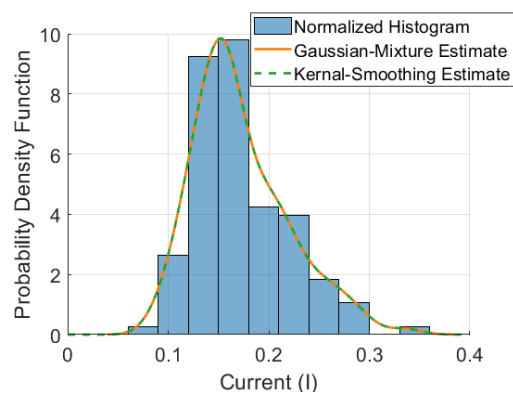
A similar treatment was given to the high-current pulsing portion of Run 1911 in Figure 6.6. The ensemble average of the current can be seen in Figure 6.6(a). It is important to note that the scopes were not set correctly to capture the full peak of

the high-current breakdown of the air. The data was clipped at 3 A and the actual peak was not measured. Since the current peaks are clearer in this case, the duration of the current pulsing was calculated. The current trace represents when a plasma is present since the flow of electrons is the physical manifestation of the current spike. Ideally, an FFT of this signal is desired for analysis of its frequency content. However, the measured current trace did not have enough points to provide a useful FFT of the signal. Therefore, a generated square wave was used to represent the current pulse and demonstrate frequency content. The full-width at half-maximum of the ensemble averaged current pulse is 69 ns and has rise and fall times of approximately 40 ns. The width of the pulse slightly lower than the setting chosen on the pulser of 100 ns. Figure 6.7 shows the spectral behavior of a square wave with the same rise time, fall time, and duration as the current pulse. Drop-off of the first lobe can be seen at frequencies well above 1 MHz. This will sufficiently excite unstable frequencies of the estimated second-mode at 200-300 kHz. The PDF seen in Figure 6.6(b) shows the behavior of the PDFs. The current pulsing had amplitudes from 2.5 to 2.9 A. This is significantly higher than the low-current pulses. Voltages in Figures 6.6(c) and 6.6(d) show similar behavior to the low-current cases but at lower maximum voltages. The mean and standard deviation of these pulses can be seen in Table 6.2.

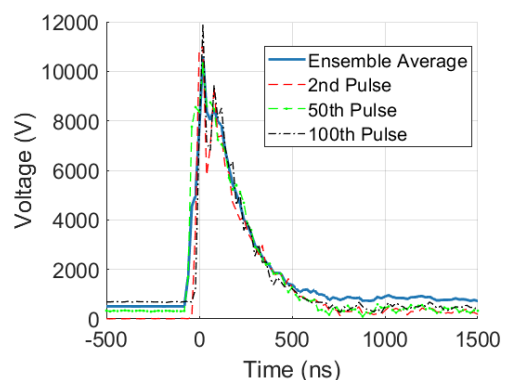
Other runs showed similar current and voltage behavior as the high-current portion of Run 1911. As such, they will not be explicitly plotted. The statistics of their RMS values are tabulated in Table 6.2.



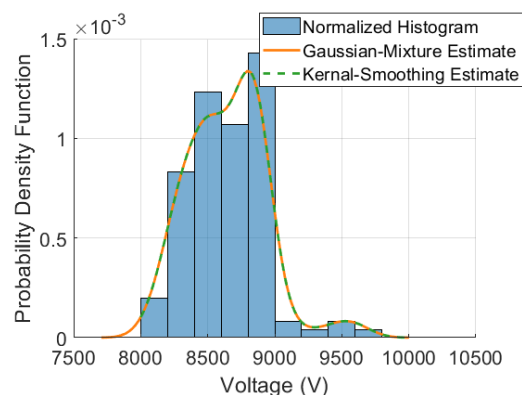
(a) Individual time traces and ensemble average current.



(b) PDF of RMS current.

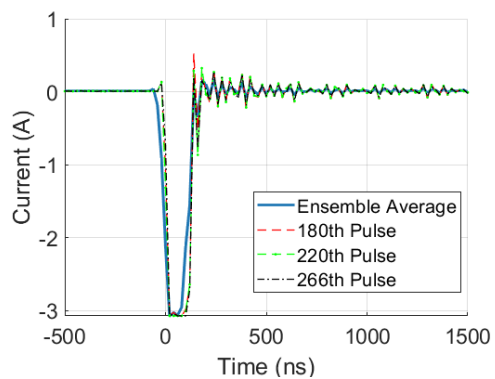


(c) Individual time traces and ensemble average voltage.

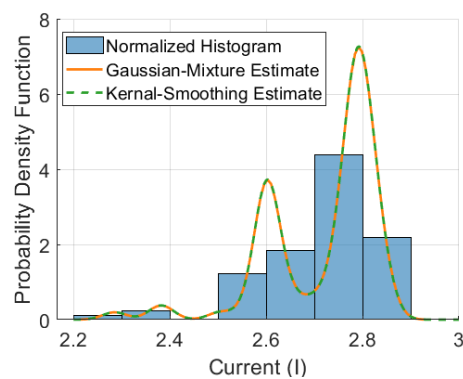


(d) PDF of RMS voltage.

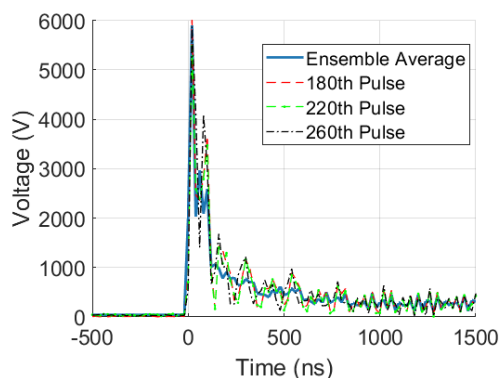
Figure 6.5. Electrical characteristics of pulser during low-current pulsing at  $Re_\infty = 7.6 \times 10^6/m$  (Run 1911).



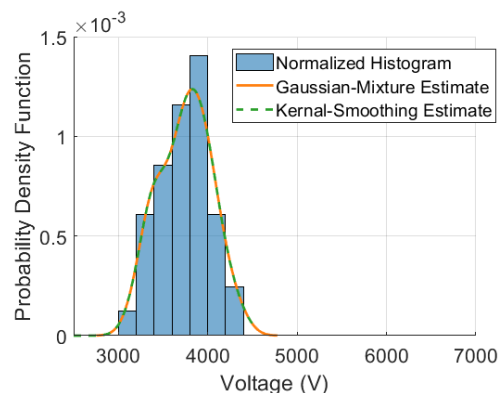
(a) Individual time traces and ensemble average current.



(b) PDF of RMS current.



(c) Individual time traces and ensemble average voltage.



(d) PDF of RMS voltage.

Figure 6.6. Electrical characteristics of pulser during high-current pulsing at  $Re_\infty = 7.6 \times 10^6/m$  (Run 1911).

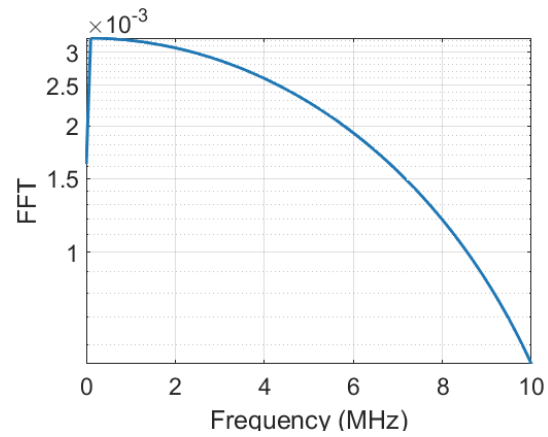


Figure 6.7. FFT of a sample square wave with a 100 ns pulse duration and 40 ns rise and fall times.

Table 6.2. Behavior of RMS Voltage and current sent to the perturber electrodes.

Run	Mean $V_{RMS}$ (V)	Stand. Dev. $V_{RMS}$ (V)	Mean $I_{RMS}$ (A)	Stand. Dev. $I_{RMS}$ (A)	Number of pulses
1907	5988	191	0.4526	0.0694	299
1908	7554	636	0.2744	0.0659	299
1910	3683	666	1.8182	0.1664	299
1911 (Low I)	8646	310	0.1724	0.0499	126
1911 (High I)	3747	313	2.7183	0.118	82

### 6.2.1 Instability Growth without Artificial Disturbances

To determine the effect of the plasma on instability growth, the natural growth needs to be known. Measurements of the natural second-mode growth on a  $110\ \mu\text{m}$  radius nosetip without perturbation were made. The AoA was zeroed in the same manner as for the long-ramp model. Peak frequencies of second-mode waves around the azimuth were within 5 kHz for all measurements. Figure 6.8 shows PSDs from all seven PCBs along the cone for the lower of the two Reynolds numbers listed in Table 6.1. The data was processed 0.5 s before the onset of pulsing over a 0.05 s window of time. The pressure fluctuations are normalized by the mean static pressure calculated using STABL-2D. No frequency content indicative of second-mode wave growth is seen in the PSD. For this condition, the Reynolds number is too low for significant second-mode growth to be measured on the cone. Figure 6.9 shows a similar plot but for the higher Reynolds number case listed in Table 6.1. It is immediately apparent that the higher Reynolds number case has second-mode growth at approximately 225-300 kHz. The peaks grow and shift to lower frequencies as you move down the body of the cone and the boundary layer thickens. However, this Reynolds number is not high enough to see any sign of breakdown or transition.

### 6.2.2 Instability Growth with Artificial Disturbances

To determine the effect of an artificial disturbance, the same run was processed when the electronics were triggered and perturbations began. The  $\text{Re}_\infty = 7.7 \times 10^6/\text{m}$  case had two distinct pulsing types and is treated as two cases: one as the “low-current” case and the other as “high-current.” Figure 6.12 shows the pressure fluctuations at the farthest upstream PCB for several times during the low-current pulsing. This was chosen as a representative case for the effect of plasma perturbation on the boundary-layer pressure fluctuations. Figure 6.12(a) shows a close up of a nominal single pulse. There is a large spike in noise that occurs when the current in the wires is rapidly changing. During this time, the data suffers from a large amount

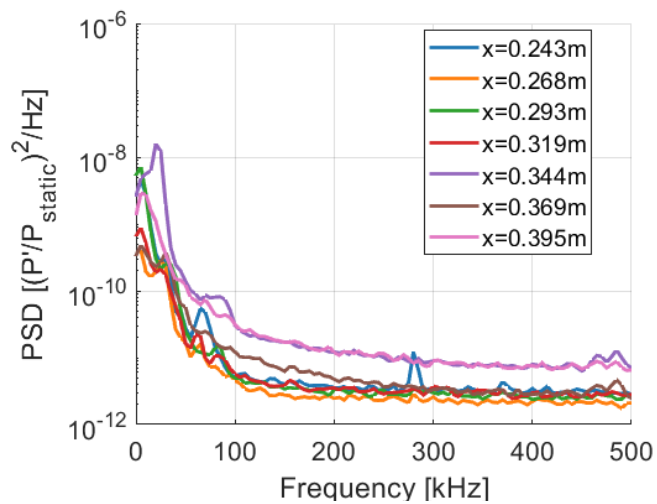


Figure 6.8. PCB PSD's down the length of the cone without perturbation at  $Re_\infty = 7.7 \times 10^6/m$  (Run 1911). The legend reports axial distance from nosetip.

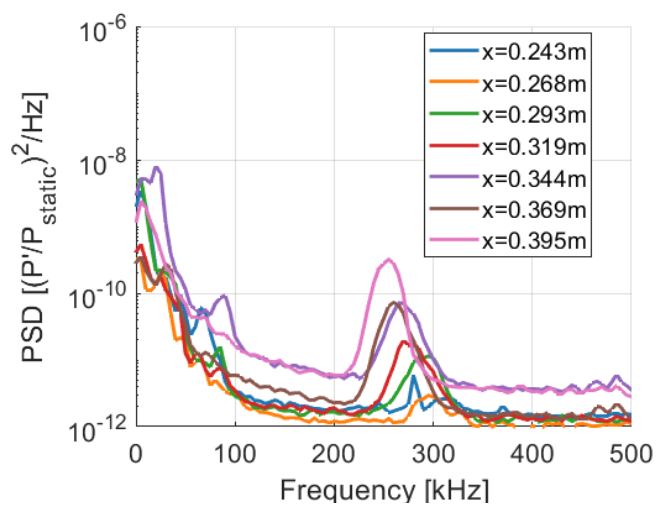


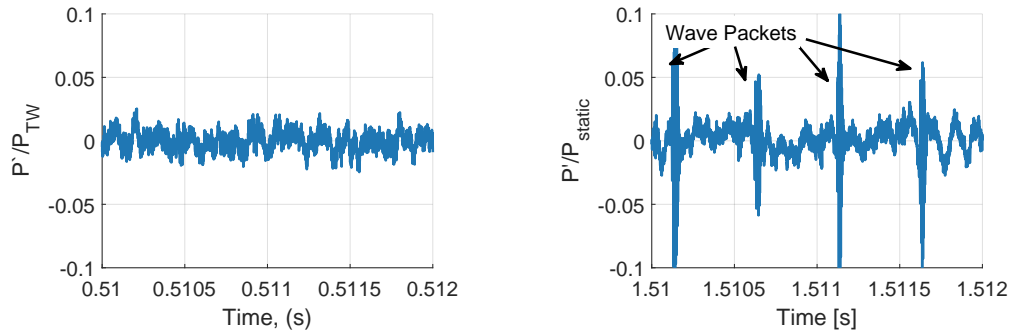
Figure 6.9. PCB PSD's down the length of the cone without perturbation at  $Re_\infty = 10.7 \times 10^6/m$  (Run 1910). The legend reports axial distance from nosetip.

of electrical noise. A delay occurs as the disturbance travels downstream and convects over the sensor as a wave packet. This time contains the relevant data for instability measurements. To avoid unnecessary interference on the wave packet, the noise must be excluded or filtered out. Figure 6.12(b) shows three individual pulses and the ensemble average of all low-current pulsing. For these, the noise was removed by selectively choosing the window of data to exclude it. The amplitudes of the wave packets vary dramatically over the course of the low-current pulsing. The breakdown of the air between perturber electrodes is inconsistent and some electronic pulses had no subsequent downstream pressure perturbation.

Calculation of the RMS pressure fluctuation magnitudes required careful analysis for artificial perturbation experiments. If the plasma perturbation was present on the model, less than 10% of the time trace during pulsing had wave packets present on the model. This caused concern with how the averaging in the PSD would affect the calculated RMS fluctuations. Figure 6.10 shows time traces with and without perturbation. The natural fluctuations seen in Figure 6.10(a) have consistent behavior during the entire time window. This is not the case for the perturbation time trace in Figure 6.10(b). If the RMS amplitude of just the wave packets is desired, the time in between the pulses must be excluded.

Figure 6.11 shows calculated amplitudes for a typical case of plasma-generated pressure fluctuations. Three techniques were used to calculate the amplitudes. The first technique was to integrate the PSD similar to the non-perturbation results. The second technique was to calculate the ensemble average of generated perturbations and taking the RMS directly from the time series. The third technique was to take the RMS of each individual perturbation and average all the individual RMSs. The integrated PSD and mean RMS show similar trends but the integrated values are lower than the mean RMS values at every Reynolds number. The discrepancy is due to the integration averaging non-perturbation periods in the time trace. The waves generated by the perturbations only appear during a small fraction of the window used for PSD calculation. The ensemble averaged RMS does not show a similar trend. This is due

to the random turbulent fluctuations being averaged out of the time trace. The RMS of the ensemble average cannot measure transitional or turbulent fluctuations and was not used. Ultimately, the mean of individual perturbation RMS fluctuations was used to calculate the magnitudes for plasma-generated disturbances since it better represented the individual wave packets in the time trace.



(a) Time trace without wave packets from plasma perturbation at  $Re_\infty = 10.9 \times 10^6/m$  (Run 1910).  
 (b) Time trace with wave packets from plasma perturbation at  $Re_\infty = 7.7 \times 10^6/m$  (Run 1911).

Figure 6.10. Sample time traces of pressure fluctuations on a  $7^\circ$  cone.

In order to quantify the variations in the boundary layer disturbance that was induced, PDFs were calculated for the RMS pressure fluctuations of the generated disturbances. The RMS values were calculated directly from the time series. A threshold was set to separate wave packets from baseline pressure fluctuations. The pressure fluctuations had to exceed 3-4% of the mean static pressure to be considered wave packets. This value effectively captured the wave packets while being large enough to avoid natural pressure fluctuations. Figure 6.13 show the PDFs for both portions of the  $Re_\infty = 7.6 \times 10^6/m$  case. The means and standard deviations of pressure fluctuations 0.243 m downstream from the nosetip are listed in Table 6.3. The mean RMS pressure fluctuations of the low-current pulsing are 70% of the high-current pulsing. The low-current glow discharges are creating much smaller boundary layer

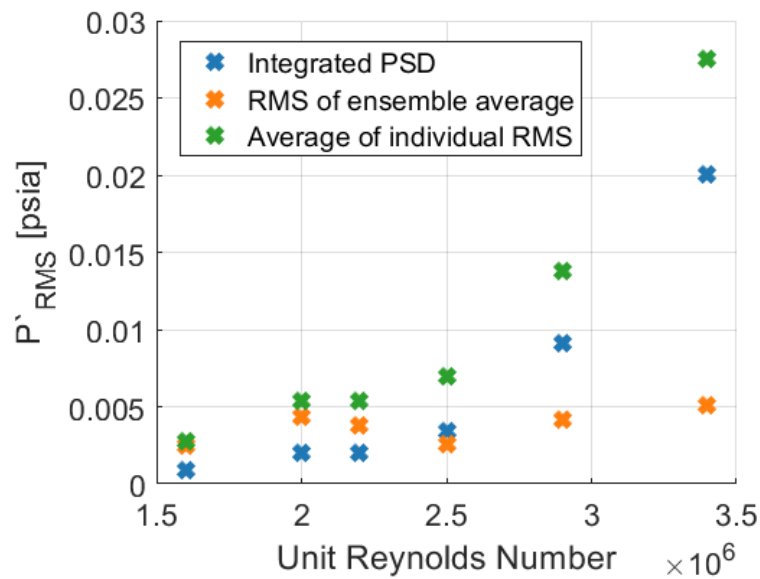
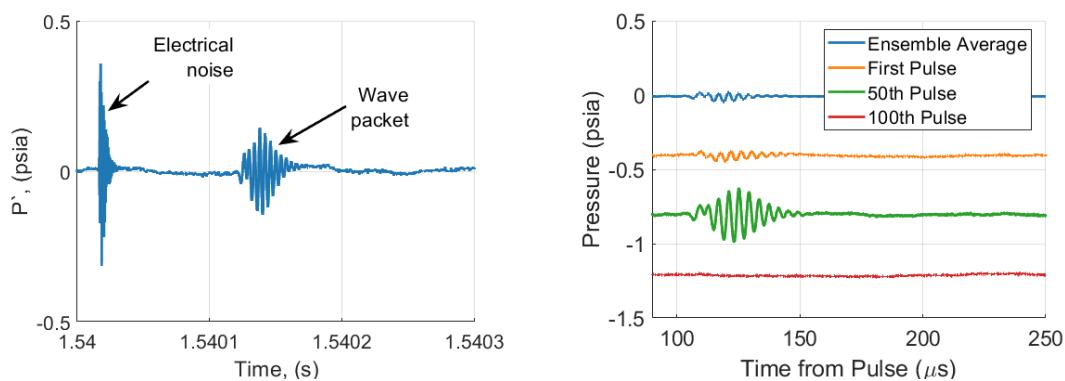


Figure 6.11. Comparison of RMS amplitudes from plasma-generated perturbations.

disturbances than the abnormal glows or sparks during the high-current pulsing. For both cases, the standard deviations are similar but these variations will have a much larger effect on the low-current disturbances which have a smaller mean.



(a) Close-up of a single pulse.

(b) Ensemble average of all pulses with select individual pulses.

Figure 6.12. Example pressure fluctuations from 0.243m downstream from the nosetip. Processed during the low-current portion at  $Re_\infty = 7.6 \times 10^6/m$  (Run 1911)

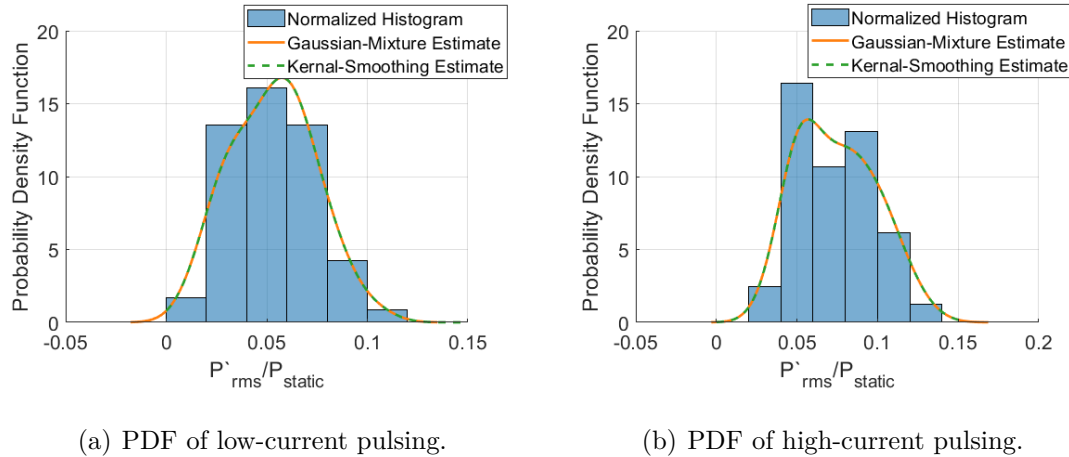


Figure 6.13. PDF's of the RMS pressure fluctuations 0.243m downstream from the nosetip at  $Re_\infty = 7.6 \times 10^6/m$  (Run 1911)

Table 6.3. Behavior of RMS pressure fluctuations at the first PCB location.

Run	Applied Voltage (V)	Mean ( $P'_{RMS}/P_{static}$ )	Standard Deviation ( $P'_{RMS}/P_{static}$ )	Number of pulses
1907	7.5	-	-	0
1908	10	0.061	0.018	16
1910	12.5	0.125	0.025	265
1911 (Low I)	12.5	0.053	0.021	59
1911 (High I)	12.5	0.074	0.024	122

With reliable pulses being generated upstream of the sensors on the cone, the growth of the disturbances on the model can be measured. Calculating PSDs of the generated disturbances is the preferred way of doing this. Unfortunately, the electrical noise present during the plasma generation introduces unwanted noise to the frequency domain. Two different methods were used to remove this. The first method was to apply a Hampel filter to the data [121]. This filter is a robust way to remove outliers with a type of moving median average. The filter looks for noise

spikes that exceed a threshold of the nearby data's median. If the filter detects a noise spike, it replaces that point with the local median. Due to the extreme spikiness of the electrical noise, this filter is effective at selectively removing electrical spikes while ignoring wave packets. Figure 6.14 shows the effect of the Hampel filter on both a series of pulses and a single pulse. The series of pulses shows that not every spike in the current to the electrodes generates a boundary-layer disturbance. The individual pulse shows the removal of the electrical noise without altering the wave packet. The second method was to take an FFT of the ensemble averaged time series and scale it to represent an estimate of the power spectral density. The scaling is necessary for comparison to PSDs generated from the Hampel filtered data. Equation 6.1 shows the relation used to generate the PSD estimate from the FFT [114].

$$PSD = \frac{2|FFT|^2}{N \cdot S}, \quad (6.1)$$

where FFT is the discrete fast-fourier transform of the ensemble average, N is the number of points in the sample, and S is the scaling factor for whatever window was used in the direct PSD calculation. For the Hamming window used in all other PSD calculations, the scaling factor is 0.54. Figure 6.15 shows the three different methods of calculating the PSD. The unfiltered time trace produced a lot of ringing at low frequencies and a higher noise floor. The Hampel filter removed the ringing and improved the noise without altering the second mode peak. The scaled FFT of the ensemble average shows a much lower power than the other two methods. This is due to the intermittent nature of the disturbances and the different methods of averaging in times without perturbations. Since the Hampel processing appears best, PSDs of the Hampel filtered data will be presented for spectral content and RMS fluctuation amplitudes were calculated directly from the time traces, identical to Table 6.3. This will avoid any issues with averaging when calculating the RMS fluctuations.

Figure 6.16 shows the difference between the power spectra before, during, and after pulsing. The obvious feature here is the large second-mode peak that is present at approximately 240 kHz during the low-current pulsing and not before and after pulsing.

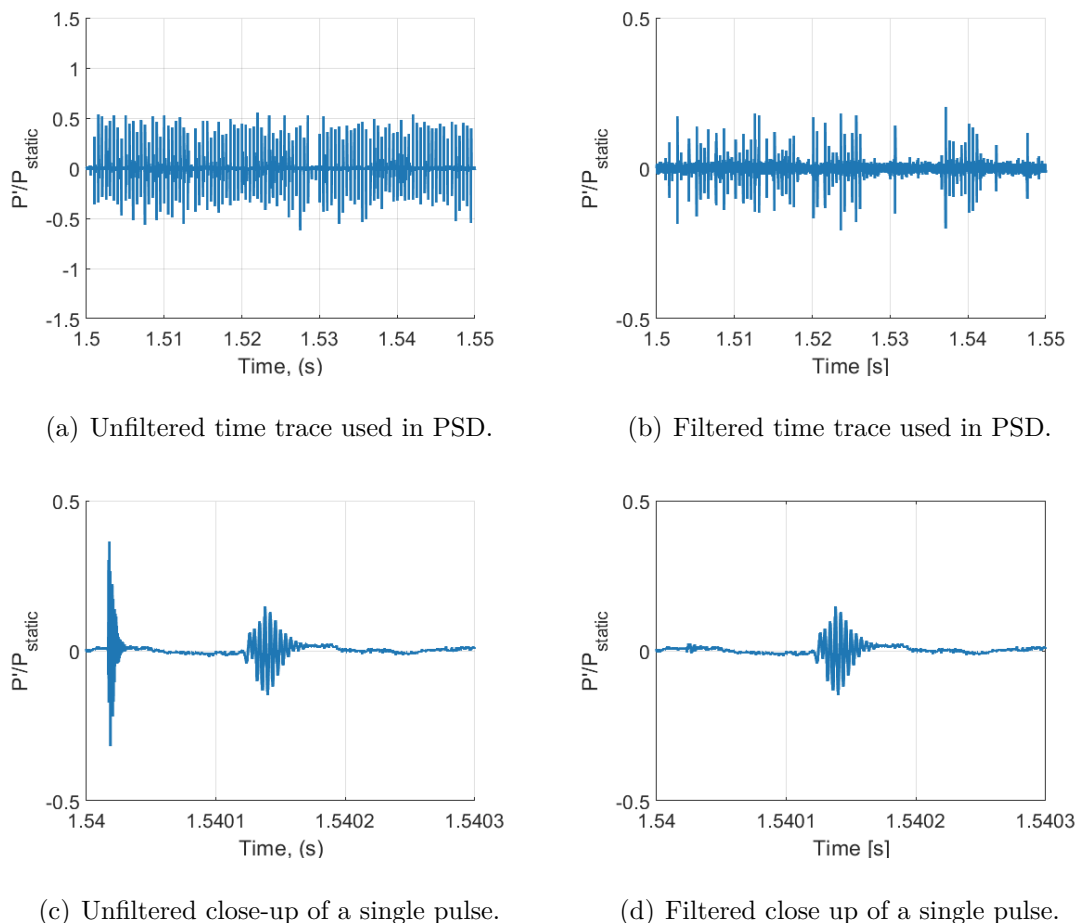


Figure 6.14. Example pressure fluctuations with and without filtering from 0.243m downstream from the nosetip. Processed during the low-current portion at  $Re_\infty = 7.6 \times 10^6/m$  (Run 1911)

This peak is not present at any location in the non-perturbation data presented in Figure 6.8. The perturber is effectively disturbing the boundary layer and the naturally unstable frequencies are growing from the disturbance.

Figure 6.17 shows the time traces and PSDs from all the sensors down the length of the cone during low current pulsing at  $Re_\infty = 7.7 \times 10^6/m$  (Run 1911). Figure 6.17(a) shows the development of the time traces for an individual pulse. The average convection velocity of this packet using the cross-correlation is 675 m/s. Each sensor

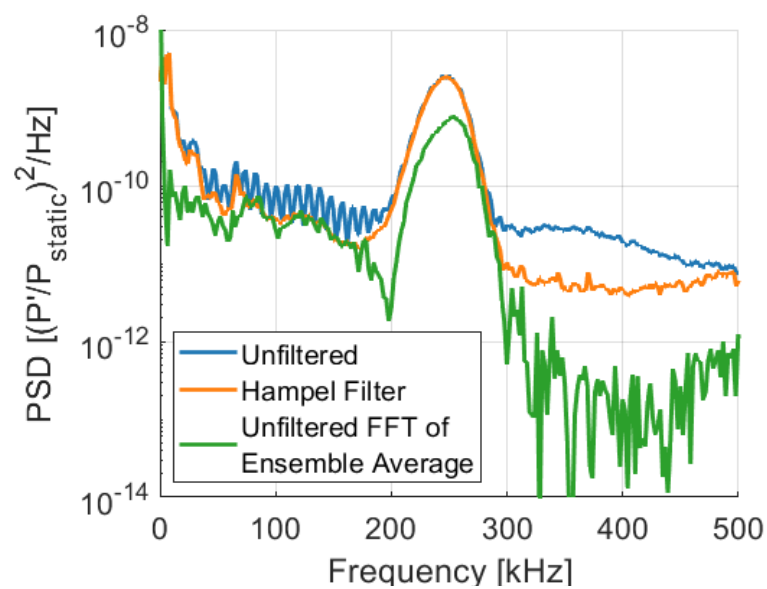


Figure 6.15. Comparison of three different PSD calculations.

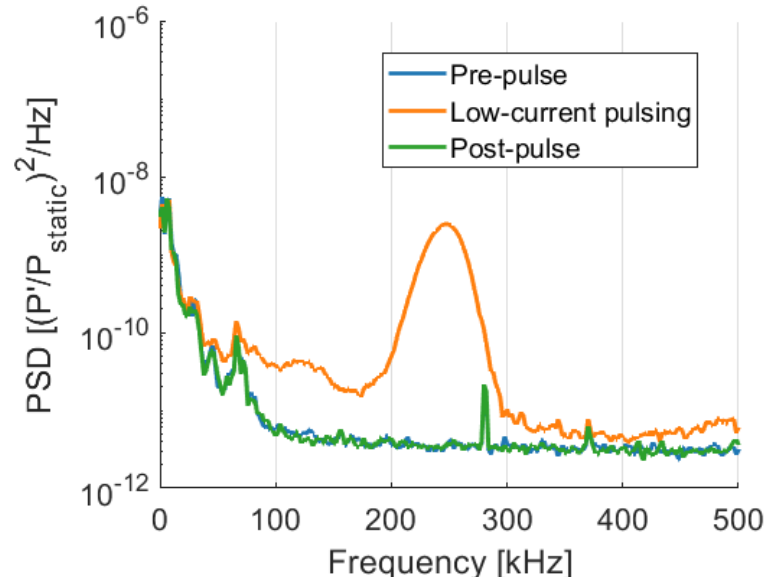


Figure 6.16. Comparison PSD's before, during, and after pulsing at  $Re_\infty = 7.6 \times 10^6/m$  (Run 1911).

is offset to clearly show pressure fluctuation development down the cone. At the initial sensors, the amplitude is small and hard to see. The wave packet amplitudes grow downstream until  $x = 0.344$  m. Downstream of this location, the amplitudes stop growing and begin to drop. The PSDs in Figures 6.17(b) and 6.17(c) show large second-mode waves at the first five sensors. The broadband power begins to increase at the last two sensors. This is indicative of transition and the locations correspond to the wave packets with decreasing amplitudes in the waterfall plot.

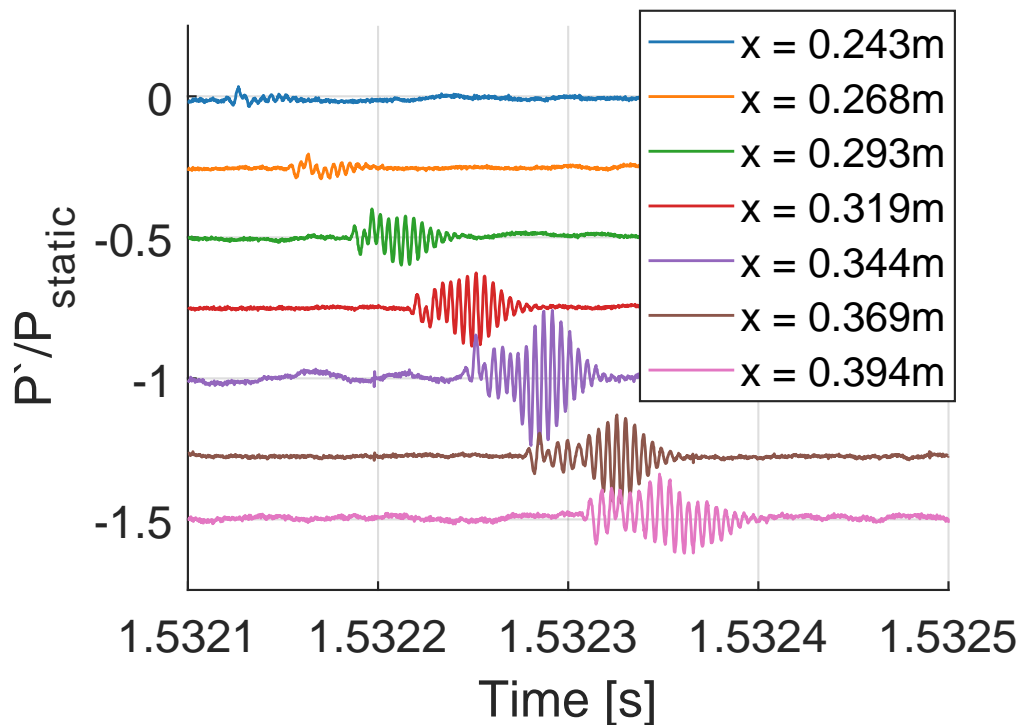
A similar plot for the high-current pulsing at  $Re_\infty = 7.6 \times 10^6/m$  (Run 1911) is seen in Figure 6.18. The waterfall plot in Figure 6.18(a) shows wave packets of much higher amplitude at this first sensor location. This is expected, since the higher current causes the temperature of the disturbance to be higher. A wave packet is seen growing until  $x = 0.293$  m and then it begins to breakdown. By the last three sensors the disturbance has completely broken down and becomes a turbulent spot. This can be seen in the PSDs in Figures 6.18(b) and 6.18(c). A peak present at the second-mode

frequency can be seen at the first several sensors. This peak is much wider than what was seen during the low current pulsing. The reason for this is not known. By  $x = 0.293$  m, the wave packets begin to breakdown and a broadband rise in spectral power is seen.

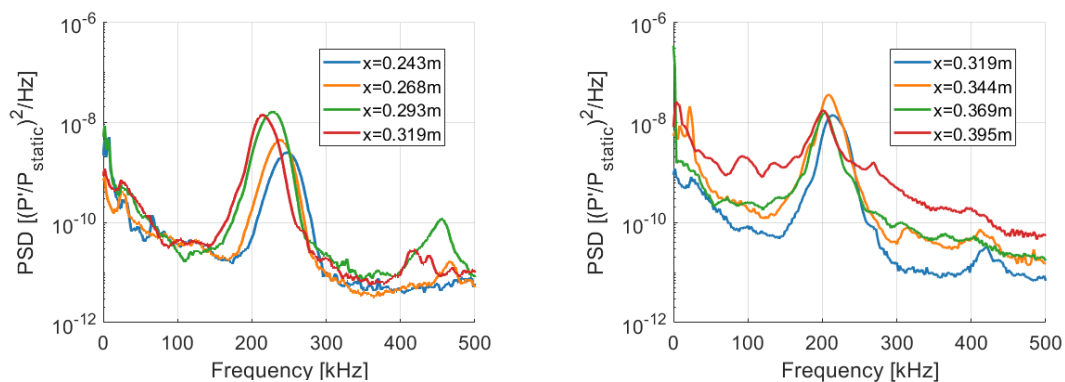
An analysis of the RMS amplitudes was done to compare the growth of fluctuations prior to transition using different perturbations. Figure 6.19 shows these for the low- and high-current pulsing at  $Re_\infty = 7.6 \times 10^6/m$ . For both perturbations, the amplitudes initially grow until the spots begin to breakdown. The highest wave amplitudes are seen just before breakdown. This is at  $x = 0.319$  m and  $x = 0.268$  m, for the low-current and high-current perturbations, respectively. After these locations, the amplitudes drop as the second-mode stops growing and broadband power begins to increase. The broadband power continues to increase until the end of the cone. This behavior is similar to that measured by Chynoweth on flared,  $2.5^\circ$ , and  $3^\circ$  cones [12]. To compare the results of artificially-generated second-mode wave packets to naturally occurring instabilities, the data were correlated with edge Mach number and compared to other data sets. Figure 6.20 shows the maximum second-mode magnitudes of several sets of data on different models from different facilities. All of these cases had transition dominated by the presence of second-mode waves within the boundary layer. Both cases of artificial perturbations lie below the linear fit provided by Marineau, but near data at similar edge Mach. Previous quiet flow data exhibited larger maximum second-mode magnitudes for a given edge Mach, except for the  $2.5^\circ$  cone. The artificial disturbances appear to saturate at lower amplitudes than other experiments under quiet flow. The second-mode waves from other experiments are likely two-dimensional or planar within the boundary layer. Unlike these cases, the artificial perturbations are three-dimensional disturbances generated at a single point on the cone. This will affect the non-linear breakdown. Natural smooth wall transition on a  $7^\circ$  cone has not been measured in quiet flow, so confirming lower second-mode amplitudes for artificial disturbances is not possible.

Figure 6.21 shows the effects of varying the voltage applied to the perturber electrodes on the model surface. The  $V_{applied} = 7.5$  kV case is not shown on this chart due to the complete lack of disturbances on the model surface for that case. At  $V_{applied} = 10$  kV and  $Re_{\infty} = 10.6 \times 10^6/m$ , a clear second mode peak is seen just below 300 kHz. Once the voltage is increased to 12.5 kV at  $Re_{\infty} = 10.7 \times 10^6/m$ , the amplitude and width of the peak increases greatly and the frequencies shift lower. The reason for the frequency change is not known, since the Reynolds numbers and boundary-layer thicknesses should be similar. It is possible that the disturbances are modulating the boundary layer in some unknown way. Lowering the Reynolds number with the 12.5 kV voltage produces a second-mode peak that looks similar to the  $V_{applied} = 10$  kV case but a lower frequency. The frequency differences are likely due to Reynolds number differences. The amplitudes and subsequent transition location on the cone can be directly controlled by varying the voltage potential applied to the electrodes. This is due to the applied voltage being directly related to the current of the breakdown and therefore, the amplitude of the perturbation.

In summary, experiments on a  $7^{\circ}$  cone with artificial perturbation were completed within the BAM6QT. Measurements of current and voltage allowed for inferences of the perturbation type and the repeatability of individual pulses. Applying appropriate filtering and data processing techniques allowed for meaningful measurements of instability content downstream of the perturbation. Wave packet behavior and breakdown were measured at various unit Reynolds numbers. Second-mode amplitudes were compared to previous experiments within the BAM6QT. Maximum second-mode pressure fluctuations reached 8-10% of the mean static pressure. Finally, the amplitude of the perturbation can be controlled by varying the voltage applied to the perturber electrodes.

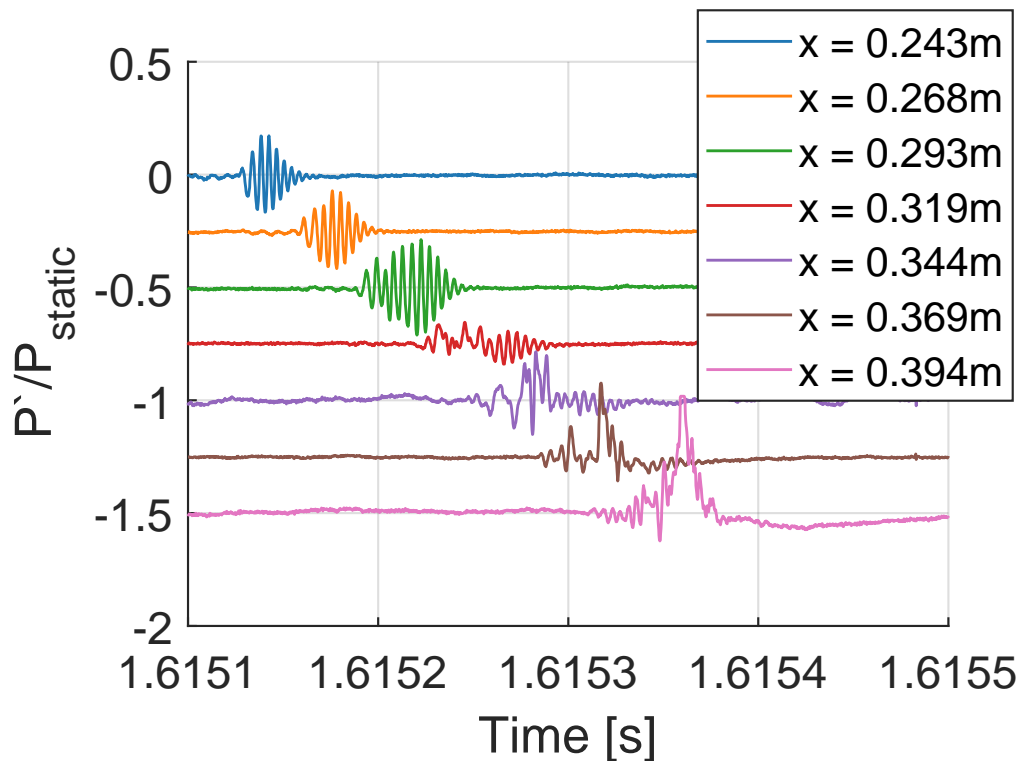


(a) Waterfall plot of an individual disturbance developing down the length of the cone. The pressures have been offset to improve readability.

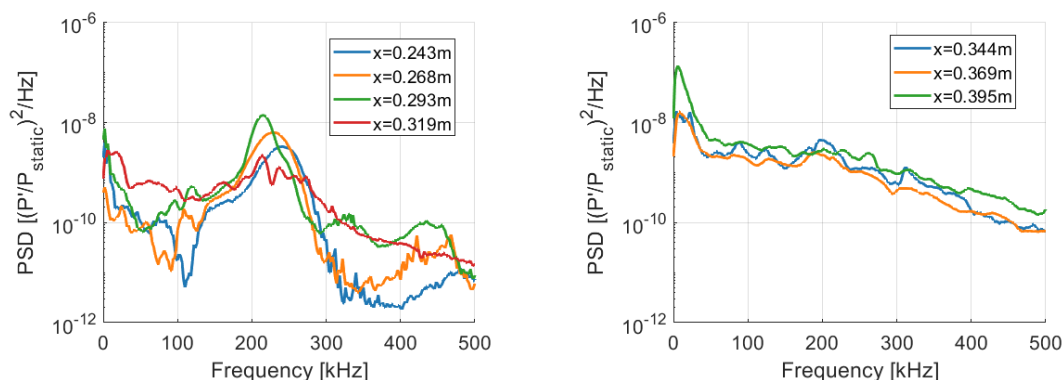


(b) PSDs of the first four sensors on the cone. (c) PSDs of the last three sensors on the cone .

Figure 6.17. PSD down the length of the cone at  $Re_\infty = 7.6 \times 10^6/m$  (Run 1911) during low-current pulsing.



(a) Waterfall plot of an individual disturbance developing down the length of the cone. The pressures have been offset to improve readability.



(b) PSDs of the first four sensors on the cone. (c) PSDs of the last three sensors on the cone .

Figure 6.18. PSD down the length of the cone at  $Re_\infty = 7.6 \times 10^6/m$  (Run 1911) during high-current pulsing.

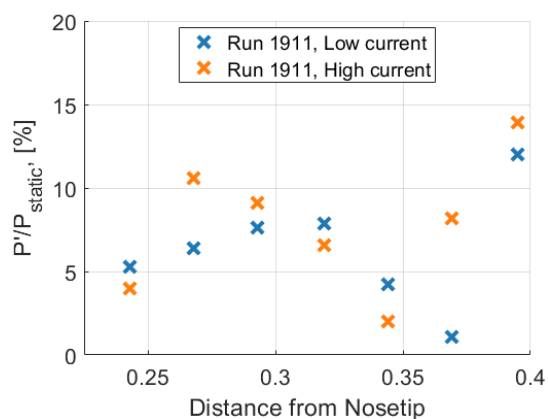


Figure 6.19. RMS pressure fluctuations on the cone for  $Re_\infty = 7.6 \times 10^6/m$  during perturbations.

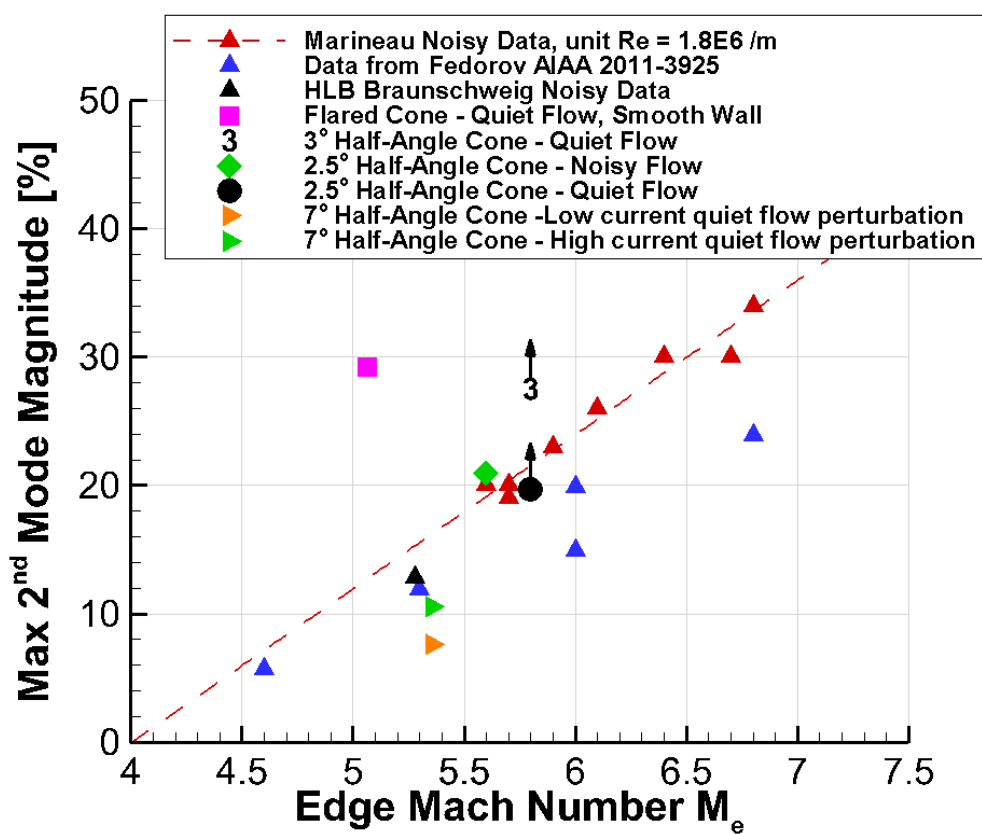


Figure 6.20. Maximum second mode amplitudes versus Mach for several models and facilities. Non-perturbation data were obtained from Chynoweth [12].

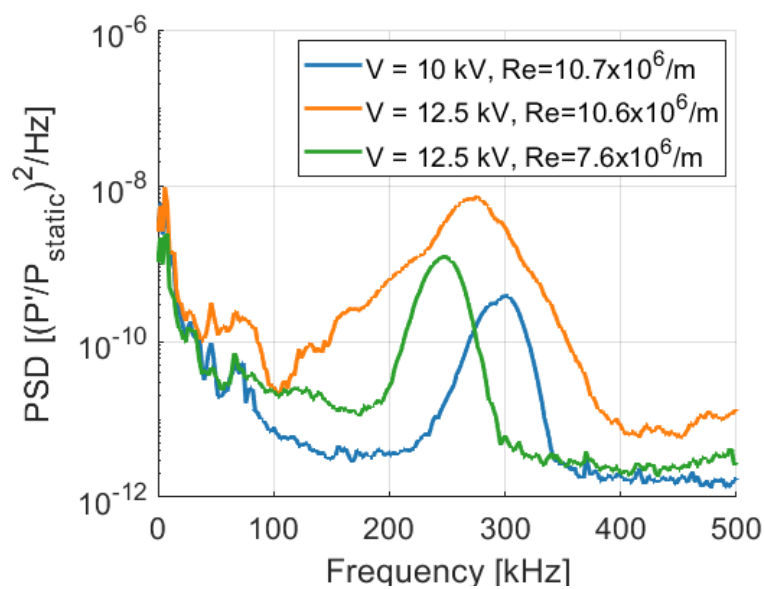


Figure 6.21. Comparison of PSD spectra with various  $V_{applied}$  at several Reynolds numbers 0.243 m from the nosetip.

## 7. MEASUREMENTS OF GENERATED DISTURBANCES ON THE LONG-RAMP MODEL

Successfully utilizing a plasma perturbation to generate disturbances on a  $7^\circ$  cone was proof that the same technique could be adapted for use on the cone with a slice and ramp. The perturbation will be introduced upstream of the slice and allowed to convect through the shear layer above the separation. This will allow any unstable frequencies that amplify within the shear layer to be measured on the post-reattachment surface. Direct measurements of the shear layer were not feasible within the scope of the present work. By varying the Reynolds number, the breakdown of any traveling instabilities should be measurable as well. Information on the model can be found in Section 4.3. For these experiments, the perturber was located upstream of the slice, 0.221 m from the nosetip. Heat transfer imaging of the perturber experiments was not completed.

### 7.1 Plasma Perturbation on the Long-ramp Model

Due to the long-ramp model requiring much lower Reynolds numbers for observing transition than the  $7^\circ$  cone, understanding the breakdown of the air under these new conditions is important. The lower stagnation pressure will change the density of the flow which will alter the breakdown physics. Table 7.1 shows the parameters chosen for testing breakdown on the long-ramp model. A sweep of Reynolds numbers was completed for every set of pulser conditions. Additional runs were completed to assess repeatability and evaluate different data-acquisition methods. Due to time constraints, only the applied voltages were varied. No changes to pulse frequency or duration were made. Varying the voltage sent to the electrodes alters the resulting current and the type of plasma seen during the breakdown of the air. Similar to the

7° cone results, the voltages and currents were measured for every run that utilized the pulser. Figure 7.1 shows the behavior of the voltages and current for a single run with the cone-slice-ramp model. For every run, pulsing was nominally constant for all 300 pulses sent to the electrodes. Figure 7.1(a) shows the ensemble average current with three individual pulses during the run. The current pulses featured an initial rise to 5 A and an additional second spike above 8 A. These currents are indicative of abnormal glows or arcing. The current pulses fell within 25% of the mean and produced a similar peak current and current pulse shapes for every pulse. A PDF of this distribution can be seen in Figure 7.1(b). Figures 7.1(c) and 7.1(d) show similar plots for the applied voltage. The voltage is consistent over the series of pulses with variations within 20% of the mean. The breakdown of air during the lower Reynolds number runs appears to be more consistent than for the high Reynolds numbers used on the 7° cone. Table 7.2 shows the means and standard deviations for the plotted case. Statistics for other runs can be found in Appendix C.

Table 7.1. Electronics settings for runs with artificially generated disturbances on the cone-slice-ramp.

Runs	Pulse Duration (ns)	Frequency (kHz)	Number of Pulses	Voltage (kV)
2310-2322	100	2	300	10
2324, 2326-2333	100	2	300	5
2325, 2334-2340	100	2	300	2.5

Table 7.2. Electronics Statistics for Run 2310.

Runs	Mean $V_{RMS}$ (V)	Stand. Dev. $V_{RMS}$ (V)	Mean $I_{RMS}$ (A)	Stand. Dev. $I_{RMS}$ (A)
2310	4433	388	5.97	0.80

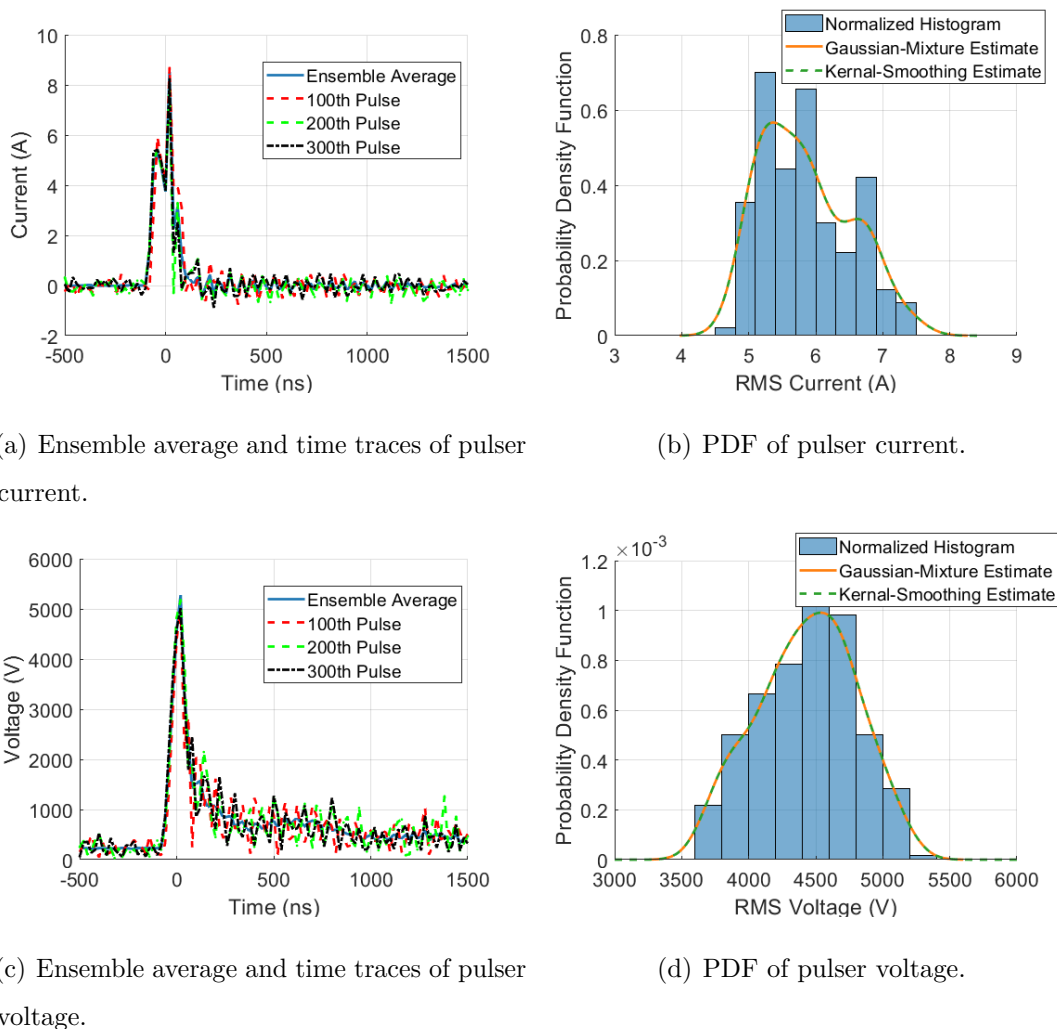


Figure 7.1. Electrical characteristics of pulser at  $Re_\infty = 1.9 \times 10^6/m$  (Run 2310).

Voltage and current measurements were taken at higher sampling rates to allow for a frequency analysis of the current pulse. Due to using a different oscilloscope, this was not possible for the  $7^\circ$  cone perturbations and only an FFT of a similar duration square wave was given. The Keysight Technologies oscilloscope was capable of sample rates of up to 5 GHz and was used to measure the current and voltage pulses at increased resolution. Figure 7.2 shows a sample pulse acquired at a 5 GHz sampling rate. The current trace in Figure 7.2(a) shows a shape similar to those observed using a lower sampling rate (Figure 7.1(a)). The peak current in this case is

higher than the peak current in Figure 7.1(a). The voltage in Figure 7.2(b) shows similar differences to the lower sampling rate case. The peak voltage is slightly higher and more ringing is seen after the main pulse. To determine the range of frequencies that are excited by the current pulse, an FFT was calculated and plotted in Figure 7.2(c) and 7.2(d). The FFT shows nearly level frequency content below 2 MHz and the first lobe extending to 8 MHz. A 100 ns pulse duration should theoretically have a first lobe extending out to 12.5 MHz but the actual breakdown differed from a perfect square wave. This pulse duration is shorter than is needed for exciting boundary layer instabilities. Previous  $7^\circ$  cone results showed it is effective.

## 7.2 Measurements of Perturbations on the Cone-Slice-Ramp

With reasonably consistent breakdown behavior of the air, the pressure fluctuations on the cone should be repeatable and the post-reattachment behavior of the perturbation can be measured. An individual PCB sensor was present immediately behind the perturber and was the first to measure any possible wave packets generated by the plasma. Figure 7.3 shows the full time trace and a close up of two individual pulses immediately behind the perturber. The electrical noise at this location dominates the time series and lasts too long to effectively use a Hampel filter to remove noise spikes. No wave packet can be seen on the sensor and the mean is changing with time. Since the PCB is an AC sensor, this behavior is not expected and worrisome. The noise at this location is too large to allow for measurements of the perturbation. It is believed that the increase in noise is due to this sensor sharing the aluminum cone body and sensor channel with the perturber. Therefore, the sensor was inadequately shielded from the EMI and did not yield useful results.

### 7.2.1 Effect of Perturbations within the Separated Region

Measurements on the slice and ramp were scrutinized to see if any effect from the perturbation can be seen within the separated region. Heat transfer and oil flow

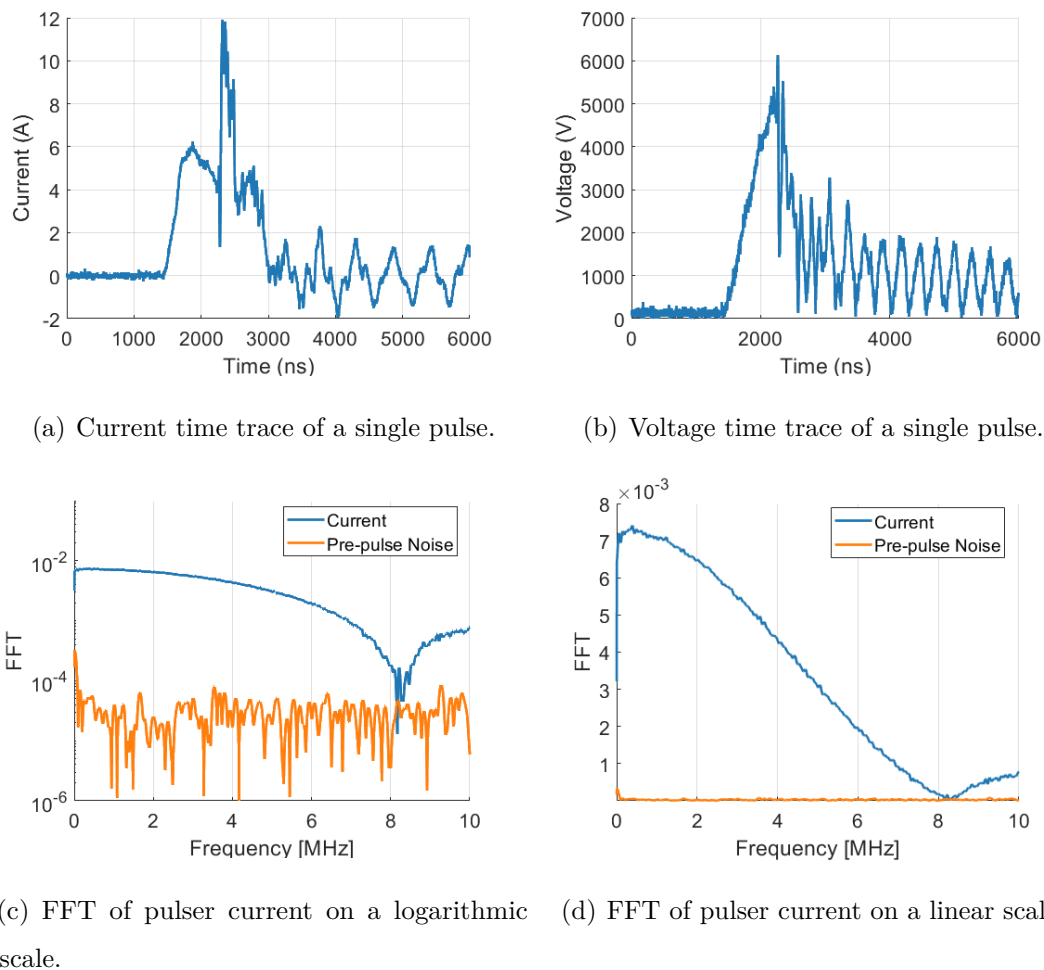


Figure 7.2. Electrical characteristics of pulser sampled at 5 GHz at  $Re_\infty = 2.1 \times 10^6/m$  (Run 2321).

measurements had indicated a reattachment location of approximately 0.36 m to 0.37 m from the nosetip. A plot of Stanton number with the ramp sensor locations within this region labeled is seen in Figure 7.4. The slice sensors are not shown but are located upstream of the ramp on the centerline. Figure 7.5 shows the time trace from the farthest downstream slice sensor. The behavior is similar to Figure 7.3. The slice sensors were in the same piece of aluminum as the perturber and increased EMI can be seen. It is particularly important for sensors to be in a different piece of metal, for

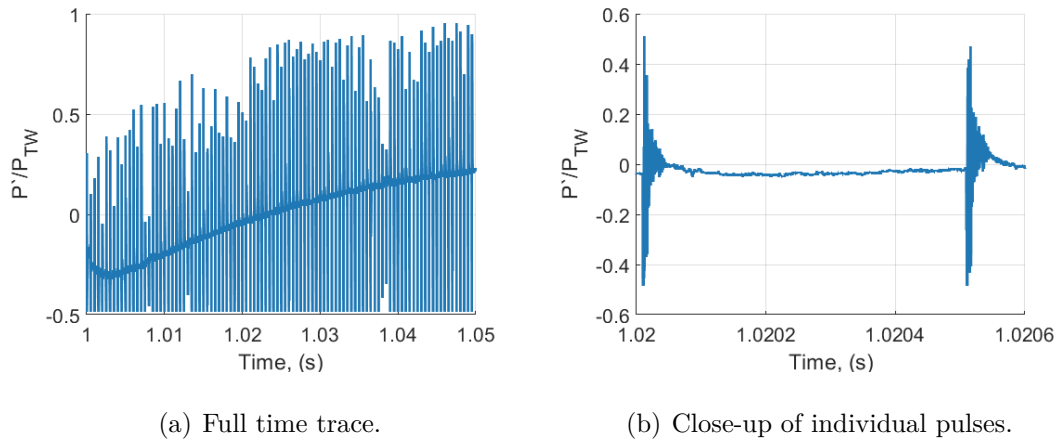


Figure 7.3. Time trace of PCB directly downstream of the perturber insert ( $x = 0.273$  m) on the cone portion of the model at  $Re_\infty = 2.0 \times 10^6/m$  (Run 2310).

EMI reduction. Due to this noise, PSDs and coherences could not be calculated for the slice sensors.

Figure 7.6 shows a waterfall plot of the slice and ramp PCBs at two unit Reynolds numbers within the separated region. The first three sensors were located on the slice. Even with the shifting mean and excessive noise, an attempt to see fluctuations indicative of the perturbation was made. EMI can be seen just after  $0 \mu$  for every slice sensor. Slight variations in the ensemble average can be seen near  $100\text{-}150 \mu$ . This could be evidence of the perturbation but interpretation is difficult due to the EMI at these sensor locations.

The first ramp PCB is at  $x = 0.329$  m downstream and every subsequent line is the next sensor downstream. At the first ramp PCB, a possible fluctuation can be seen at approximately  $175 \mu$ . Starting at the second PCB, a wave is measured at approximately  $150 \mu$ . Oddly, this is before the possible fluctuation seen at the farther upstream sensor. The reason for this is known but the fluctuations measured on the first ramp sensor are not traveling in the downstream direction. From  $x = 0.341$  m to  $0.365$  m downstream, the wave occurs at later times after the trigger. Based on the presence of traveling waves, it appears the perturbation affects the surface pressure

fluctuations within the separated region or affects the extent of the separation itself. The mechanism for this is not known.

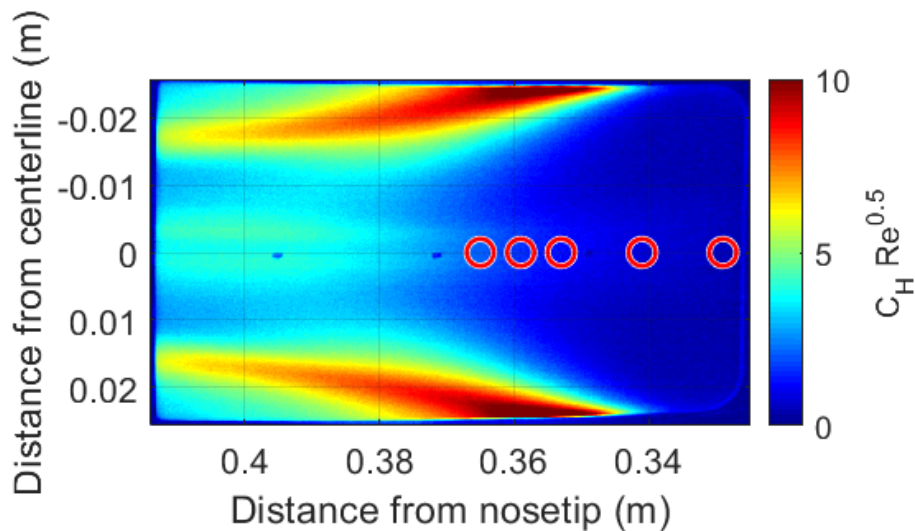


Figure 7.4. IR Stanton number of the ramp at  $Re_\infty=2.5\times 10^6/m$  (Run 2013). The red circles represent the PCBs located within separation on the ramp. Flow is from right to left.

PSDs and coherences were calculated to get a better understanding of the wave packet behavior on the ramp. Figure 7.7 shows PSDs and coherences for ramp PCBs within the separated region with and without 10 kV pulsing. The results without perturbation are shown in Figures 7.7(a) and 7.7(b). No distinct peaks can be seen in the PSD for any of the sensor locations. This is similar to what was presented in Section 5.2 for this Reynolds number. The coherences show little relation. Some small peaks exist below 100 kHz for three of the sensors but they barely reach significant levels and without peaks in the spectra no conclusion can be made. The results with perturbation can be seen in Figures 7.7(c) and 7.7(d). The two farthest upstream sensors do not have any significant peaks in the power spectra. The next three show

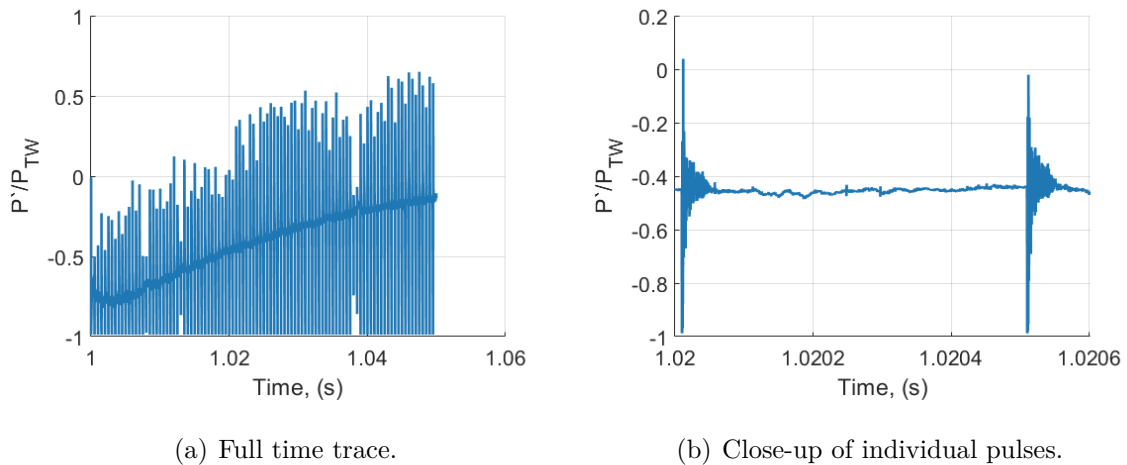
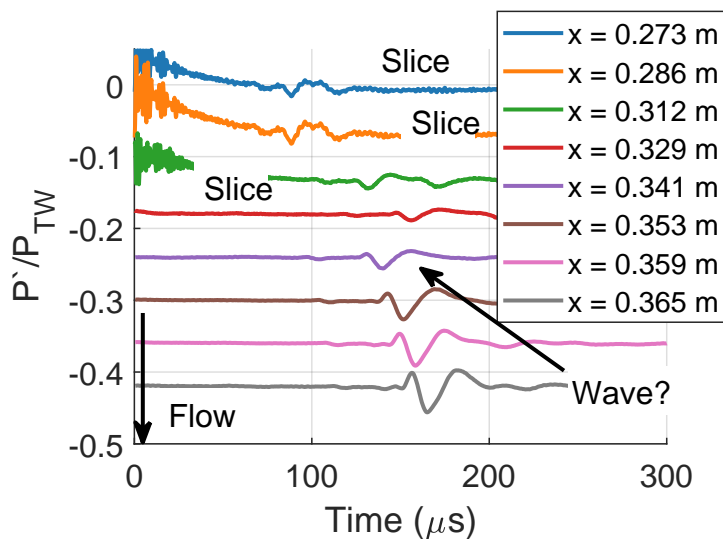


Figure 7.5. Time trace of last PCB on the slice ( $x = 0.312$  m) at  $Re_\infty = 2.0 \times 10^6/m$  (Run 2310).

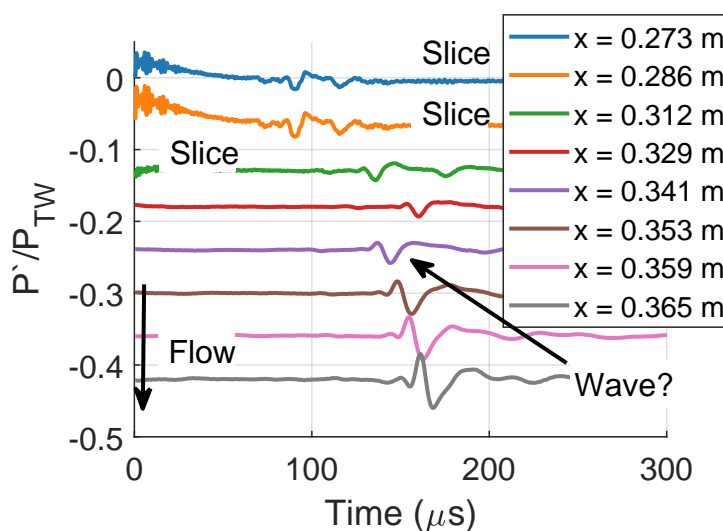
frequency content below 110kHz. Two peaks appear to form at approximately 35 and 85 kHz. Coherences between these sensors show significant relation at these frequencies and at all frequencies below 100 kHz. This behavior is possibly due to the perturbations convecting near the surface or some other mechanism in the flow.

### 7.2.2 Measurements of Traveling Waves Post-Reattachment

The first sensor definitively after the reattachment location from Section 4.2 is believed to be 0.371 m downstream of the nosetip. This location will be considered the first post-reattachment sensor. Figure 7.8 shows the locations of all post-reattachment centerline sensors with reference to IR Stanton number. Exact locations of these sensors can be seen in Table 7.3. Figure 7.9 shows a waterfall plot at two Reynolds numbers for these sensors. Waves are seen at every sensor location and are larger than any of those seen within the separated region. This is presumably due to the surface pressure fluctuations being largest when the boundary layer is completely reattached. The  $Re_\infty = 2.0 \times 10^6/m$  case, seen in Figure 7.9(a), shows continuous convection of the wave with no breakdown to turbulence. The wave packets grow and lengthen as the



(a)  $Re_\infty = 2.0 \times 10^6 / m$  (Run 2310).



(b)  $Re_\infty = 3.3 \times 10^6 / m$  (Run 2314).

Figure 7.6. Waterfall plots of ensemble averaged separation PCB time traces. Each time trace is offset from the others for clarity. TSP and IR indicated that reattachment occurs between 0.36-0.37 m downstream from nosetip.

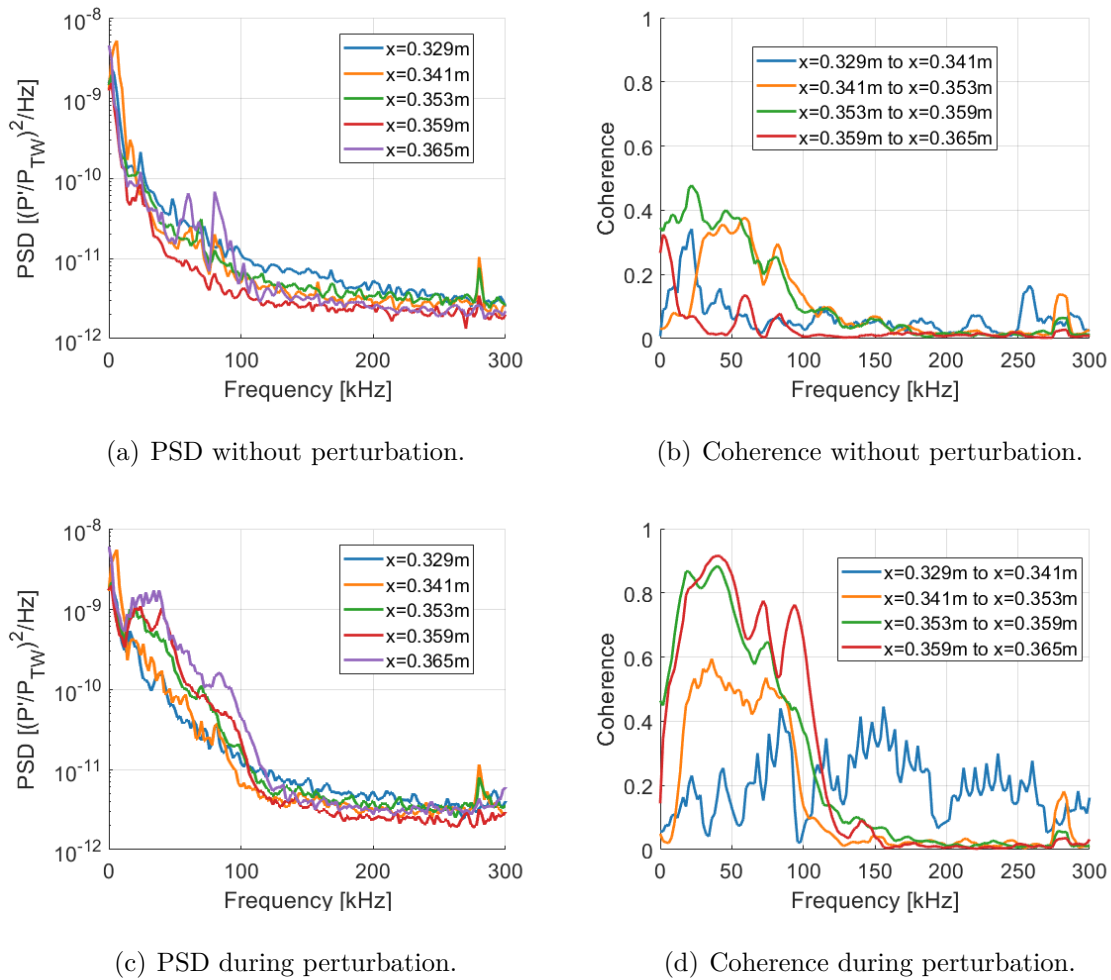


Figure 7.7. PSDs and coherences of separation PCBs with and without 10 kV perturbation at  $\text{Re}_\infty = 2.0 \times 10^6/\text{m}$  (Run 2310).

travel downstream. The  $\text{Re}_\infty = 3.3 \times 10^6/\text{m}$  case does show breakdown of the waves. This can initially be seen as the reduction in peak wave amplitude and spreading out of the wave packet at the third to last sensor. The wave packet becomes less smooth and more erratic as the packets break down. Similar wave packets, generated by a freestream laser perturbations, were measured by Chou on a flared cone [122]. Average convection velocity of the wave packet for the  $\text{Re}_\infty = 2.0 \times 10^6/\text{m}$  case according to cross-correlation time lags was found to be 768 m/s, or 88.8% of the freestream velocity.

Table 7.4 shows the average convection velocities for various Reynolds numbers for the post-reattachment perturbations. The measurements show that it is possible to measure a post-reattachment wave packet and its breakdown to turbulence with the current capabilities of the BAM6QT.

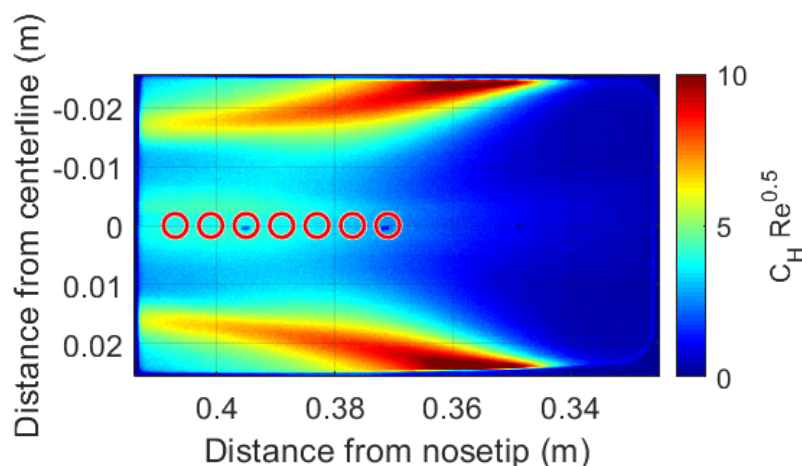


Figure 7.8. IR Stanton number of the ramp at  $Re_\infty=2.5\times 10^6/m$ . The red circles represent the PCBs located on the ramp. Flow is from right to left.

Since the perturbations traveled through the shear layer, PSDs and coherences for post-reattachment sensors can show the behavior of traveling instabilities that reattach to the surface and continue convecting. Figures 7.10 and 7.11 show PSDs and coherences for PCB signals with no perturbation and with 10 kV perturbations. Figure 7.10 shows the first four post-reattachment PCBs and Figure 7.11 show the final three. The upstream sensor boundary-layer behavior with no perturbation can be seen in Figures 7.10(a) and 7.10(b). No frequency content is seen at any post-reattachment PCB location and low coherences can be seen between any two sensors. This agrees with previous results at this unit Reynolds number. Similar plots for the upstream sensors at 10 kV perturbations can be seen in Figures 7.10(c) and 7.10(d). PSDs show

Table 7.3. Locations of sensors shown in Figure 7.8.

Distance from nosetip (m)
0.371
0.377
0.383
0.389
0.395
0.401
0.407

Table 7.4. Post-reattachment wave packet convection velocities for 10 kV pulsing at various Re.

Run	Reynolds Number (1/m)	Mean Convection Velocity ( $\frac{u_{spot}}{u_{\infty}}$ )
2310	$2.0 \times 10^6 / \text{m}$	88.8
2311	$2.2 \times 10^6 / \text{m}$	89.0
2312	$2.5 \times 10^6 / \text{m}$	89.6
2313	$2.9 \times 10^6 / \text{m}$	86.1

a clear peak progressing from 40 kHz at  $x = 0.371$  m to 70 kHz at 0.389 m. The peak on the first two sensors is harder to distinguish but strong coherences are centered at approximately 50 kHz.

The downstream PCBs with no perturbation and 10 kV perturbations can be seen in figure 7.11. The no-perturbation behavior can be seen in Figures 7.11(a) and 7.11(b) and is similar to the four upstream sensors. The downstream sensors with the 10 kV perturbation are shown in Figures 7.11(c) and 7.11(d). The peak has shifted in frequency to approximately 80kHz and does not continue to shift to

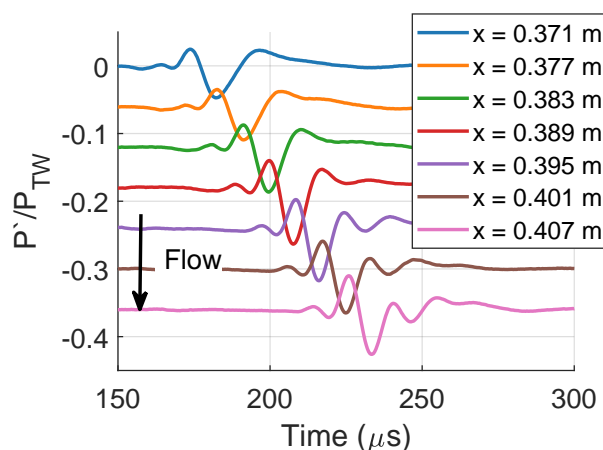
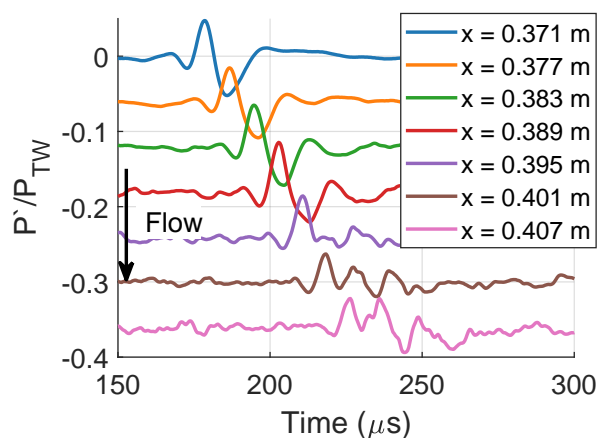
(a)  $Re_{\infty} = 2.0 \times 10^6 / m$  (Run 2310).(b)  $Re_{\infty} = 3.3 \times 10^6 / m$  (Run 2314).

Figure 7.9. Waterfall plots of ensemble averaged post-reattachment PCB time traces with 10 kV pulsing. Each time trace is offset from the others for clarity.

higher frequencies. Additionally, the amplitude has appeared to stop growing at this location. The coherences are near unity between these sensors. Without knowledge of the physical mechanisms for how these waves grow and convect, inferring the reason for this behavior is difficult. If they behave like second-mode waves, this could be a

sign of the boundary-layer thinning after reattachment. It might also be how the wave packets, that have grown in the shear layer respond to the boundary layer reattaching to the model surface. The development of RMS amplitudes with streamwise distance is show in Figure 7.12. The wave packets amplify until 0.389 m downstream of the nosetip. At all three Reynolds numbers, the largest amplitude is measured 0.389 m downstream from the nosetip. After this point, the RMS amplitudes of the fluctuations reduce. This behavior could be due to the reattached boundary-layer having different stability properties than the shear layer. It is assumed that these waves constitute an instability and are primarily due to the unstable frequencies in the shear layer being amplified in the perturbation and reattaching to the surface with the boundary layer. It is then measurable by the PCB sensors. This is the first measurement of a traveling instability due to a finite-span hypersonic shear layer under quiet flow. Computations were not available at the time for comparison.

It is desired for the perturbations generated by the plasma to be repeatable. This would ensure that when other parameters are changed, any difference in the resulting measurement is not due to variations in the perturbation. Two methods were used to assess the repeatability of the perturbations for runs at similar conditions. The first was looking at the PSDs and comparing the amplified frequencies within the perturbations. This also gave a qualitative look at the amplitude of the perturbation. The second method was directly comparing the RMS fluctuation amplitudes of the pulses to gain a quantitative understanding of the amplitude repeatability. Figure 7.13 shows the power spectra for three post-reattachment PCBs over four different runs during the course of several days. The unit Reynolds numbers for each run are shown in the legends. Every run had a slightly different Reynolds number due to issues with diaphragms not bursting reliably at lower Reynolds numbers. Triggering of the pulser always occurred one second into the run and only lasted 0.15 seconds. Thus, fine control of Reynolds numbers during a run was not available due to the short window to process data. The best attempt at matching unit Reynolds number was made and

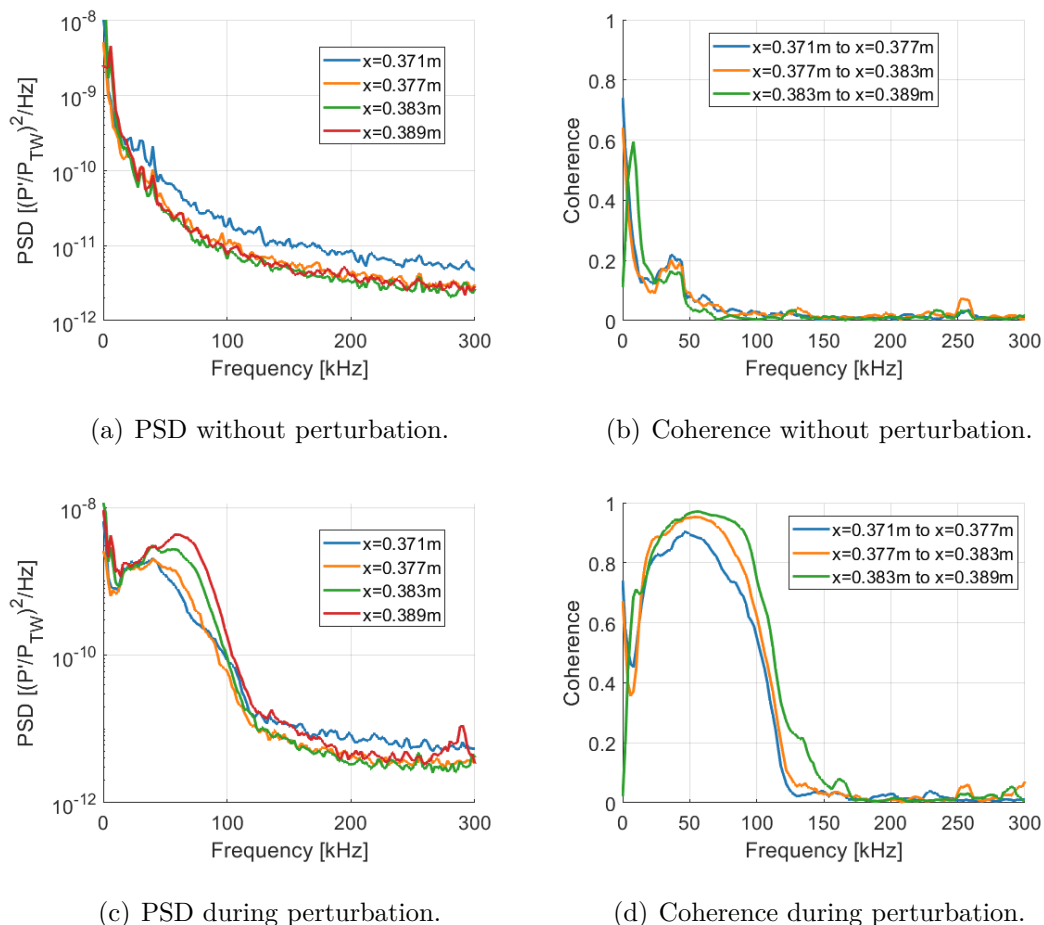


Figure 7.10. PSDs and coherences of upstream post-reattachment PCBs with and without perturbation at  $\text{Re}_\infty = 2.0 \times 10^6/\text{m}$  (Run 2310).

presented. Reynolds numbers for the four repeatability runs were within 5% of the average unit Reynolds number.

For all three sensor locations, the centers of the primary peaks are nearly identical. There is little variation in the frequency bands at which instabilities grow downstream of the perturber insert. Frequencies above 100 kHz match well with some variation in broadband power for Figure 7.13(c). Qualitatively, peak amplitudes vary by a small amount at each sensor location. This is likely due to variations in the breakdown of the air but the small differences in unit Reynolds number could be contributing as

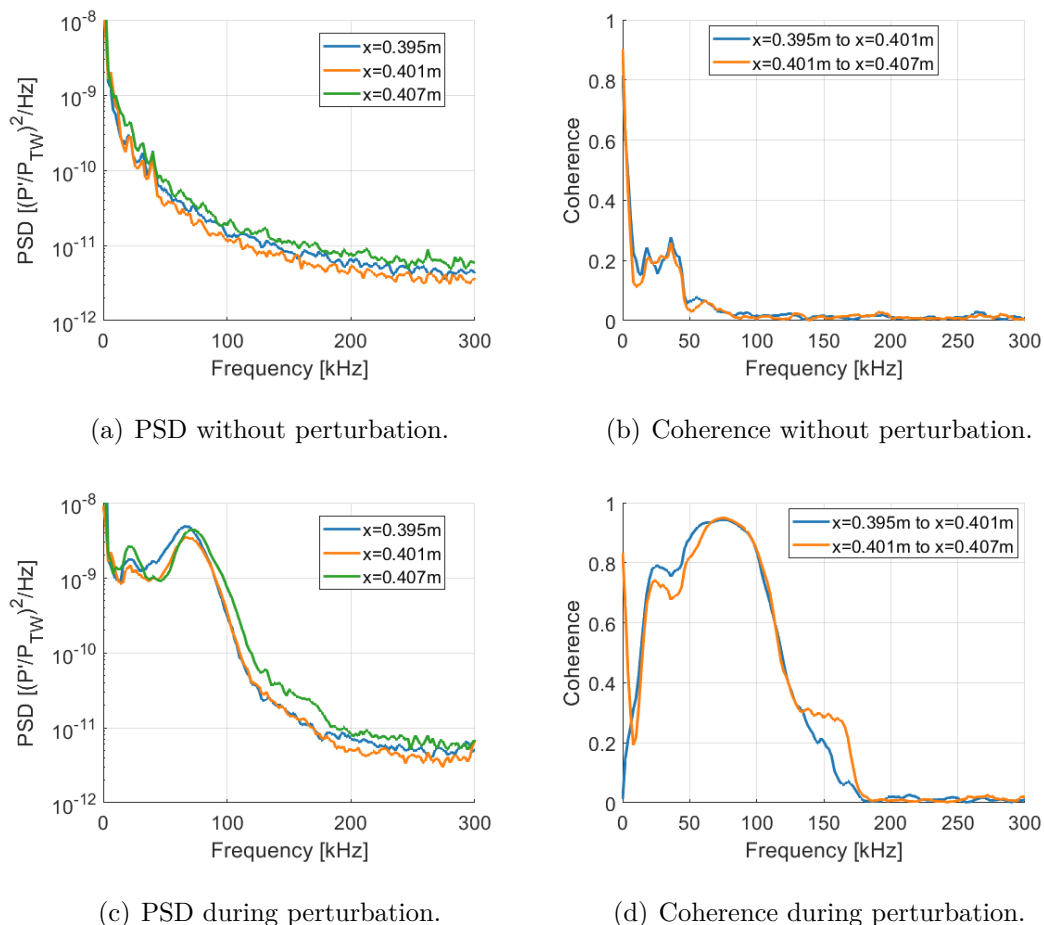


Figure 7.11. PSDs and coherences of downstream post-reattachment PCBs with and without perturbation at  $\text{Re}_\infty = 2.0 \times 10^6/\text{m}$  (Run 2310).

well. Figures 7.13(b) and Figure 7.13(c) have differences at frequencies below the primary peak at approximately 20 kHz. The reason for this is not known. However, these are not the primary amplified peaks and are at the very low end of frequency capability for the PCB132's. The amplitudes of the primary instability peaks for each plot were calculated. The PSDs were integrated for a 20 kHz band centered on the peak frequencies annotated on each plot in Figure 7.13. Variations in just the local amplitude of the peak at  $x = 0.383\text{ m}$  were within  $\pm 18\%$  of the mean amplitude. This improved at  $x = 0.395\text{ m}$  and  $x = 0.407\text{ m}$  to  $\pm 12\%$  and  $\pm 8\%$  of the mean

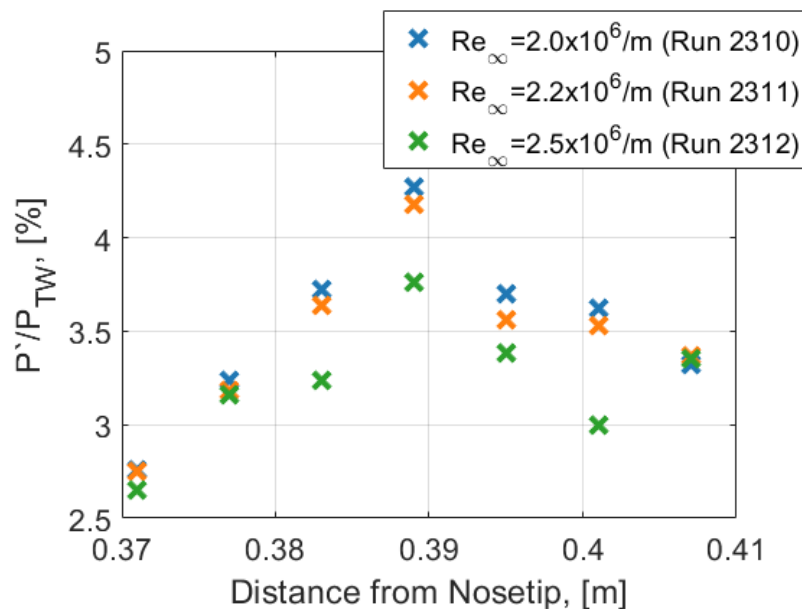


Figure 7.12. Effect of streamwise distance on Perturbation RMS amplitudes. Each color represents an individual run and each point is data from a single sensor on the ramp.

amplitude, respectively. Even with these small differences, the repeatability of PSDs seem acceptable for further experiments.

To quantify the repeatability, two different types of RMS amplitudes were evaluated to determine the reliability of the perturbations that are generated from the breakdown of the air. First is the repeatability of each individual perturbation generated during the 300 pulse burst. Table 7.5 shows the RMS mean and RMS standard deviation for a Reynolds number sweep at 10kV pulsing. The lower Reynolds number runs have less variation in pulse-to-pulse RMS fluctuations. As the Reynolds number increases, the fluctuation amplitudes increase and the standard deviations slightly increase. The two highest Reynolds numbers cases are transitional or turbulent and have an increase in amplitudes. Standard deviations of the RMS amplitudes were between 30% and 50% of the mean RMS amplitude. Run-to-run variations of the mean perturbations were also calculated. Table 7.6 shows the variations in mean fluctuations for the

same runs and sensors as Figure 7.13. For every sensor location, the single-run RMS fluctuations are within 10% of the mean run-to-run RMS fluctuation. This confirms the repeatability seen in the PSDs. It was deemed that this level of repeatability was acceptable for the current experiments.

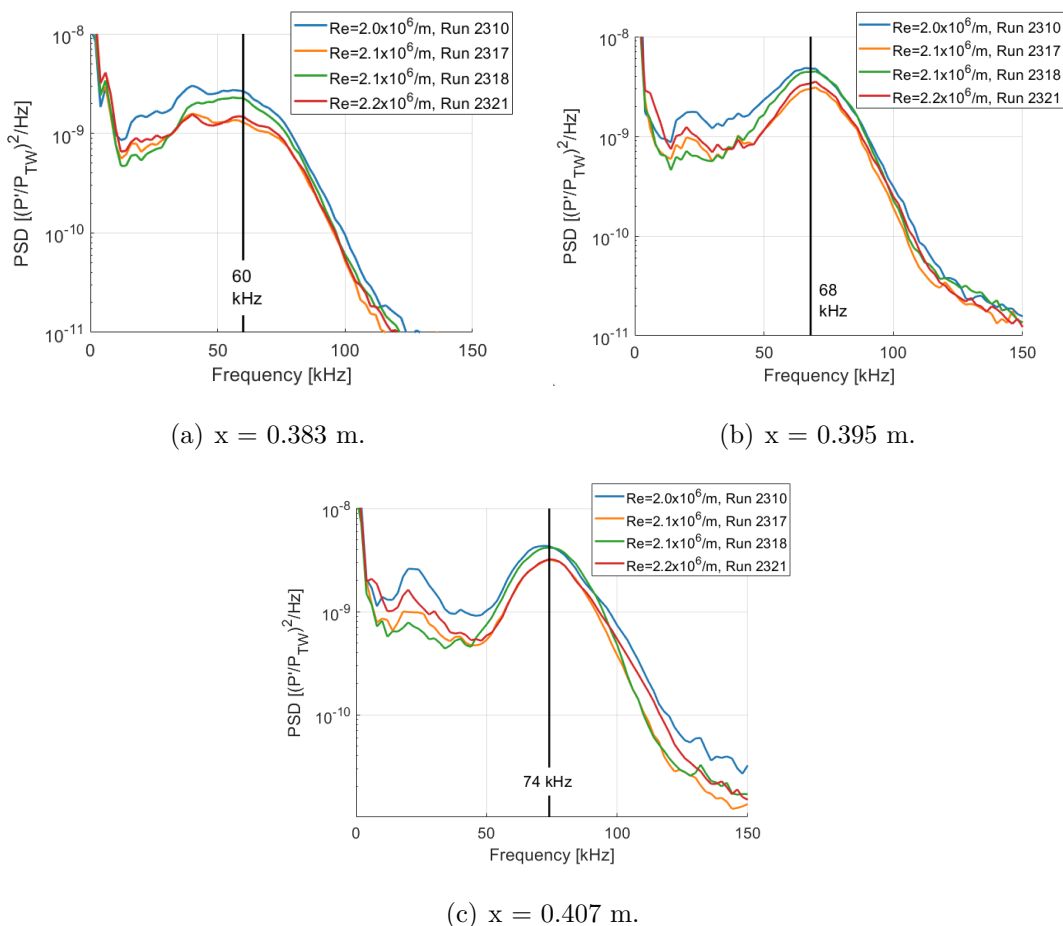


Figure 7.13. Spectral repeatability for several sensors downstream of reattachment.

The spanwise extent of the disturbances was investigated to determine if the perturbations were not traveling perfectly on the centerline or if they are growing and spreading. Spanwise sensors were located  $\pm 6.4$  mm off-centerline at every other streamwise sensor location. Two post-reattachment spanwise arrays will be scrutinized. Annotated locations of these sensors can be seen on a plot of Stanton number in Figure 7.14. The PSDs and coherences for these sensors are shown in Figures 7.15

Table 7.5. Pulse-to-pulse RMS pressure fluctuation statistics for the farthest downstream PCB at  $x = 0.407\text{m}$  and 10 kV pulsing.

Run	Unit Re (1/m)	$P'_{RMS}/P_{TW}$ Mean	$P'_{RMS}/P_{TW}$ St. Dev.	St. Dev./Mean (%)
2320	$1.5 \times 10^6/\text{m}$	0.0261	0.0079	30.3
2310	$2.0 \times 10^6/\text{m}$	0.0332	0.0147	44.3
2311	$2.2 \times 10^6/\text{m}$	0.0337	0.0162	48.1
2312	$2.5 \times 10^6/\text{m}$	0.0335	0.0148	44.2
2313	$2.9 \times 10^6/\text{m}$	0.0482	0.0215	44.7
2314	$3.3 \times 10^6/\text{m}$	0.0845	0.0224	26.5

Table 7.6. Run-to-run RMS pressure fluctuation repeatability for three sample sensors.

Run	PCB at $x = 0.383\text{ m}$ $P'_{RMS}/P_{TW}$ Mean	PCB at $x = 0.395\text{ m}$ $P'_{RMS}/P_{TW}$ Mean	PCB at $x = 0.407\text{ m}$ $P'_{RMS}/P_{TW}$ Mean
2310	0.0372	0.0370	0.0332
2317	0.0334	0.0328	0.0350
2318	0.0336	0.0331	0.0354
2321	0.0319	0.0318	0.0334
Mean	0.0340	0.0337	0.0343

and 7.16. The sensors immediately in front of the spanwise arrays were included to determine if any coherence exists between them and the off-centerline sensors. This will help determine if there is any spanwise movement in the perturbations. PSDs in Figure 7.15(a) show the two centerline sensors with large peaks at 80 kHz. The off-centerline sensors show small peaks at 80 kHz but they are harder to distinguish from the broadband noise. The amplitudes of these off-centerline peaks are similar.

Coherences in Figure 7.15(b) show the corresponding coherences for the spanwise sensors with the PCB immediately upstream. The centerline sensors show coherences near unity at and around the 80 kHz peak. Off-centerline coherences are significantly lower and are below the 80 kHz peak in power. It appears the perturbation is small and predominantly centered on the ramp at this location with some slight asymmetries appearing in the off-centerline coherences.

A similar plot for the downstream spanwise array can be seen in Figure 7.16. The centerline PCB PSDs show behavior that is similar to the upstream array. The perturbation amplitude is approximately the same at this location and clearer peaks can be seen off-centerline. The disturbance is not perfectly symmetric about the centerline. The frequencies of the off-centerline peaks have increased at the further downstream location. Coherences in Figure 7.16(b) show similar behavior as the other spanwise array. Near-unity coherence is present on the centerline sensors. The coherence from centerline to off-centerline locations show a significant peak at approximately 30 kHz. This does not correspond to the main peak within the perturbation and no significant coherence exists at the primary frequency. As a result, it appears that the perturbation is primarily located on the centerline. PCB fluctuation amplitudes drastically decrease with distance from the centerline and small coherences indicate little off-centerline movement of wave packets. Some asymmetries were present and could possibly be due to small non-zero yaw.

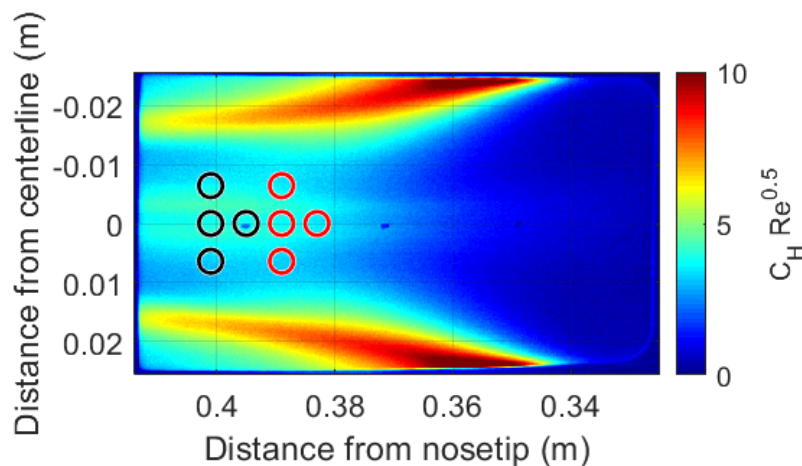


Figure 7.14. IR Stanton number of the ramp at  $Re_\infty=2.5 \times 10^6/m$  (Run 2013). The red circles represent the PCBs used in Figure 7.15. The black circles represent the PCBs used in Figure 7.16. Flow is from right to left.

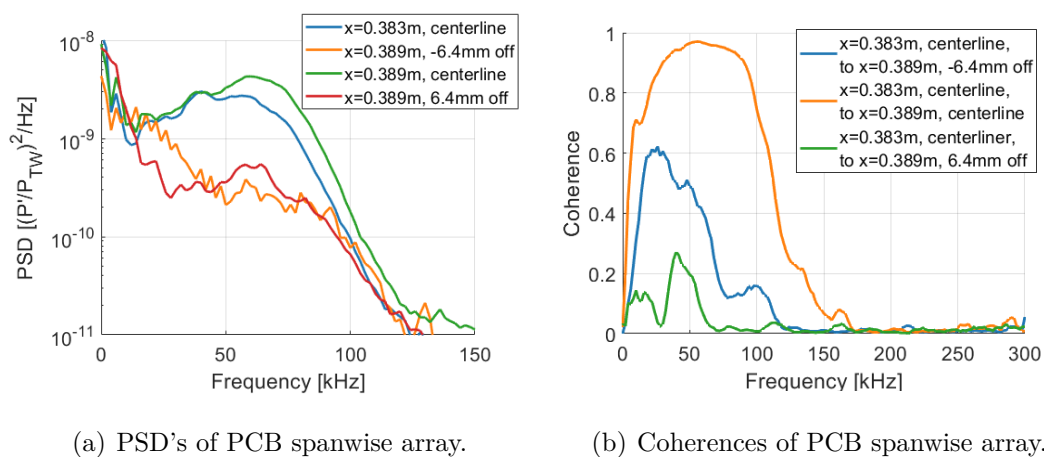
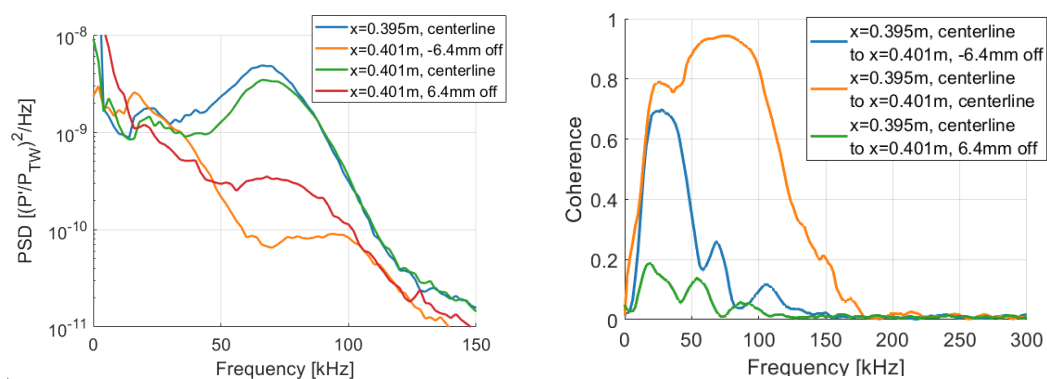


Figure 7.15. Spanwise effects on perturbation PSDs and coherences for a post-reattachment spanwise sensor array at  $x = 0.389$  m and  $Re_\infty = 2.5 \times 10^6/m$  (Run 2310). Coherences were taken from centerline sensor immediately in front of the spanwise array.



(a) PSD's of PCB spanwise array.

(b) Coherences of PCB spanwise array.

Figure 7.16. Spanwise effects on perturbation PSDs and coherences for a post-reattachment spanwise sensor array at  $x = 0.401$  m and  $\text{Re}_\infty = 2.5 \times 10^6/\text{m}$  (Run 2310). Coherences were taken from centerline sensor immediately in front of the spanwise array.

### 7.2.3 Effect of Reynolds Number on Post-Reattachment Waves

The previous section outlined the streamwise behavior, repeatability, and spanwise behavior of a sample perturbation on the cone-slice-ramp. Additionally, data were collected over a range of Reynolds numbers that encompass the transitional region for the experiments without perturbation. This allows for a comparison of transition location with and without perturbation at various Reynolds numbers.

A general idea of Reynolds number effects on post-reattachment pressure fluctuations can be gained by studying the time traces from each individual sensor. Figure 7.17 shows individual time traces and ensemble averages for the farthest downstream PCB at various unit Reynolds numbers. The three lowest Reynolds numbers in Figures 7.17(a)-7.17(c) show a wave packet present in every time trace. The amplitude of the wave increases slightly with Reynolds number and the durations are relatively similar. No other features can be seen before or after the perturbation. This was representative of every perturbation at these Reynolds numbers. The  $Re_\infty = 2.5 \times 10^6/m$  case in Figure 7.17(d) shows the typical perturbations generated by the pulser. The individual perturbations appear to be more chaotic and random than for the lower Reynolds number cases. This could be an indication of the wave packet breaking down to turbulence. However, fluctuations and a single large spot appear before and after the artificial perturbations. This implies that the undisturbed boundary layer is also beginning to transition at this Reynolds number. Figure 7.17(e) shows data from  $Re_\infty = 2.9 \times 10^6/m$ . The artificial perturbations are larger and even more chaotic, with smaller fluctuations present before and after. The presence of fluctuations in the undisturbed boundary layer appears random and no large spots appear at this instant in time. At  $Re_\infty > 2.5 \times 10^6/m$  the ensemble-averaged perturbation is smaller than any individual perturbation. This could be due to the wave packets breaking down into random fluctuations that average out. The highest tested Reynolds number is shown in Figure 7.17(f). The individual fluctuations are dominated by turbulent spots before, during, and after the pulsing. The ensemble average shows very small fluctuations

due to all the randomness being averaged out. Intermittency was calculated for each of the individual time traces for this case. The intermittency calculation picks up high-frequency content within the time trace to determine turbulence. Therefore, it appears that the large fluctuations present in the individual pulses are deemed turbulent for this window of time. The 100th pulse has more turbulent spots than the other two time traces.

Spectral development was investigated by computing PSDs of the time traces during pulsing at the various Reynolds numbers. A comparison of the streamwise spectral development at two Reynolds numbers can be seen in Figures 7.18 and 7.19. These plots expand upon the  $Re_\infty = 2.0 \times 10^6/m$  case from the previous section. The spectra in Figure 7.18(a) show a slightly higher Reynolds number of  $Re_\infty = 2.5 \times 10^6/m$ . Similar peaks can be seen growing downstream and shifting in frequency from 50 kHz to 80 kHz. However, at this Reynolds number broadband power levels are beginning to rise at  $x = 0.389$  m downstream. This is indicative of transition at those locations. Figure 7.18(b) shows the corresponding coherences between sensor pairs for this Reynolds number. The coherence peaks have widened for the transitional locations and more high-frequency coherence is measured between sensor pairs. Significant coherences extend above 150 kHz between sensors in this case. Figure 7.19 shows PSDs and coherences for a slightly higher Reynolds number of  $Re_\infty = 3.3 \times 10^6/m$ . PCB locations do not show clear peaks between 50-100 kHz. Instead, broadband power levels steadily rise at every sensor location. This is indicative of transition and no evidence of the perturbation can be seen. The coherences in Figure 7.19(b) show a large reduction in coherence from the lower Reynolds number case. Moderate coherence exists across a broad range of frequencies below 200 kHz. In this case, transition appears to be begin prior to reattachment. The post-reattachment measurements are not measuring instability at any location.

By looking at the spectral development with Reynolds number at a single location, the effect of Reynolds number can be directly observed. Figure 7.20 shows the spectral behavior at three downstream locations for a range of Reynolds numbers. Figure

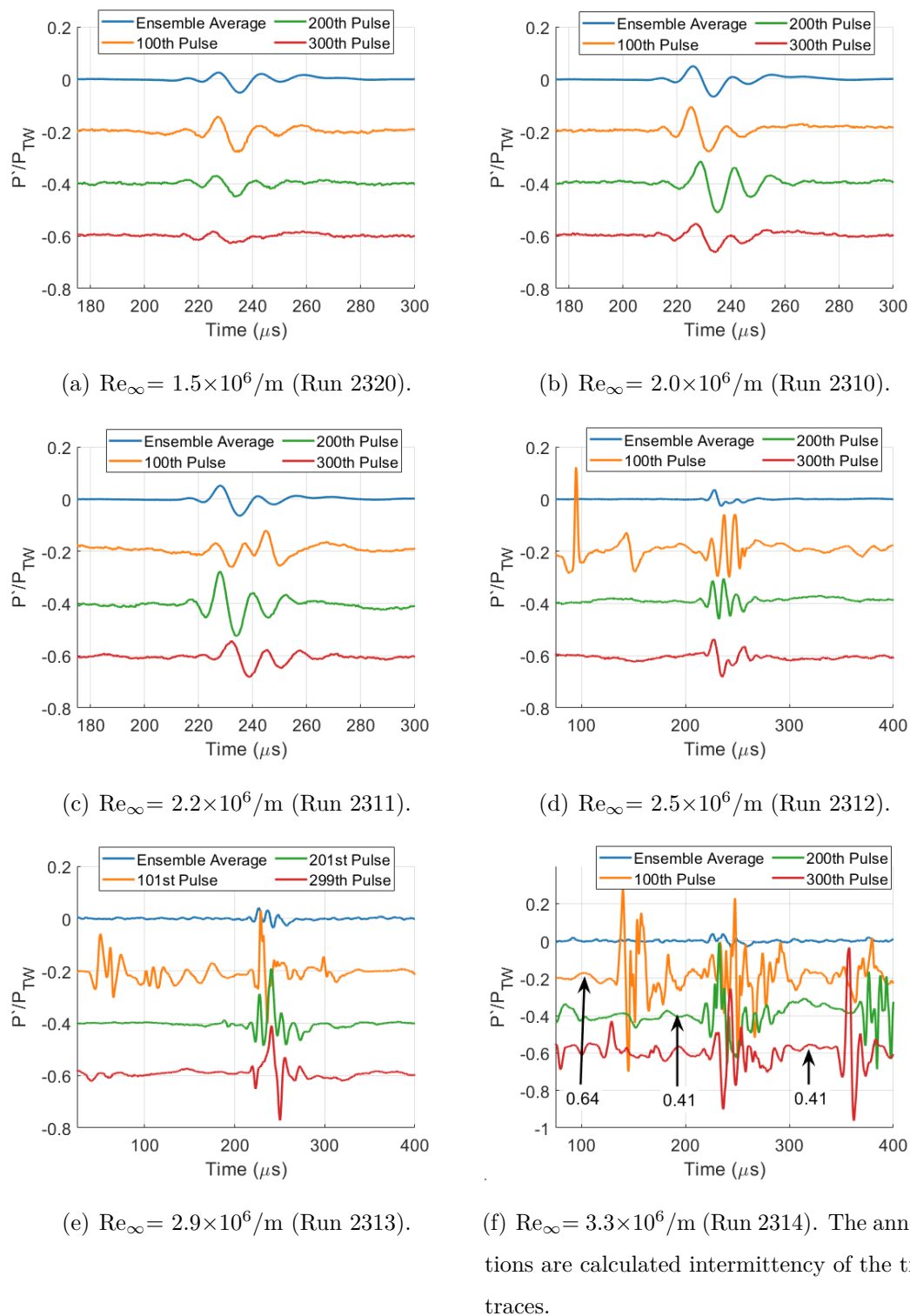


Figure 7.17. Ensemble averages and individual pulses of a PCB 0.407 m from the nosetip at various unit Reynolds numbers.

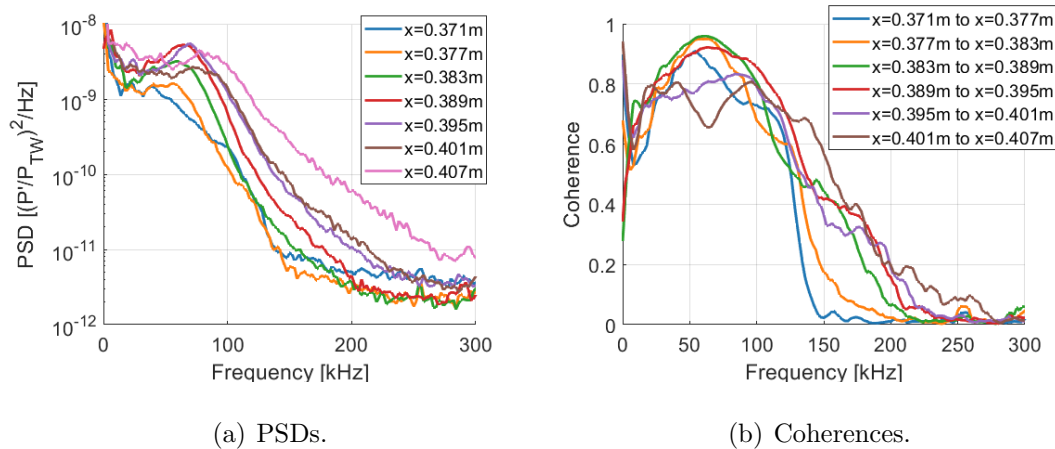


Figure 7.18. PCB PSDs and coherences during 10 kV perturbations at  $Re_\infty = 2.5 \times 10^6/\text{m}$  (Run 2312).

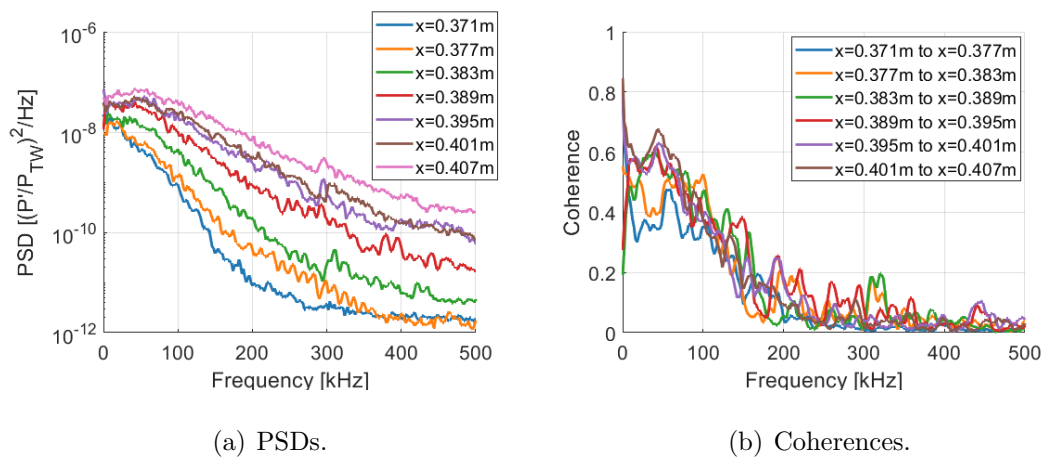


Figure 7.19. PCB PSDs and coherences during 10 kV perturbations at  $Re_\infty = 3.3 \times 10^6/\text{m}$  (Run 2314).

7.20(a) shows the effect of Reynolds number on the perturbation spectra near the reattachment location. The instability peak begins at 45 kHz and increases with Reynolds number until  $Re_\infty = 2.9 \times 10^6/m$ . At this point, transition appears to be beginning and the broadband power has started to rise. Figure 7.20(b) is the same Reynolds number sweep but at a further downstream location. Instability peaks are present at higher frequencies, beginning at 60 kHz and progressing to 80 kHz. Broadband power begins to increase around  $Re_\infty = 2.5 \times 10^6/m$  and fully eclipse the instability peak at  $Re_\infty = 2.9 \times 10^6/m$ , indicating transition. Spectra from the farthest downstream sensor can be seen in Figure 7.20(c). The perturbation instability can be seen from 75 kHz at the lowest Reynolds number to 95 kHz at the highest Reynolds number. Based on an increase in broadband power, transition begins at  $Re_\infty = 2.5 \times 10^6/m$ . Transition occurs slightly earlier at the further downstream sensors. This is expected since the length Reynolds number will be increasing with downstream distance.

While the spectral behavior of the perturbations can show a lot of their development post-reattachment, little can be said of the mechanism by which the boundary layer is breaking down to turbulence. In an attempt to learn how the perturbations and any instability affects transition, the amplitude of the RMS pressure fluctuations were calculated for several Reynolds numbers and sensor locations. Figure 7.21 plots the fluctuations against the Reynolds number based on sensor distance from the nosetip. Each color represents data from a single run at various unit Reynolds number. The individual symbols are the RMS amplitude from a single sensor during that run. Only the last six sensors of the ramp were used for every run. Since the Reynolds number is based on distance from the nosetip, each sensor will have a different length Reynolds number. The no-perturbation and 10 kV perturbation data were taken from different times during the same run. The perturbation fluctuations were calculated by finding the individual perturbations and calculating the RMS of the time trace. Defining the perturbation was an important part of calculating these RMS fluctuations. The start and end of a perturbation was defined as the first and last locations that exceed

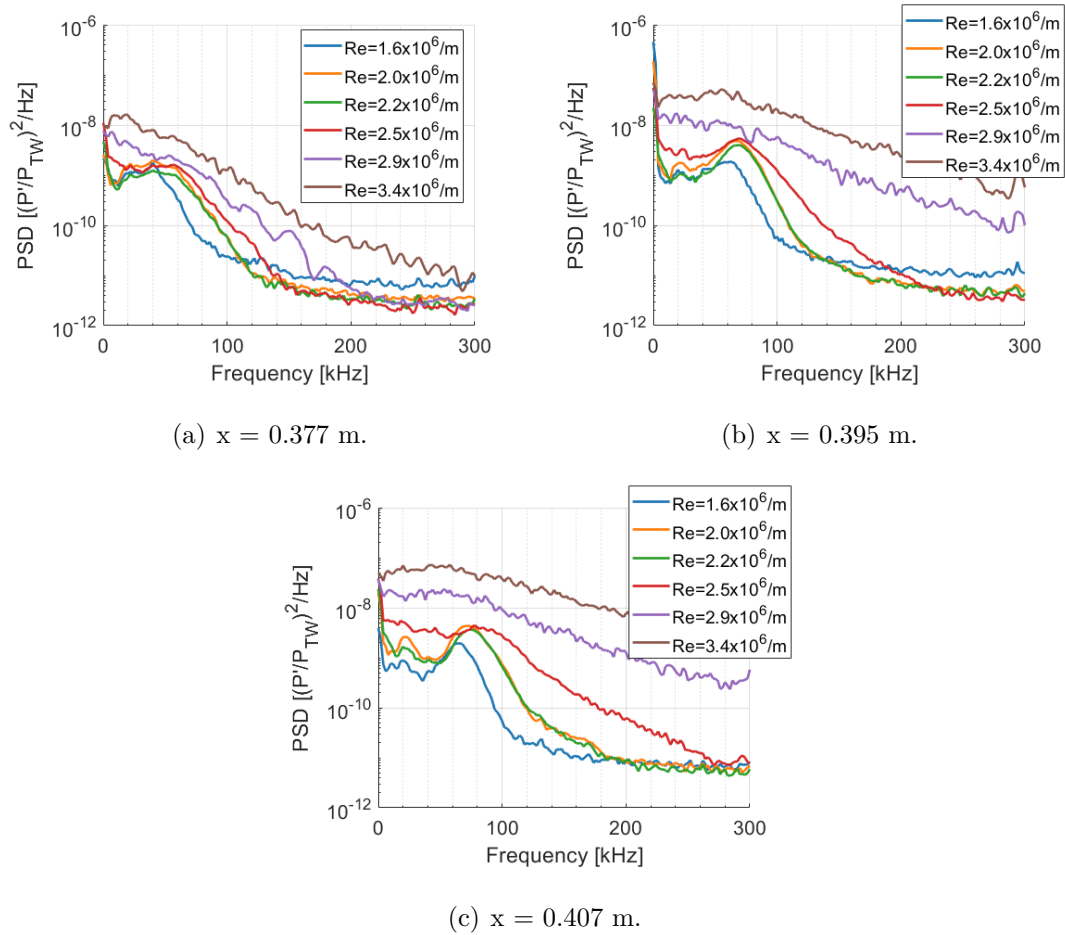


Figure 7.20. Effect of Reynolds number on perturbation instability growth at various centerline locations.

a 2% threshold of  $P_{TW}$ . This was deemed successful at capturing the fluctuating portion of the perturbation while not including time with small fluctuations. Other levels were tested, but they did not robustly capture the perturbations. Intermittency was calculated for each run at the farthest downstream PCB location. This highlights and confirms that the increase in fluctuations is due to the presence of turbulent spots with broadband frequency content.

At low  $Re_{sensor}$  the fluctuation magnitudes without perturbation are near the sensor noise floor and little sensor-to-sensor variation is seen within a single run. At  $Re_{sensor} =$

$9 \times 10^5$  the boundary layer begins to transition and the slope of the fluctuations changes drastically. This location the slope changes is considered the transition onset. Figure 7.21 was plotted on a log scale so this increase in fluctuation magnitudes is exponential. This was similar to the measurements presented in Section 5.3.2. Additionally, the intermittency begins to depart from laminar levels in between  $Re_{sensor} = 9 \times 10^5$  and  $Re_{sensor} = 10.1 \times 10^5$ . The intermittency lags behind the RMS amplitudes. This is a result of the RMS amplitudes including lower frequency fluctuations that begin to increase before the higher frequency fluctuations used in turbulent spot detection.

At low  $Re_{sensor}$ , the RMS fluctuations with the perturbation were much higher than the no-perturbation values. This is due the disturbances generated by the perturber. The peak RMS fluctuation for a single run typically occurred at the third-to-last sensor on the ramp. This is  $x = 0.397$  m downstream from the nosetip. The fluctuation levels do not begin to increase at  $Re_{sensor} = 9 \times 10^5$ . The perturbation fluctuations stay flat until  $Re_{sensor} = 11 \times 10^5$ . This actually corresponds to the location at which the no-perturbation fluctuations reach the magnitude of the perturbation case. At this point, the fluctuation levels increase similar to the no-perturbation cases. The magnitudes are slightly higher with perturbations but follow the same trend of changing slope and increasing with transition. Based on this behavior, it doesn't seem that the perturbation has an effect on transition location. No early transition is seen on any of the pressure sensors when the pulser is inducing perturbations. Instead, the instability is present within the boundary layer but not growing much over the range of laminar Reynolds numbers. Before any significant growth or breakdown of the perturbation instability occurs, the boundary layer transitions through another mechanism. This conclusion is based on two points. First, the no-perturbation case transitions earlier and secondly, the perturbed fluctuations don't begin to rise until fluctuations due to the different transition mechanism overtake the perturbation RMS fluctuations. This is further supported by the time traces seen previously in Figure 7.17. Turbulent spots begin to randomly appear at the same time that the perturbations appear to breakdown. Calculations of the intermittency were used to quantify the production of

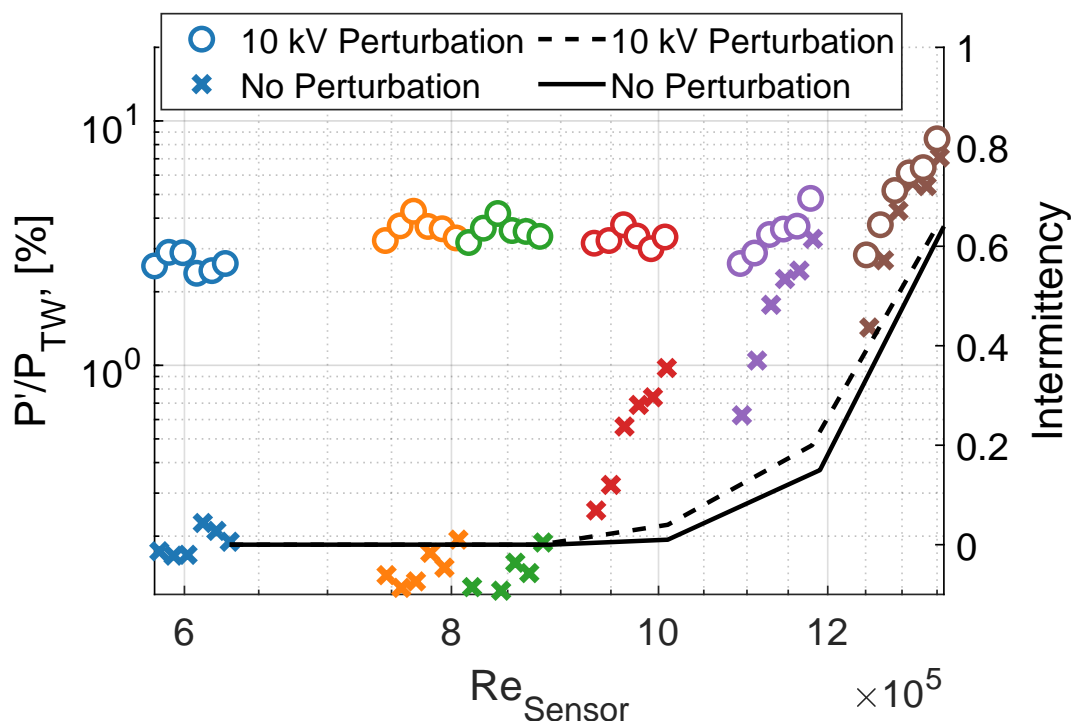


Figure 7.21. Comparison of PCB RMS pressure fluctuations magnitudes post-reattachment. The different colors represent runs of different unit Reynolds number.  $Re_{sensor}$  is the Reynolds number based on sensor distance from nosetip. The black lines are the computed intermittency of the final sensor on the ramp for every run.

turbulent spots with high frequency content. For both the no perturbation and 10 kV perturbation, the intermittency begins to rise at similar locations and remains similar for the entire range of Reynolds number. The generated traveling instability does not have a large effect on the portion of time the flow is under turbulent flow. The transition process is indifferent to the presence of any instability that was amplified by the perturbation. This is a significant result for understanding possible transition mechanisms on finite span compression ramps.

### 7.2.4 Effect of Pulser Voltage on Instability Growth

Even with transition on the cone-slice-ramp being indifferent to the perturbations, the ability to generate disturbances that can grow into boundary-layer instabilities is useful. For that reason, a discussion of controlling the perturbation size will be presented. The Eagle Harbor Technologies pulser used in the current experiments was capable of a large range of output voltages. The present experiments were repeated for several voltages and the resulting downstream pressure fluctuations were measured on the cone-slice-ramp. The exact perturber settings can be found at the beginning of this chapter in Table 7.1.

An initial investigation into the effects of the applied voltage was made by analyzing the perturbation at a single downstream location for a variety of Reynolds numbers. Figure 7.22 shows the spectra for a range of Reynolds numbers with three applied voltages at  $x = 0.395$  m. This location corresponds to the largest RMS amplitudes seen for the laminar perturbation runs in Figure 7.21. The 10 kV case is seen in Figure 7.22(a) and is the same as the previous results. A frequency peak starts at near 75 kHz and the amplitude increases with downstream distance. Transition begins at  $Re_\infty = 2.5 \times 10^6/m$  and no peaks are seen above that Reynolds number. Figure 7.22(b) shows the same plot for an applied voltage of 5 kV. The unit Reynolds numbers are slightly different due to the pre-run conditions being slightly different. Peaks are present at the same frequencies as for the 10 kV perturbations. The unstable frequencies shown by the spectral peak are unaffected by the change in voltage. Vertical lines at 70 kHz were included for referencing unstable frequency locations. This is expected since the growth of instability occurs downstream of the electrodes and should be independent of the plasma. Amplitudes of the 70 kHz peak for the 5 kV voltage at the lowest Reynolds number have dropped to 29% of the 10 kV amplitude. At  $Re_\infty = 2.5 \times 10^6/m$ , the 5 kV voltage amplitude dropped to 51% of the 10 kV amplitudes. Transition location is unchanged, and broadband power rises above the perturbation at  $Re_\infty = 3.1 \times 10^6/m$ . The applied voltage was again halved to 2.5 kV and is shown in Figure

7.22(c). Tested Reynolds numbers vary slightly from the other voltage cases due to time constraints during testing. However, the trends can still be discerned. The instability is not noticeable at the lowest Reynolds number. It is present at the next two Reynolds numbers but again at lower amplitudes. Transition is seen at  $Re_\infty = 2.8 \times 10^6/m$  and evidence of the perturbation cannot be seen. Adjusting the output voltage of the pulser provides direct control over the extent of pressure perturbation within the boundary layer.

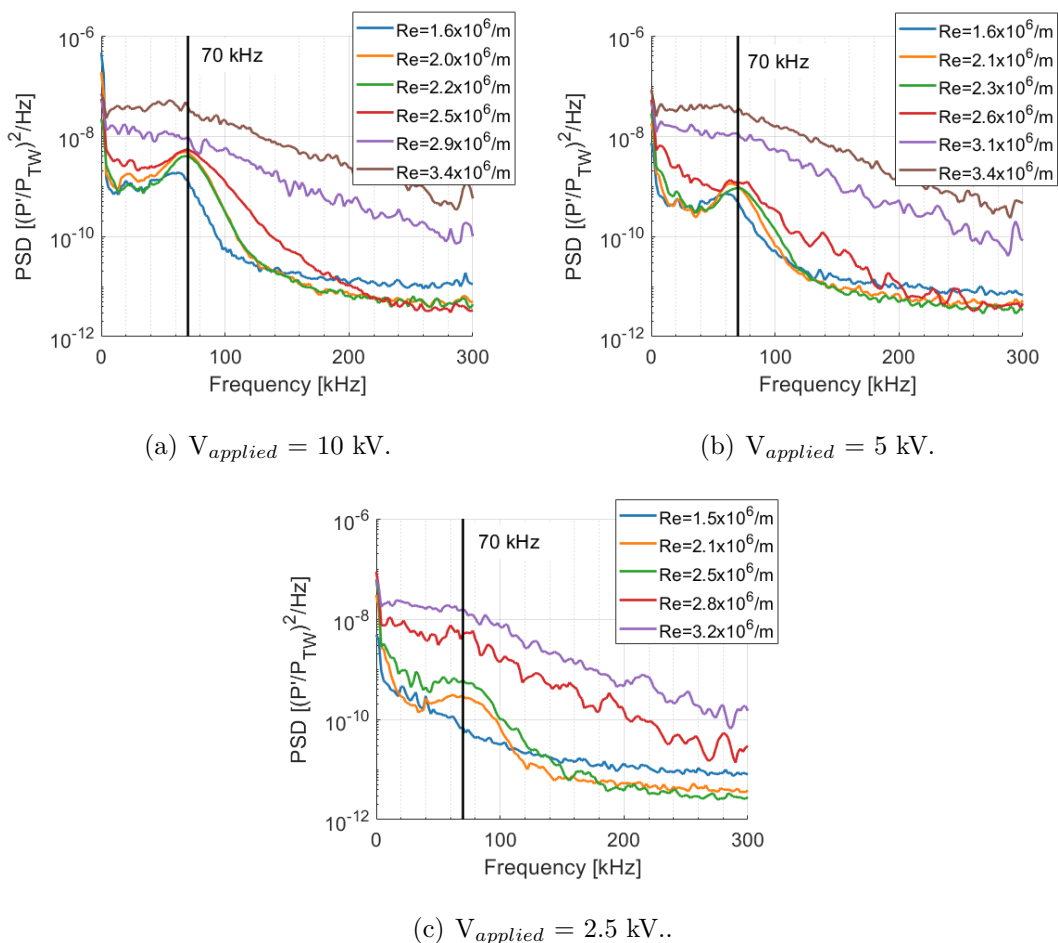


Figure 7.22. Effect of applied voltage on instability growth at  $x = 0.395 \text{ m}$ .

A closer look at the effects of pulser voltage can be seen in Figure 7.23. Four different applied voltages from 0 kV to 10 kV are shown on the same plot for two

downstream distances. The effect of the applied voltage is clearly seen for both locations. As the pulser voltage increases, the peak increases in amplitude. The frequency at which the peaks appear are independent of the applied voltage. The use of this perturber, or similar ones, on future models seems to be a promising tool for determining which frequencies are unstable within a boundary layer. This is particularly useful if current quiet flow capabilities are unable to reach Reynolds numbers where instability growth is measurable. In those cases, a perturber can be used to simulate instability growth and compare to computations.

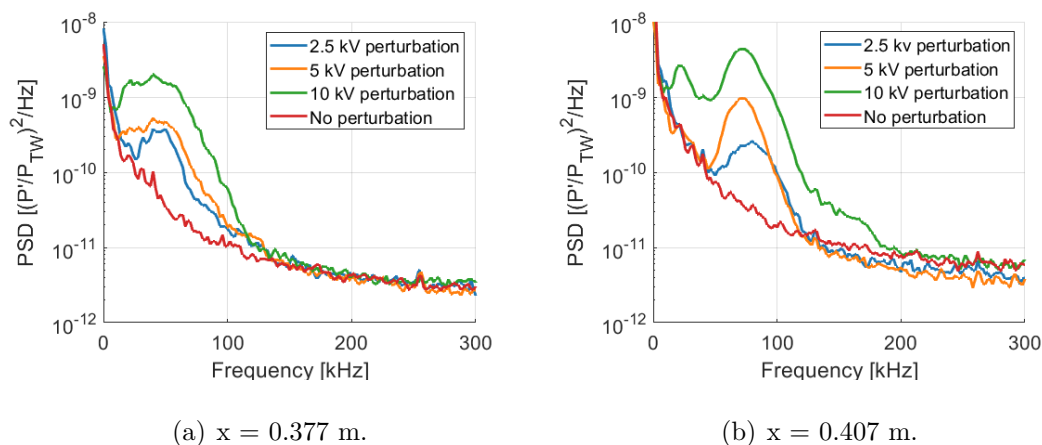


Figure 7.23. Effect of applied pulser voltage on instability growth at various centerline locations at  $Re_\infty = 2.0 \times 10^6/m$ .

To help show the effects of pulser voltage on the instability growth, the RMS pressure fluctuation amplitudes and the intermittency were again plotted versus the Reynolds number based on sensor distance from the nosetip. Figure 7.24 shows the amplitude and the intermittency for the 0 kV, 5 kV, and 10 kV applied voltages. The 2.5 kV case was left off of this plot for clarity. Perturbation RMS amplitudes were calculated similarly to those in Figure 7.21. However, the 2%-of- $P_{TW}$  threshold was too high to capture some of the wave packets that were generated for the 5 kV pulsing. As a result, a threshold of 1% of  $P_{TW}$  was used for the 5 kV case. The RMS fluctuation amplitudes for the 5 kV pulsing lie in between the 0 kV and 10 kV cases. Depending

on the Reynolds number, the 5 kV perturbations are 29-51% of the 10 kV amplitude. The relation between pulser voltage and disturbance amplitude is dependent on the unit Reynolds number. As was previously discussed, the no-perturbation case begins to transition at  $Re_{sensor} = 9 \times 10^5$  and the 10 kV case begins to transition at  $Re_{sensor} = 11 \times 10^5$ . The 5 kV pulsing RMS fluctuations depart from the nearly flat low Reynolds number cases at approximately  $Re_{sensor} = 10 \times 10^5$ . At this point, the no-perturbation amplitudes have nearly reached the 5 kV instability amplitudes and a measurable change in slope can be seen for transition. The behavior of transition is nearly identical to the 10 kV pulsing and reinforces the belief that a different mechanism is causing transition. All three perturbations collapse to the same line during the transition process by  $Re_{\infty} = 12 \times 10^5$ . This is very near the 10% amplitudes that were measured for turbulent boundary layers. The intermittency for the 5 kV perturbation is similar to the 10 kv and no perturbation cases. The change in pulser voltage did not change the point at which turbulent spots appear within the post-reattachment boundary layer. Based on this, it does not appear that a traveling instability is a dominant transition mechanism on the cone-slice-ramp model.

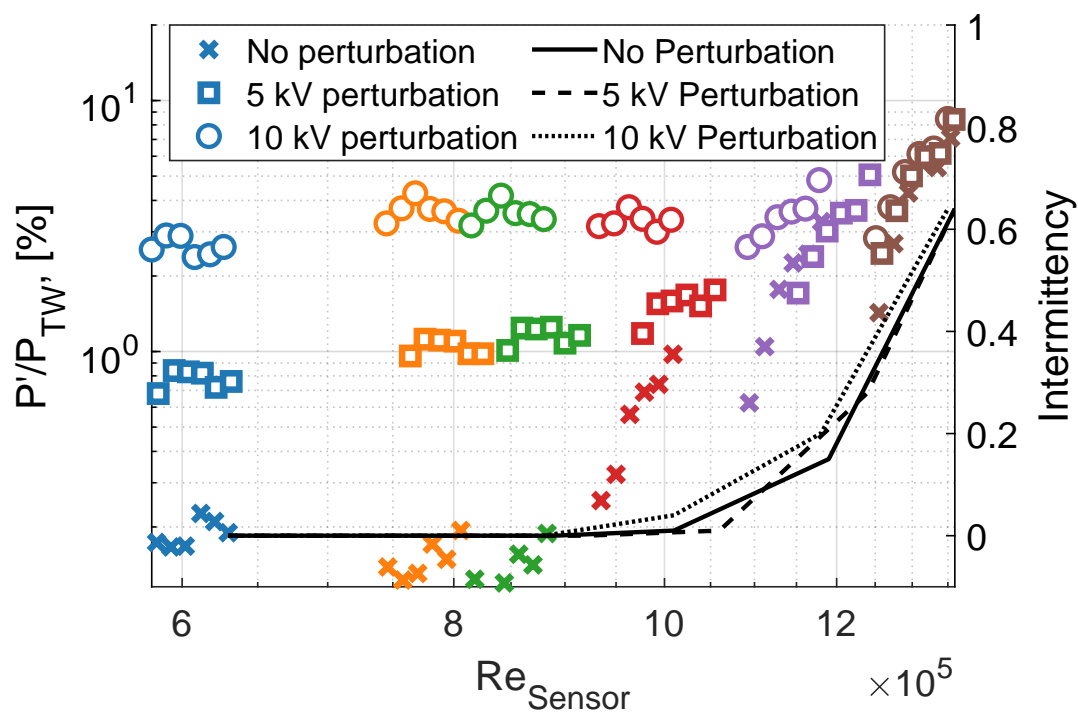


Figure 7.24. Comparison of PCB RMS pressure fluctuations magnitudes post-reattachment. The different colors represent runs of different initial unit Reynolds number.  $Re_{sensor}$  is the Reynolds number base on sensor distance from nosetip. The black lines are the computed intermittency of the final sensor on the ramp for every run.

## 8. SUMMARY AND RECOMMENDATIONS

### 8.1 Summary

Shock/boundary-layer interactions can produce adverse pressure gradients strong enough to separate the boundary layer from a surface and produce a recirculating region with a hypersonic shear layer above it. Boundary-layer separation produces complicated flow fields that make predicting boundary-layer transition difficult. The present experiments focus on a  $7^\circ$  cone with a flat slice and compression ramp in the Boeing/AFOSR Mach-6 Quiet Tunnel (BAM6QT). This finite-span compression corner was developed to make measurements of the instability of the shear-layer above a separation bubble and to develop an understanding of the physical mechanism by which transition occurs. Current experiments focus on whether traveling instabilities within the shear layer above the separation amplify to measurable magnitudes upon reattachment and cause boundary layer transition.

It was necessary to develop a finite-span compression corner geometry with known separation and reattachment points. The reattachment location cannot be near the downstream ramp edge, or the base flow behind a model will couple with the recirculating region and complicate the flow field. Additionally, streamwise space is needed for placement of surface pressure sensors prior to the ramp end and downstream of reattachment. Oil flow, surface heat transfer, and computational comparisons were used for assessing reattachment in the flow fields of various cone-slice-ramp geometries. A long slice was needed to enable a long ramp, to enable post-reattachment measurements. A parametric study of ramp angles was carried out. The  $20^\circ$  ramp was the best angle for measurements of possible traveling instabilities of a hypersonic shear layer. Varying the Reynolds number allowed control of transition on the ramp.

Boundary-layer transition on the long-ramp model was measured to occur approximately at a Reynolds number based on freestream conditions and distance from the nosetip of 900000, under quiet flow. Heat transfer measurements in quiet flow showed reattachment moving upstream with increasing Reynolds number. One or two streamwise streaks developed post-reattachment but there was no evidence of a Görtler-like instability. Heat transfer measurements in noisy flow showed the boundary layer transitioning prior to separation and a decrease in separation size.

Post-reattachment pressure fluctuations showed the presence of wave packets and turbulent spots at Reynolds numbers between  $Re_\infty = 2.5 \times 10^6 / \text{m}$  and  $Re_\infty = 3.5 \times 10^6 / \text{m}$ . The convection velocities of these spots were approximately 73-83% of the isentropic freestream velocity. The frequency content of individual wave packets varied but was consistently below 150 kHz. Transitional power spectra were dependent on the amount and amplitude of wave packets and turbulent spots within the chosen window of time. RMS pressure fluctuation magnitudes during the transition process were repeatable. Laminar fluctuation magnitudes remained between 0.1-0.3% of the tangent-wedge surface pressure. Transition began at length Reynolds numbers near  $0.9 \times 10^6$ , based on axial location and freestream conditions. The surface pressure fluctuations exhibited exponential growth until length Reynolds numbers of  $2.0 \times 10^6$  where they leveled out near 10% of the tangent-wedge surface pressure. Fluctuations were strongest on the centerline and dropped off quickly with distance from the ramp centerline. The presence of wave packets indicated possible traveling shear-layer instabilities, but inconsistent frequency content made interpretation difficult.

Disturbances were introduced into the boundary-layer with a pulsed plasma perturber. The ability to generate disturbances that can naturally grow within a hypersonic boundary was confirmed on a sharp  $7^\circ$  cone at  $0^\circ$  angle of attack. Second-mode waves were measured and breakdown to turbulence was observed. Maximum second-mode amplitudes reached approximately 10% of the surface static pressure. Comparisons to other second-mode dominated experiments were made.

Artificial disturbances were introduced to the cone-slice-ramp geometry just upstream of separation and were allowed to amplify within the shear layer. Traveling instabilities were measured post-reattachment at frequencies of 50-90 kHz. RMS fluctuations peaked at 3-4% of the tangent wedge pressure and had convection velocities of approximately 89% of isentropic freestream velocity. The instability amplitude was largest on the centerline and was less than 12 mm wide. Varying the applied pulser voltage provided control of the perturbation amplitude. Transition location did not change when using any of the artificial perturbations. Turbulent spots lead to transition and the spots seemed independent of the artificial disturbances.

It seems that traveling shear-layer instabilities are not a dominant mechanism of transition for this geometry under these conditions. It appears that a different mechanism is producing turbulent spots on the model.

## 8.2 Recommendations for Future Work

Numerous open questions still exist for future researchers to answer.

1. The present work focused on surface measurement techniques and the use of controlled disturbance generators. Off-surface techniques can allow direct measurements of shear-layer location, instability, and transition. Schlieren measurements of the flow field would help to better understand the shear-layer and the extent of separation. If the location of the shear layer is known, a focused laser differential interferometer (FLDI) could be used. The FLDI developed by Benitez et al. would be an ideal tool for making density fluctuation measurements within the shear layer [123].
2. The high-voltage pulser used to disturb the boundary layer can be improved. The present work tested perturbation by generating second-mode waves on a  $7^\circ$  cone. If a geometry that can naturally transition under quiet flow were tested, comparisons of natural and artificial transition can be made. This would determine if artificial perturbations obey the same transition mechanisms as the

undisturbed cases. Additionally, characterizing the type of waves being generated is of interest. Individual wave packets were demonstrated with generation of second-mode waves on the  $7^\circ$  cone, but what oblique modes are excited and for what wave angles? Utilizing the perturber within different flow fields could assess the limitations of this technique.

3. The current work focused on the growth of shear-layer instabilities without prior instability being measurable within the boundary layer. Currently, work using axisymmetric separations with second-mode growth prior to separation is being carried out in the BAM6QT. Expanding this work to a geometry that features significant instability growth prior to a finite-span separation could determine if shear layer traveling instabilities play an important role under different conditions.
4. The present experiments were carried out at  $0^\circ$  angle of attack. Hypersonic maneuverable vehicles will fly at non-zero angles of attack. Measurement of pressure fluctuations and transition for the shock/boundary-layer interactions on the windward and leeward rays could help researchers better predict flight vehicle behavior.

## LIST OF REFERENCES

## LIST OF REFERENCES

- [1] S. P. Schneider. Laminar-Turbulent Transition on Reentry Capsules and Planetary Probes. *Journal of Spacecraft and Rockets*, 43(6):1153–1173, 2006.
- [2] S. P. Schneider. Developing Mechanism-Based Methods for Estimating Hypersonic Boundary-Layer Transition in Flight: The Role of Quiet Tunnels. *Progress in Aerospace Sciences*, 72:17–29, 2015.
- [3] S. P. Schneider. Effects of High-Speed Tunnel Noise on Laminar-Turbulent Transition. *Journal of Spacecraft and Rockets*, 38(3):323–333, 2001.
- [4] E. Reshotko. Transition Issues for Atmospheric Entry. *Journal of Spacecraft and Rockets*, 45(2):161–164, 2008.
- [5] J. L. van Ingen. A Suggested Semi-Empirical Method for the Calculation of the Boundary Layer Transition Region. Technische Hogeschool Delft, Vliegtuigbouwkunde, Report VTH-74, TU Delft, Netherlands, September 1956.
- [6] S. P. Schneider. Development of Hypersonic Quiet Tunnels. *Journal of Spacecraft and Rockets*, 45(4), 2008.
- [7] S. P. Schneider. Hypersonic Laminar-Turbulent Transition on Circular Cones and Scramjet Forebodies. *Progress in Aerospace Sciences*, 40:1–50, 2004.
- [8] R. L. Wright and E. V. Zoby. Flight Boundary Layer Transition Measurements on a Slender Cone at Mach 20. *AIAA Paper 1977-0719*, June 1977.
- [9] S. Dhawan and R. Narasimha. Some Properties of Boundary Layer Flow during the Transition from Laminar to Turbulent Motion. *Journal of Fluid Mechanics*, 3(4):418–436, January 1958.
- [10] R. Narasimha. The Laminar-Turbulent Transition Zone in the Boundary Layer. *Progress in Aerospace Sciences*, 22:29–80, 1985.
- [11] K. M. Casper, S. J. Beresh, J. F. Henfling, R. W. Spillers, and B. O. M. Pruett. Toward Transition Statistics Measured on a 7-Degree Hypersonic Cone for Turbulent Spot Modeling. *AIAA Paper 2014-0427*, January 2014.
- [12] B. C. Chynoweth. *Measurements of Transition Dominated by the Second-Mode Instability at Mach 6*. PhD thesis, Purdue University, School of Aeronautics and Astronautics, May 2018.
- [13] T. C. Lin. Development of U.S. Air Force Intercontinental Ballistic Missile Weapon Systems. *Journal of Spacecraft and Rockets*, 40(4):491–509, 2003.

- [14] M. S. Holden. Experimental Studies of Shock Wave-Boundary-Layer Interactions in Hypersonic Flows. In H. Babinsky and J. K. Harvey, editors, *Shock Wave-Boundary-Layer Interactions*, chapter 6, pages 259–313. Cambridge University Press, 2011.
- [15] T. J. Horvath, S. A. Berry, B. R. Hollis, D. S. Liechty, H. H. Hamilton II, and N. R. Merski. X-33 Experimental Aeroheating at Mach 6 Using Phosphor Thermography. *Journal of Spacecraft and Rockets*, 38(5):634–635, September-October 2001.
- [16] T. J. Horvath, S. A. Berry, N. R. Merski, and S. M. Fitzgerald. X-38 Experimental Aerothermodynamics. *Journal of Spacecraft and Rockets*, 41(2):272, March-April 2004.
- [17] S. A. Berry, M DiFulvio, and M. K. Kowalkowski. Forced Boundary-Layer Transition on X-43 (Hyper-X) in NASA LaRC 20-Inch Mach 6 Air Tunnel. NASA Technical Memorandum TM-2000-210316.
- [18] J. Delery. Physical Introduction. In H. Babinsky and J. K. Harvey, editors, *Shock Wave-Boundary-Layer Interactions*, chapter 2, pages 5–86. Cambridge University Press, 2011.
- [19] R. D. Neumann. Developing Configuration Requirements for Hypersonic Flight. The Third Joint Europe/US Short Course in Hypersonics, October 1990.
- [20] G. V. Candler. Numerical Simulation of Hypersonic Shock Wave-Boundary-Layer Interactions. In H. Babinsky and J. K. Harvey, editors, *Shock Wave-Boundary-Layer Interactions*, chapter 7, pages 314–335. Cambridge University Press, 2011.
- [21] D. R. Chapman, D. M. Kuehn, and H. K. Larson. Investigation of Separated Flows in Supersonic and Subsonic Streams with Emphasis on the Effect of Transition. NACA Report 1356, 1958.
- [22] J. Ackeret, F. Feldman, and N Rott. Investigations of Compression Shocks and Boundary Layers in Gases Moving at High Speeds. NACA Technical Memorandum No. 1113, 1947.
- [23] G. S. Settles and L. J. Dodson. Supersonic and Hypersonic Shock/Boundary Layer Interaction Database. *AIAA Journal*, 32(7), July 1994.
- [24] A. Demetriades. Transition in High-Speed Free Shear Layers. In M. Y. Hussaini and R. G. Voigt, editors, *Instability and Transition Volume 1. ICASE/NASA LaRC Series*, pages 52–67. Springer, 1990.
- [25] A. V. Dovgal, V. V. Kozlov, and A. Michalke. Laminar Boundary Layer Separation: Instability and Associated Phenomena. *Progress in Aerospace Sciences*, 30:61–94, 1994.
- [26] A. Demetriades and T. L. Brower. Experimental Study of Transition in a Compressible Free Shear Layer. AFOSR Technical Report 83-0144, December 1982.
- [27] F. Liang, E. Roshotko, and A. Demetriades. A Stability Study of the Developing Mixing Layer Formed by Two Supersonic Laminar Streams. *Physics of Fluids*, 8(12), December 1996.

- [28] D. Papamoschou and A. Roshko. Observations of Supersonic Free Shear Layers. *Sadhana*, 12(1-2):1–14, 1998.
- [29] R. A. King, T. R. Creel, and D. M. Bushnell. Experimental Transition Investigations of a Free-Shear Layer above a Cavity at Mach 3.5. *Journal of Propulsion and Power*, 7(4):626–634, 1991.
- [30] W. Behrens and D. R. S. Ko. Experimental Stability Studies in Wakes of Two-Dimensional Slender Bodies at Hypersonic Speeds. *AIAA Journal*, 9(5):851–857, May 1971.
- [31] D. T. Papageorgiou. The Stability of Two-Dimensional Wakes and Shear Layers at High Mach Numbers. *Physics of Fluids*, 3(5):793–802, May 1991.
- [32] A. A. Maslov, S. G. Mironov, and V. M. Aniskin. Hypersonic Shear Layer Stability Experiments. *Journal of Spacecraft and Rockets*, 42(6):999–1004, November-December 2005.
- [33] B. E. Schmidt and J. E. Shepherd. Stability of Supersonic Flow with Injection. *AIAA Journal*, 57(12):5230–5240, December 2019.
- [34] G. E. Gadd, D. W. Holder, and J. D. Regan. An Experimental Investigation of the Interaction between Shock Waves and Boundary Layers. *Proceedings of the Royal Society of London A: Mathematical, Physical and Engineering Sciences*, 226(1165):227–253, 1954.
- [35] F. T. Hung and D. O. Barnett. Shock Wave-Boundary Layer Interference Heating Analysis. AIAA Paper No. 73-237, January 1973.
- [36] J. J. Ginoux. On some Properties of Reattaching Laminar and Transitional High Speed Flows. von Karman Institute Technical Note 53, September 1969.
- [37] A. Chpoun. Hypersonic Flow in a Compression Corner in 2-D and 3-D Configurations. AIAA Paper 89-1876, June 1989.
- [38] G. Simeonides and J.F. Wendt. An Experimental Contribution to the Flat Plate 2D Compression Ramp, Shock/Boundary Layer Interaction Problem at Mach 14: Test Case 3.7. In: Desideri, Glowinski, Periaux (eds) Hypersonic Flows for Reentry Problems. Springer-Verlag, 1990.
- [39] J. P. Vermuelen and G. Simeonides. Parametric Studies of Shock Wave/Boundary Layer Interactions over 2D Compression Corners at Mach 6. von Karman Institute for Fluid Dynamics Technical Note 181, September 1992.
- [40] K. S. Heffner, A. Chpoun, and J. C. Lengrand. Experiment Study of Transitional Axisymmetric Shock-Boundary Layer Interactions at Mach 5. AIAA Paper 93-3131, July 1993.
- [41] F. Grasso, G. Leone, and J. M. Delery. Validation Procedure for the Analysis of Shock-Wave/Boundary-Layer Interaction Problems. *AIAA Journal*, 32(9), September 1994.
- [42] L. de Luca, G. Cardone, D. Aymer de la Chevalerie, and A. Fonte. Viscous Interaction Phenomena in Hypersonic Wedge Flow. *AIAA Journal*, 33(12), December 1995.

- [43] G. Simeonides and W. Haase. Experimental and Computations Investigations of Hypersonic Flow about Compression Ramps. *Journal of Fluid Mechanics*, 283:17–42, June 1995.
- [44] L. Vandomme, B. Chanetz, R. Benay, and J. Perraud. Transitional Shock Wave Boundary Layer Interactions in Hypersonic Flow at Mach 5. AIAA Paper 2003-6966, December 2003.
- [45] R. Benay, B. Chanetz, B. Mangin, and L. Vandomme. Shock Wave/Transitional Boundary-Layer Interactions in Hypersonic Flow. *AIAA Journal*, 44(6):1243–1254, June 2006.
- [46] L. M. Brown, R. B. Boyce, N. Mumford, and S. O’Byrne. Intrinsic Three-Dimensionality of Laminar Hypersonic Shock Wave/Boundary Layer Interactions. AIAA Paper 2009-7205, October 2009.
- [47] R. Bur and B. Chanetz. Experimental Study of the PRE-X Vehicle Focusing on the Transitional Shock-Wave/Boundary-Layer Interactions. *Aerospace Science and Technology*, 13(4):393–401, 2009.
- [48] D. Estruch-Semper and B. Ganapathisubramani. Axisymmetric Flare-Induced Separation of High-Speed Transitional Boundary Layers. AIAA Paper 2012-0067, January 2012.
- [49] N. D. Sandham, E. Schülein, A. Wagner, S. Willems, and J. Steelant. Transitional Shock-Wave/Boundary-Layer Interactions in Hypersonic Flow. *Journal of Fluid Mechanics*, 752:349–382, 2014.
- [50] J. Thome, J. Reinert, A. Dwivedi, and G. Candler. Computational Study of High Speed Flow on a Sliced Cone-Flap Geometry. AIAA Paper 2018-3397, June 2018.
- [51] C. L. Running and T. J. Juliano. Hypersonic Shock-Wave/Boundary-Layer Interactions on a Cone/Flare Model. AIAA Paper 2018-3702, June 2018.
- [52] M. Leinemann, R. Radespiel, F. Munoz, S. Esquieu, G. McKiernan, and S. R. Schneider. Boundary Layer Transition on a Generic Model of Control Flaps in Hypersonic Flow. AIAA Paper 2019-1908, January 2019.
- [53] A. Roghelia, H. Olivier, I. Egorov, and P. Chuvakov. Experimental Investigation of Görtler Vortices in Hypersonic Ramp Flows. *Experiments in Fluids*, 58(139), 2017.
- [54] G. M. D. Currao, R. Choudhury, S. L. Gai, A. J. Neely, and D. R. Buttsworth. Hypersonic Transitional Shock-Wave-Boundary-Layer Interaction on a Flat Plate. *AIAA Journal*, 58(2):814–829, February 2020.
- [55] J. M. Floryan. On the Görtler Instability of Boundary Layers. *Progress of Aerospace Sciences*, 28:235–271, 1991.
- [56] H. Ludéke, R. Radespiel, and E. Schülein. Simulation of Streamwise Vortices at the Flaps of Re-entry Vehicles. AIAA Paper 2004-0915, January 2004.
- [57] G. R. Inger. Three-Dimensional Heat-and Mass-Transfer Effects across High-Speed Reattaching Flows. *AIAA Journal*, 15(3):383–389, March 1977.

- [58] P. Balakumar, H. Zhao, and H. Atkins. Stability of Hypersonic Boundary Layers over a Compression Corner. *AIAA Journal*, 43(4):760–767, April 2005.
- [59] S. Matsumura, S. P. Schneider, and S. A. Berry. Streamwise Vortex Instability and Transition on the Hyper-2000 Scramjet Forebody. *Journal of Spacecraft and Rockets*, 42(1):78–89, 2005.
- [60] G. S. Sidharth, A. Dwivedi, G. V. Candler, and J. W. Nichols. Global Linear Stability Analysis of High Speed Flows on Compression Ramps. AIAA Paper 2017-3455, June 2017.
- [61] A. Dwivedi, G. S. Sidharth, G. V. Candler, and J. W. Nichols. Input-Output Analysis of Shock Boundary Layer Interaction. AIAA Paper 2018-3220, June 2018.
- [62] A. Dwivedi, G. S. Sidharth, J. W. Nichols, G. V. Candler, and M. R. Jovanovic. Reattachment Streaks in Hypersonic Compression Ramp Flow: an Input-Output Analysis. *Journal of Fluid Mechanics*, 880:113–135, 2019.
- [63] K. W. Cassel, A. I Ruban, and J. D. A. Roger. An Instability in Supersonic Boundary-Layer Flow over a Compression Ramp. *Journal of Fluid Mechanics*, 300:265–285, 1995.
- [64] K. W. Cassel, A. I Ruban, and J. D. A. Roger. Separation and Instability in the Hypersonic Boundary Layer on a Cold Wall. AIAA Paper 95-2272, June 1995.
- [65] L. Mack. Boundary Layer Stability Theory. Jet Propulsion Lab Report 900-277, November 1969.
- [66] A. Pagella, U. Rist, and S. Wagner. Numerical Investigations of Small-Amplitude Disturbances in a Boundary Layer with Impinging Shock Wave at  $Ma = 4.8$ . *Physics of Fluids*, 14(7), 2002.
- [67] I. V. Egorov, A. V. Novikov, and A. V. Federov. Numerical Modeling of the Disturbances of the Separated Flow in a Rounded Compression Corner. *Fluid Dynamics*, 41(4):521–530, December 2006.
- [68] A. Novikov, I. Egorov, and A. Federov. Numerical Simulation of Three-Dimensional Wave Packet in Supersonic Flow over a Compression Corner. AIAA Paper 2015-2624, June 2015.
- [69] A. Novikov, A. Federov, and I. Egorov. Numerical Study of Wave Trains in Supersonic Flow over a Compression Corner. AIAA Paper 2016-0049, January 2016.
- [70] A. Novikov, I. Egorov, and A. Federov. Direct Numerical Simulation of Wave Packets in Hypersonic Compression-Corner Flow. *AIAA Journal*, 54(7):2034–2050, July 2016.
- [71] T. Whalen, R. Kennedy, S. Laurence, B. Sullivan, D. Bodony, and G. Buck. Unsteady Surface and Flowfield Measurements in Ramp-induced Turbulent and Transitional Shock-Wave Boundary-Layer Interactions at Mach 6. AIAA Paper 2019-1127, January 2019.

- [72] B. Hedlund, A. Houpt, S. Gordeyev, and S. Leonov. Measurement of Flow Perturbation Spectra in Mach 4.5 Corner Separation Zone. *AIAA Journal*, 56(7):2699–2711, 2018.
- [73] E. K. Benitez, J. S. Jewell, S. P. Schneider, and S. Esquieu. Instability Measurements on an Axisymmetric Separation Bubble at Mach 6. To be presented at AIAA Aviation Forum, June 2020.
- [74] P. Portoni. Effect of Boundary-Layer Suction on a Cone-Flare Model at Mach 6. Boeing/AFOSR Mach 6 Quiet Tunnel Internal Report, December 2019.
- [75] S. Esquieu, E. Benitez, S. P. Schneider, and J. Brazier. Flow and Stability Analysis of a Hypersonic Boundary-Layer over an Axisymmetric Cone-Cylinder-Flare Configuration. AIAA Paper 2019-2115, January 2019.
- [76] J.E. Green. Interactions between Shock Waves and Turbulent Boundary Layers. *Progress in Aerospace Sciences*, 11:235–340, 1970.
- [77] J. E. Lewis. *Experimental Investigation of Supersonic Laminar, Two-Dimensional Boundary Layer Separation in a Compression Corner with and without Cooling*. PhD thesis, California Institute of Technology, November 1967.
- [78] W. L. Oberkampf, D. P. Aeschliman, R. E. Tate, and J.F. Henfling. Experimental Aerodynamics Research on a Hypersonic Vehicle. Sandia Report SAND92-1411, April 1993.
- [79] J. Tan, J. Tu, X. Sun, F. Lin, and L. Meng. Numerical Study of Hypersonic Shock-Wave/Laminar Boundary-Layer Interactions of a Typical Lifting Vehicle. AIAA Paper 2017-2280, March 2017.
- [80] E. A. Vogel, J. G. Coder, B. C. Chynoweth, and S. P. Schneider. Experimental and Computations Results of a Cone-Slice-Ramp Geometry at Mach 6. AIAA Paper 2019-3593, June 2019.
- [81] L. E. Steen. Characterization and Development of Nozzles for a Hypersonic Quiet Wind Tunnel. Master’s thesis, Purdue University, School of Aeronautics and Astronautics, West Lafayette, IN, December 2010.
- [82] K. A. Gray. Flowfield Characterization of the Boeing/AFOSR Mach-6 Quiet Tunnel. Master’s Thesis, Purdue University, School of Aeronautics and Astronautics, West Lafayette, IN, December 2018.
- [83] Kulite Semiconductor Products Inc. Miniature Ruggedized High Temperature IS Pressure Transducer XTEL-190(M) Series Data Sheet.
- [84] B. M. Wheaton. Roughness-Induced Instability in a Laminar Boundary Layer at Mach 6. Master’s Thesis, Purdue University, School of Aeronautics and Astronautics, West Lafayette, IN, September 2009.
- [85] PCB Piezoelectronics. Micro ICP Pressure Sensor Model 132B38 Datasheet, 2019.
- [86] D. C. Berridge. *Generating Low-Pressure Shock Waves for Calibrating High-Frequency Pressure sensors*. PhD thesis, Purdue University, School of Aeronautics and Astronautics, December 2015.

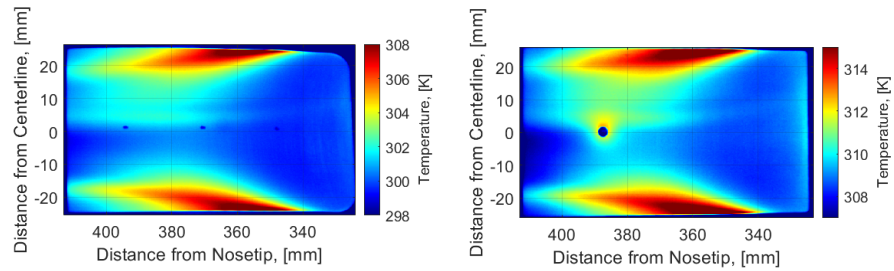
- [87] M. P. Wason. Calibration of High-Frequency Pressure Sensors using Low-Pressure Shock Waves. Master's thesis, Purdue University, School of Aeronautics and Astronautics, May 2019.
- [88] K. M. Casper, S. J. Beresh, J. F. Henfling, R. W. Spillers, and S. P. Schneider. Pressure Fluctuations in a Laminar, Transitional, and Turbulent Hypersonic Boundary Layers. *AIAA Paper 2009-4054*, June 2009.
- [89] K. Fujii. Experiment of the Two-Dimensional Roughness Effect on Hypersonic Boundary-Layer Transition. *Journal of Spacecraft and Rockets*, 43(4):731, 2006.
- [90] S. J. Beresh, J. F. Henfling, R. W. Spillers, and B. O. M. Pruett. Fluctuating Wall Pressures Measured Beneath a Supersonic Turbulent Boundary Layer. *Physics of Fluids*, 23(7), 2011.
- [91] H. B. Johnson and G. V. Candler. Hypersonic Boundary Layer Stability Analysis Using PSE-Chem. *AIAA Paper 2005-5023*, June 2005.
- [92] H. W. Liepmann and A. Roshko. *Elements of Gasdynamics*. Dover Publications Inc., 1957.
- [93] Kulite Semiconductor Products Inc. High Temperature Ultraminiature Pressure Transducer XCE-062 Series Data Sheet.
- [94] P. L. Gilbert. Effect of Tunnel Noise on Laminar Stagnation-Point Heating at Mach 6. Master's Thesis, Purdue University, School of Aeronautics and Astronautics, West Lafayette, IN, December 2010.
- [95] J. D. Anderson. *Hypersonic and High-Temperature Gas Dynamics Second Edition*. AIAA, 2nd edition, 2006.
- [96] J. P. Sullivan, S. P. Schneider, T. Liu, J. Rubal, C. Ward, C. Rice, R. Foley, Z. Cai, B. Wang, and S. Woodiga. Quantitative Global Heat Transfer in a Mach-6 Quiet Tunnel. *NASA/CR-2012-217331*, February 2012.
- [97] T. Liu and J. Sullivan. *Pressure and Temperature Sensitive Paints*. Springer, first edition, 2005.
- [98] S. Cerasuolo. Heat Flux Measurements by Infrared Thermography in the Boeing/AFOSR Mach-6 Quiet Tunnel. Master's thesis, Università degli Studi di Napoli Federico II, January 2017.
- [99] M. Zaccara. Infrared Thermography Data Reduction for Heat Transfer Measurements in the Boeing/AFOSR Mach-6 Quiet Tunnel. Master's thesis, Università degli Studi di Napoli Federico II, January 2018.
- [100] J. B. Edelman. *Nonlinear Growth and Breakdown of the Hypersonic Crossflow Instability*. PhD thesis, Purdue University, School of Aeronautics and Astronautics, August 2019.
- [101] Infratec Infrared LLC. ImageIR 8300 Series Data Sheet.
- [102] M. P. Borg and R. L. Kimmel. Simultaneous Infrared and Pressure Measurements of Crossflow Instability Modes for HIFiRE-5. *AIAA Paper 2016-0354*, January 2016.

- [103] F. D. Turbeville. Private Communication, 2019.
- [104] C. F. Boyd and A. Howell. Numerical Investigation of One-dimensional Heat-Flux Calculations. NSWCDD/TR-94/114, October 1994.
- [105] S. Matsumura and S. P. Schneider. Flow Visualization Measurement Techniques for High-Speed Transition Research in the Boeing/AFOSR Mach-6 Tunnel. AIAA Paper 2003-4583, July 2003.
- [106] B. M. Wheaton. *Roughness-Induced Instabilities in a Mach-6 Boundary Layer*. PhD thesis, Purdue University, School of Aeronautics and Astronautics, November 2012.
- [107] M. J. Wright, F. S. Milos, and P. Tran. Afterbody Aeroheating Flight Data for Planetary Probe Thermal Protection System Design. *Journal of Spacecraft and Rockets*, 43(5):929–943, 2006.
- [108] J. Poggie, R. L. Kimmel, and S. N. Schwoerke. Traveling Instability Waves in a Mach 8 Flow over an Elliptic Cone. *AIAA Journal*, 38(2):251–258, February 2000.
- [109] M. P. Borg, R. L. Kimmel, and S. Stanfield. Traveling Crossflow Instability for the HIFiRE-5 Elliptic Cone. *Journal of Spacecraft and Rockets*, 52(3):664–673, May 2015.
- [110] E. Husain and R. S. Nema. Analysis of Paschen Curves for Air, N<sub>2</sub>, and SF<sub>6</sub> Using the Townsend Breakdown Equation. *IEEE Transactions on Electrical Insulation*, EI-17(4):350–353, August 1985.
- [111] M. Khalifa, editor. *High-Voltage Engineering: Theory and Practice*. Marcel Dekker, Inc., 1990.
- [112] K. M. Casper. *Pressure Fluctuations Beneath Instability Wave Packets and Turbulent Spots in a Hypersonic Boundary Layer*. PhD thesis, Purdue University, School of Aeronautics and Astronautics, August 2012.
- [113] C. Y. Ching and J. E. Lagraff. Measurement of turbulent spot convection rates in a transitional boundary layer. *Experimental Thermal and Fluid Science*, 11:52–60, 1995.
- [114] J. G. Proakis and D. G. Manolakis. *Digital Signal Processing: Principles, Algorithms, and Applications*. Prentice-Hall Inc., 1996.
- [115] D. W. Ladoon. *Wave Packets Generated by a Surface Glow Discharge on a Cone at Mach 4*. PhD thesis, Purdue University, School of Aeronautics and Astronautics, December 1998.
- [116] Eagle Harbor Technologies Inc. User’s Manual for Nanosecond Pulser NSP-3300-20-F.
- [117] K. M. Casper, S. J. Beresh, J. F. Henfling, R. W. Spillers, and P. Hunter. Fluid-Structure Interactions using Controlled Disturbances on a Slender Cone at Mach 8. AIAA Paper 2016-1126, January 2016.
- [118] K. M. Casper. Fluid-Structure Interactions on a Slender Cone under Quiet Flow Conditions at Mach 6. AIAA Paper 2017-0402, January 2016.

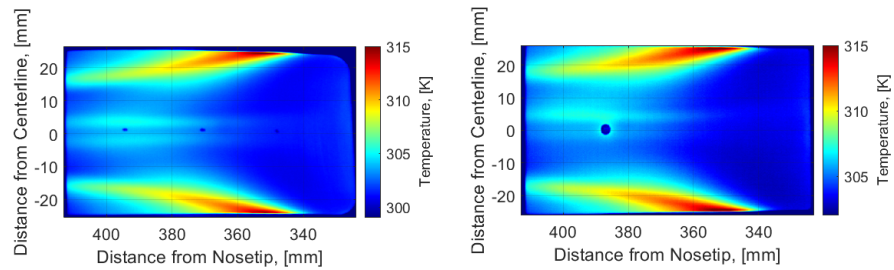
- [119] K. M. Casper, S. J. Beresh, J. F. Henfling, R. W. Spillers, P. Hunter, and S. Spitzer. Hypersonic Fluid-Structure Interactions on a Slender Cone. AIAA Paper 2018-1825, January 2018.
- [120] K. M. Casper, S. J. Beresh, J. F. Henfling, R. W. Spillers, and P. Hunter. Hypersonic Fluid-Structure Interactions due to Intermittent Turbulent Spots on a Slender Cone. *AIAA Journal*, 57(2):749–759, February 2019.
- [121] R. K. Pearson. Outliers in Process Modeling and Identification. *IEEE Transactions on Control Systems Technology*, 10(1):55–63, January 2002.
- [122] A. Chou, P. Balakumar, and S. P. Schneider. Development of Instabilities Generated by Freestream Laser Perturbations in a Hypersonic Boundary Layer. *AIAA Journal*, 55(3):799–807, March 2017.
- [123] E. K. Benitez, J. S. Jewell, and S. P. Schneider. Focused Laser Differential Interferometry for Hypersonic Flow Instability Measurements with Contour Tunnel Windows. AIAA Paper 2020-1282, January 2020.

## APPENDICES

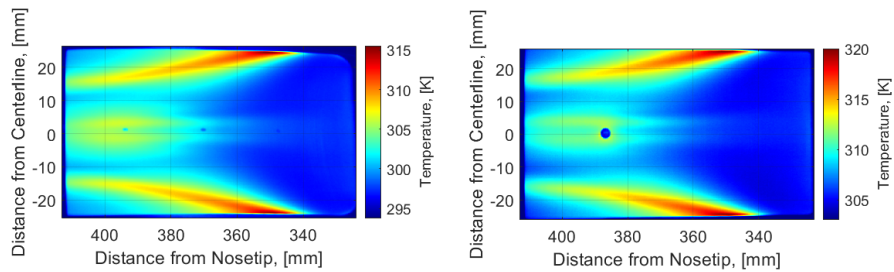
## A. EFFECTS OF CORNER RADII ON RAMP SURFACE TEMPERATURE



(a) 4.8 mm corner radii at  $Re_\infty = 1.8 \times 10^6 / \text{m}$  (Run 1212). (b) 1.6 mm corner radii at  $Re_\infty = 1.9 \times 10^6 / \text{m}$  (Run 2303).



(c) 4.8 mm corner radii at  $Re_\infty = 2.6 \times 10^6 / \text{m}$  (Run 1213). (d) 1.6 mm corner radii at  $Re_\infty = 2.6 \times 10^6 / \text{m}$  (Run 2306).



(e) 4.8 mm corner radii at  $Re_\infty = 3.2 \times 10^6 / \text{m}$  (Run 1215). (f) 1.6 mm corner radii at  $Re_\infty = 3.2 \times 10^6 / \text{m}$  (Run 2307).

Figure A.1. Comparison of surface temperature with varying ramp corner radii.

## B. SELECTED RUN CONDITIONS

Table B.1. Entry 2 (March 2016).

Run	$P_0$ [psia]	$T_0$ [°C]	Quiet/Noisy	Ramp Angle (°)
0203	168.5	144.8	Quiet	10
0204	169.2	149.0	Quiet	20
0206	171.5	154.2	Quiet	30
0212	156.4	153.3	Noisy	30

Table B.2. Entry 5 (August 2016).

Run	$P_0$ [psia]	$T_0$ [°C]	Quiet/Noisy	Ramp Angle (°)
0517	167.5	156.9	Quiet	30
0518	152.8	154.9	Noisy	30
0521	168.6	157.3	Quiet	20
0522	154.6	154.4	Noisy	20
0525	169.9	155.5	Quiet	10
0526	155.3	156.1	Noisy	10

Table B.3. Entry 7 (February 2017).

Run	$P_0$ [psia]	$T_0$ [°C]	Quiet/Noisy	Ramp Angle (°)
0704	112.5	151.8	Noisy	20
0718	44.0	151.2	Quiet	20
0720	76.1	154.7	Quiet	20

Table B.4. Entry 8 (April 2017).

Run	$P_0$ [psia]	$T_0$ [°C]	Quiet/Noisy	Ramp Angle (°)
0809	45.7	153.1	Quiet	10

Table B.5. Entry 9 (May 2017).

Run	$P_0$ [psia]	$T_0$ [°C]	Quiet/Noisy	Ramp Angle (°)
0908	41.2	149.4	Quiet	15

Table B.6. Entry 10 (May 2017).

Run	$P_0$ [psia]	$T_0$ [°C]	Quiet/Noisy	Ramp Angle (°)
1003	109.7	149.6	Noisy	20
1005	30.4	145.1	Quiet	20
1006	34.7	155.3	Quiet	20
1007	40.6	153.6	Quiet	20
1008	44.6	153.3	Quiet	20
1010	76.1	152.9	Quiet	20
1011	89.5	156.8	Quiet	20
1013	130.6	156.8	Quiet	20
1018	32.8	152.2	Noisy	20

Table B.7. Entry 18 (December 2018).

Run	$P_0$ [psia]	$T_0$ [°C]	Quiet/Noisy	Ramp Angle (°)
1812	124.1	147.9	Quiet	20
1815	128.2	153.7	Quiet	15
1817	128.4	154.6	Quiet	10

Table B.8. Entry 19 (June 2019).

Run	$P_0$ [psia]	$T_0$ [°C]	Quiet/Noisy	Ramp Angle (°)
1907	151.9	157.7	Quiet	-
1908	151.8	155.7	Quiet	-
1910	151.5	158.0	Quiet	-
1911	108.1	156.8	Quiet	-

Table B.9. Entry 20 (September 2019).

Run	$P_0$ [psia]	$T_0$ [°C]	Quiet/Noisy	Ramp Angle (°)
2004	114.1	156.9	Noisy	20
2007	21.7	151.1	Quiet	20
2009	14.4	154.7	Quiet	20
2010	29.7	147.3	Quiet	20
2012	25.5	153.5	Quiet	20
2013	36.3	153.7	Quiet	20
2015	44.9	154.7	Quiet	20
2017	102.4	157.1	Quiet	20
2018	27.2	156.6	Noisy	20
2019	14.4	154.8	Noisy	20
2020	20.4	148.6	Noisy	20
2021	37.6	153.4	Noisy	20
2022	45.8	154.7	Noisy	20

Table B.10. Entry 21 (October 2019).

Run	$P_0$ [psia]	$T_0$ [°C]	Quiet/Noisy	Ramp Angle (°)
2103	30.3	155.9	Quiet	20
2104	35.0	153.9	Quiet	20
2105	39.8	153.7	Quiet	20
2107	49.7	153.8	Quiet	20
2112	85.1	159.1	Quiet	20
2115	125.1	158.4	Quiet	20

Table B.11. Entry 22 (November 2019).

Run	$P_0$ [psia]	$T_0$ [°C]	Quiet/Noisy	Ramp Angle (°)
2208	27.0	151.2	Quiet	20
2209	31.0	148.9	Quiet	20
2212	35.1	156.2	Quiet	20
2213	40.5	156.5	Quiet	20
2214	45.2	155.0	Quiet	20
2215	45.2	155.0	Quiet	20

Table B.12. Entry 23 (December 2019).

Run	$P_0$ [psia]	$T_0$ [°C]	Quiet/Noisy	Ramp Angle (°)
2303	27.1	152.9	Quiet	20
2306	35.6	151.0	Quiet	20
2307	44.1	152.1	Quiet	20
2310	27.0	151.2	Quiet	20
2311	31.0	148.9	Quiet	20
2312	35.1	156.2	Quiet	20
2313	40.0	152.9	Quiet	20
2314	45.8	153.2	Quiet	20
2315	28.1	151.7	Quiet	20
2318	27.4	145.8	Quiet	20
2320	20.4	142.9	Quiet	20
2321	29.2	150.0	Quiet	20
2323	27.2	152.5	Quiet	20
2324	27.7	151.4	Quiet	20
2325	28.2	151.3	Quiet	20

Table B.13. Entry 23 continued.

Run	$P_0$ [psia]	$T_0$ [°C]	Quiet/Noisy	Ramp Angle (°)
2326	30.7	151.8	Quiet	20
2327	35.5	152.0	Quiet	20
2328	41.9	152.0	Quiet	20
2329	45.5	150.7	Quiet	20
2330	20.6	147.6	Quiet	20
2331	29.1	152.7	Quiet	20
2332	27.8	150.2	Quiet	20
2333	27.7	150.6	Quiet	20
2334	19.8	149.2	Quiet	20
2335	27.8	150.1	Quiet	20
2336	32.8	144.4	Quiet	20
2337	38.0	151.2	Quiet	20
2338	42.8	151.4	Quiet	20

## C. SUPPLEMENTARY MEASUREMENTS OF PULSER BEHAVIOR

Table C.1. Electronics settings for runs with artificially generated disturbances on the cone-slice-ramp.

Runs	Pulse Duration (ns)	Frequency (kHz)	Number of Pulses	Voltage (kV)
2310-2322	100	2	300	10
2324, 2326-2333	100	2	300	5
2325, 2334-2340	100	2	300	2.5

Table C.2. Electronics statistics for relevant runs on the long-ramp perturbation model.

Run	Mean $V_{RMS}$ (V)	St. Dev. $V_{RMS}$ (V)	St. Dev./ Mean	Mean $I_{RMS}$ (A)	Mean $I_{RMS}$ (A)	St. Dev. /Mean
2310	4433	383	0.086	5.97	0.80	0.134
2311	4441	393	0.089	5.94	0.66	0.111
2312	4310	399	0.093	6.06	0.63	0.104
2313	4112	396	0.096	6.06	0.42	0.069
2314	4040	422	0.104	5.99	0.42	0.070
2318	4315	507	0.117	5.98	0.63	0.105
2319	2849	399	0.140	5.58	0.19	0.034
2320	4494	237	0.053	4.80	0.18	0.038
2324	2767	118	0.043	2.38	0.19	0.080
2326	2728	108	0.040	2.31	0.25	0.108
2327	2680	86	0.032	2.24	0.24	0.107
2328	2641	99	0.037	2.13	0.19	0.089
2329	2553	113	0.044	2.28	0.15	0.066
2330	2780	110	0.040	2.38	0.20	0.084
2332	2750	88	0.032	2.08	0.25	0.120
2334	1603	14	0.009	1.20	0.03	0.025
2336	1588	14	0.009	1.20	0.05	0.042
2337	1591	20	0.013	1.19	0.06	0.050
2338	1589	18	0.011	1.19	0.06	0.050

## D. CUSTOM HARDWARE DRAWINGS

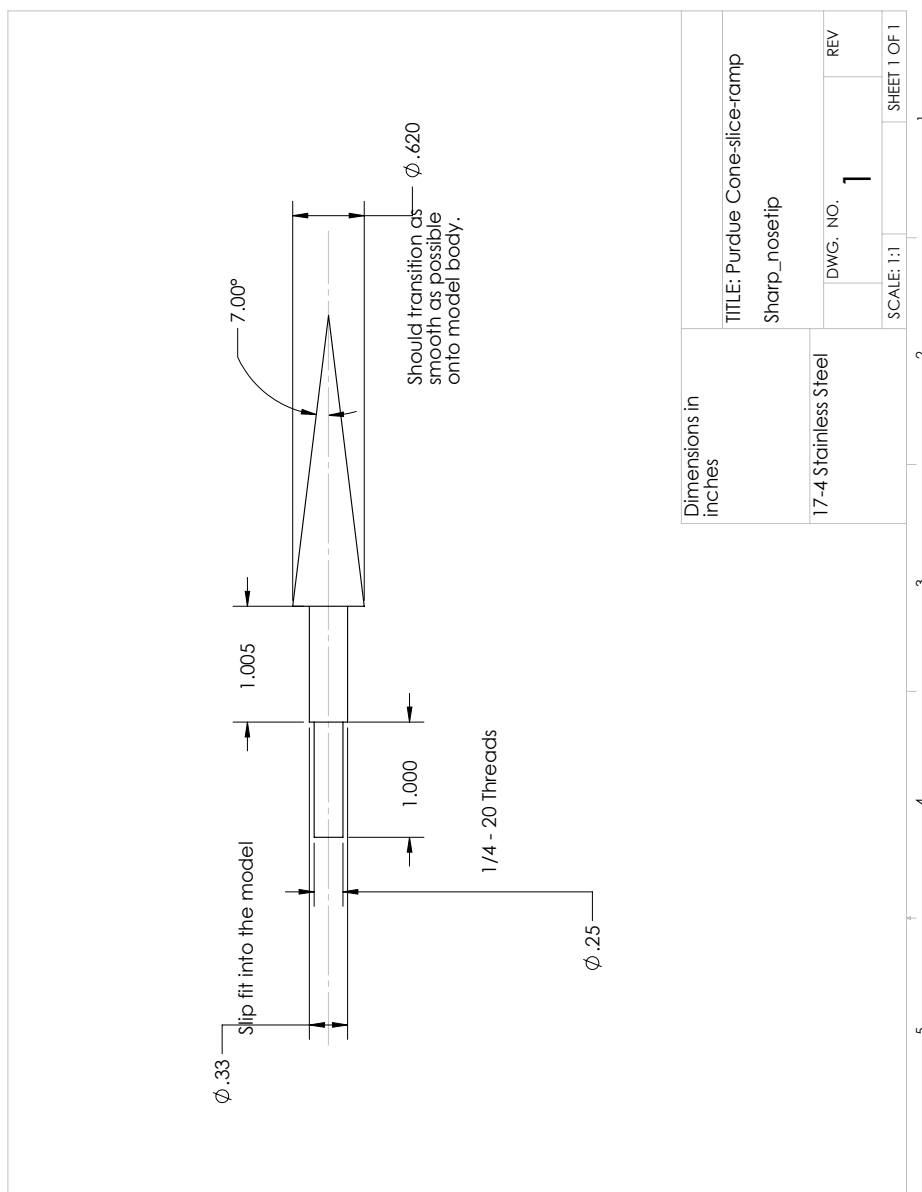


Figure D.1. Drawing of the sharp nosetip used for every model

## D.1 Short-Ramp Model

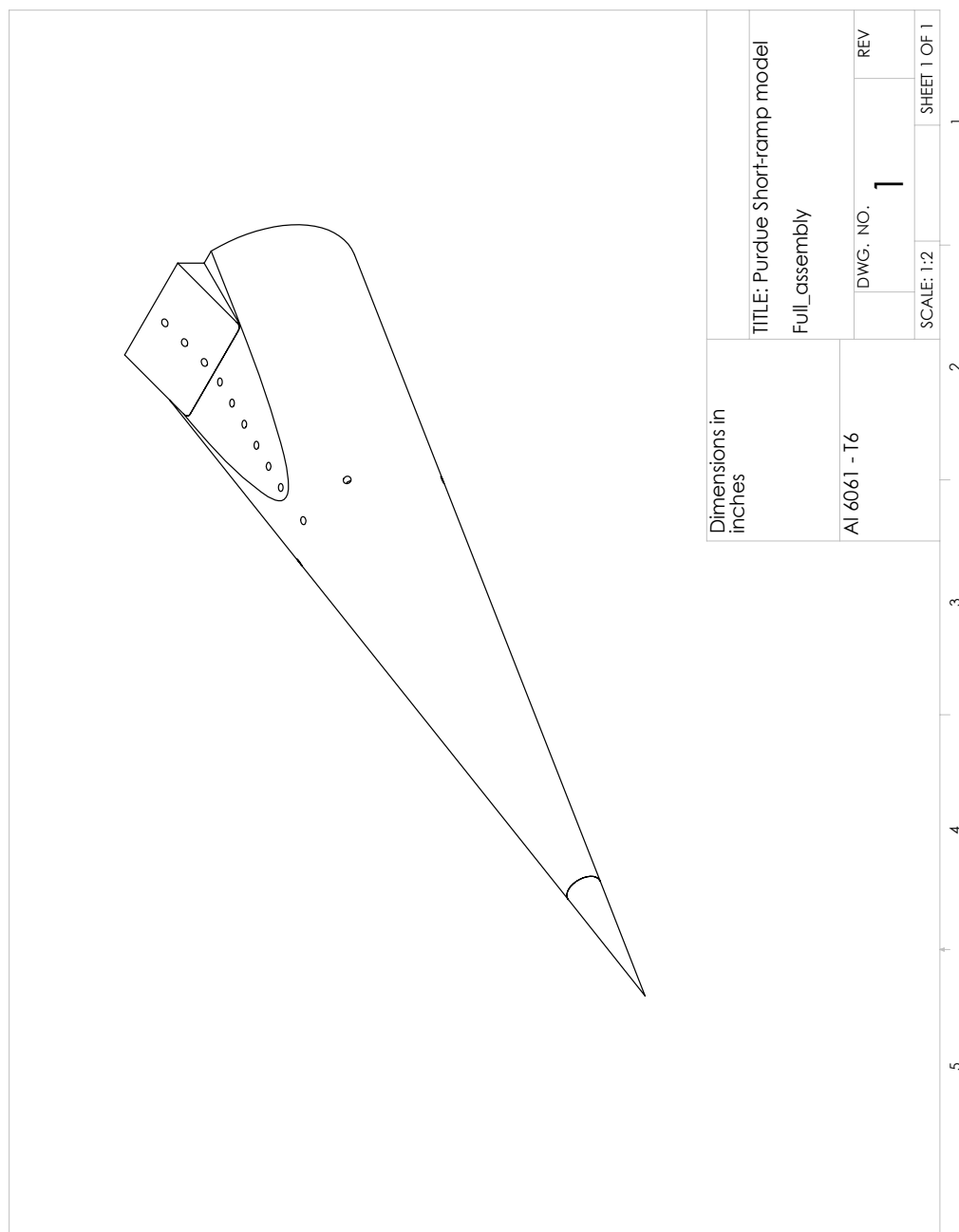
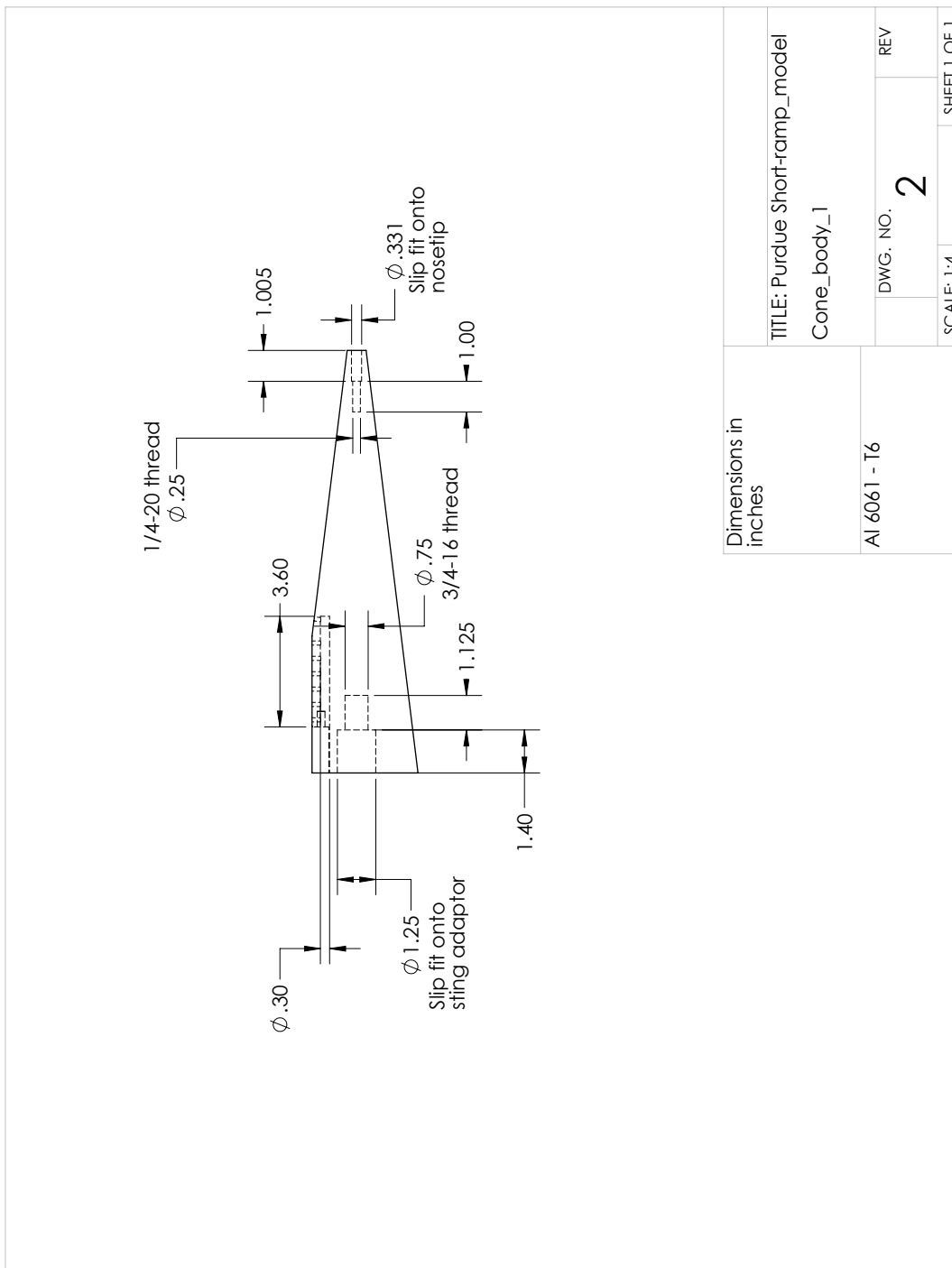


Figure D.2. Drawing of the short-ramp cone assembly



Dimensions in inches	TITLE: Purdue Short-ramp_model Cone_body_1	
	DWG. NO. <b>2</b>	REV
AI 6061 - T6	SCALE: 1:4	SHEET 1 OF 1

Figure D.3. Drawing of the short-ramp cone body - Part 1

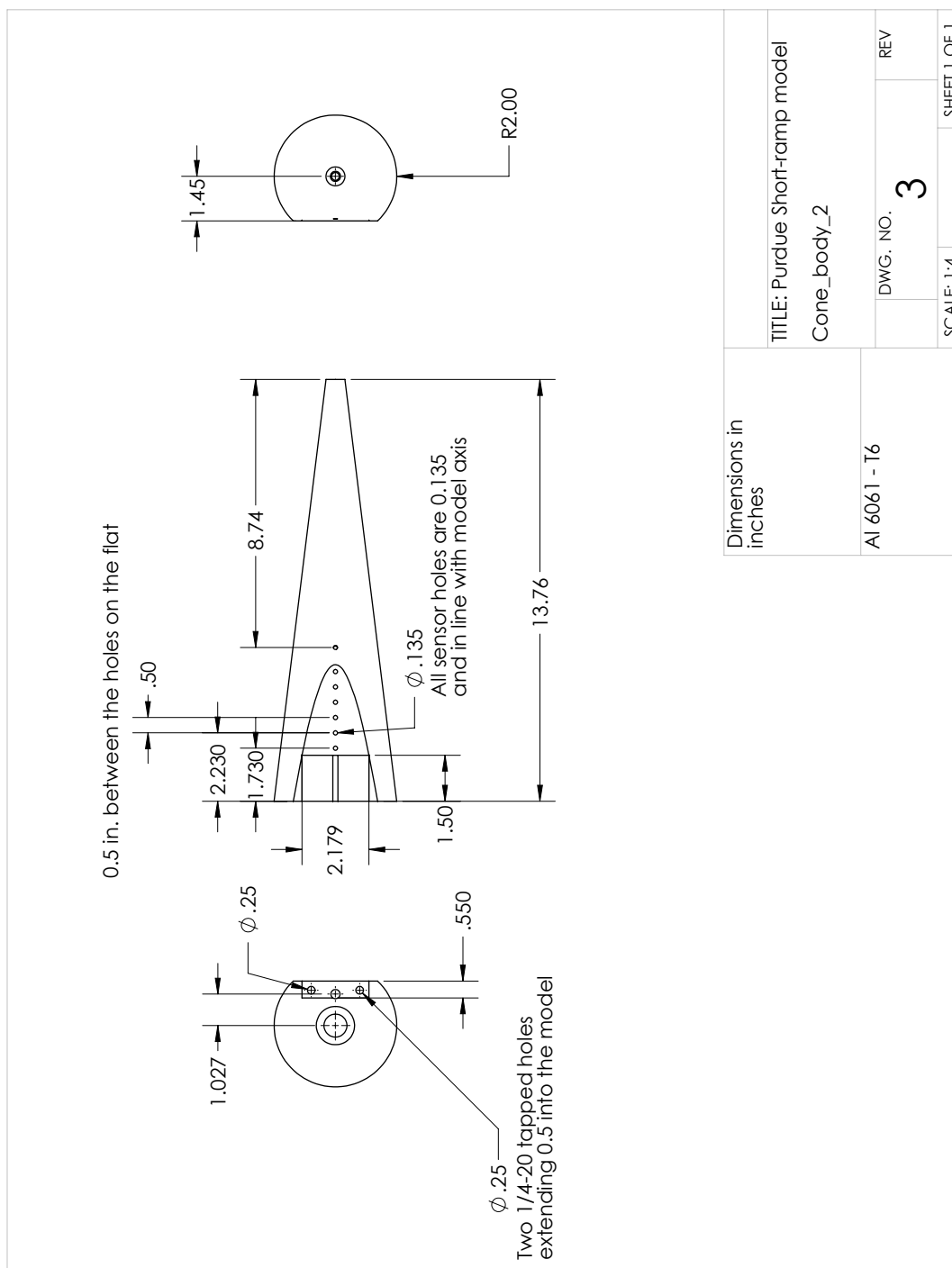


Figure D.4. Drawing of the short-ramp cone body - Part 2.

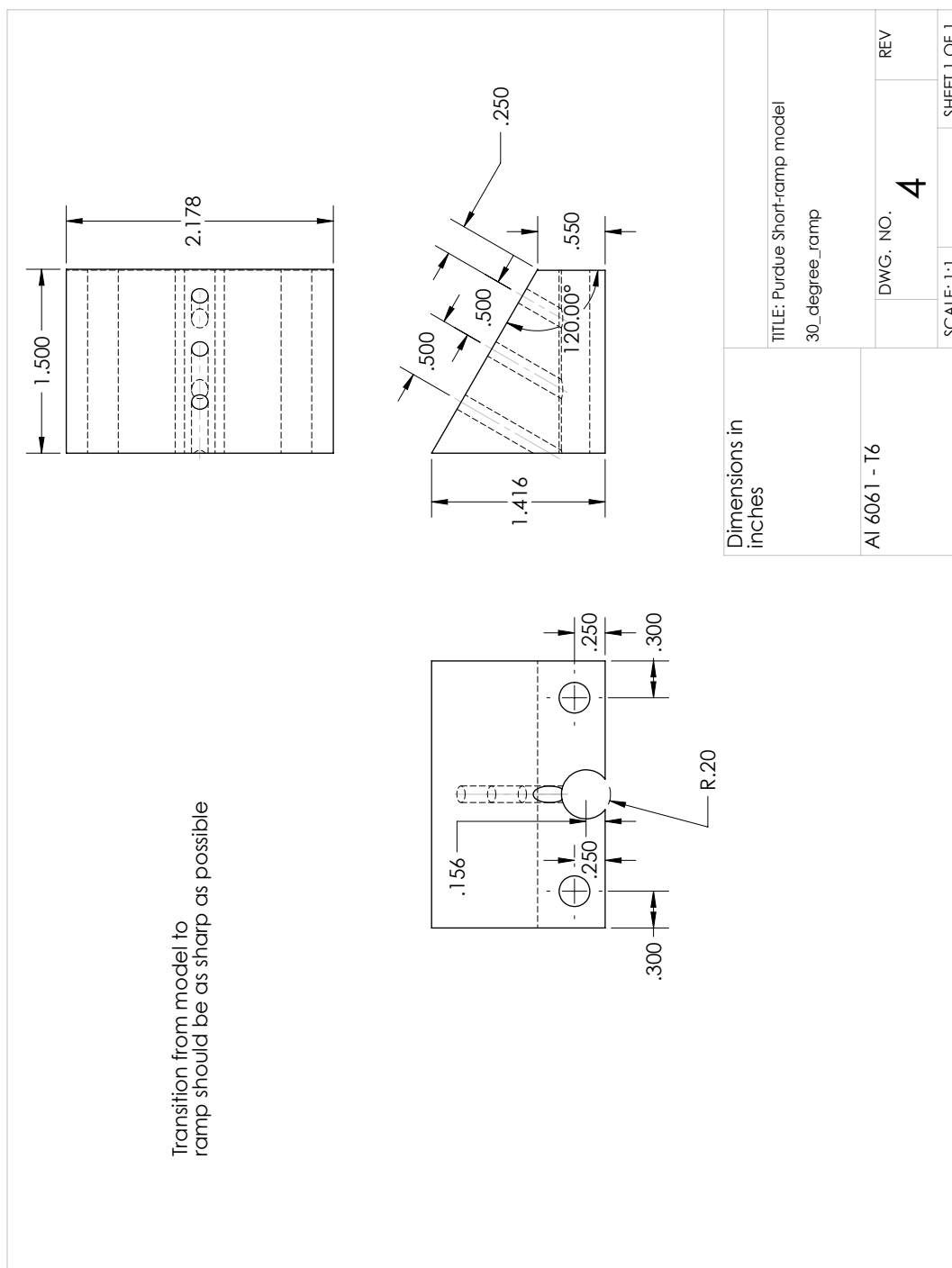


Figure D.5. Drawing of the short-ramp 10° spanwise ramp.

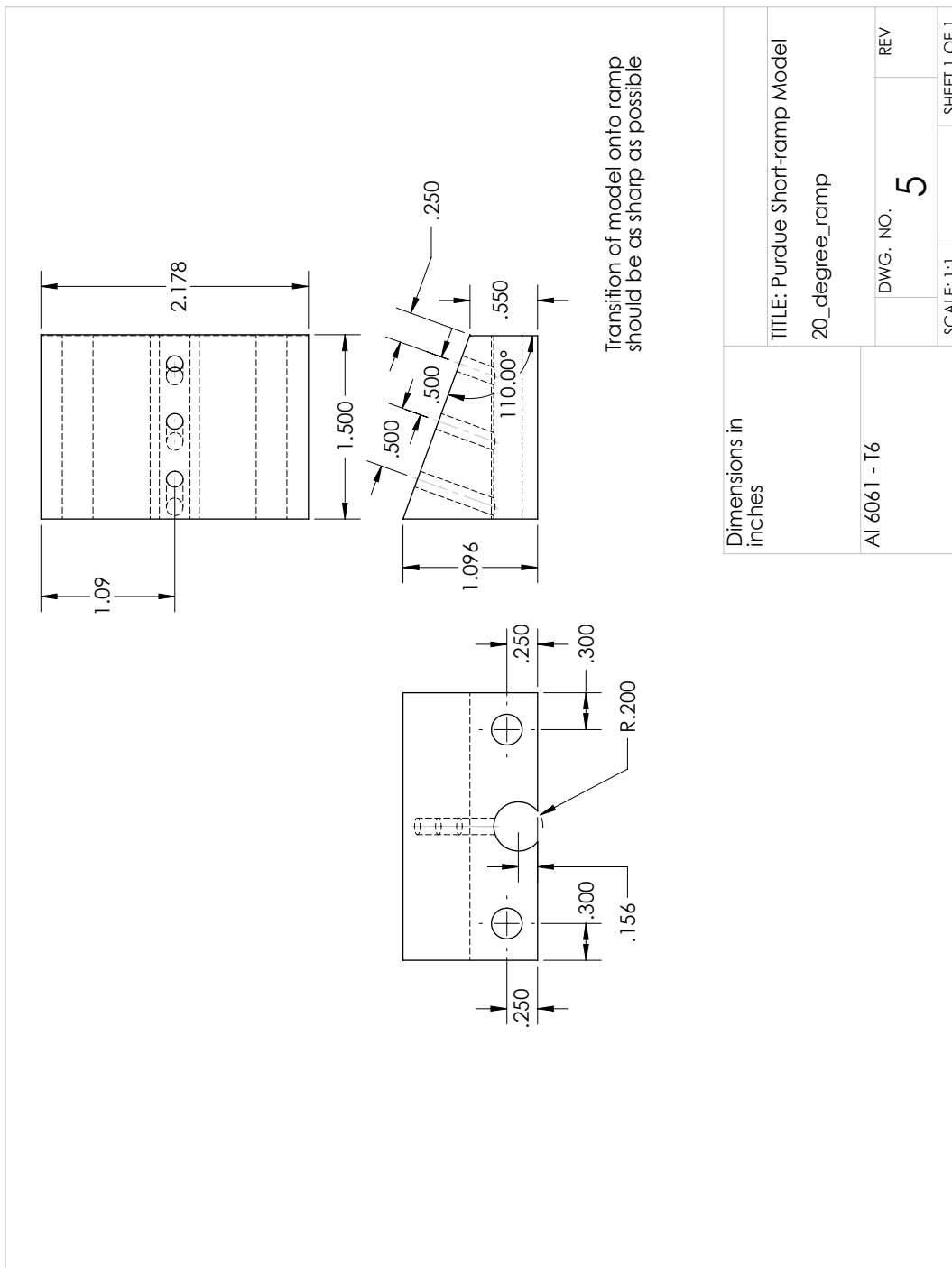


Figure D.6. Drawing of the short-ramp 20° spanwise ramp.

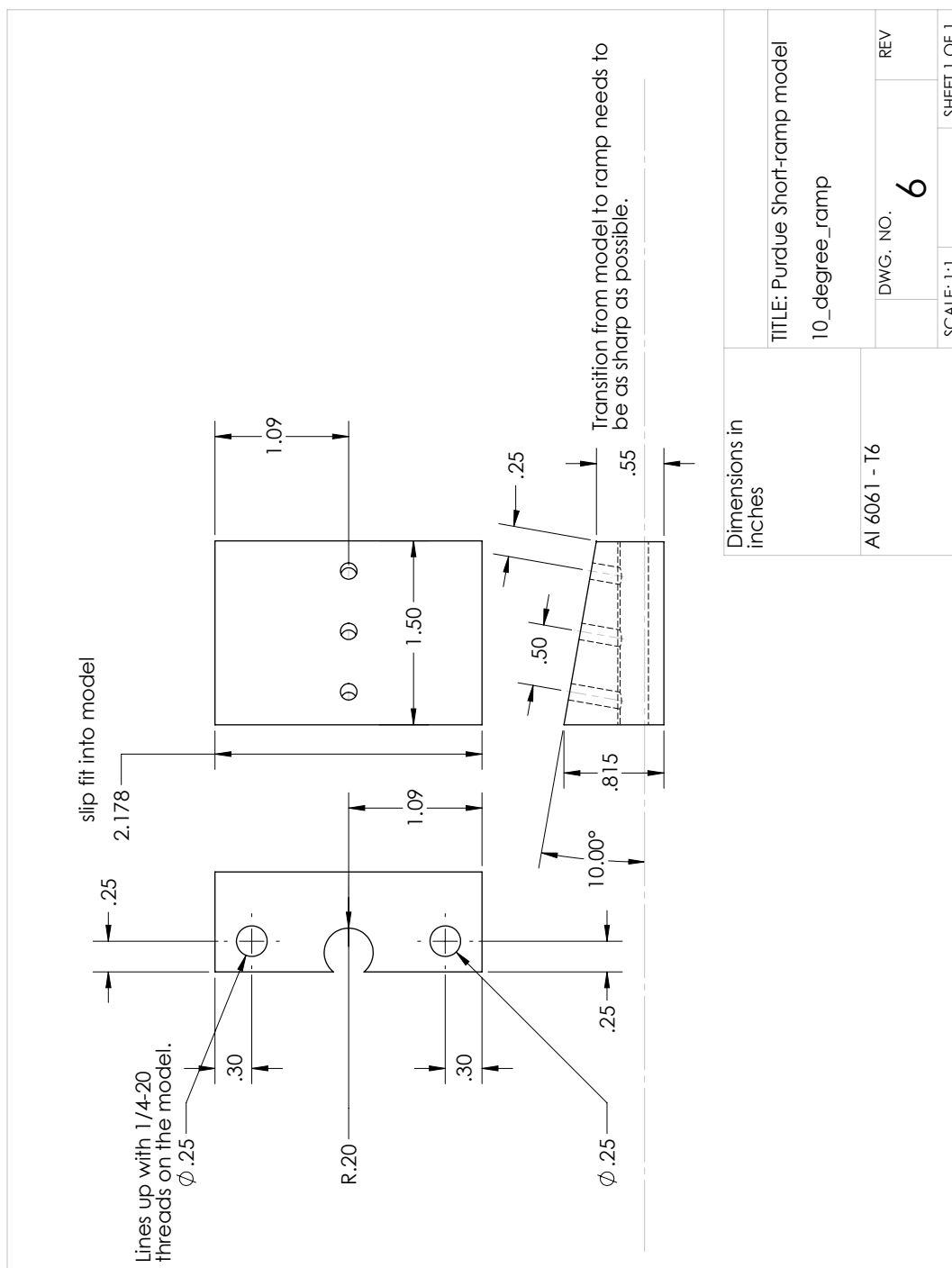


Figure D.7. Drawing of the short-ramp 30° spanwise ramp.

## D.2 Long-Ramp Model

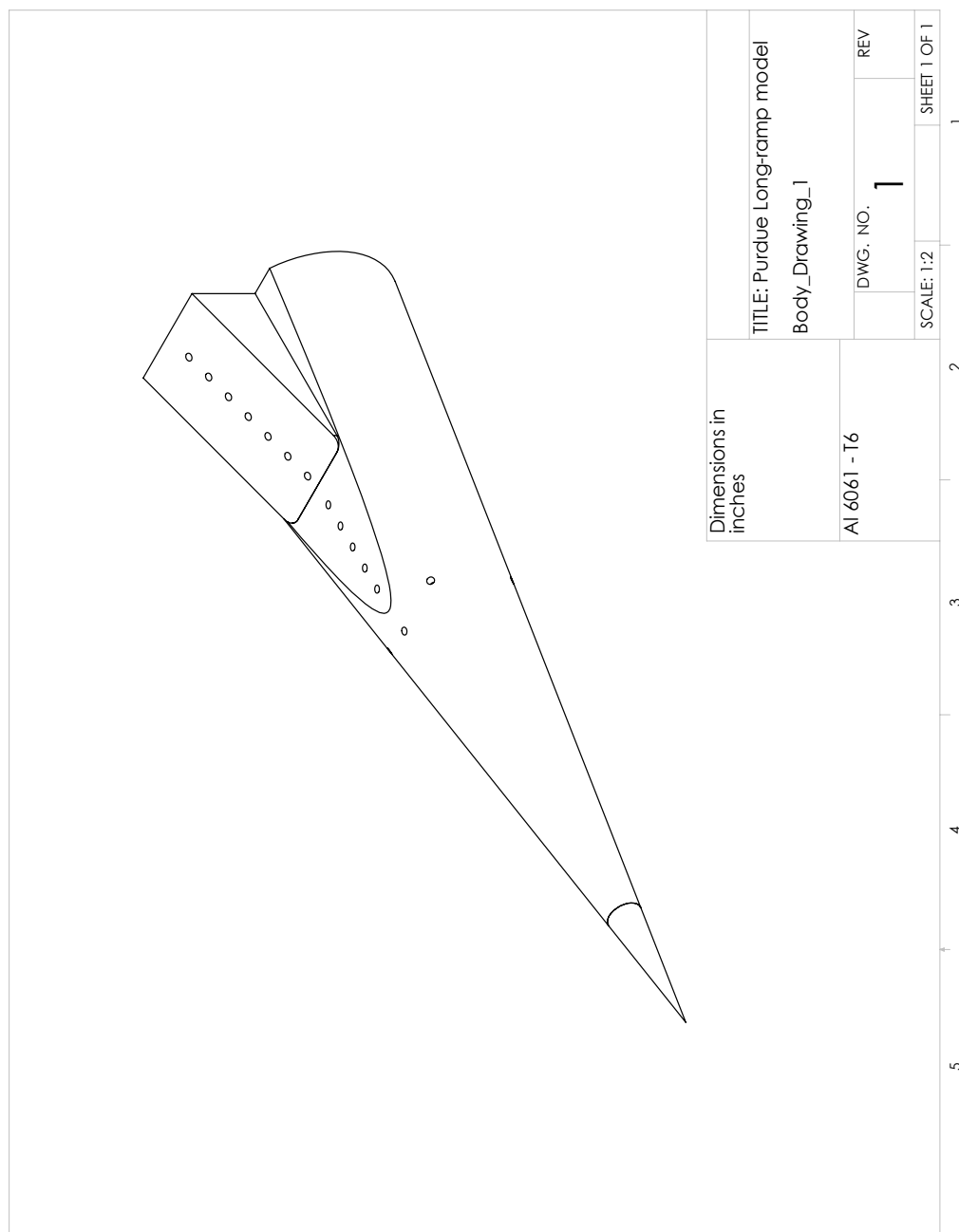


Figure D.8. Drawing of the Long-ramp cone assembly

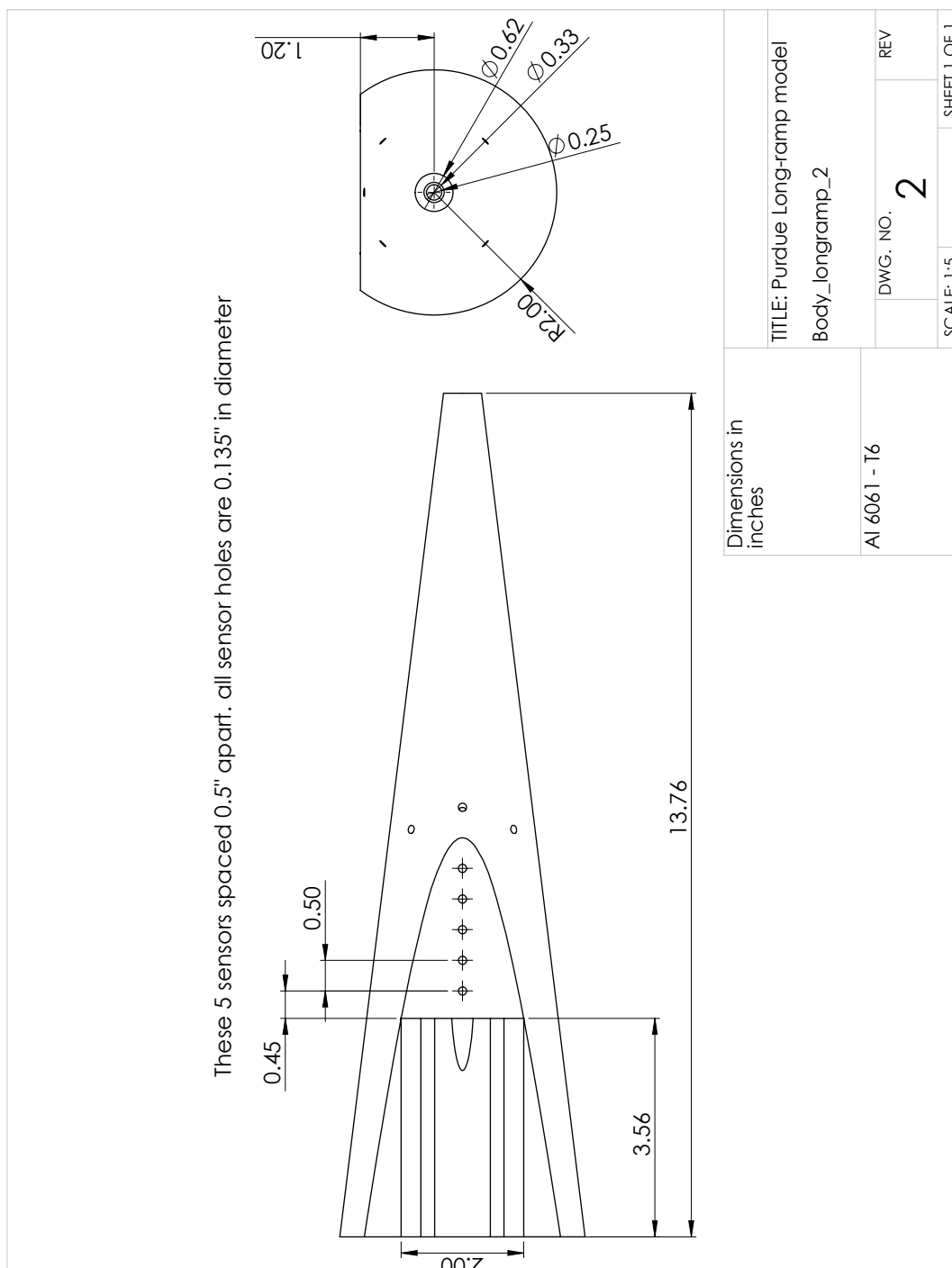


Figure D.9. Drawing of the Long-ramp cone body - Part 1

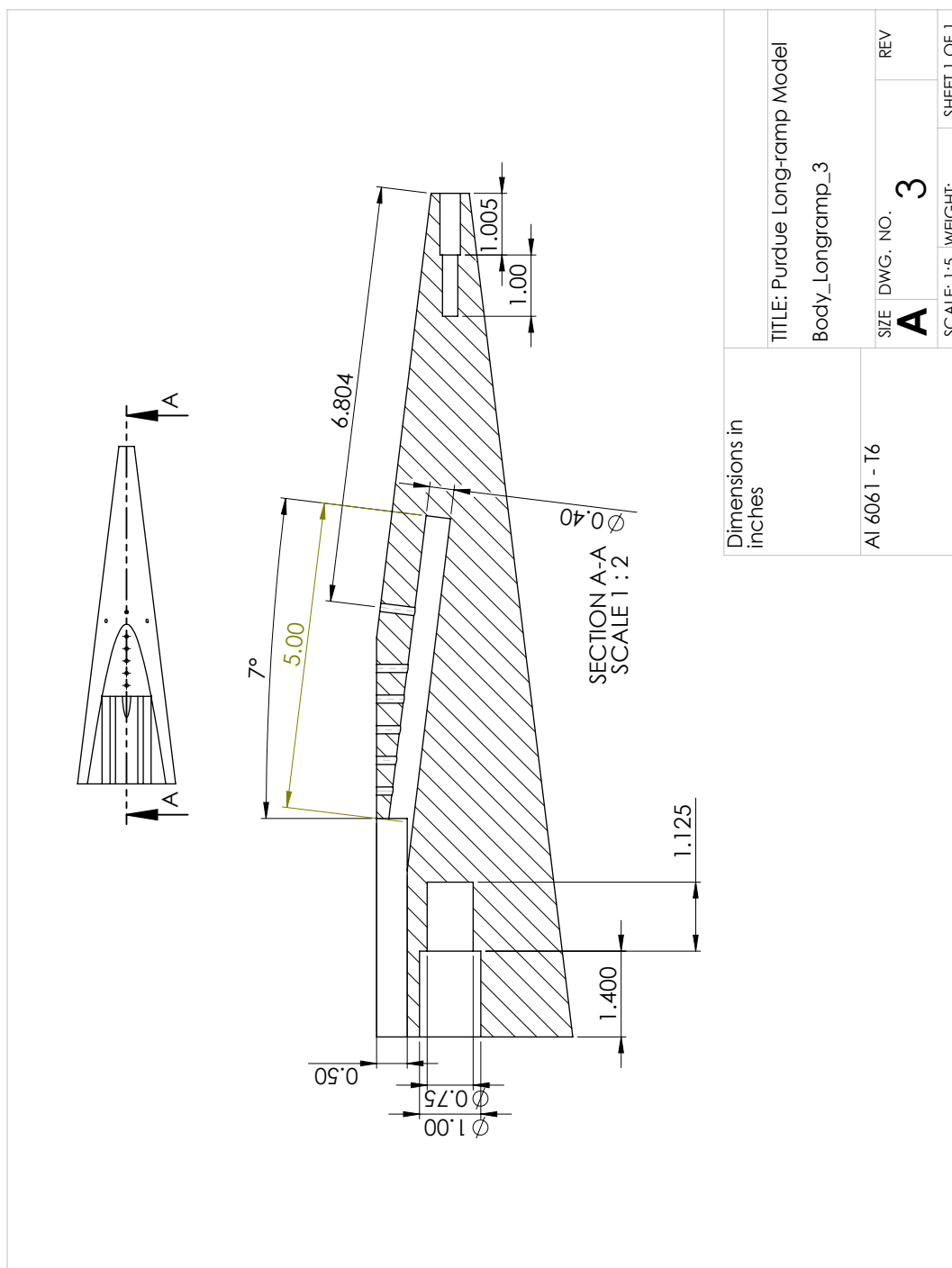


Figure D.10. Drawing of the Long-ramp cone body - Part 2.

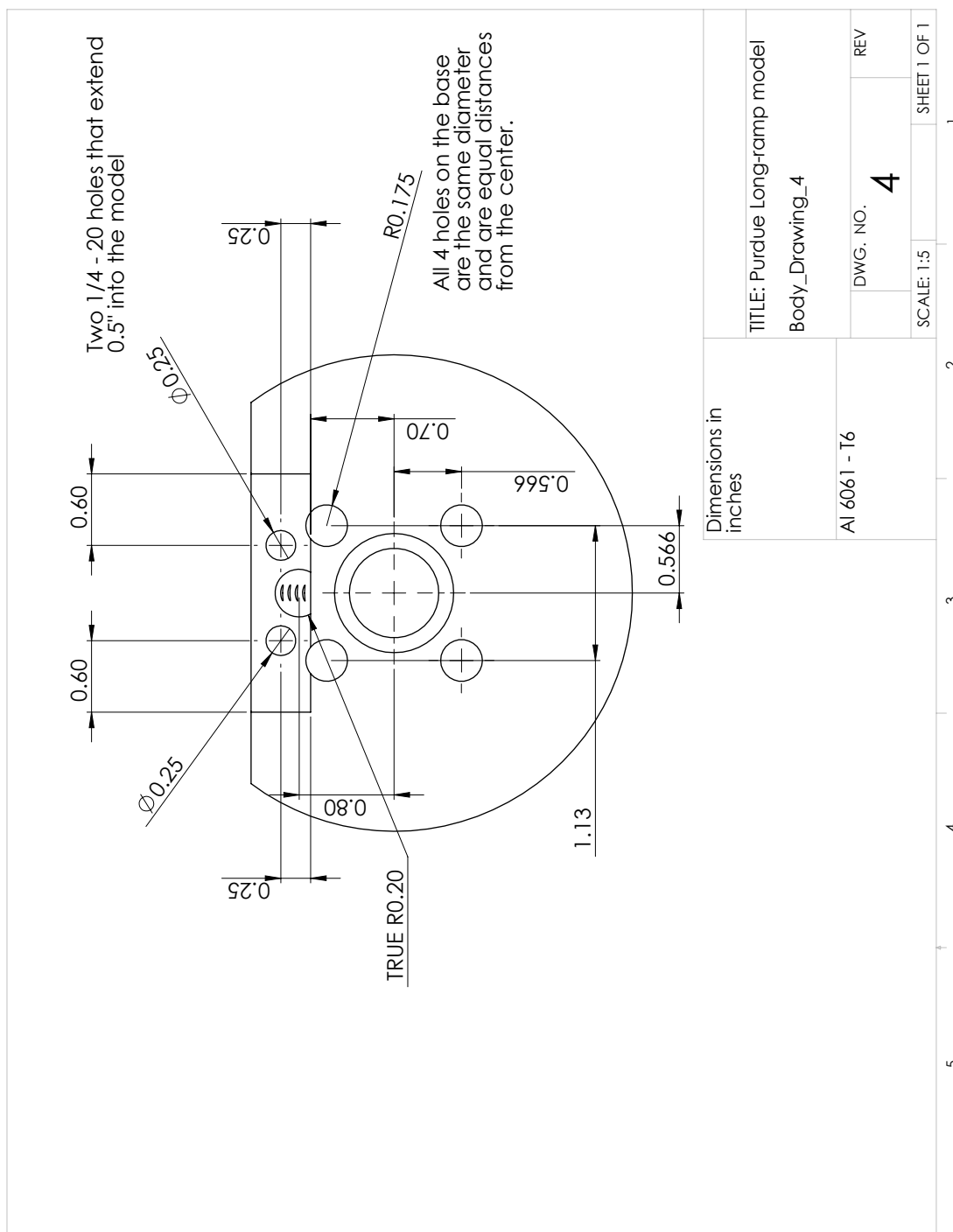


Figure D.11. Drawing of the Long-ramp cone body - Part 3.

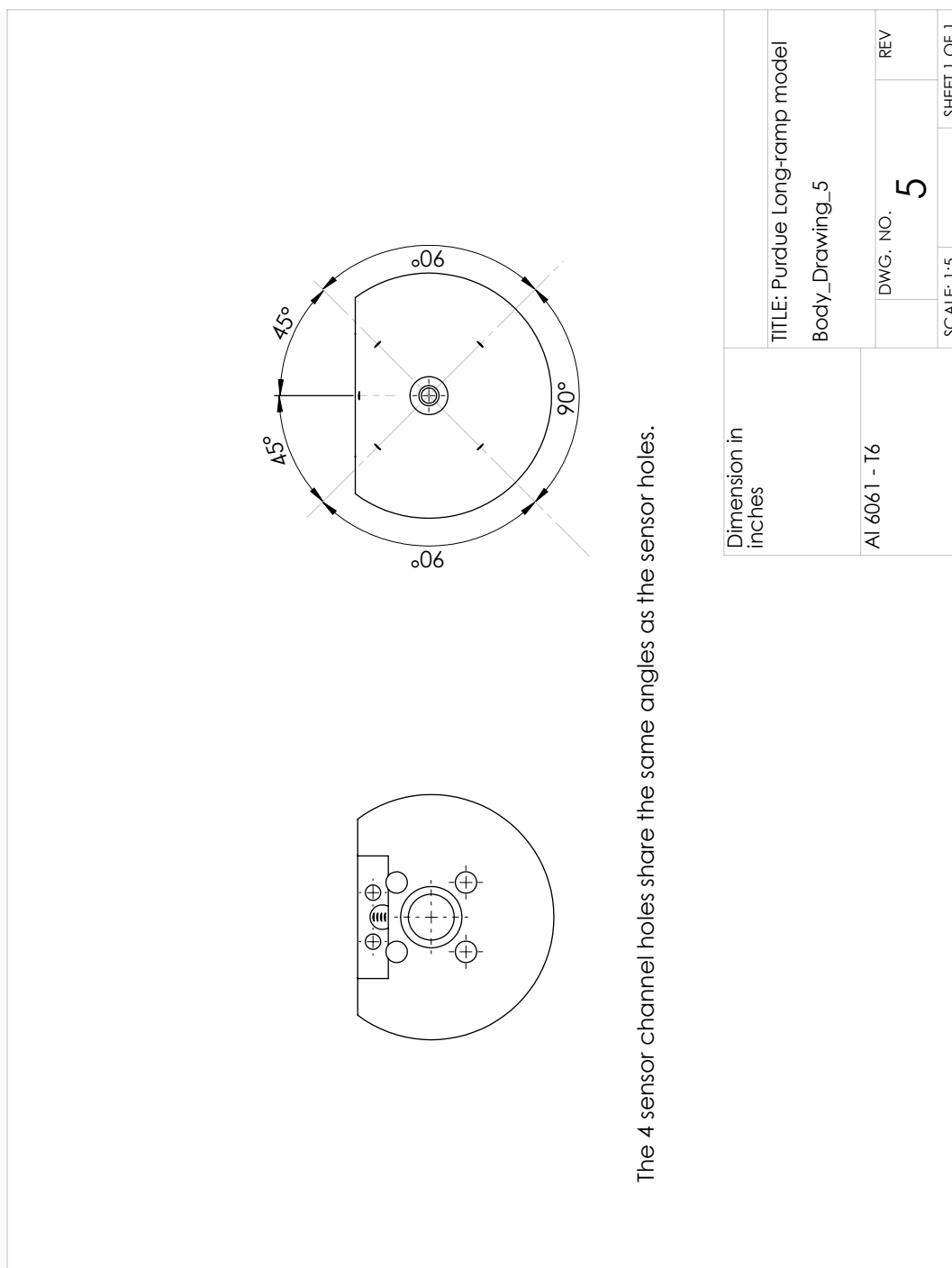


Figure D.12. Drawing of the Long-ramp cone body - Part 4.

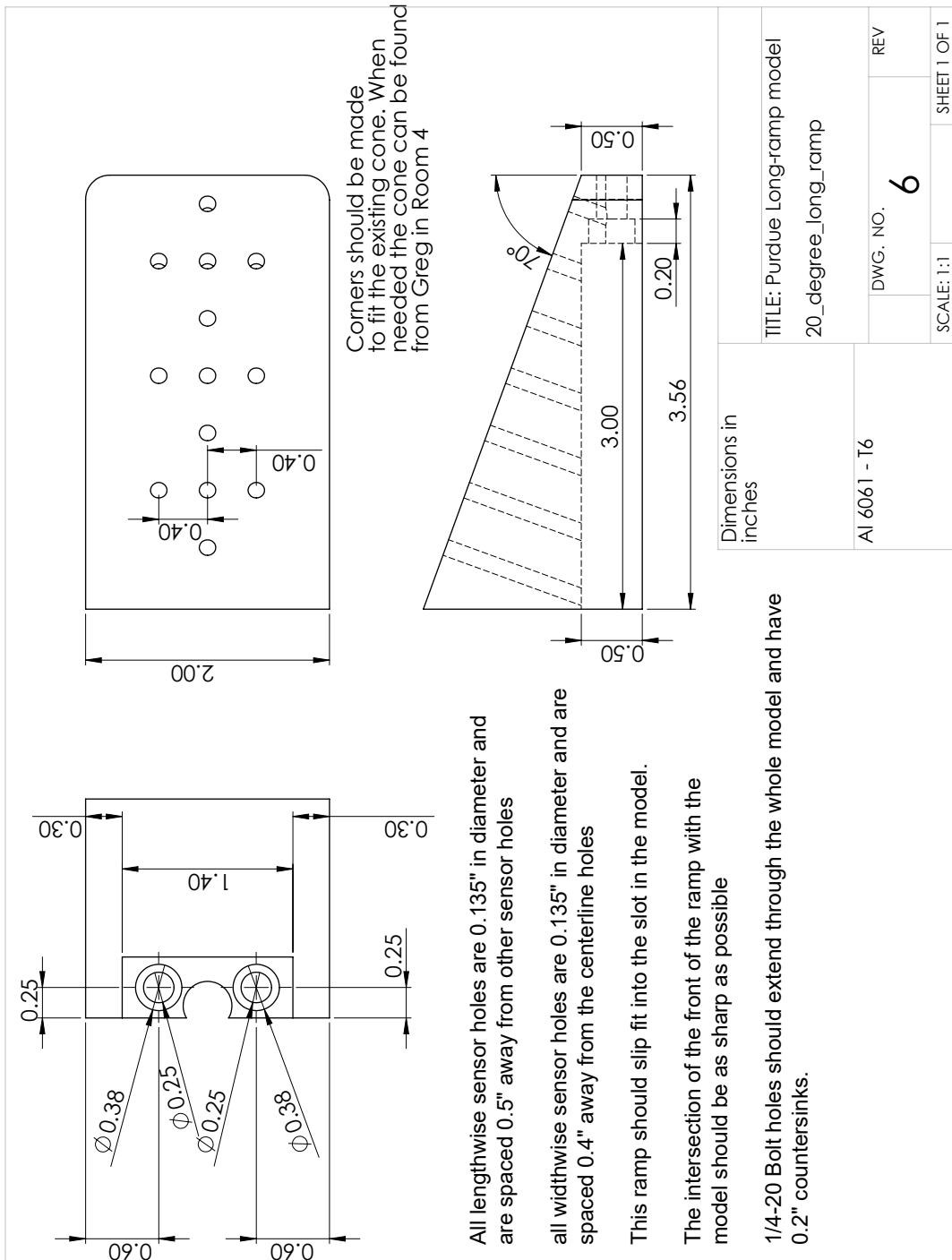


Figure D.13. Drawing of the 20° spanwise ramp.

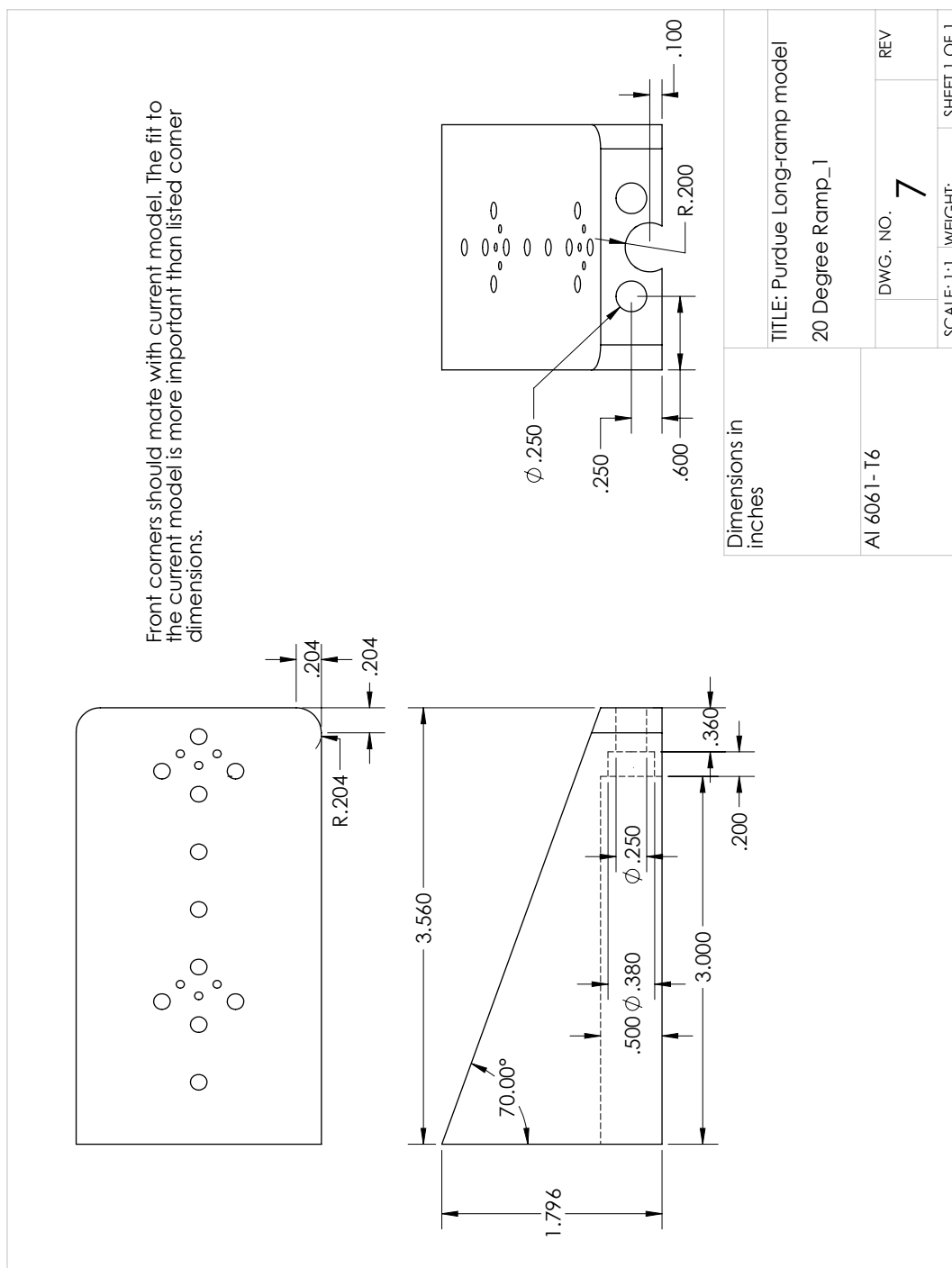


Figure D.14. Drawing of the 20° cluster ramp - Part 1.

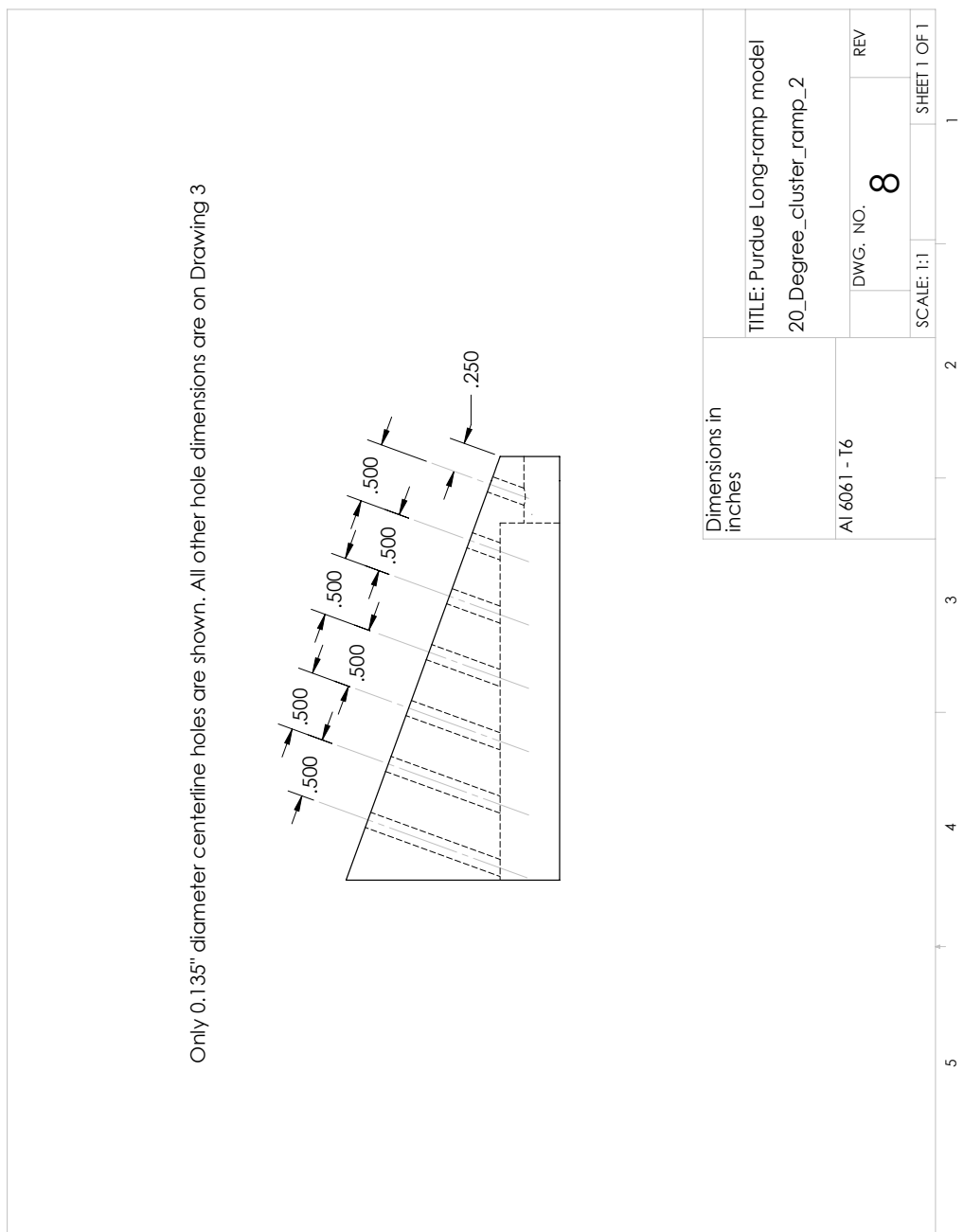


Figure D.15. Drawing of the 20° cluster ramp - Part 2.

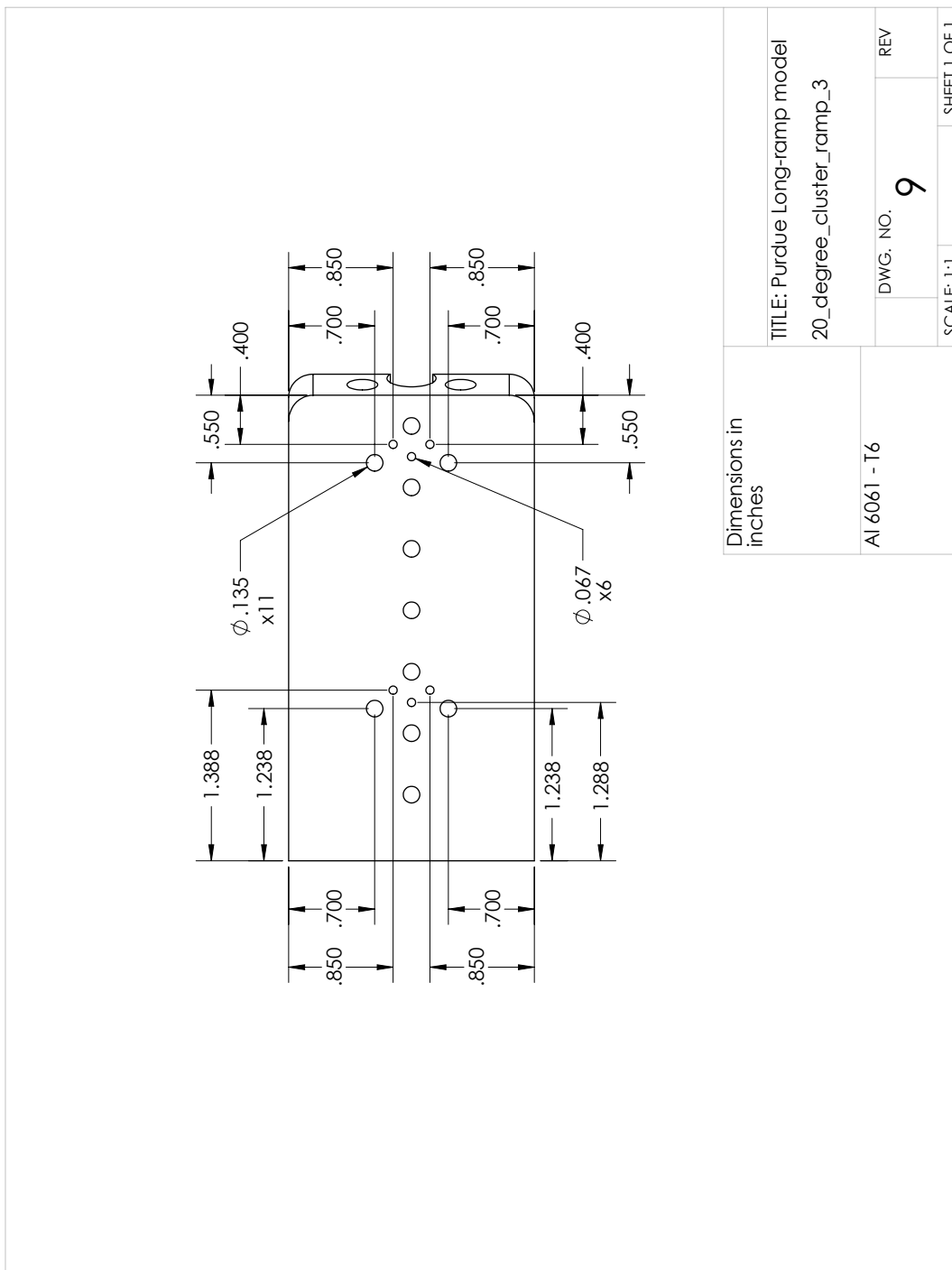


Figure D.16. Drawing of the 20° cluster ramp - Part 3.

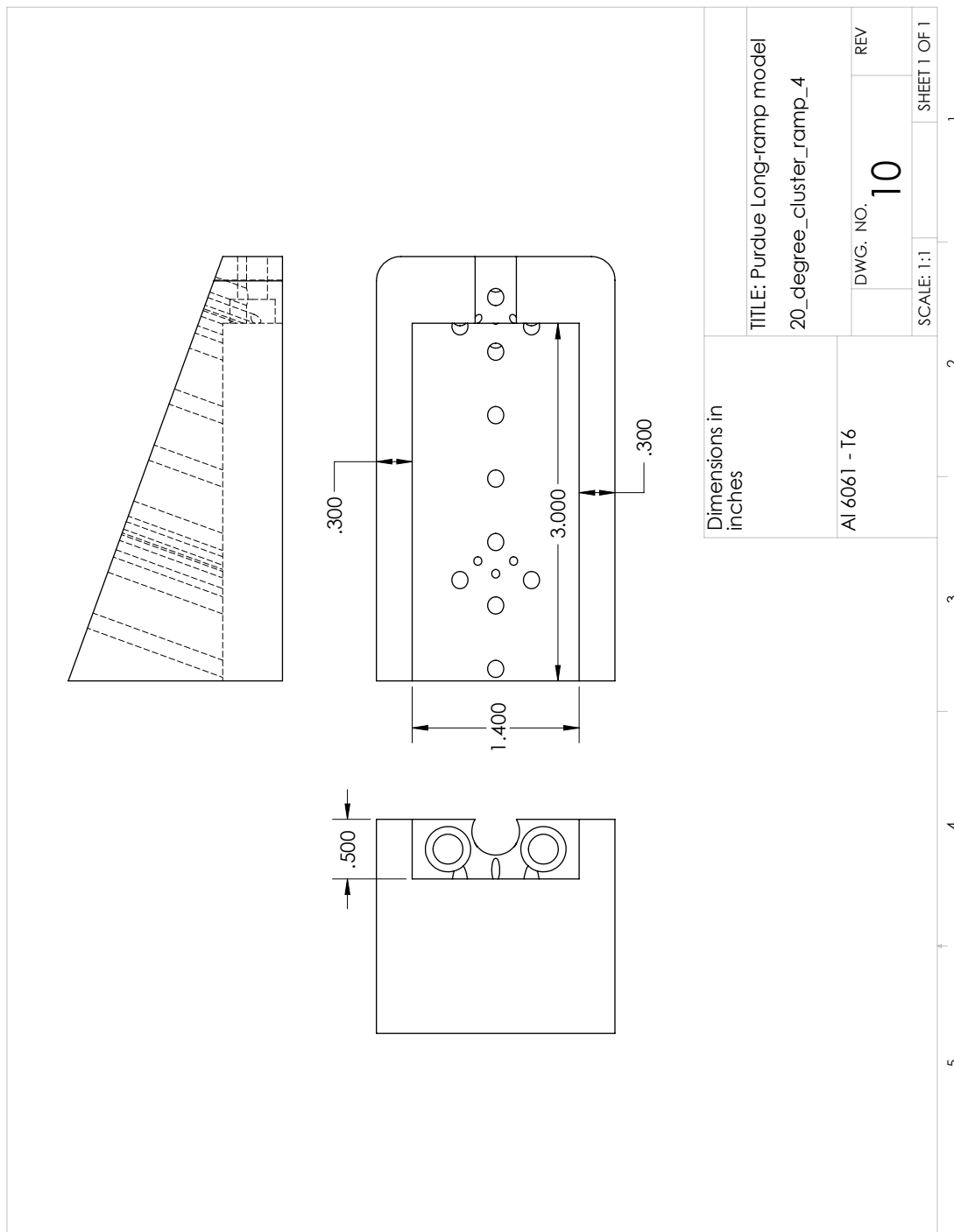


Figure D.17. Drawing of the 20° cluster ramp - Part 4.

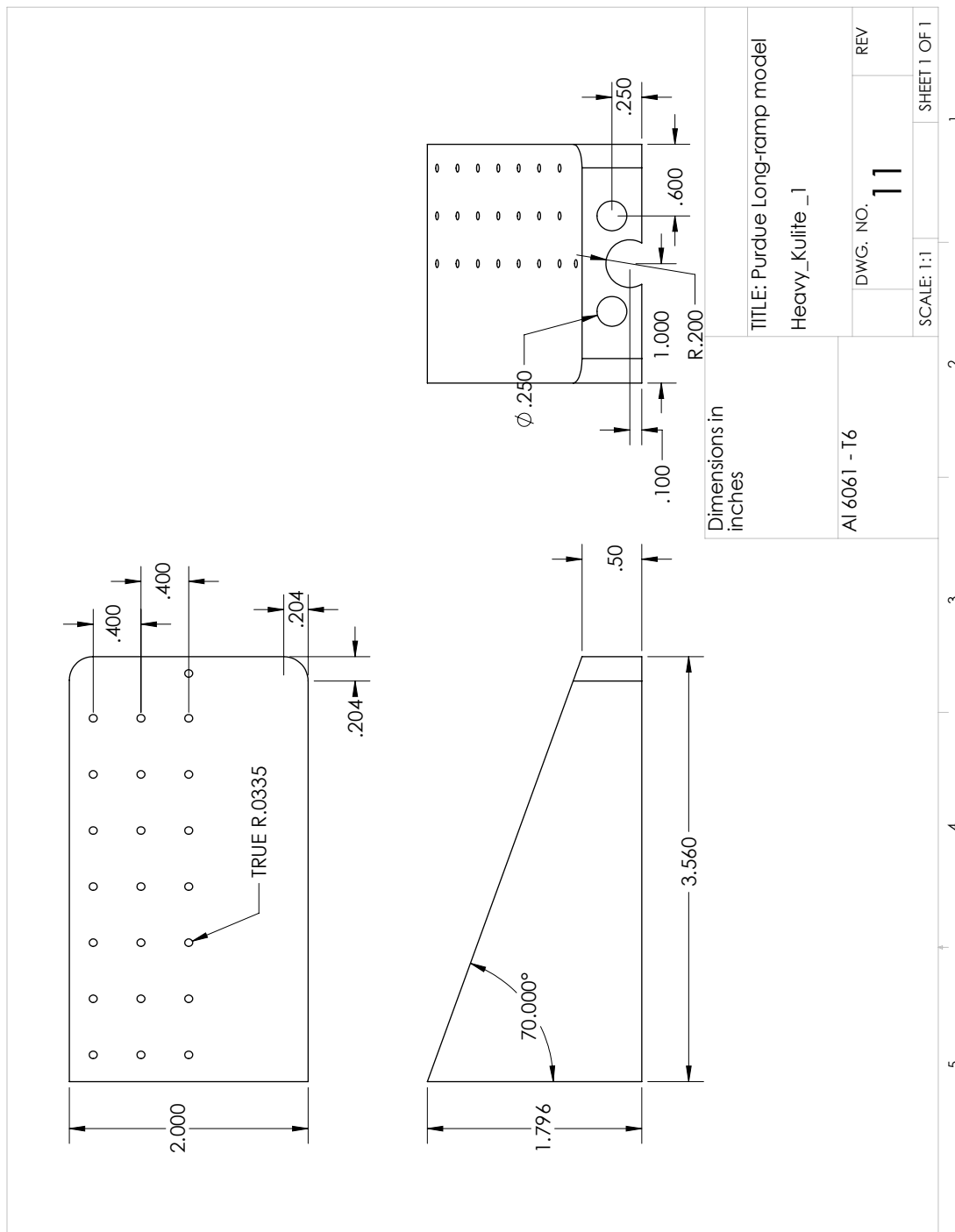


Figure D.18. Drawing of the 20° Kulite ramp - Part 1.

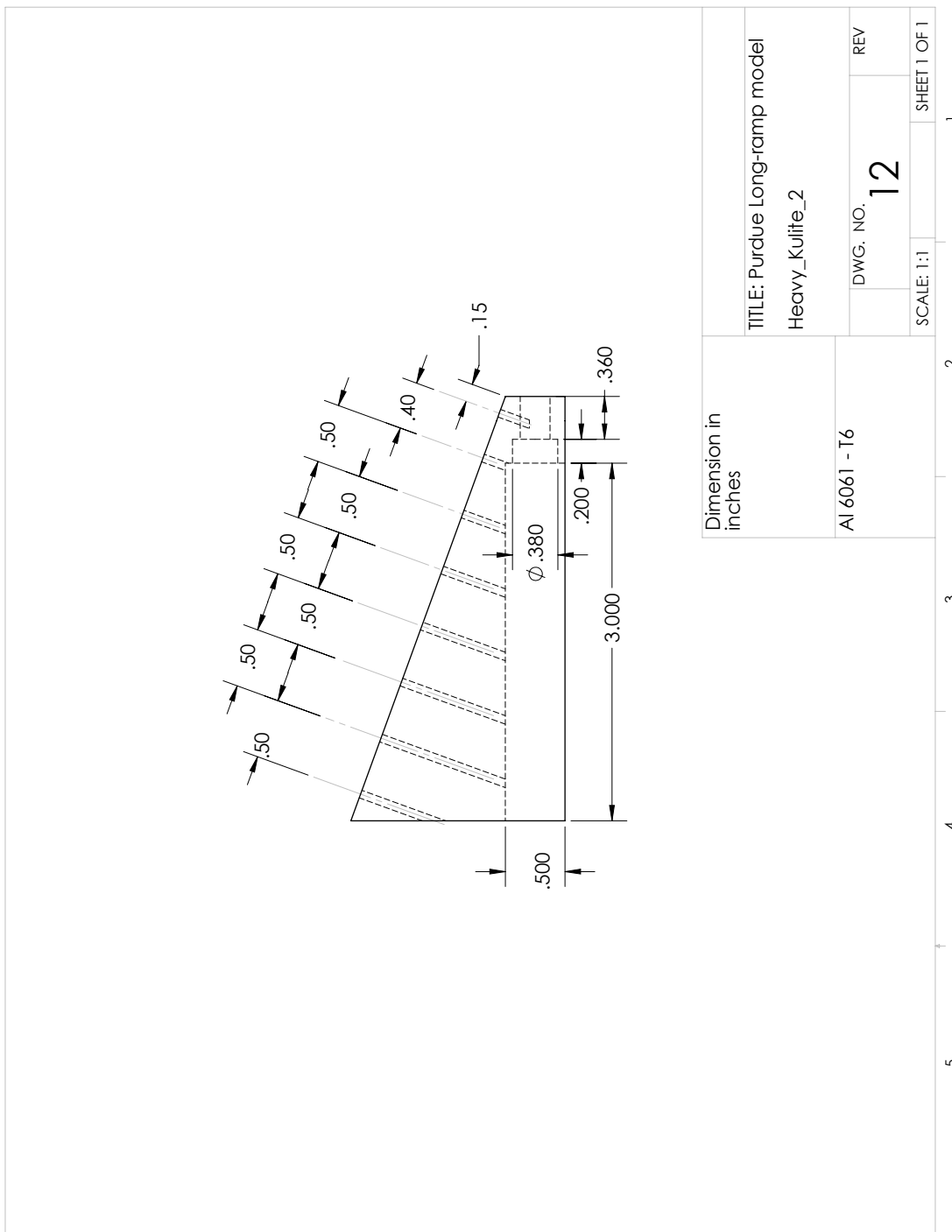


Figure D.19. Drawing of the 20° Kulite ramp - Part 2.

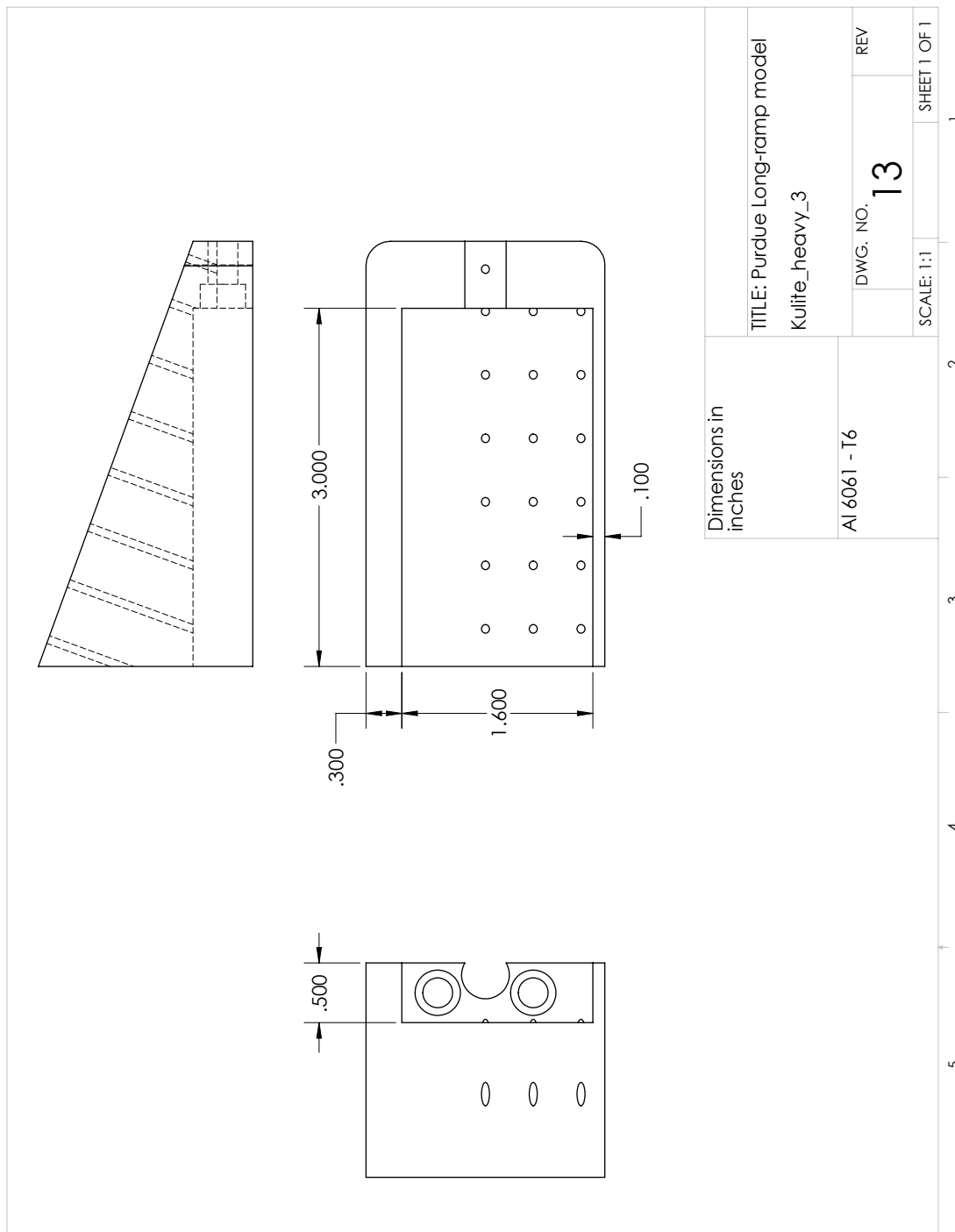


Figure D.20. Drawing of the 20° Kulite ramp - Part 3.

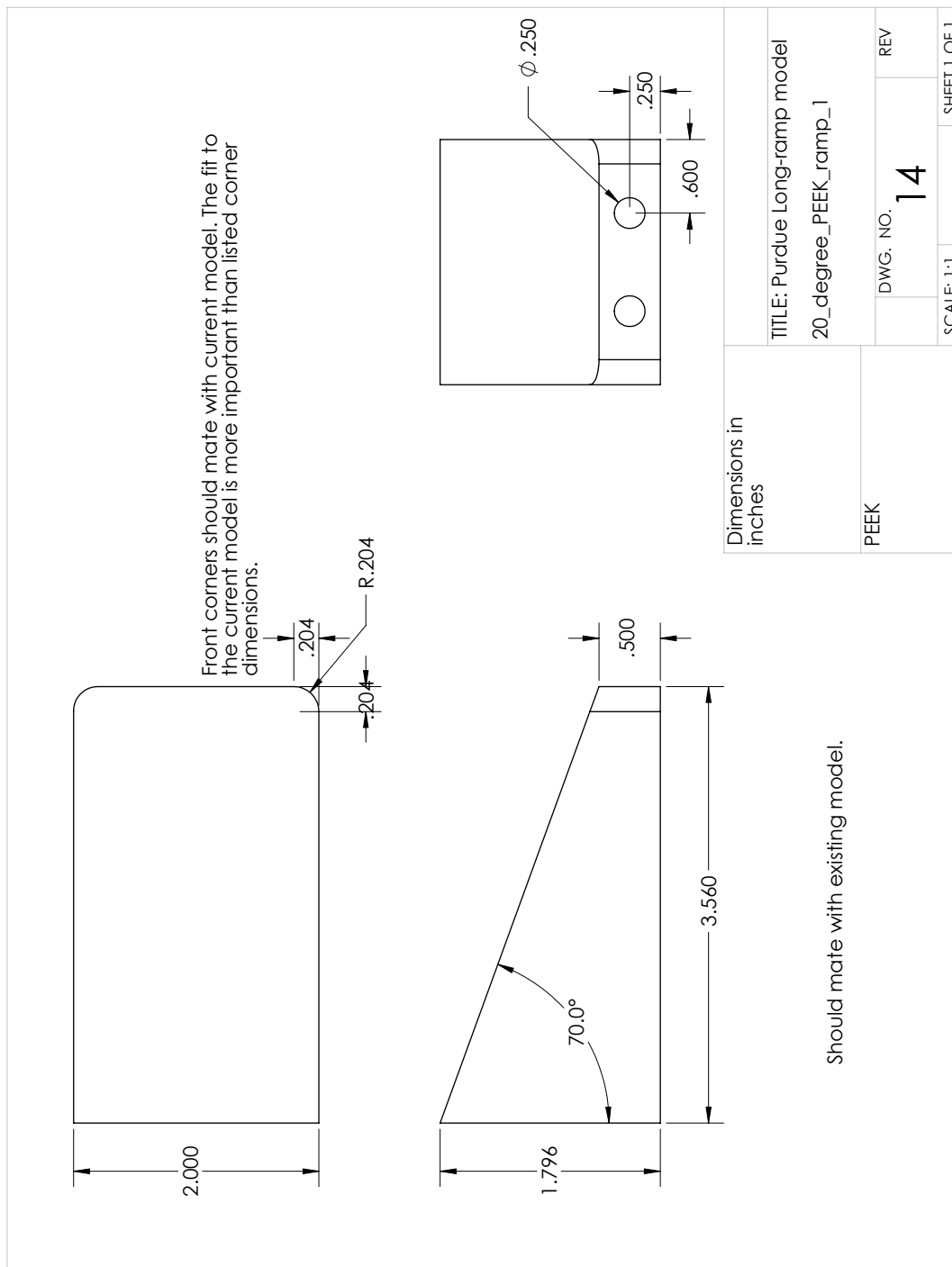


Figure D.21. Drawing of the 20° PEEK ramp - Part 1.

### D.3 7° Cone Perturbation model

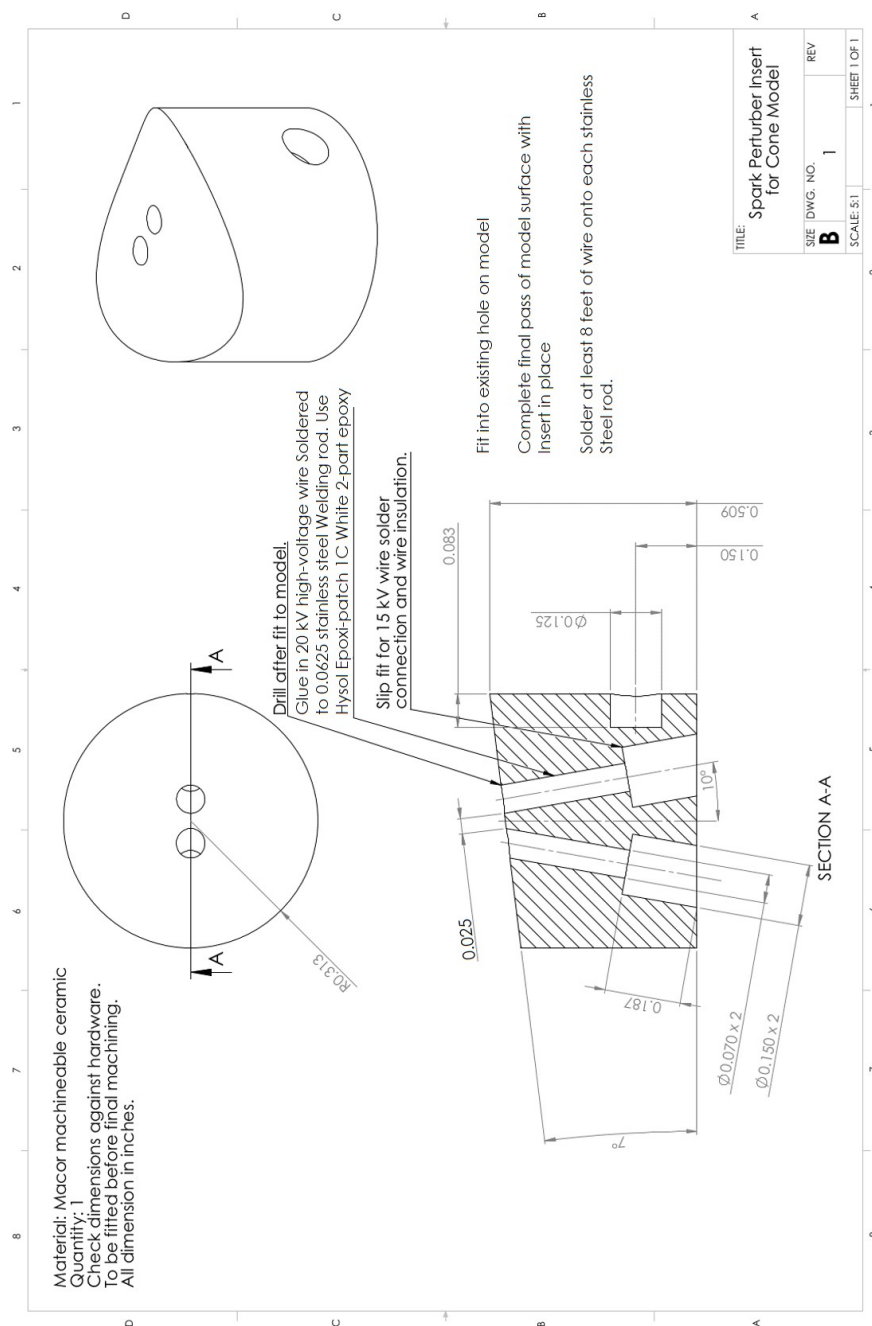


Figure D.22. Drawing of the MACOR perturber insert. This was utilized in all perturbation models and was adapted from Casper [112].

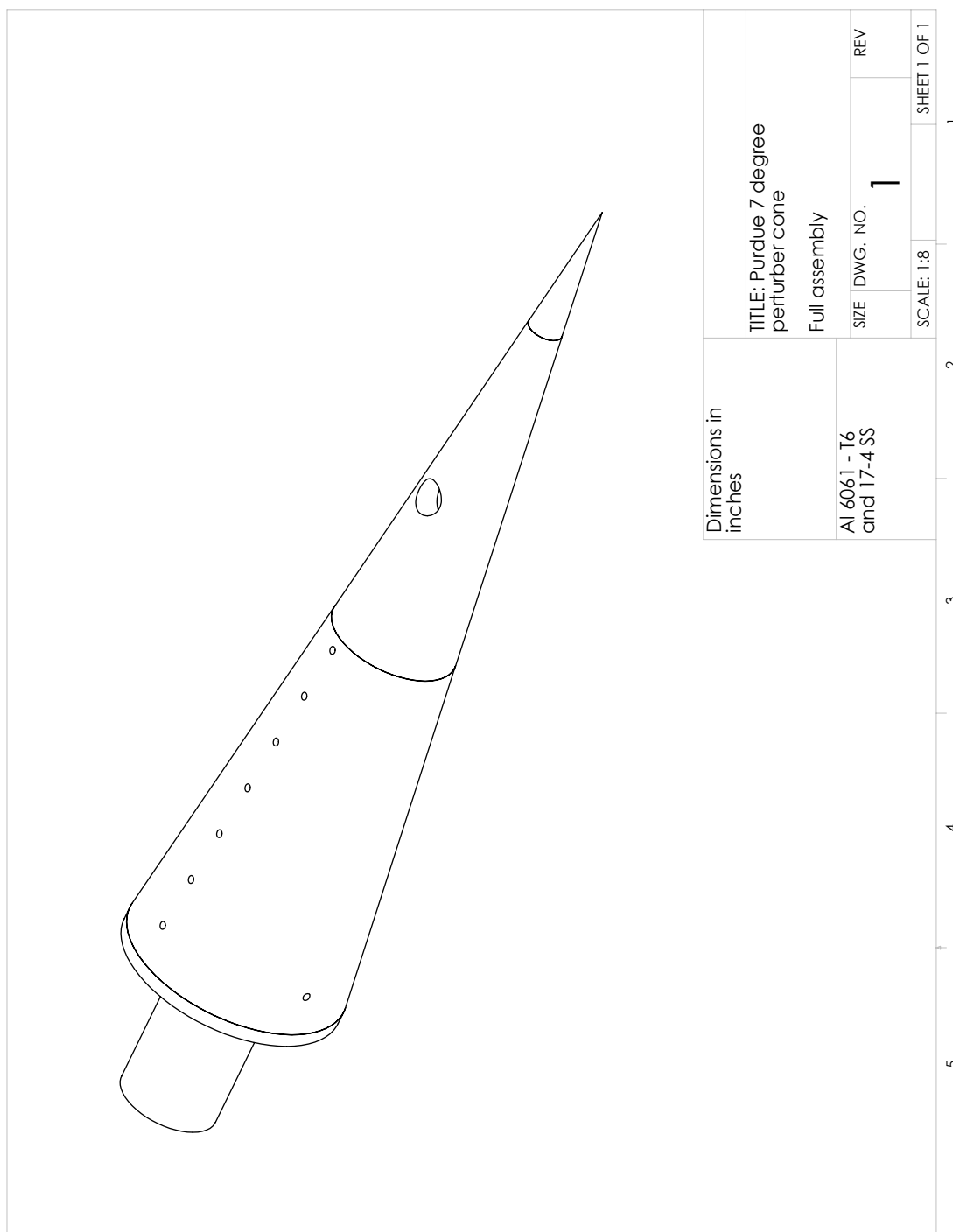


Figure D.23. Drawing of the 7° cone assembly

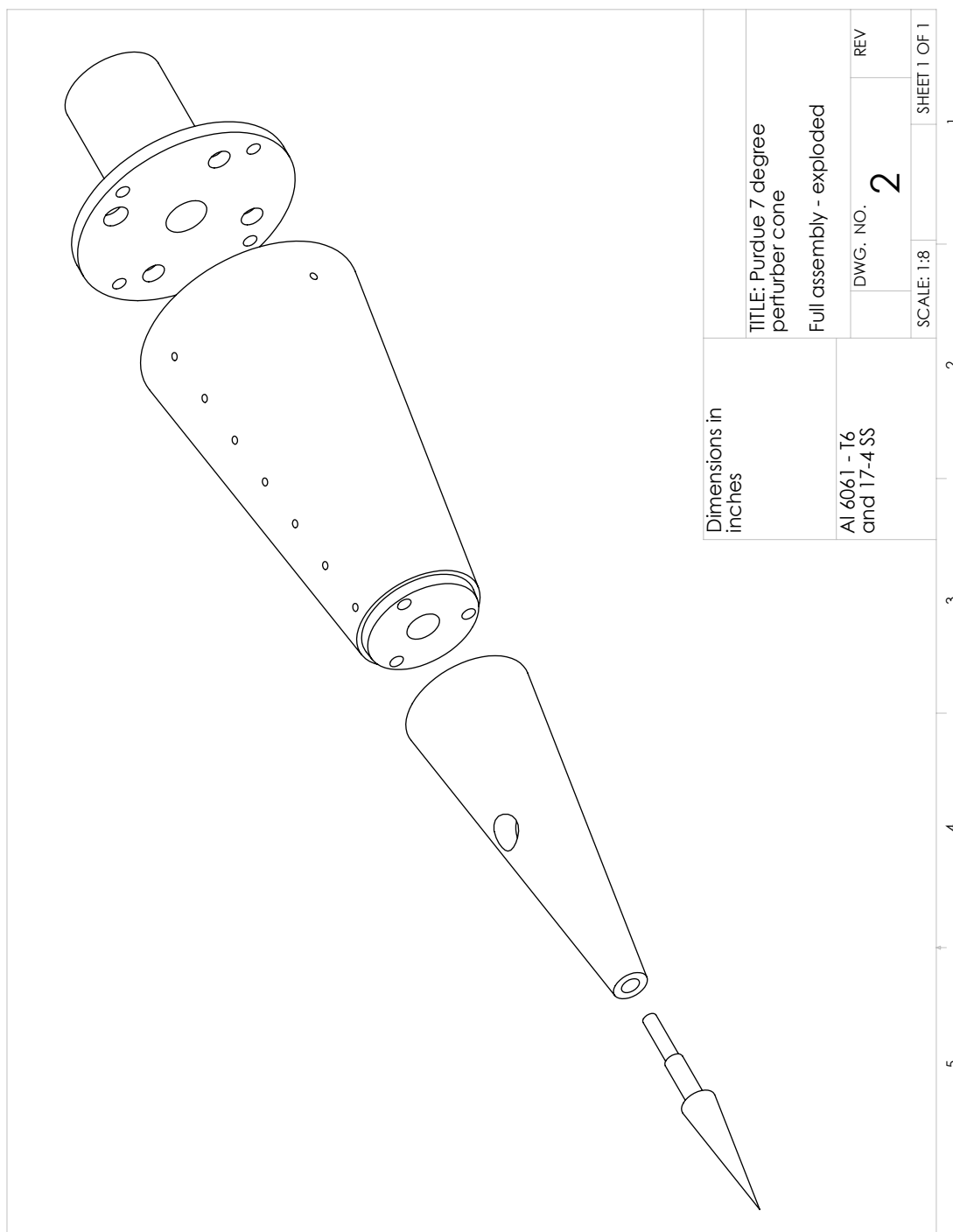


Figure D.24. Drawing of the 7° cone exploded assembly



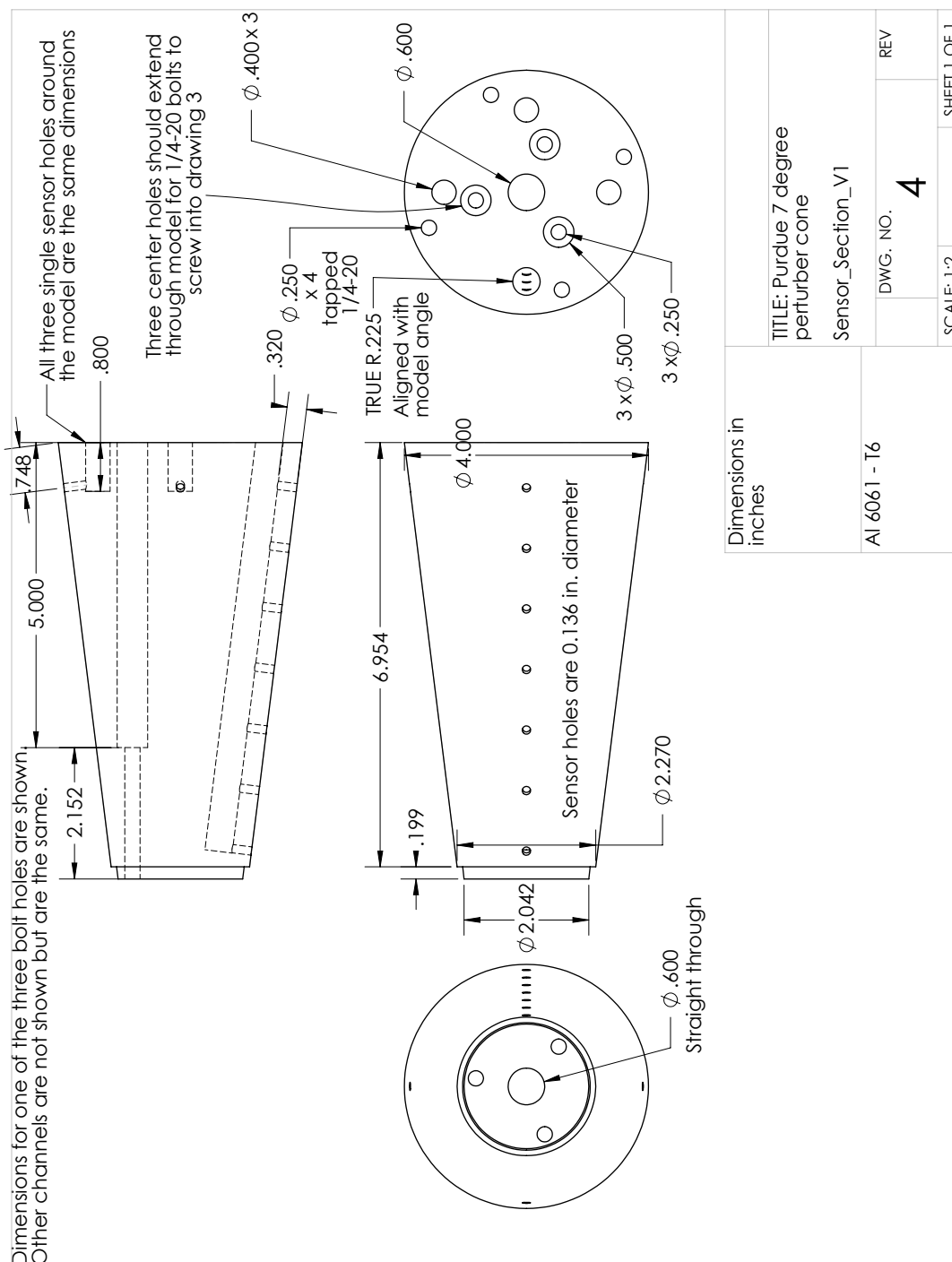


Figure D.26. Drawing of the 7° cone sensor body - Part 1.

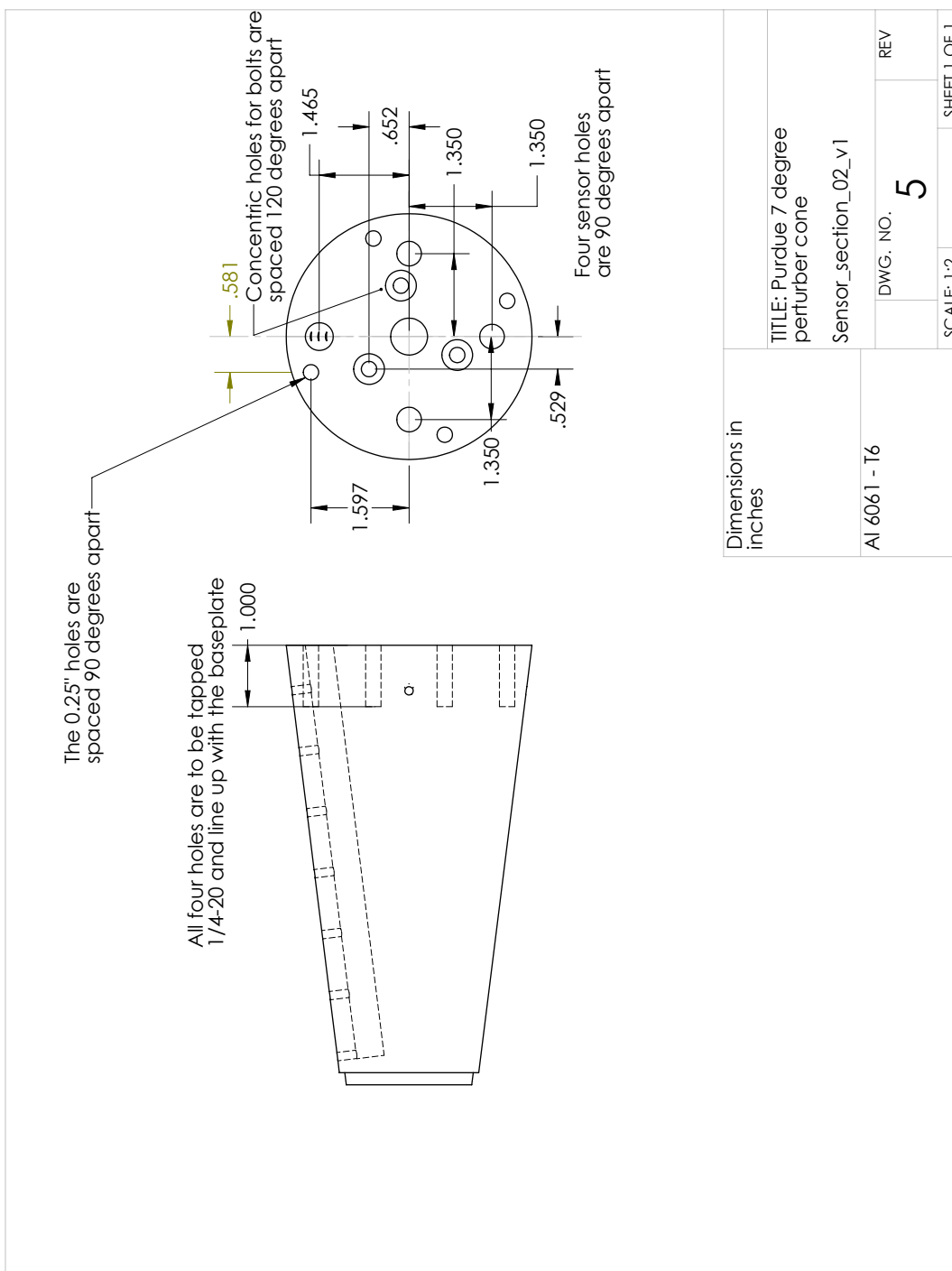


Figure D.27. Drawing of the 7° cone sensor body - Part 2.





## D.4 Long-Ramp Perturbation model

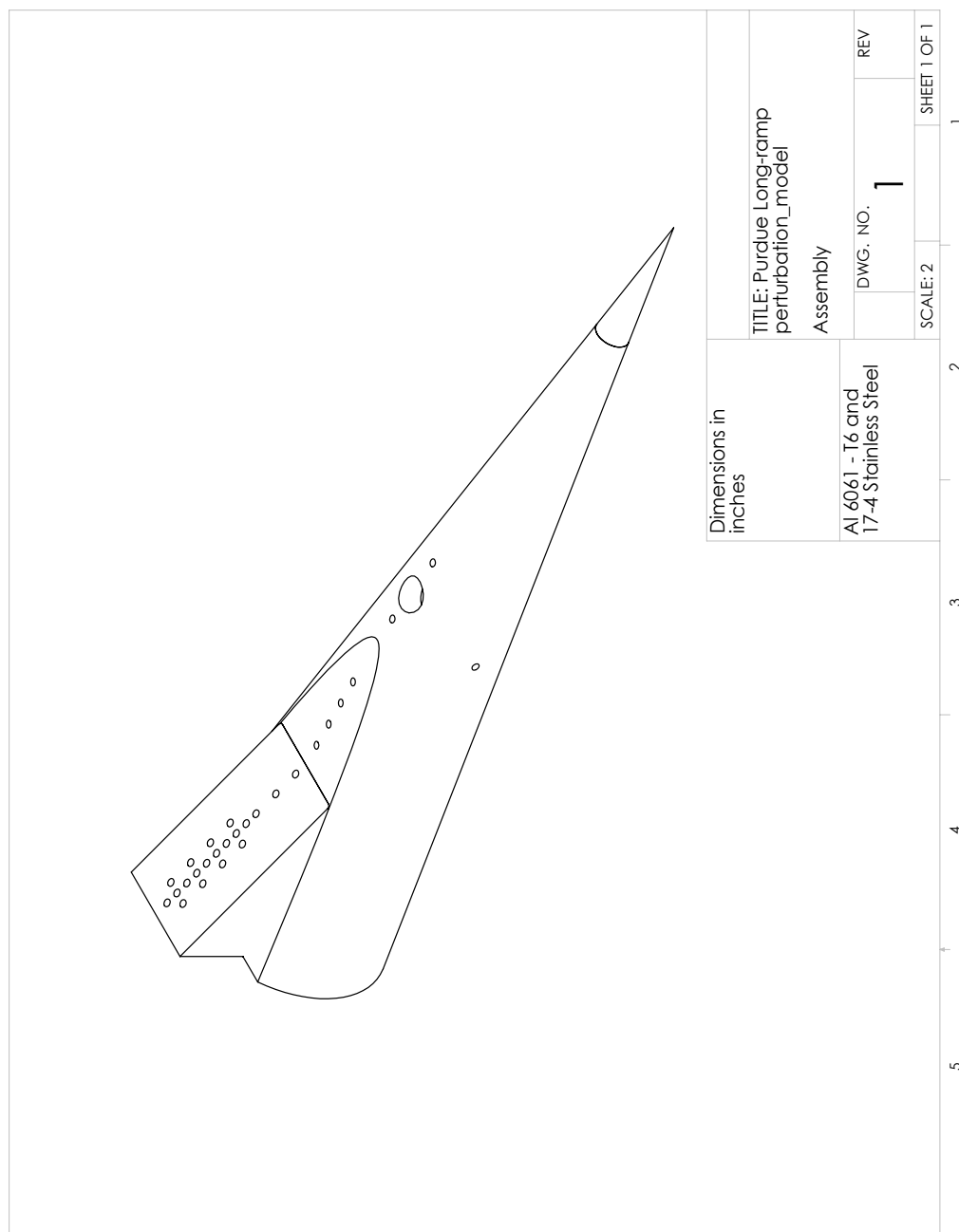


Figure D.30. Drawing of the long-ramp perturbation model assembly

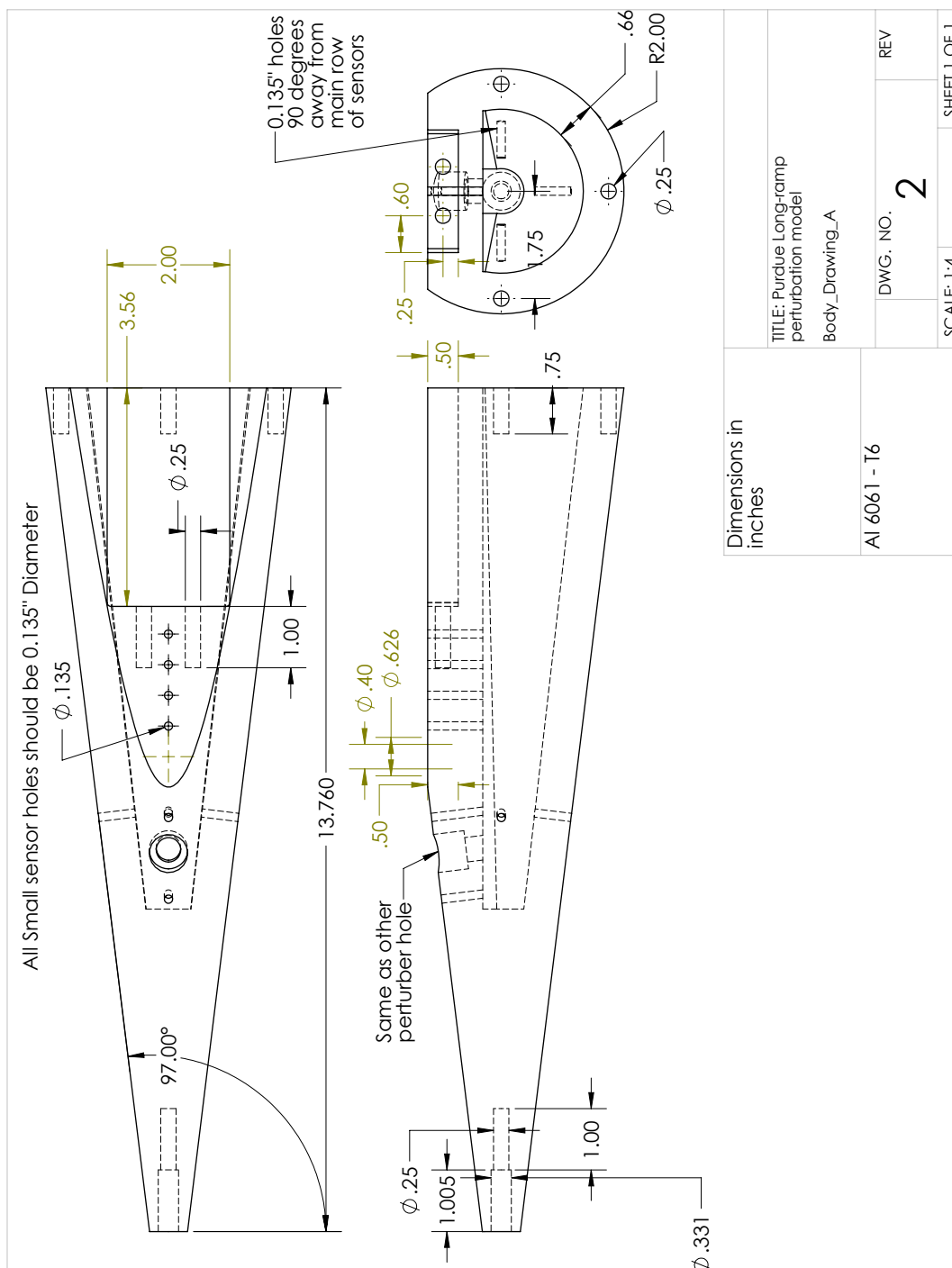


Figure D.31. Drawing of the long-ramp perturbation model body - Part 1.



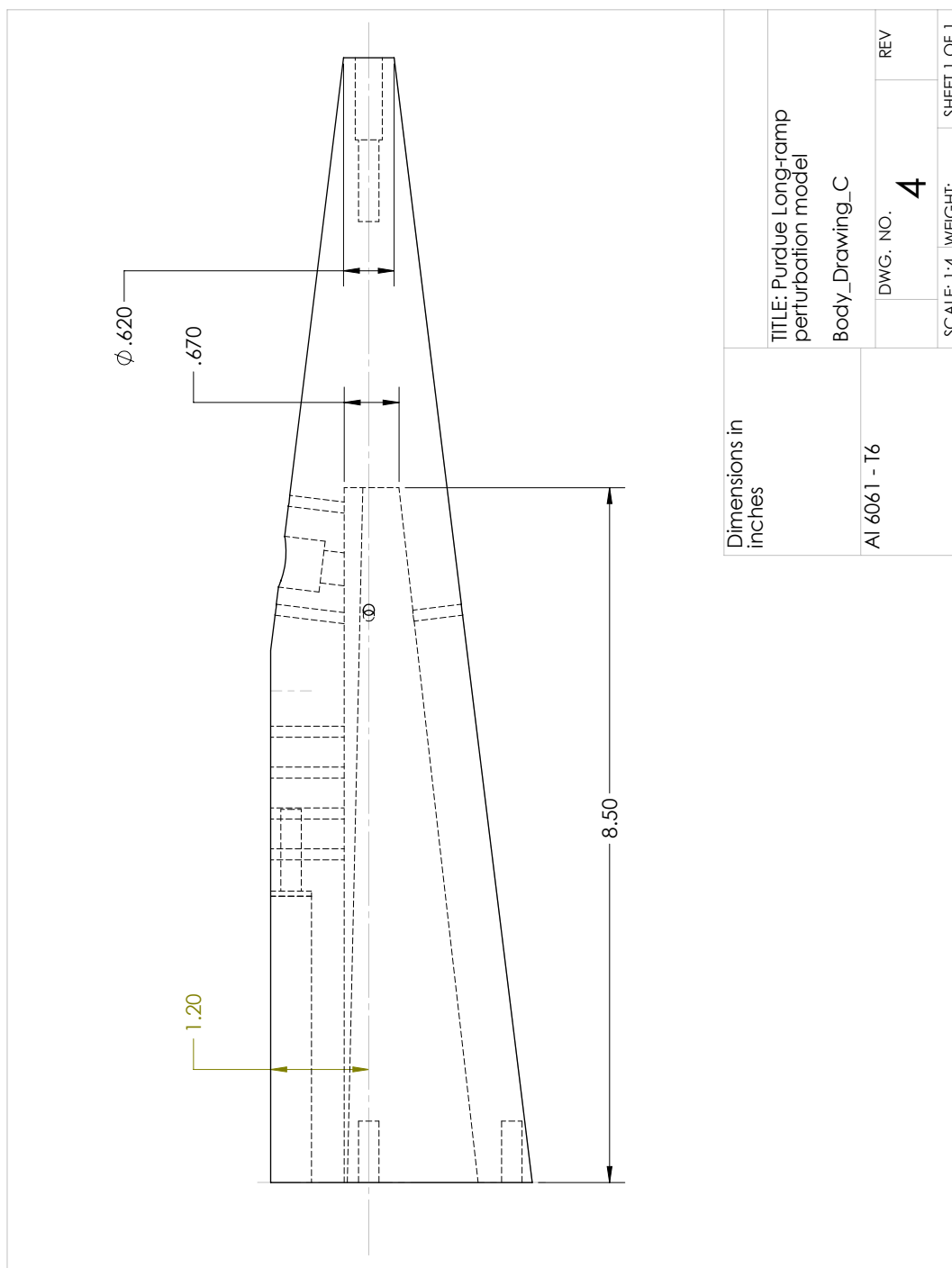


Figure D.33. Drawing of the long-ramp perturbation model body - Part 3.

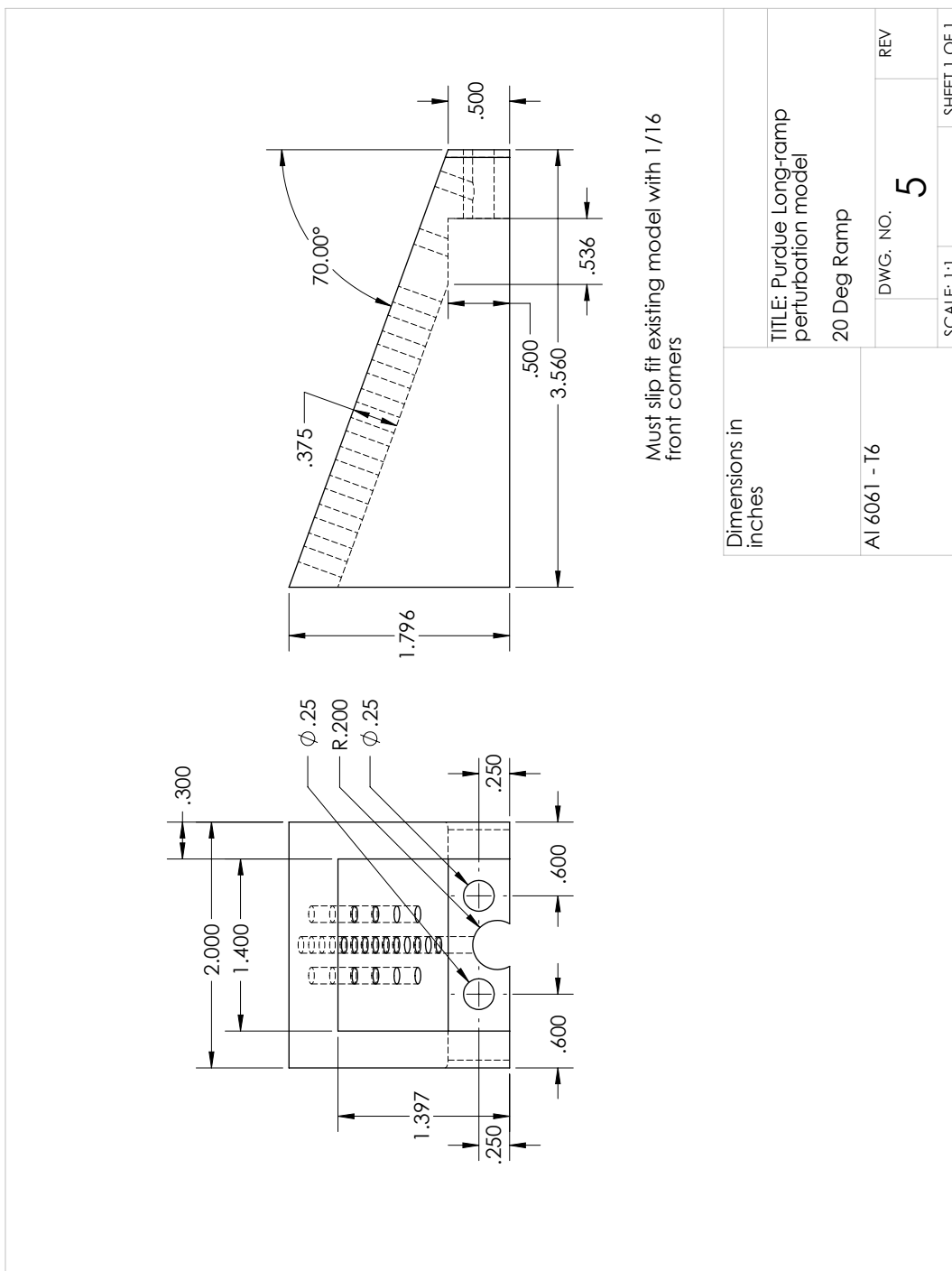


Figure D.34. Drawing of the long-ramp perturbation model instrumented 20° ramp - Part 1.

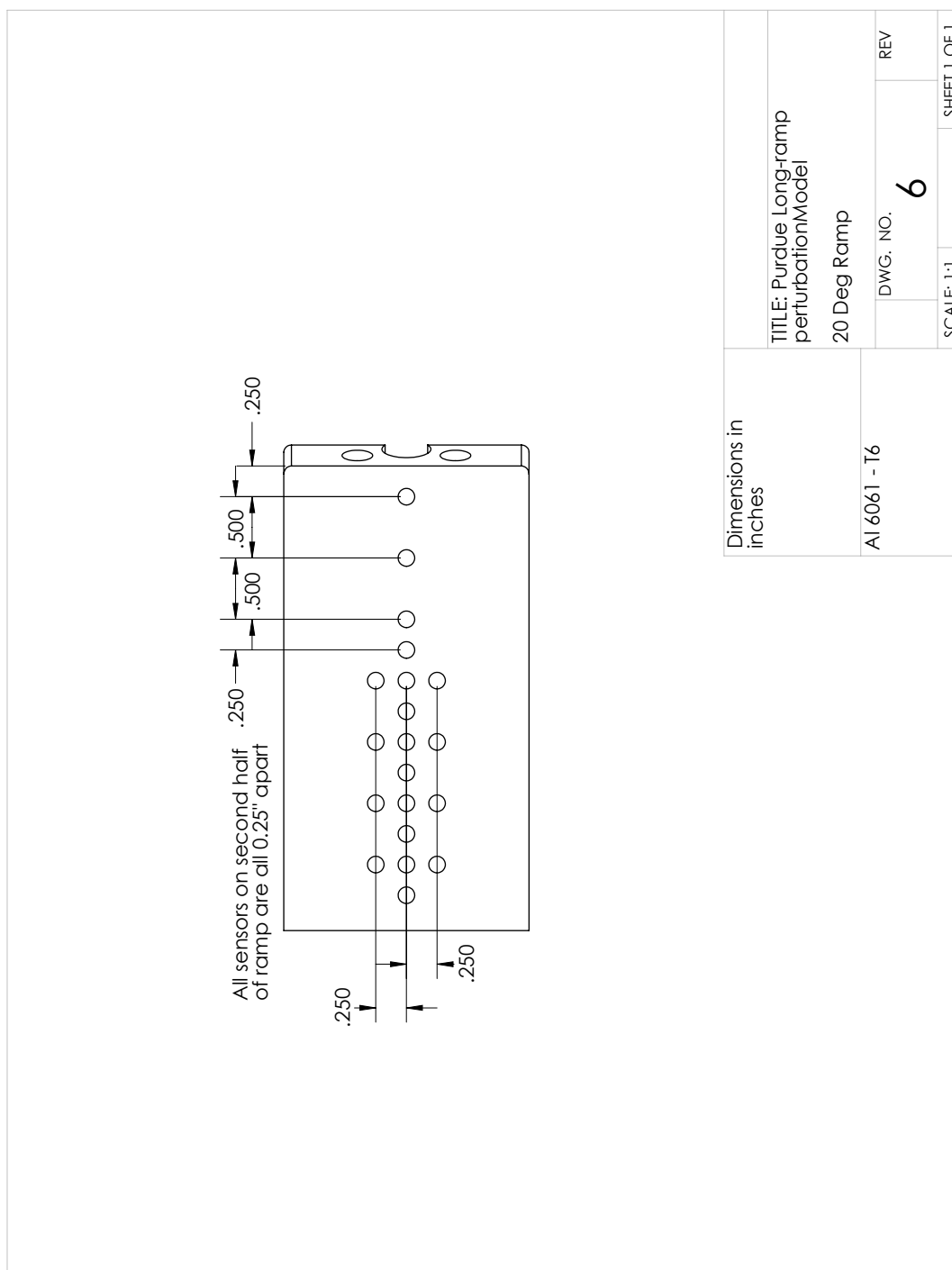


Figure D.35. Drawing of the long-ramp perturbation model instrumented 20° ramp - Part 2.

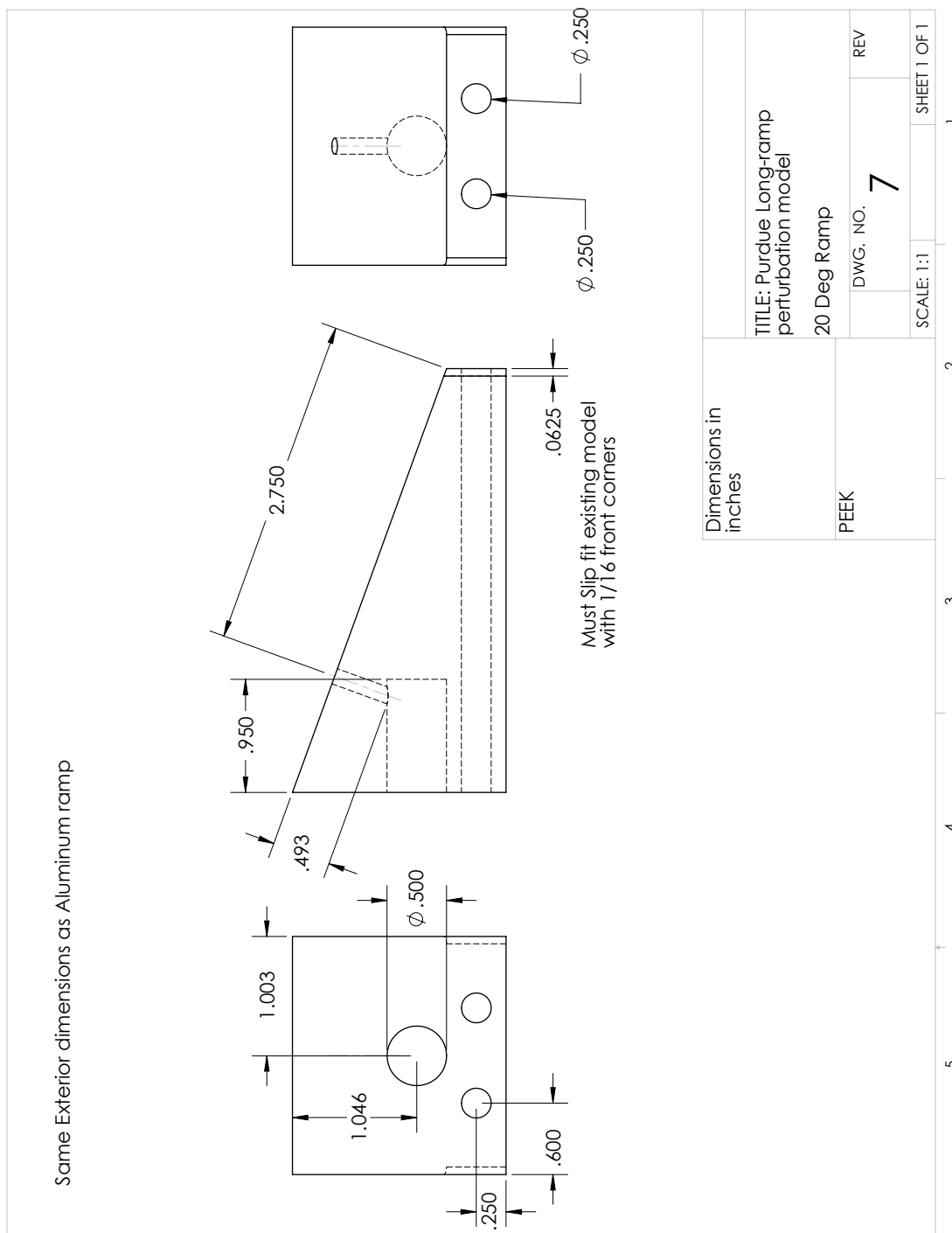


Figure D.36. Drawing of the long-ramp perturbation model PEEK 20° ramp.

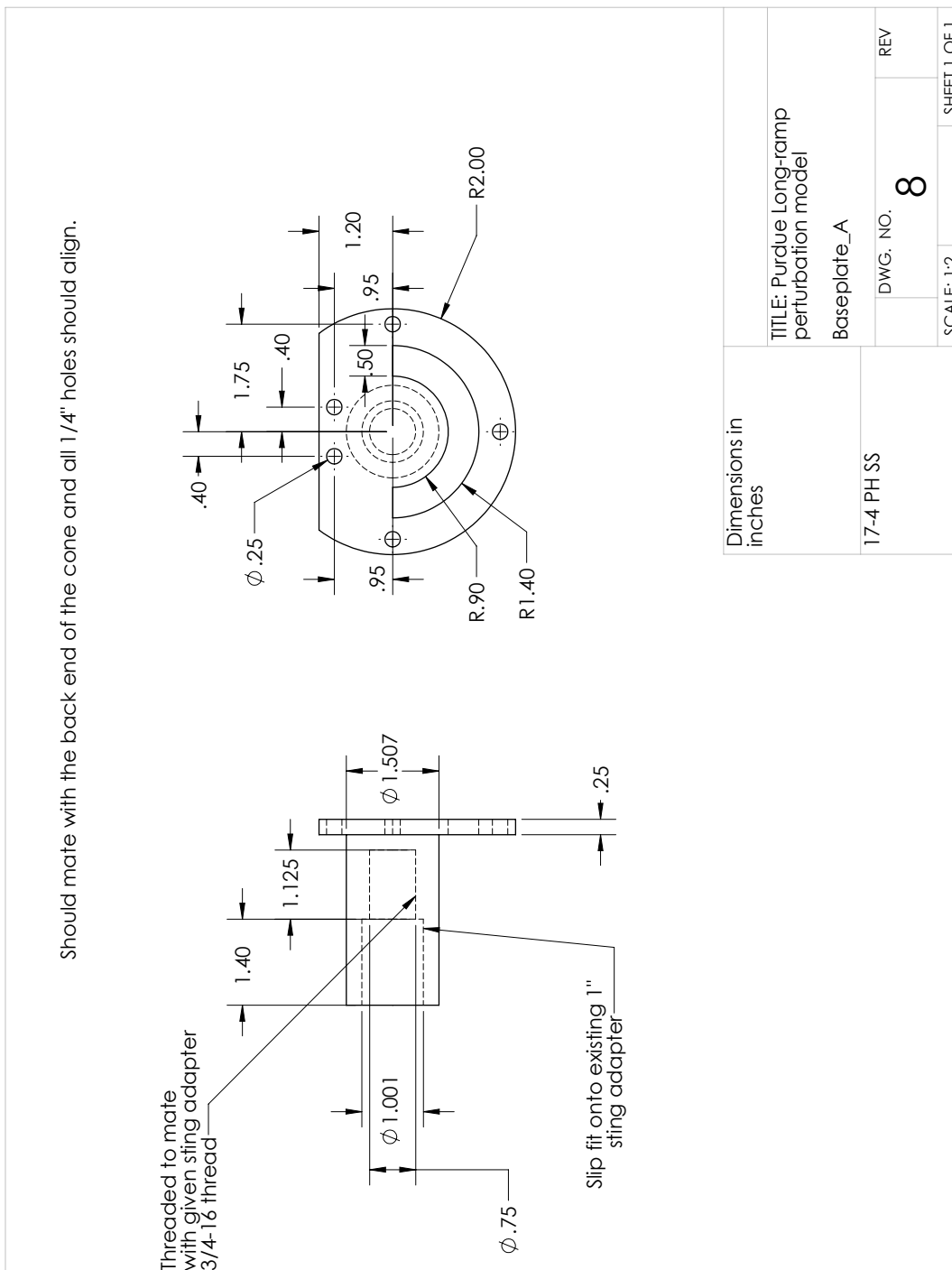


Figure D.37. Drawing of the long-ramp perturbation model baseplate - Part 1.

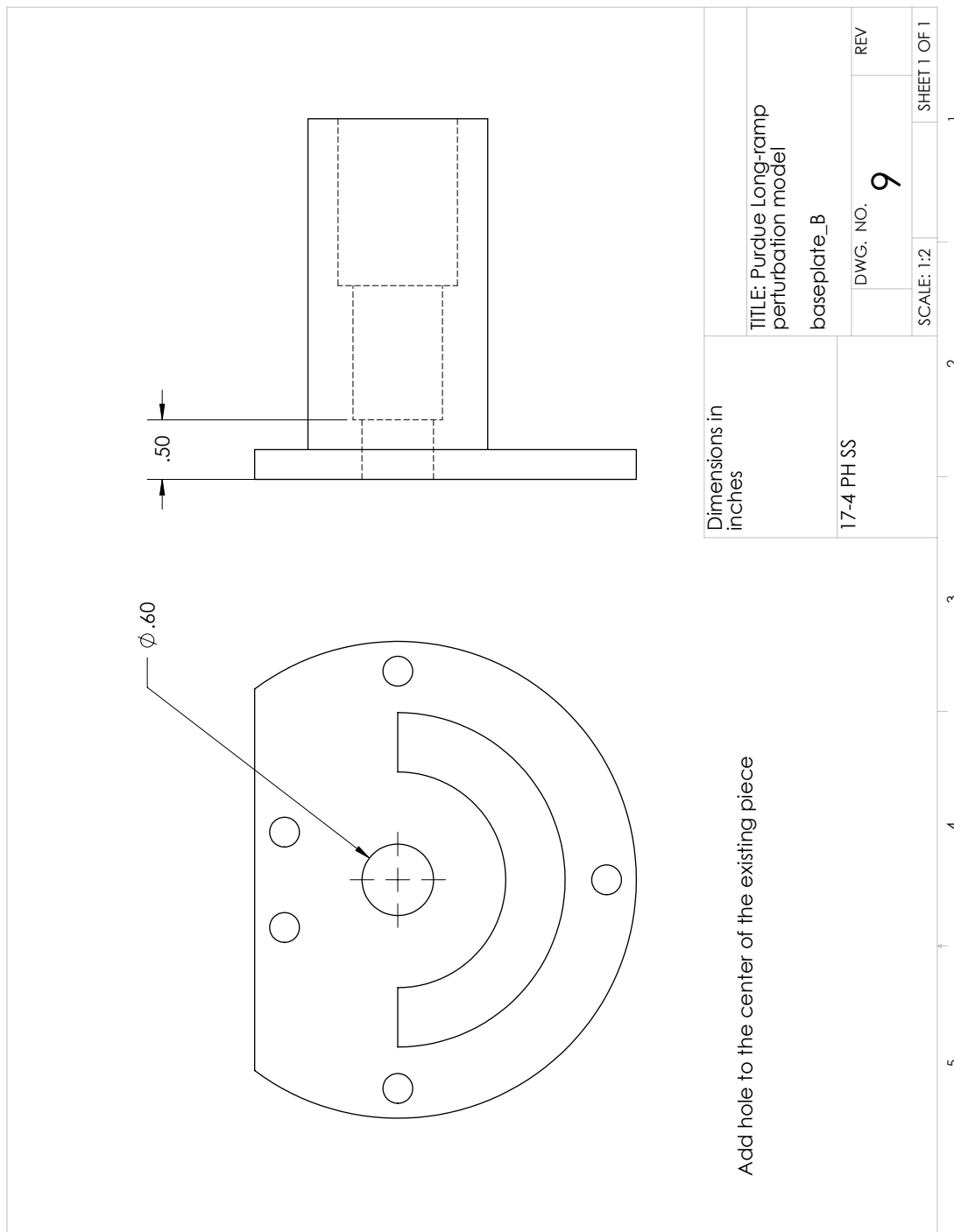


Figure D.38. Drawing of the long-ramp perturbation model baseplate - Part 2.